FAST SPECTRUM MATERIALS TESTING REACTOR WITH VARIABLE ENERGY SPECTRA TO SUPPORT ADVANCED REACTORS PROGRAM AND LIGHT WATER REACTOR SUSTAINABILITY PROGRAM R&D

A Thesis

by

JONATHAN B. SCHERR

Submitted to the Office of Graduate and Professional Studies of
Texas A&M University
in partial fulfillment of the requirements for the degree of

MASTER OF SCIENCE

Chair of Committee,	Pavel V. Tsvetkov
Committee Members,	Sean M. McDeavitt
	Michael Pate
Head of Department,	Yassin A. Hassan

May 2016

Major Subject: Nuclear Engineering

ABSTRACT

The current US fleet of LWR's are approaching the end of their original 40 year licenses. Most of these have applied for and been granted 20 year license extensions. Further increases in license length require more materials research into, amongst other things, neutron damage and stress corrosion cracking. In addition to the Light Water Reactor Sustainability program, the US maintains an Advanced Reactor program and Next Generation Nuclear Plant program. All three programs require extensive materials research, especially into fast neutron damage of core materials. A sodium cooled fast reactor based on EBR-II was designed in accordance with requirements generated by a Nuclear Energy Advisor Commission subcommittee released in November 2014. The reactor operates at 600 MW_{th} and has sections of epithermal and thermal flux within the outer reflector. LEU metallic fuel was used without any plutonium. The active core is 1 meter tall and has an effective diameter of 1.13 meters. Magnesium Oxide was used as a reflector.

The fast flux within the core depends on the enrichment of the core. Many different fuel loadings were investigated. Peak fast fluxes within the central irradiation positions vary from 5E15 to 7.5E15 n/cm^2s. Higher fluxes are associated with longer core lifetimes, which vary from greater than one year to approximately 100 days. Shuffling schemes were not analyzed, but simple refueling schemes were analyzed. The recommended driver irradiation locations provide more space at higher fluxes than comparable research reactors from around the world. The moderating region, which is composed of graphite, is highly versatile. While the size of the region was constant throughout the investigation, a wide range of configurations were studied. It is possible to irradiate materials within the reactor at fission powers and neutrons spectra typical of PWR’s and VHTR’s. Transient testing flux traps are located in the outer reflector, away from the moderating region and driver. Assemblies can be subjected to transients at constant reactor power. Both control drums and control rods can be used to control reactivity. The use of rods versus drums depends on initial k_{eff} and the degree of acceptable flux perturbation within the driver and reflector.

TABLE OF CONTENTS

Page

ABSTRACT ii

TABLE OF CONTENTS iv

LIST OF FIGURES vi

LIST OF TABLES xii

1. INTRODUCTION 1

    1.1 Design objectives 3
    1.2 Characteristics of test reactors 5
    1.3 Design criteria 14
    1.4 Design approach 15

2. THE CORE 18

    2.1 Outline of the base geometry 20
    2.2 The driver region 35
    2.3 Burnup simulations 54

3. TRANSIENT TESTING LOOPS 81

    3.1 PWR transient testing 88
    3.2 SFR transient testing 100
    3.3 VHTR transient testing 110

4. THE MODERATING REGION 117

    4.1 Unperturbed behavior of the moderating region 119
    4.2 The effects of graphite and light water 146
    4.3 PWR test assemblies in the moderating region 157
    4.4 VHTR test assemblies in the moderating region 170
    4.5 Passive irradiation capsules 179

5. CONTROL SYSTEMS 197

    5.1 Control rods 199

5.2 Control drums....212
6. CONCLUSION 220
6.1 Description of the base geometry....229
REFERENCES....233

LIST OF FIGURES

Page

Figure 1.1 Excerpt from the ATR User’s Manual (FY, 2009). 9

Figure 2.1 Driver fuel assembly 21

Figure 2.2 Outer reflector assembly 22

Figure 2.3 The whole core. The origin of the geometry is in the center of the figure, in the middle of the central irradiation position. This figure is plotted on the x-y axis. Positive x is towards the right, positive y is towards the top, and positive z is out of the page. This follows the right hand rule. The core was designed in two vertical halves, one in the positive z and the other in the negative z. The active core is 100 cm tall; its upper dimension is at z=50.0cm and its lower dimension is at z=-50.0 cm. 24

Figure 2.4 The whole core, plotted on the x-z axis through the origin. The sodium gap between assemblies makes it appear that there is more sodium in the core.. 28

Figure 2.5 Mesh of the base geometry. Used to zone the core....................................... 31

Figure 2.6 Close up of the central region. 32

Figure 2.7 Close up of the outer driver. 32

Figure 2.8 Close up of the outer driver and barrier assemblies. 33

Figure 2.9 Radial flux with the MgO reflector 38

Figure 2.10 Radial flux fraction with the MgO reflector 38

Figure 2.11 Axial flux with the MgO reflector 40

Figure 2.12 Axial flux fraction with the MgO reflector 41

Figure 2.13 Radial flux fractions with the BeO reflector 41

Figure 2.14 Radial flux fraction with the graphite reflector 42

Figure 2.15 Radial relative slow group flux with MgO, BeO, and graphite reflectors... 43

Figure 2.16 Radial flux fractions with the PbO reflector 44

Figure 2.17 Radial relative fast flux with MgO, graphite, BeO, and PbO 44

Figure 2.18 Configuration 1 47

Figure 2.19 Configuration 2 48

Figure 2.20 Configuration 3 48

Figure 2.21 Core geometry with 7 small irradiation positions in the inner driver and 2 large irradiation positions in the outer driver.. 51

Figure 2.22 The core with the large irradiation positions replaced by an equivalent number of smaller irradiation positions. 52

Figure 2.23 k_{eff} versus total burnup for the base geometry with linear best fit 57

Figure 2.24 Comparison of the two burnup schemes 60

Figure 2.25 Benchmark of the base geometry performed with more materials 62

Figure 2.26 Neutron spectra of the base geometry driver region at 0 MWd/kgU and 50 MWd/kgU. 66

Figure 2.27 k_{eff} versus time for the 20_11 core and refueling scheme............................ 74

Figure 2.28 Breeding ratio for cores with different enrichments and fuel volume fractions but the same amount of fissile material 78

Figure 3.1 Locations of flux trap and transient test assembly.. 82

Figure 3.2 ^{113}Cd absorption cross section. Generated with JANIS 4.0 (Soppera, 2014) 85

Figure 3.3 ^{10}B absorption cross section. Generated with JANIS 4.0 (Soppera, 2014).... 86

Figure 3.4 PWR test assembly in the transient test trap. The cadmium doped reflectors assemblies and boron control assemblies are highlighted. 89

Figure 3.5 Axial power profile of a PWR test assembly at full power 92

Figure 3.6 PWR test assembly neutron spectra at full power 95

Figure 3.7 Pin power of the PWR test assembly. The square lattice has three rows and three columns. Each line gives pins power for constant horizontal pin rows. The x-axis gives the x-coordinate of the pins, while each line gives the y-coordinate of the pin. The y-axis gives average pin power. 96

Figure 3.8 SFR test assembly and flux trap. The flux trap is the same configuration as presented in the PWR section. The SFR test assembly uses a hexagonal lattice with dimensions derived from a generic oxide fueled sodium fast reactor (Fast, 2006). 101

Figure 3.9 SFR transient test assembly neutron spectrum as full power. 102

Figure 3.10 Axial power profile for a SFR test assembly at full power........................ 104

Figure 3.11 Pin power of the SFR test assembly at full power. The y-axis gives linear power of each pin and the x-axis gives the x-coordinate of each pin. The lines are for constant y-coordinate... 107

Figure 3.12 Pin power for a SFR test assembly with one fuel rod replaced with a fuel rod. 109

Figure 3.13 A VHTR test assembly with a close up of a fuel particle 111

Figure 3.14 Axial power profile of VHTR test assembly at full power 113

Figure 3.15 Neutron spectra in a VHTR test assembly at full power 116

Figure 4.1 Location of central region and tails within core 121

Figure 4.2 Central region with each smaller section outlined....................................... 122

Figure 4.3 The red arrow represents the orientation of the fast and epithermal flux maps while the yellow arrow represents the orientation of the thermal flux map.. 123

Figure 4.4 Fast flux in the moderating region with graphite 124

Figure 4.5 Epithermal flux in the moderating region with graphite 126

Figure 4.6 Thermal flux in the moderating region with graphite 127

Figure 4.7 Locations of regions in Table 4.1. Graphite moderator 129

Figure 4.8 Orientation of Figure 4.9.. 131

Figure 4.9 Thermal flux in the moderating region composed of light water 132

Figure 4.10 Locations of sections for Table 4.2 133

Figure 4.11 Location of beryllium in barrier assemblies 135

Figure 4.12 Orientation of Figure 4.13. 137

Figure 4.13 Thermal flux with graphite moderator and beryllium in the barrier assemblies. 138

Figure 4.14 Cadmium doped barrier assembly 140

Figure 4.15 Thermal flux in graphite without canned assemblies 142

Figure 4.16 Thermal flux with light water without assembly cans 145

Figure 4.17 Picture of the core with two irradiation test assemblies and twelve flux shaping assemblies around it. 147

Figure 4.18 Flux fraction versus graphite fraction 149

Figure 4.19 Reactivity penalty of graphite fraction with two irradiation assemblies ... 151

Figure 4.20 Simulation 13, light water near the irradiation positions 152

Figure 4.21 Simulation 14, graphite near the irradiation positions 152

Figure 4.22 Simulation 19, graphite near the irradiation locations. 154

Figure 4.23 PWR test assembly 159

Figure 4.24 Location of PWR test assemblies near core 160

Figure 4.25 Flux in the PWR test assemblies near the driver with the flux a prototypic PWR pin. 162

Figure 4.26 Relative flux of the PWR test assemblies near the driver and a prototypic PWR pin 163

Figure 4.27 PWR test assembly far from driver with Er_2O_3 absorber and light water in the flux shaping assemblies. 165

Figure 4.28 Location of PWR test assemblies and flux shaping assemblies in driver.. 166

Figure 4.29 Flux of the PWR test assemblies far from the driver with Er2O3 and light water flux shaping assemblies with a prototypic PWR flux................. 167

Figure 4.30 PWR test assembly and prototypic PWR axial power profiles................. 169

Figure 4.31 Location of VHTR test assemblies near driver... 170

Figure 4.32 VHTR test assembly and flux shaping assembly...................................... 172

Figure 4.33 Flux of VHTR test assemblies with Er2O3 pin and graphite pins in light water flux shaping assemblies 174

Figure 4.34 Graphite capsule in light water filled irradiation assembly 180

Figure 4.35 Flux in graphite capsule in light water filled irradiation assembly............ 182

Figure 4.36 Steel capsule in light water filled irradiation position. The steel is shifted 1.2 cm to the left, or away from the driver. As the local origin of the assemblies is the center of each assembly, the steel is centered at (-1.2 cm, 0.0 cm, 0.0 cm). 184

Figure 4.37 Steel capsule centered at 1.2 cm in a light water filled irradiation assembly.. 185

Figure 4.38 Flux in each group for the steel capsule at different positions in a light water filled irradiation assembly.. 186

Figure 4.39 Relative flux for a steel capsule centered at 1.2 cm and a prototypic PWR.. 188

Figure 4.40 A steel capsule centered at 1.2 cm with a dividing line between light water and graphite at -2.0 cm... 190

Figure 4.41 A steel capsule centered at 2.0 cm with the dividing line between light water and graphite at 2.0 cm. 191

Figure 4.42 4 group fluxes and total fluxes for a steel capsule centered at 1.2 cm with different locations at the dividing line between light water and graphite...... 192

Figure 4.43 Relative flux of steel capsule centered at 1.2 cm surrounded by graphite in an irradiation assembly next to the driver and a prototypic PWR pin....... 195

Figure 4.44 Relative flux of steel capsule centered at 1.2 cm surrounded by graphite in an irradiation assembly next to the driver with the dividing line between light water and graphite at 0.0 cm and a prototypic PWR pin. 196

Figure 5.1 Locations of the control rod banks within the core and reflector 199

Figure 5.2 Control rods within the core 200

Figure 5.3 Differential rod worth 202

Figure 5.4 Integral rod worth 202

Figure 5.5 Axial fast flux 204

Figure 5.6 Axial epithermal flux 205

Figure 5.7 Radial fast flux 206

Figure 5.8 Radial epithermal flux 206

Figure 5.9 Locations of control rods in base geometry 210

Figure 5.10 Control drums in the reflector fully away from the driver 213

Figure 5.11 Close up of Figure 5.10 214

Figure 5.12 Drums at 180° 216

Figure 5.13 Drums at 120° with subdivisions of the reflector highlighted 218

LIST OF TABLES

Page

Table 1.1 HFIR 6

Table 1.2 ATR 6

Table 1.3 JHR 7

Table 1.4 MBIR 7

Table 1.5 MYRRHA 8

Table 2.1 k_{eff}, fast flux within the central region, and fast fraction within the central region with different reflectors. 36

Table 2.2 k_{eff} and fast flux within the central and surrounding flux traps for each configuration 47

Table 2.3 k_{eff} and fast fluxes within various irradiation positions with large outer irradiation positions 52

Table 2.4 k_{eff} and fast fluxes within various irradiation positions without large outer irradiation positions 52

Table 2.5 Core lifetime and fast fluxes for different configurations 54

Table 2.6 End of life isotopics for the same core with different irradiation schemes 58

Table 2.7 Initial keff, final burnup, core lifetime, initial fast flux, and final fast flux for the base and benchmark simulations. Burnup is in MWd/kgU, core lifetime is in days, and flux is in n/cm^{2}s. 63

Table 2.8 Select whole core isotopics for the base and benchmark cases 64

Table 2.9 4 group neutron spectra in the driver region of the base geometry. 67

Table 2.10 Burnup behavior of different core loadings with varying enrichments. Burnup is in MWd/kgU, core lifetime is in days, flux is in n/cm^{2}s, and Δflux/day is in n/(cm^2*s*d). 68

Table 2.11 Burnup behavior of different core shapes. Flux is given in n/cm2s, burnup is in MWd/kgU, core lifetime is in days, and Δflux/day is in n/(cm2s*d). 72

Table 2.12 Burnup behavior of different core loadings, all with greater fuel volumes. Flux is given in n/cm2s, burnup is in MWd/kgU, core lifetime is in days, and Δflux/day is in n/(cm2s*d). 73

Table 2.13 Burnup behavior for two cores with the same fissile mass but different enrichments and fuel volume fractions. Burnup in MWd/kgU, core lifetime in days, flux in n/cm2s, and Δflux/day in n/(cm^2*s*d) 77

Table 2.14 End of life isotopics for two core with different enrichments and fuel volume fractions but the same fissile mass. 80

Table 3.1 Reactivity's associated with PWR transient testing 90

Table 3.2 Power per energy group for a PWR test assembly at full power 93

Table 3.3 Power per group with rods fully inserted 94

Table 3.4 Reactivity's associated with a PWR transient test assembly with no cadmium in the reflector assemblies surrounding the flux trap. 98

Table 3.5 Reactivity's associated with a PWR transient test assembly with 1.0% cadmium in the reflector assemblies surrounding the flux trap. 99

Table 3.6 Reactivity's associated with SFR transient testing 103

Table 3.7 Power per energy bin for a SFR test assembly at full power 105

Table 3.8 Power per energy bin for a SFR test assembly with rods fully inserted 105

Table 3.9 Dimensions and compositions of the fuel particle 112

Table 3.10 Reactivity's associated with a VHTR test assembly 112

Table 3.11 Power per energy group in a VHTR test assembly at full power 114

Table 3.12 Power per energy group for a VHTR test assembly with rods fully inserted 115

Table 4.1 Flux fractions and total fluxes in different sections of the moderating region with graphite. 127

Table 4.2 Flux fractions and total flux with light water 132

Table 4.3 Flux fractions and total fluxes with graphite moderator and beryllium in the barrier assemblies 138

Table 4.4 Flux ratios for the graphite moderator without canned assemblies 143

Table 4.5 Flux ratios comparing light water in the moderating region with and without assembly cans. 144

Table 4.6 Comparison of the graphite pins in light water versus light water holes in graphite for the same volume fraction. Greatest difference between the two. 148

Table 4.7 Fluxes, flux fractions, k_{eff} and relative error for simulations 13, 14, and 15. 153

Table 4.8 Graphite fraction, material near irradiation position, and the thicknesses of the light water and graphite in Simulations 16, 17, 18, and 19 155

Table 4.9 Flux in each group, flux fraction, k_{eff}, and relative error for each Simulations 16, 17, 18, and 19... 157

Table 4.10 Fluxes and flux ratios within a PWR test assembly near the core 164

Table 4.11 Flux data for a PWR test assembly far from the core surrounded by moderating and absorbing flux shaping assemblies. 168

Table 4.12 Flux fractions and ratios for a VHTR test assembly near the core surrounded by graphite and light water flux shaping assemblies. 175

Table 4.13 Flux fractions and ratios for a VHTR test assembly near the core surrounded by Er_2O_3 and light water flux shaping assemblies. 175

Table 4.14 Fluxes and flux ratios for a VHTR test assembly far from the driver surrounded by light water and depleted uranium filled flux shaping assemblies 177

Table 4.15 Fluxes and flux ratios for a VHTR test assembly far from the driver surrounded by Er_2O_3 and light water filled flux shaping assemblies. 178

Table 4.16 Fluxes, fractions, and ratios for a graphite capsule in the center of a light water filled assembly. 181

Table 4.17 Steel capsule in light water filled assembly at position 1.2 cm.................. 187

Table 4.18 Steel capsule in graphite filled assembly position centered 1.2 cm towards the driver. 194

Table 4.19 Steel capsule centered 1.2 cm towards the driver with dividing line between light water and graphite at 0.0 cm. 194

Table 5.1 k_{eff} associated with different materials that follow the control rods. Calculated with a lower enriched core and rod height at 90.0 cm.................. 212

Table 5.2 Reactivity worth associated with drum position 217

Table 6.1 Base geometry 230

1. INTRODUCTION

Nuclear power in the United States makes extensive use of LWRs, which were built using materials considered state of the art in the 1960’s. Ongoing and projected developments in nuclear energy will subject these materials to scenarios beyond their current operating conditions. In order to verify that these materials will remain effective under future conditions, they must be tested in Materials Testing Reactors (MTRs), low power high flux reactors designed to subject materials to conditions mimicking what they would experience in operational reactors. Current materials are not ideal for certain advanced reactor types, which require materials that have not yet be fully vetted under advanced conditions. These new materials must be irradiated in MTRs to confirm their expected performance characteristics. Several examples will illustrate the need for MTRs.

The Light Water Reactor Sustainability (LWRS) program is a DOE funded project to increase the lifetime of today’s fleet of LWRs. The NRC has already issued 20 year license extensions for most current reactors, with some operators already looking at the possibility of another 20 year license extension, making the expected lifetime of these reactors 80 years. Demonstrating that these materials are safe after such a lengthy period of time is no easy task, requiring extensive irradiation time in a materials testing reactor. The ATR is essential for this purpose, but is limited by the amount of fast flux generated. A new MTR operating in the fast spectrum would be able to subject materials to extensive fast neutron damage. Two materials currently irradiated at the ATR as part of the LWRS are structural steel and SiC (Light 2014) (Bragg-Sitton 2013). The core barrel is an irreplaceable part of a Generation II LWR, and its behavior after 80 years of use is not well established. As such, sections of structural steel from decommissioned reactors are irradiated in the ATR to study its behavior. SiC is a completely new cladding type currently being developed at INL for the LWRS. It is composed of woven ceramic fibers and has a greater strength and failure temperature than Zircalloy, the current cladding for LWRs. This proposed cladding material must be subjected to extensive study before it can be used in a reactor, studies which would be accelerated in a fast spectrum MTR.

While the ATR is adequate for the needs of the LWRS, it has limited capabilities for the needs of advanced reactor testing. Advanced reactors are a series of proposed reactor types in varying stages of readiness that offer significant advantages over today's LWRs. Some of these reactor types make use of a fast (sodium fast reactor) or epithermal spectrum (molten salt reactor). The fast flux in the ATR is significantly below that of a prototypic fast reactor, meaning that materials would have to be irradiated for far longer in the ATR to achieve that same level of neutron damage as they would receive in a commercial fast reactor. Proposed fast reactor materials were tested many years ago, but their behavior was not fully characterized. Of particular interest is the behavior of the uranium-zirconium fuel alloy at high burnup, where significant quantities of actinides and fission products are present and the behavior of various steels useful as claddings (Hilton 2007).

1.1 Design objectives

The Nuclear Reactor Technology Subcommittee, a subcommittee of the Nuclear Energy Advisory Council, released a report on November 18, 2014 that requested designs for a new materials testing reactor in support of the Generation IV and LWRS programs. This thesis will propose a design for a new MTR that will meet the requirements outlined this report (Report, 2014). The report provided some background on the need for a new MTR and listed several features a new MTR should have. This section will describe the requested features for a new MTR and show how the proposed reactor will satisfy them.

A prerequisite for the construction of commercial advanced power reactors is a demonstrator reactor. A demonstrator reactor is a medium power reactor with similar systems to the commercial power reactor that demonstrates the operational characteristics of the commercial power reactor. This demonstrator reactor cannot be used to study reactor types dissimilar to it. For example, a demonstrator reactor built around the graphite moderated helium cooled Next Generation Nuclear Power plant would not provide much relevant data to a sodium cooled fast reactor. The DOE requests more flexibility before choosing the next US advanced reactor type. For this reason, the NEAC report recommended the construction of a test reactor that could emulate the behavior of as many reactor types as possible, while still functioning as a demonstrator reactor for a specific reactor type. The sodium cooled fast reactor is the most promising reactor design usable in a breeding fuel cycle. The proposed reactor would serve as a demonstrator reactor for the sodium fast reactor technology, while also being flexible enough to serve as a testing platform for alternative reactor designs.

The report emphasized the need to test fuels and claddings to enable very long core lifetimes and to improve accident tolerance. Both the LWRS program and advanced reactors program require a platform to provide extensive neutron irradiation of core materials. The high fast flux in the reactor would allow for accelerated neutron damage compared to the ATR. Improving the risk tolerance of LWR fuels requires a platform to simulate expected accidents. The reactor will hold multiple light water coolant loops to emulate LWR accident conditions in single assemblies. The NEAC report focused on operations and maintenance methods for cost reduction, which could be studied in the reactor. As the reactor is meant to be a demonstrator reactor for the metallic fuel sodium fast reactor type, it will have similar operation and maintenance situations as a commercial power reactor of the same type. In support of the materials testing functions of the proposed reactor, the NECA report listed several requirements directly pertaining to the testing conditions; the reactor will satisfy all of these requirements. It is desired to place lead test assemblies in the core; large test volumes are thereby necessitated. In support of multiple reactor types, the core should have regions where a different neutron spectra are present. Similarly, the core should incorporate multiple coolant loops to simulate reactor behavior under steady state and transient conditions. The report also specified that the proposed reactor should be licensed under 10 CFR 50 Class 104 and listed the ATR, HFIR, JHR, MYRRHA, and MBIR as test reactors whose performance should be evaluated.

1.2 Characteristics of test reactors

The test reactors mentioned in the Report of the Nuclear Reactor Technology Subcommittee were examined to relative degrees of thoroughness corresponding to the amount of information freely available online and the degree to which information was relevant to the design objectives. For example, HFIR offers high thermal fluxes throughout the core. This reactor is designed around providing a high fast flux, so little information about the fluxes within HFIR are relevant to the present task. The thermal flux in the central trap is noted when discussing the thermal region of the proposed reactor. Five tables are presented first with essential information, followed by more in depth discussions of each system. The proposed reactor will be compared to these test reactors. Far more information was collected about these reactors than will be presented here. The references list all the sources considered for each reactor, although information from each source is not directly presented here. The sources are listed at the end of each descriptive paragraph in order of decreasing importance to this overview. The definition of fast flux differs between the sources for the research reactors. Values of the MBIR are given in total flux and the fast neutron fraction measures divides flux of E > 0.1 MeV by total flux. Fast flux values for the JHR use E > 0.9 MeV, for the ATR use E > 1 MeV, and for the MYRRHA use E > 0.75 MeV.

Table 1.1 HFIR

Nominal power	85 MWth
Maximum flux	2.6E10^{15} n/cm^{2}s thermal flux
Center flux trap size	12.7 cm diameter
Active fuel height	50.8 cm
Other positions in Be reflector	N/A and far less

Table 1.2 ATR

Maximum power	250 MWth
Normal operating power	110 MWth
Active core height	122 cm
Power tilt ratio	3:1
Largest corner traps (5.25 in diameter)	4.4E10^{14}/2.2E10^{14} n/cm^{2}s thermal/fast
Other corner traps (3.0 in diameter)	4.4E10^{14}/9.7E10^{13} n/cm^{2}s thermal/fast
Largest A traps (1.59 in diameter)	1.9E10^{14}/1.7E10^{14} n/cm^{2}s thermal/fast
Other A traps (0.66 in and 0.5 in diameter)	2.0E10^{14}/2.3E10^{14} n/cm^{2}s thermal/fast
Other positions are smaller	Other positions have lower fluxes

Table 1.3 JHR

Nominal power	100 MWth
Active core height	60 cm
3 in core irradiation assemblies (94.5 mm)	4.2E10^{14} /2.9E10^{14} n/cm^{2}s fast/thermal
7 in the center of an assembly (32 mm)	5.5E10^{14}/2.2E10^{14} n/cm^{2}s fast/thermal
12 positions between assemblies	N/A
6 PWR testing loops	4.3E10^{14} n/cm^{2}s thermal 1% enriched pin

Table 1.4 MBIR

Nominal power	150 MWth
Active fuel height	55 cm
Fast neutron fraction	~0.7
Maximum/average core flux	5.5E15/3.5E15 n/cm^{2}s in the core
14 materials testing assemblies, 7.22 cm flat to flat. Maximum/average flux	4.9E15/3.6E15 n/cm^{2}s
3 external loops, assemblies 5 cm by 144 cm	5.0E15, 2.0E15, 1.3E15 n/cm^{2}s
3 instrumented in core loops for alternate coolant types, assemblies 4.5 cm wide.	3.2-4.0E15 n/cm^{2}s
6 horizontal beam ports	N/A

Table 1.5 MYRRHA

Subcritical/critical power	65 MWth/100 MWth
Subcritical fast/total flux in central channel	1.01E15/3.75E15 n/cm^{2}s
Critical fast/total flux in central channel	4.05E14/2.61E15 n/cm^{2}s
Subcritical fast/total flux in off central channel	4.2E14/2.6E15 n/cm^{2}s
Critical fast/total flux in off central channel	2.56E14/1.75E15 n/cm^{2}s

The ATR or Advanced Test Reactor, is a HEU fueled light water moderated research reactor. The ATR has a serpentine core; it is composed of four circular leafs that are joined together. Each leaf contains a few thin plates of fuel and a deal of light water. The centers of the leaves do not contain fuel, and are the location of the ATR's largest flux traps. Outer traps are available throughout. The fast flux in the ATR is far below that in the proposed reactor. There are three types of irradiation positions: simple, open assembly with few instruments, closed assembly with many instruments, fully enclosed flux trap with a separate coolant loop to simulate LWR conditions. Such level of detail is beyond the level of analysis in the present work. The core is surrounded by control drums, which enable the power within a leaf to be somewhat different from the other leaves. The power tilt was estimated at 3:1. Different irradiation positions have different spectra. Figure 1.1 is an excerpt from the ATR User's Manual, and gives sizes and fluxes for the different irradiation positions at a power of 110 MW$_{th}$. The maximum core power is 250 MW$_{th}$, but the ATR is normally operated at 110 MW$_{th}$. Core height is

4 feet, or 121.92 cm. Positions not listed are out of core and have lower fluxes (FY, 2009).

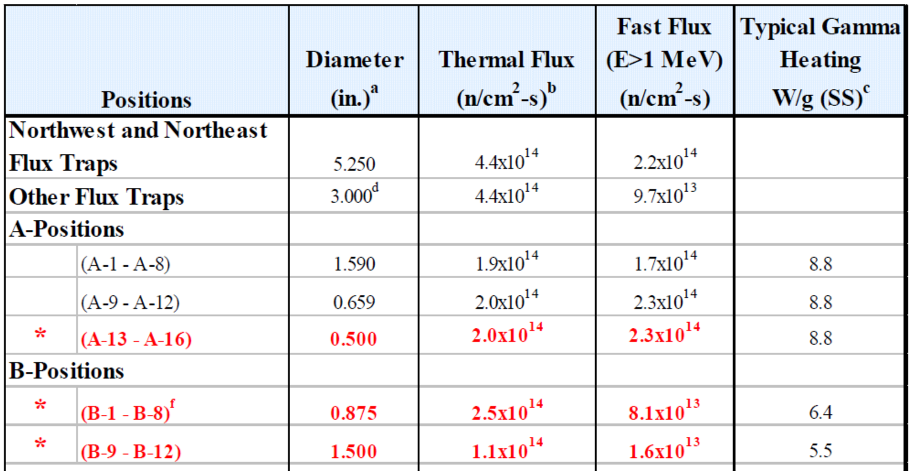

	Positions	Diameter (in.)[a]	Thermal Flux (n/cm^2-s)[b]	Fast Flux (E>1 MeV) (n/cm^2-s)	Typical Gamma Heating W/g (SS)[c]
Northwest and Northeast Flux Traps		5.250	$4.4\text{x}10^{14}$	$2.2\text{x}10^{14}$	
Other Flux Traps		3.000[d]	$4.4\text{x}10^{14}$	$9.7\text{x}10^{13}$	
A-Positions					
	(A-1 - A-8)	1.590	$1.9\text{x}10^{14}$	$1.7\text{x}10^{14}$	8.8
	(A-9 - A-12)	0.659	$2.0\text{x}10^{14}$	$2.3\text{x}10^{14}$	8.8
*	**(A-13 - A-16)**	**0.500**	$\mathbf{2.0x10^{14}}$	$\mathbf{2.3x10^{14}}$	8.8
B-Positions					
*	**(B-1 - B-8)[f]**	**0.875**	$\mathbf{2.5x10^{14}}$	$\mathbf{8.1x10^{13}}$	6.4
*	**(B-9 - B-12)**	**1.500**	$\mathbf{1.1x10^{14}}$	$\mathbf{1.6x10^{13}}$	5.5

Figure 1.1 Excerpt from the ATR User's Manual (FY, 2009).

HFIR, of the High Flux Isotope Reactor, is a HEU fueled, light water moderated, beryllium reflected test reactor that operates at Oak Ridge National Laboratories. HFIR boasts the highest thermal flux in the world, at 2.6E15 n/cm^{2}s. HFIR is a small under moderated core with a high power density and a core power of 85 MWth. Although it is under moderated, the fast flux in the central flux trap is lower than the thermal flux. The central flux trap is 12.71 cm wide and is subdivided into 37 smaller positions on a hexagonal lattice. The central trap can be reconfigured, but this is uncommon. Multiple irradiation positions are located in the beryllium reflector around the core. Four beam ports provide neutrons outside the vessel. Some of the neutrons are further cooled to ultra-low temperatures and used for extremely precise neutron radiography experiments.

The design objectives do not specify beam ports, so this feature of HFIR will not be replicated in the new MTR. Similarly, the focus of the new MTR is on a high fast flux, so the high thermal flux in HFIR will not be replicated either. ORNL provides a complete MCNP input deck for cycle 400 (Xoubi and Primm, 2005).

The JHR, or Jules Horowitz Reactor, is being constructed in Cadarache France. It is the new materials testing reactor for France and the EU. Many of the old MTRs in Europe are nearing the end of their licenses and must be shutdown. This reactor is planned as their replacement. As such, it must have a great deal of flexibility. It has a higher fast flux than thermal flux in the core due to its being severely under-moderated. That being said, the fast fluxes are not high enough to meet the design objectives. The thermal flux is higher in the reflector. The reactor also accommodates a large number of test loops and apparatuses. Reactor power is 100 MW_{th}. The fuel is intended to be 19.75% enriched UMo in the future, but it will utilize 27% enriched U_3Si_2 until the completion of materials testing for the UMo. The fuel assemblies are cylindrical and contain 8 cylindrical plates per assembly with a hole in the center. The assemblies are 9.45 cm across and the inner hole is 3.2 cm across. The 8 radial plates are split into 3 sections each, spanning 120°. There are 37 assembly positions, 34 of which are filled with fuel assemblies. The three assembly positions not filled with fuel assemblies are in core positions irradiation positions. They have a peak fast flux $E > 0.9$ MeV of 4.2E14 n/cm^2s and a peak thermal flux of 2.9E14 n/cm^2s. There are 7 irradiation positions within the fuel assemblies. They have a peak fast flux $E > 0.9$ MeV of 5.5E14 n/cm^2s and a peak thermal flux of 2.9E14 n/cm^2s. There are 12 smaller positions between assemblies. The core is surrounded by a beryllium reflector, which contains slots for movable testing apparatus The reflector also contains 6 slots for PWR like testing positions with a thermal flux of 4.3E14 n/cm^{2}s attained with a 1% enriched fuel pin. The core contains 3 cooling loops: one for the core and in core irradiation positions, one for the reflector irradiation positions, and one for core cooling. The document mainly quoted for this is (Boyard, 2005). This document is older, and the remaining documents offer slightly different values for the fluxes, but are not significantly different (Bignan, 2011, presentation) (Bignan et al., 2011, paper) (Bignan, 2013) (Farrant, 2014) (Camprini, 2011) (Gaillot, 2010).

The MBIR is the newest Russian test reactor. It is intended to replace BOR-60 as a test vehicle for advanced reactors. While also offering a fast spectrum courtesy of its sodium coolant and oxide or nitride fuel, it offers larger irradiation positions, higher fluxes, more beam ports, and separate coolant loops. The reactor will be expensive to build and Russia is looking to foreign investment early in construction. Japan and the US have put forward money towards the MBIR. Core power is 150 MW$_{th}$. The expected startup date is in 2020 and it is expected to last for at least 50 years. The intermediate loop is sodium and the tertiary loop is water with a Rankine cycle to generate 55 MW$_e$. Vibro MOX fuel will be used with up to 38.5% Pu in the MOX. The core active height is 55 cm. The maximum flux/average flux =5.5/3.5E15 n/cm^{2}s in the core. The fast fraction within the core, defined as fast flux E > 0.1 MeV divided by the total flux, is ~0.7. 14 materials testing assemblies are in the core, 7.22 cm flat to flat. These assemblies have a maximum and average flux of 4.9E15 and 3.6E15 n/cm^{2}s, respectively. 3 external loops which can accommodate assemblies 5 cm across and 144 cm tall. The central loop has a flux of 5.0E15 n/cm^{2}s while the other two have fluxes of 2.0E15 and 1.3E15 n/cm^{2}s. 3 instrumented in core loops for alternate coolant types like LBE can accommodate assemblies 4.5 cm wide. Total fluxes for these loops vary from 3.2E15 to 4.0E15 n/cm^{2}s. There are 6 horizontal beam ports. The principal source is (Tretiyakov, 2014). Secondary sources offer slightly different flux values, core layouts, and more details (Tuzov, 2014) (Zayko, 2013) (Dragunov, 2012).

MYRRHA is an accelerator driven LBE cooled reactor under consideration in Belgium. While the SFR is the most favored fast reactor type in Europe, the LFR and GFR and also being developed as alternatives to the SFR. It is recognized internationally that the LFR and GFR both lack research experience when compared to the SFR. As such MYRRHA is being developed to test advanced reactor materials and develop invaluable operating experience with a LFR. This reactor is being built in Belgium as a part of SCK•CEN. The previous Belgian MTR is BR2, a PWR completed in 1962. JHR has the same cylindrical fuel assemblies as BR2. MYRRHA is planned to go on line in 2026. MYRRHA can be operated in subcritical mode (65 MWth) or critical mode (100 MWth). The spallation target is designed to operate for temperatures up to 500 °C for 3 months at a time, producing ~10^{17} n/s. This corresponds to one operating cycle. A 600 MeV proton beam is used for subcritical operations. The reactor is pool type. As such, it can use fully passive decay heat removal systems. Four cooling loops are used. All four loops use water for the secondary and air as the ultimate heat sink. The first two use forced circulation for full power operations. The second two loops use natural circulation for the water and air sections. The reactor uses four shell and tube heat exchangers for full power operations. There is also a RVACS. The secondary heat exchangers are steam generators. A steam separator is schematically shown in a secondary flow diagram. The steam is sent to an air steam condenser as waste heat. The core has buoyancy driven control rods and gravity driven SCRAM rods. The SCRAM rods are weighted with tungsten. Both sets of rods use 90% enriched B_4C. Used fuel assemblies are stored in the pool, cooled by LBE in natural circulation diverted from the core flow. The spent fuel pool is right next to the core. As such, there are two in vessel fuel handling machines. The fuel is MOX, and floats in the LBE. For this reason, the fuel assemblies are restrained from above. They float upwards until they contact the upper restraint. There are 7 irradiation locations in the core and 21 positions in the core periphery. The overall size of a fuel assembly is 10.405 cm flat to flat. Fuel handling is done from below. The fuel assemblies are held in place by buoyancy and are slotted into place. The fuel shuffling arm is located in the cold plenum, below the baffle while the whole machine is accessible from the top of the vessel. Because the beam generates high energy neutrons form the spallation source, the spectrum is harder in the subcritical mode. The peak radiation damage is 22 dpa/year in the central channel in critical mode, although 31 dpa/year can be reached in subcritical mode in the off-central channel. The central channel when critical has a fast flux of 4.05E14 n/cm^2s and a total flux of 2.61E15. The primary source is (Van Tichelen, 2014). Secondary sources are (MYRRHA, 2011) and (Abderrahim, 2012).

1.3 Design criteria

The design objectives were formulated as specific design criteria. These criteria were influenced by the capabilities of the test reactors outlined previously. The design criteria are intended to be specific enough to guide and evaluate a design but also flexible enough to allow for some freedom in how they will be satisfied. Each criteria is listed below.

LEU fuel must be utilized.

The core must have a fast flux, defined as $E > 0.1$ MeV, greater than 5E15 n/cm^{2}s in a hypothetical materials testing assembly. This requirement makes the system as good as the MBIR, and superior to the ATR, HFIR, JHR, and MYRRHA.

The core should be able to simulate multiple reactors, defined as having regions of fast, epithermal, and thermal spectra.

Coolants loops of sodium, lead, helium, FLiBe (or other molten salt), and water (boiling, liquid, and supercritical) must be implementable.

Materials testing assemblies should be at least as large as those in the MBIR, JHR, and ATR.

The coolant loops must be designed to undergo severe transients. This is less of an issue as it otherwise seems; transient coolant loops have been successfully designed and implemented in US research reactors for some time now. Only the in core portion of the loop will be designed.

Core breeding ratio should be maximized without compromising any of the other requirements. This will decrease fuel costs and extend the lifetime of the core, increasing the cycle length and operational usability.

1.4 Design approach

The design must make use of previous developments in US fast reactor technology. Specifically, the core must be based on the EBR-II as the safety of the EBR-II was proven many years ago by subjecting the design to severe transients. The most difficult reactivity coefficient to estimate is the coefficient of thermal expansion, as the thermo-structural behavior of the core must be extremely well known. This involves a complex and intensive structural analysis, beyond the scope of the present effort. After selecting a reference core configuration from historical US reactors (EBR-II), a core will be designed that fulfils the design criteria based on neutronics characteristics. Despite the emphasis on neutronics in design phase, two parameters must be limited to ensure decent thermal hydraulics characteristics. The first is coolant volume fraction. In PWR's the coolant volume fraction is decided by the necessity of maintaining an under-moderated core. In a fast reactor, coolant moderates and absorbs neutrons. For neutronics reasons, coolant volume should be minimized in a fast reactor. This is undesirable for two reasons based on operational and safety concerns. Firstly, a reduction of flow area with fixed inlet and outlet temperatures and power density must cause an increase in coolant velocity. This increases the core pressure drop, requiring stronger pumps with greater electrical power consumption. Similarly, by keeping mass flow rate constant the core inlet temperature must decrease. This induces unfavorable thermal stresses within the core. Secondly, there are limits to the core power density. A higher core power density requires a higher mass flow rate to cool. This could increase core pressure drop or thermal stresses for reasons outlined previously. However, the driving reason behind minimizing power density stems from the accident response. The decay power density is proportional to the operational power density. Accidents usually result in a decreased ability to provide core cooling; decay power density should therefore be minimized. Bearing these reasons in mind, it was decided that both coolant volume fraction and power density must not be allowed to change substantially beyond those in the EBR-II. It is conjectured that by maintaining approximate EBR-II assembly dimensions and powers per assembly, the thermo-structural and thermal hydraulic behavior of the core will be the same.

SERPENT 2 is a continuous energy Monte Carlo neutron transport code developed by Jaakko Leppanen (Leppanen, 2013). The code is a complete rewrite of SERPENT, which began development approximately ten years ago. Code capabilities are very similar to MCNP6, with a few notable exceptions. SERPENT uses the Woodcock delta tracking model, not ray tracing. As such, the collisional estimate of scalar flux is used as the track length estimate of flux is not available. Therefore, flux tallies are defined differently in SERPENT than in MCNP, but without any loss of capability. In SERPENT, cells can only be defined as the intersection of planes, and each cell must be completely enclosed in planes. As such, there is no union operator in

SERPENT. SERPENT has predefined geometrical surfaces (hexagons, cylinders, cubes) to simplify the creation of an input deck. SERPENT stores the relevant cross section data for a problem in very large matrices and calls them throughout the calculations (unionized energy grids). This greatly accelerates cross section table look ups while increasing memory usage. Burn up simulations in particular are very RAM intensive; OpenMP had to be used for parallel processing not OpenMPI. The use of one parallelization technique over the other did not affect the runtime or results in any way. The single greatest drawback with SERPENT lies with the fact that it is not as rigorously benchmarked as MCNP because it is so much newer and has a smaller user base. Its greatest advantage lies with the fact that it much faster than MCNP. This is especially noticeable when performing burnup simulations.

2. THE CORE

A core was designed to fulfill the criteria listed in the previous section. This section covers three different aspects of the core: an outline of the overall design, an in-depth analysis of the driver region, and the burnup behavior of the core. Later sections of this paper will deal with the remaining sections of the core and with the control systems. This core makes use of a previously designed assembly. This assembly, and the fuel type that it uses, have proven irradiation swelling and severe accident characteristics. The fuel assembly was based on fuel assemblies used in EBR-II, a sodium cooled fast breeder reactor operated at Idaho National Laboratories from 1963 to 1994 (Fast 2006). EBR-II primarily used metallic fuel, but oxide fuel assemblies were tested in the core as well. Metallic fuels have varying material compositions, but the most promising fuel form was an initially uranium-zirconium alloy, with 10% zirconium by mass (Chang, 2007). Higher actinides accumulated with burnup and reprocessing, so the final fuel composition differed somewhat from the initial fuel composition. The benefits of metallic fuels are briefly outlined here and compared to oxide fuels. Metallic fuel has a low thermal conductivity, resulting in lower fuel temperatures. Although the melting point of metallic fuels is lower than that of uranium dioxide, the higher thermal conductivity more than compensates (Chang, 2007). Metallic fuels have higher thermal expansion coefficients than uranium dioxide, meaning that the fuel assemblies expand both vertically and axially with increasing fuel temperature more than uranium dioxide fueled assemblies. This expansion increases neutron leakage and increases the amount of sodium in the core (Chang, 2007). More sodium in the core inserts negative reactivity and reduces the coolant temperature, which lowers pin temperatures. The severe accident behavior of metallic fuels was clearly demonstrated when the EBR-II successfully underwent an unprotected loss of flow accident (Chang, 2007). Zirconium present in the fuel improves the irradiation swelling behavior of the fuel. Metallic fuel assemblies have been successfully irradiated to burnups of 19.9 atom percent (Chang, 2007). Although metallic fuel does expand with burnup, an initial smear density of ~75% leaves enough room within the fuel pin for the fuel to expand (Chang, 2007). Metallic fuels have a higher fissile density than oxide fuels. Metallic fuels have a higher density and uranium weight percent (Chang 2007). A higher fissile density inserts reactivity into the core. These favorable characteristics underlie Terrapower's choice to use metallic fuels in the Traveling Wave Reactor (Hackett 2012).

Throughout this work, references will be made to different flux groups; these groups should be defined. As noted in the previous section, references for different test reactors used different definitions of fast flux. To provide as much information for comparison, fast flux was divided into two groups. The first group is from 1.0 MeV to 20 MeV. The second group is from 0.1 MeV to 1.0 MeV. If the fast flux is mentioned without any qualifications, it refers to flux E > 0.1 MeV. Fast flux above 1.0 MeV will be explicitly stated. The thermal energy cut off is 0.625 eV, which is from an example in the SERPENT User's Manual. Epithermal flux is from 0.625 eV to 0.1 MeV. This four group flux is standard throughout this work; a three group flux will be used in conjunction with VHTR conditions in Section 4. To provide a finer description of the flux spectrum, a 120 equal lethargy group spectrum was also used.

2.1 Outline of the base geometry

For the reasons given above the fuel assembly used in the present work was based on the EBR-II. Characteristics of the EBR-II assembly were acquired from the Fast Reactor Database 2006 Update. This IAEA TECDOC is meant to be a single source of information on historical fast reactors to ensure that such information is preserved for future use. As the database covers several dozen designs, some actually built and some only existing on paper, the level of detail on each design is somewhat less than ideal. However, sufficient dimensions were provided that a fuel assembly could be modeled. Fuel pin diameter is 0.381 cm with a 0.0305 thick steel cladding. The fuel was modeled as pure ^{235}U and ^{238}U with 10% natural zirconium by mass. 900 K cross sections were used for the fuel. Fuel in the EBR-II had a 75% smear density measured relative to the theoretical density of 17.7 g/cm^3. The fuel was sodium bonded. In the present investigation, the fuel was assumed to occupy the entire volume of the fuel pin at a density of 13.275 g/cm^3. Although EBR-II used SS 316, this reactor uses HT9. The use of HT9 will give this reactor better irradiation swelling characteristics than SS 316. HT9 is a steel that received extensive research in the US fast reactor program. This material had excellent swelling behavior above 200 dpa, and a modified form of HT9 comprises the cladding and duct material used in the traveling wave reactor. The HT9 used in this investigation was 87% natural iron, 12% natural chromium and 1% natural molybdenum by mass (Hackett 2012). HT9 was simulated with a density of 7.8 g/cm^3. 600K cross sections were used. EBR-II pins were wire wrapped; rather than model the individual wire wrappers the steel associated with the wrap was added to the cladding. For this reason, the cladding thickness was increased to 0.0429 cm. All of the sodium used in this investigation was modeled at a density of 0.8 g/cm3 with 600K cross sections.

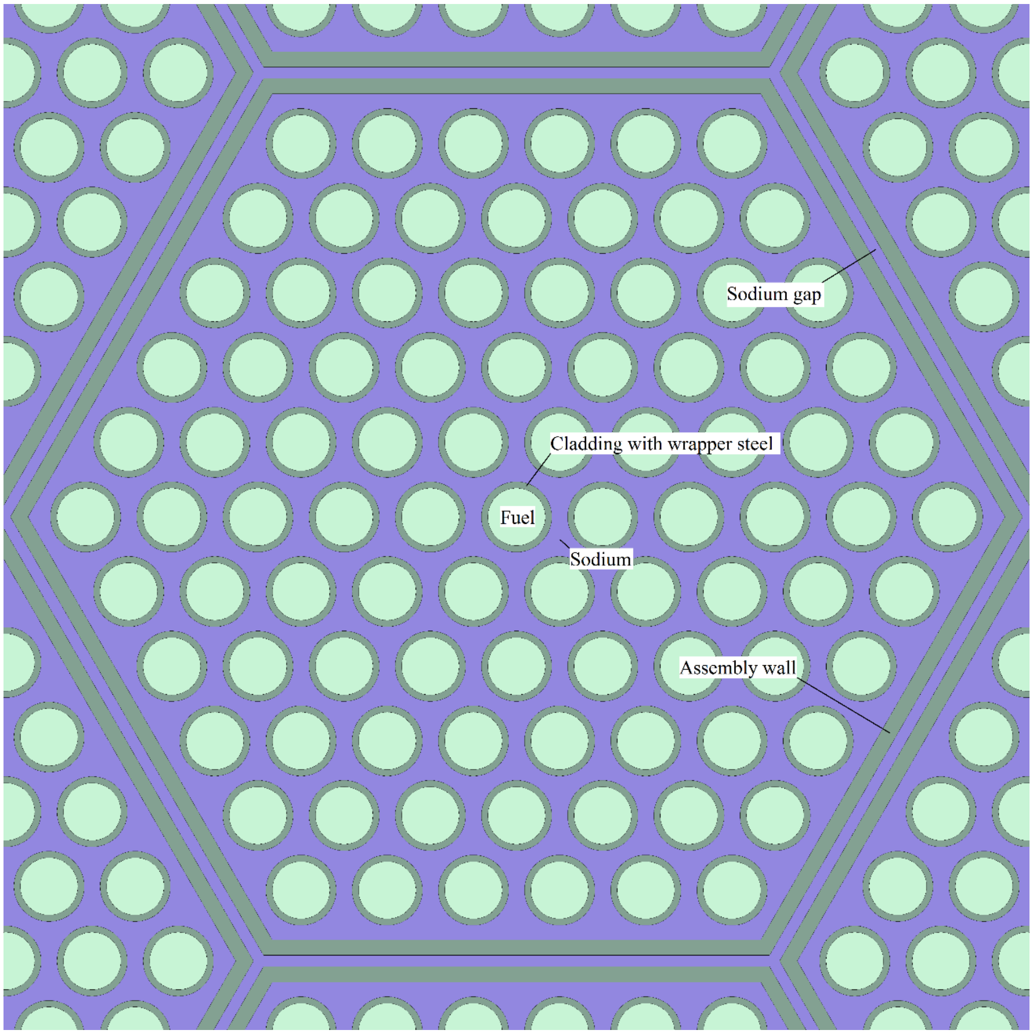

Figure 2.1 Driver fuel assembly

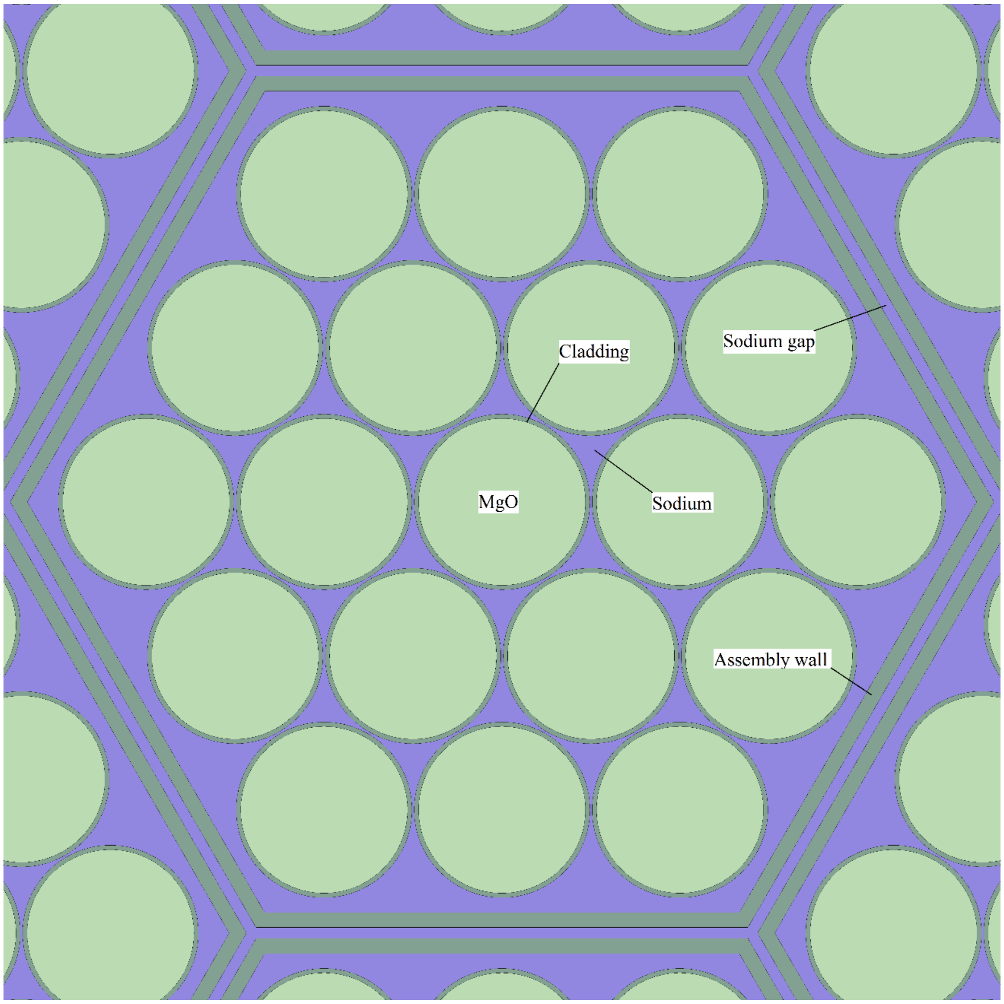

Figure 2.2 Outer reflector assembly

The fuel pin lattice pitch was not directly given in the Fast Reactor Database, but it could be conjectured from other details presented. The breeding blanket assemblies and driver assemblies had the same duct dimensions in the EBR-II. The fuel assembly pitch at operating temperatures for the EBR-II was 5.893 cm, which was used in this investigation instead of the pitch at cold conditions. The outer duct flat to flat thickness was 5.817 cm, and the duct walls were 0.1016 cm thick. The assembly lattice pitch, duct dimensions and duct material compositions are common to every position simulated here except where noted. This is done to ensure adequate cooling of all parts of the core, but more importantly, it ensures that the core has an easily interchangeable geometry. The core is meant to be easily adaptable to whatever conditions are needed; a common lattice and duct type facilitates that outcome. Light water will be used in this investigation; the 0.1016 cm thick steel walls are the primary barrier preventing explosive sodium-water interactions within the core. The number of fuel pins per assembly (91) was provided in the Fast Reactor Database, so the fuel pin lattice pitch was determined to be 0.57192 cm. The breeding blanket pin outer diameter given in the Fast Reactor Database was too large to actually fit inside the dimensions provided for the ducts. Therefore, the given outer blanket pin diameter and cladding thickness dimensions were ignored. It should also be noted that there is not breeding blanket in this reactor, only a thick MgO reflector. The MgO reflector pins were 1.2 cm in diameter with a 0.0305 cm thick cladding and a lattice pitch of 1.215 cm. This corresponds to 19 such pins per assembly. Such pins can be replaced with solid blocks of MgO, the effects of which will be outlined in preceding sections. EBR-II contained breeding blankets above and below the core. Horizontal cross sections of the driver assembly and outer reflector are presented in Fig 2.1 and Fig 2.2, respectively.

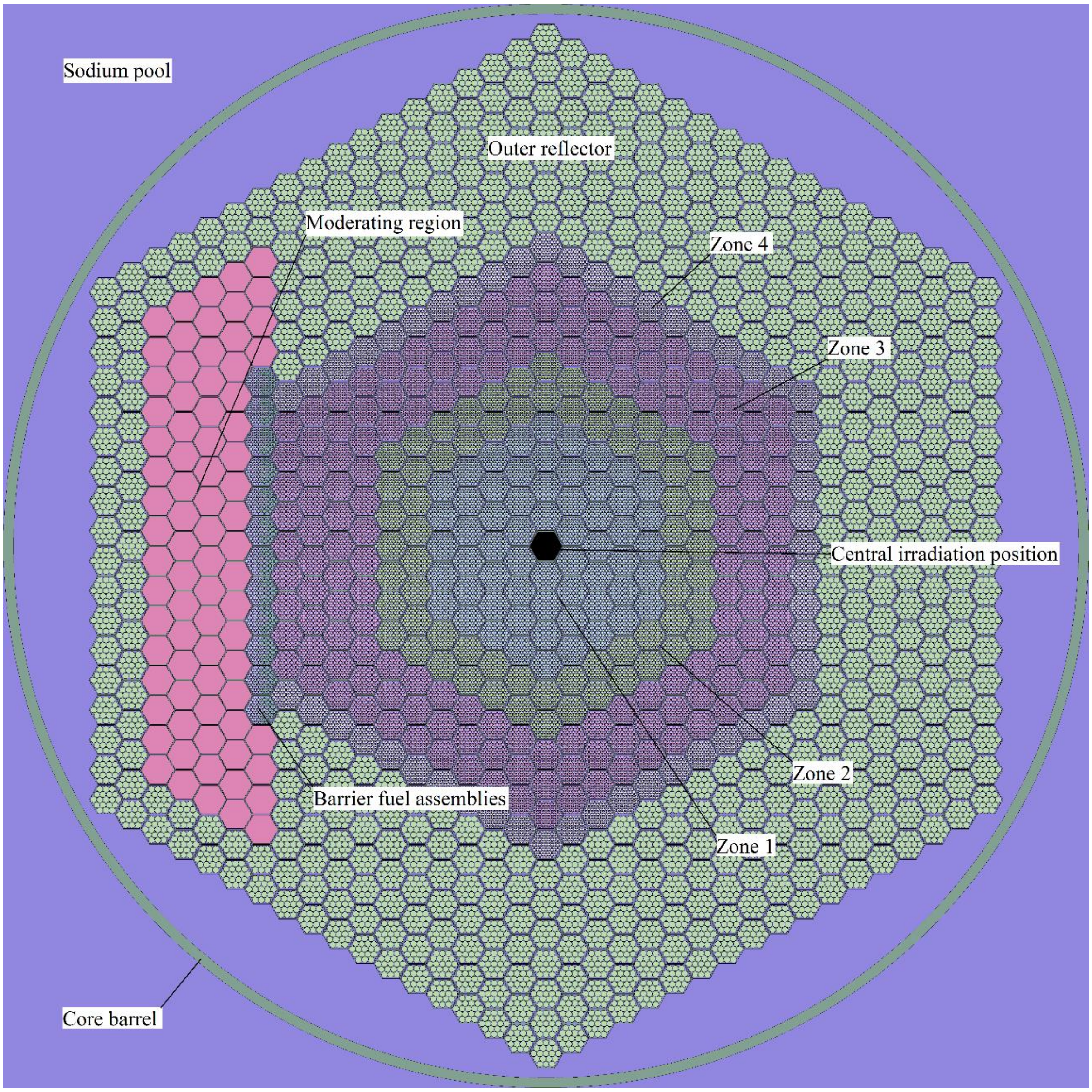

Figure 2.3 The whole core. The origin of the geometry is in the center of the figure, in the middle of the central irradiation position. This figure is plotted on the x-y axis. Positive x is towards the right, positive y is towards the top, and positive z is out of the page. This follows the right hand rule. The core was designed in two vertical halves, one in the positive z and the other in the negative z. The active core is 100 cm tall; its upper dimension is at z=50.0cm and its lower dimension is at z=-50.0 cm.

Vertical and horizontal dimensions for the EBR-II were provided in the Fast Reactor Database, as well as fuel loadings and total number of fissile and fertile assemblies. However, these details could not be used because of limitations on driver fuel enrichment listed in the preceding section. The driver fuel for the EBR-II was 67% enriched with no added plutonium. Such a fuel cannot be used in the present design; this investigation confined itself to a maximum enrichment of 19.9%. A lower enrichment in the driver can be counterbalanced in several different ways. Increasing the fuel volume fraction would compensate for the lower enrichment, but would perturb the internal assembly dimensions from the EBR-II. This option was examined and the results will be presented in future sections. Similarly, the core volume could be increased. As mentioned previously, the overall core diameter must be less than 2 meters while the active core must be less than 1 meter in diameter. The core is hexagonal, so the flat to flat dimensions are different from the effective diameters. Fig 2.3 shows a horizontal cross section of the core and Fig 2.4 shows a vertical cross section of the core. The active fuel height is 100 cm, taller than the EBR-II, which had an active fuel height of 34.3 cm. The upper and lower reflectors are 35 cm thick, and a 5 cm sodium gap separates the active core and reflectors. The upper and lower reflectors are shorter than the breeding blankets in the EBR-II. The EBR-II assemblies contained mechanisms above and below each section of the assembly that held the lattices in place. These complex mechanisms were not modeled in this investigation. Ultimately, the upper and lower reflectors are 21.44 cm shorter than the vertical breeding blankets in the EBR-II while the active core height is 65.7 cm taller. The outer reflector and moderating assemblies were 180 cm tall. The basic geometry of the reactor is a fast reactor driver region and a thick outer reflector, part of which is composed of a thermalizing material. This will most likely be graphite. In this manner, the center of the reactor provides a region of high fast flux while the outside of the reactor provides regions of lower energy fluxes. The outer reflector is essential to maintaining criticality, while the moderating region provides low energy neutrons at the cost of a lower k_{eff}. For this reason, the volume of moderating region within the core was minimized. However, considering the modularity of the core, it is possible to reconfigure the outer reflector to whatever geometry is needed. The geometry and associated materials including enrichments are considered to be the base geometry for the reactor. Many permutations on this design will be presented throughout this investigation, but this is always the reference geometry. Similarly, the behavior of future permutations is always given in reference to the behavior of this geometry. Relevant characteristics of the base geometry are described later in this work. The active core is approximately 108 cm flat to flat. This is not an exact value as the active core is composed of smaller hexagonal assemblies, which lead to a somewhat jagged boundary between the driver and reflector. The driver, including the central irradiation position, has an effective diameter of 112.58 cm. The central irradiation position is an assembly of the same duct dimensions and compositions as the other assemblies but with void within the assembly. This void region (meaning it contains no material, SERPENT 2 only considers streaming across the region without interaction) is 100 cm tall, and a 0.1 cm thick steel wall caps the void region above and below. An infinite sodium pool is located above and below the steel caps. The outer reflector is approximately 180 cm flat to flat for an effective diameter of 187.59 cm. The sodium pool extends outwards 300 cm radially from the origin before ending. This boundary is black. An infinite sodium pool is modeled above and below the core.

The core barrel is a 2 cm thick steel wall with an overall diameter of 214 cm. This represents the outer boundary of the core.

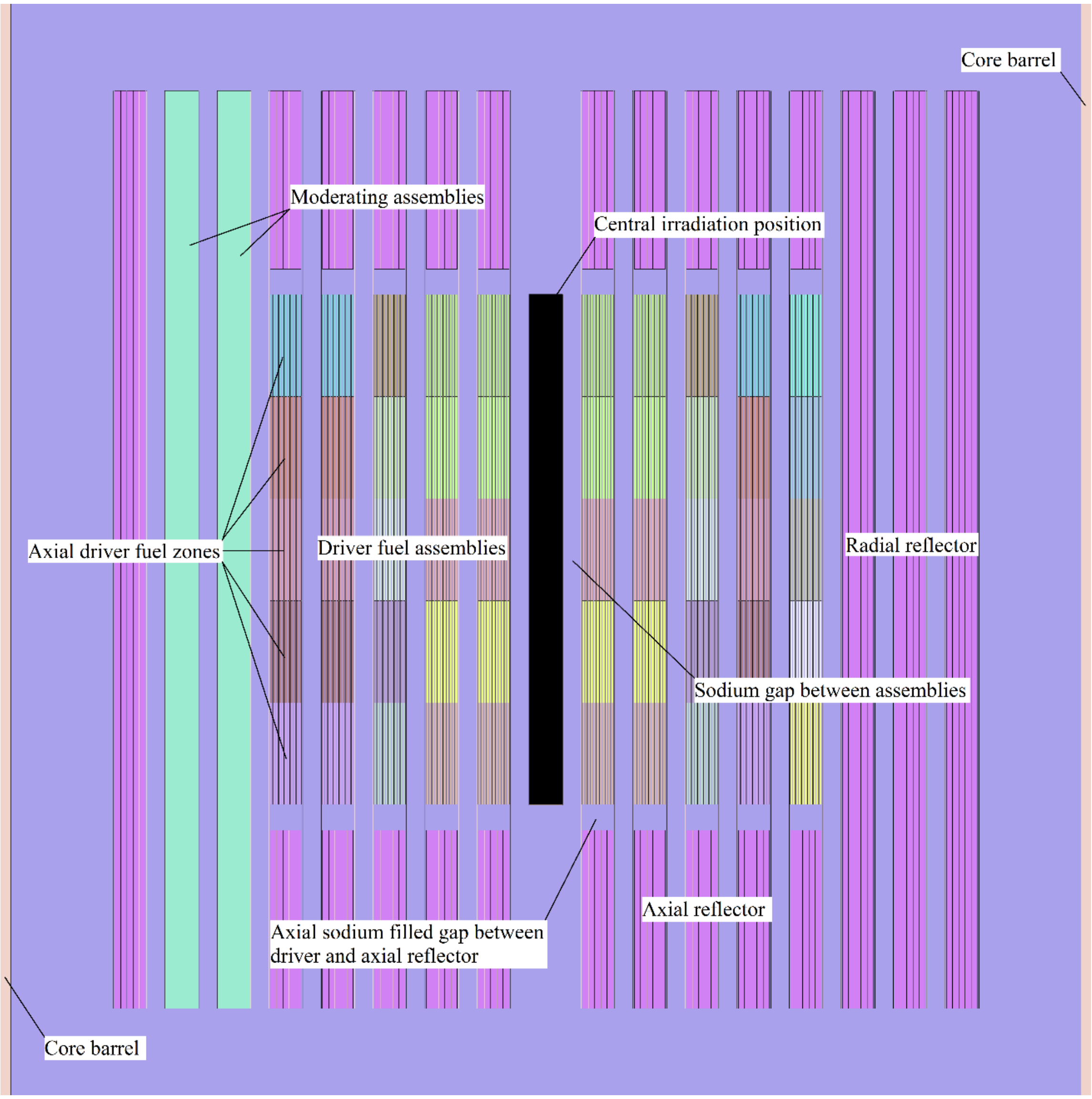

Figure 2.4 The whole core, plotted on the x-z axis through the origin. The sodium gap between assemblies makes it appear that there is more sodium in the core.

The sections labeled Zone 1, Zone 2, Zone 3, and Zone 4 are driver fuel assemblies within the core. There are 330 driver fuel assemblies. These represent different fuel materials for use in a burn up simulation. The first three zones are 19.9%

enriched while Zone 4 is 16% enriched. The outer reflector down scatters the fast flux leaving the core to epithermal energies and sends them back into the core, a phenomenon which will be demonstrated in greater detail later in this section. These epithermal neutrons cause an increase in fission density in those pins nearest the reflector. For this reason, the assemblies bordering the reflector are at a lower enrichment than the rest of the driver. The barrier assemblies, described later, have lower enrichment for the same reasons. SERPENT 2 generates plots of the thermal flux and fission rate density over user defined 2D plots. Fission densities are shown in reds, oranges, yellows, and whites, while thermal flux is shown in various shades of blue. The hues are relative, not absolute. Darker hues represent lower values for thermal flux and fission density and lighter hues represent higher values for thermal flux and fission density. Meshes were instrumental in zoning the core. It was decided to zone the core by fission density of the unburned core. 5 vertical materials of equal length were used in each radial zone. Fig 2.5 shows a mesh of the base geometry. The large white section to the right is the moderating region. The outer reflector provides a limited amount of moderation, shown in the mesh as a light blue within the outer reflector. The mesh is generated by tallying the thermal flux and fission density over very small volumes. The resolution of the mesh naturally improves with more particles being simulated. Fig 2.5 was generated with 80E6 neutrons. The central irradiation position is light blue; few thermal neutrons are present in the fast region but there is a significant epithermal flux, which will be quantified later. The fission density exhibits a broad maximum, reflected in the white color of the central region. The pins nearest the reflector and moderating region are white in color, which demonstrates the large epithermal flux reflected back into the core.

The mesh shown in Fig 2.5 measures 5000 pixels by 5000 pixels. To compare the fission density of various parts of the core and indicate how the core was zoned, Fig 2.6, Fig 2.7, and Fig 2.8 are close ups of various sections of the mesh. Deciding on fuel materials zones and enrichments for those assemblies was done by color. The yellow color in the four central rings of fuel assemblies was deemed sufficiently close in fission density for those rings to be zoned together. The orange color that dominates the next two rings of fuel assemblies signified that these should become Zone 2, while the red color of the next three rings signified that these should become Zone 3. Zone 4 contains fuel at a lower enrichment than the inner zones. Those pins in Zone 4 nearest the reflector are white in color, exceeding the pale yellow of the central core. While this means that the hottest point of the driver is actually in the lower enriched fuel bordering the reflector, reducing the enrichment of Zone 4 reduces k_{eff}. 16% enriched was deemed an acceptable balance between power peaking and k_{eff}.

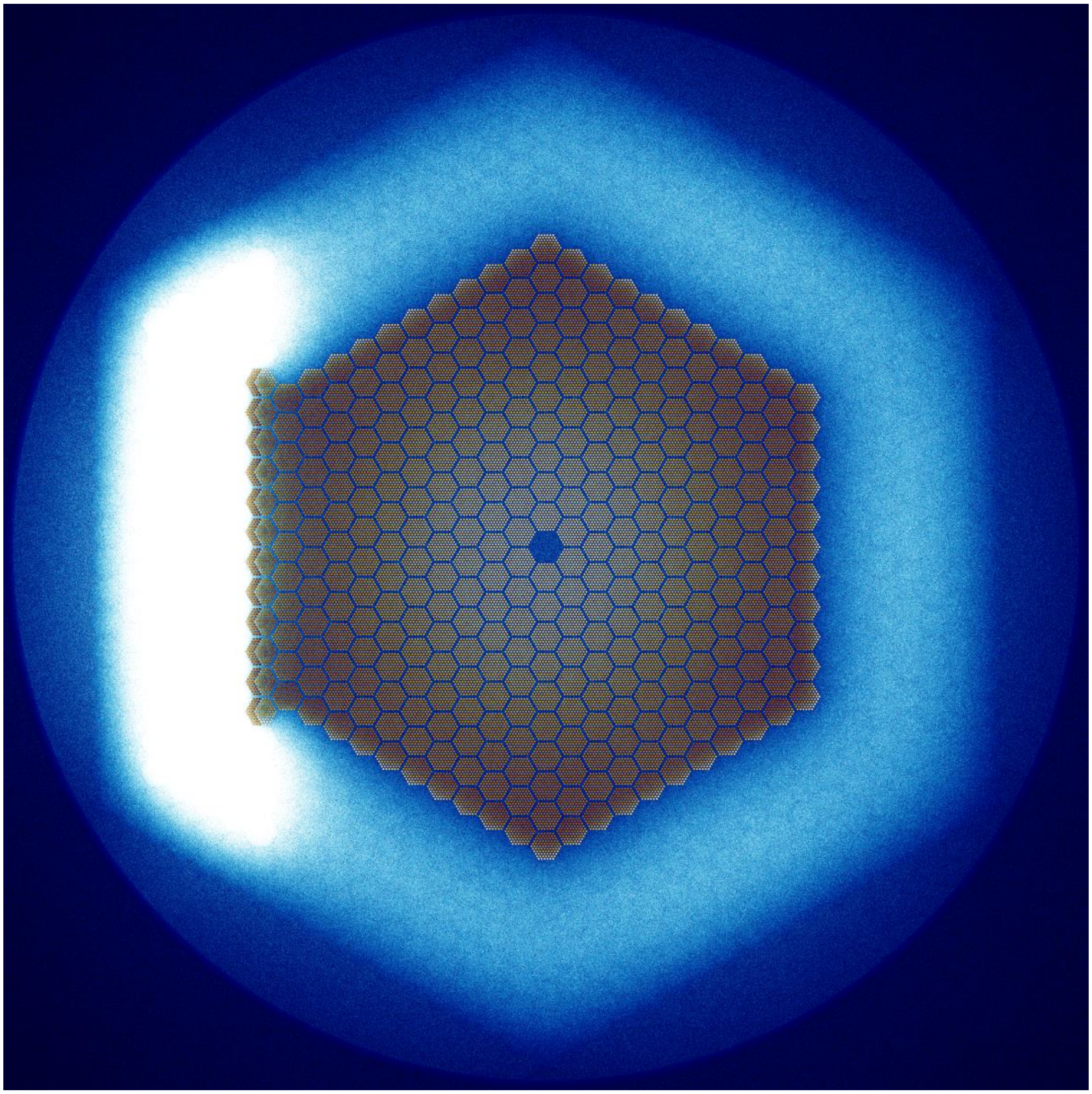

Figure 2.5 Mesh of the base geometry. Used to zone the core

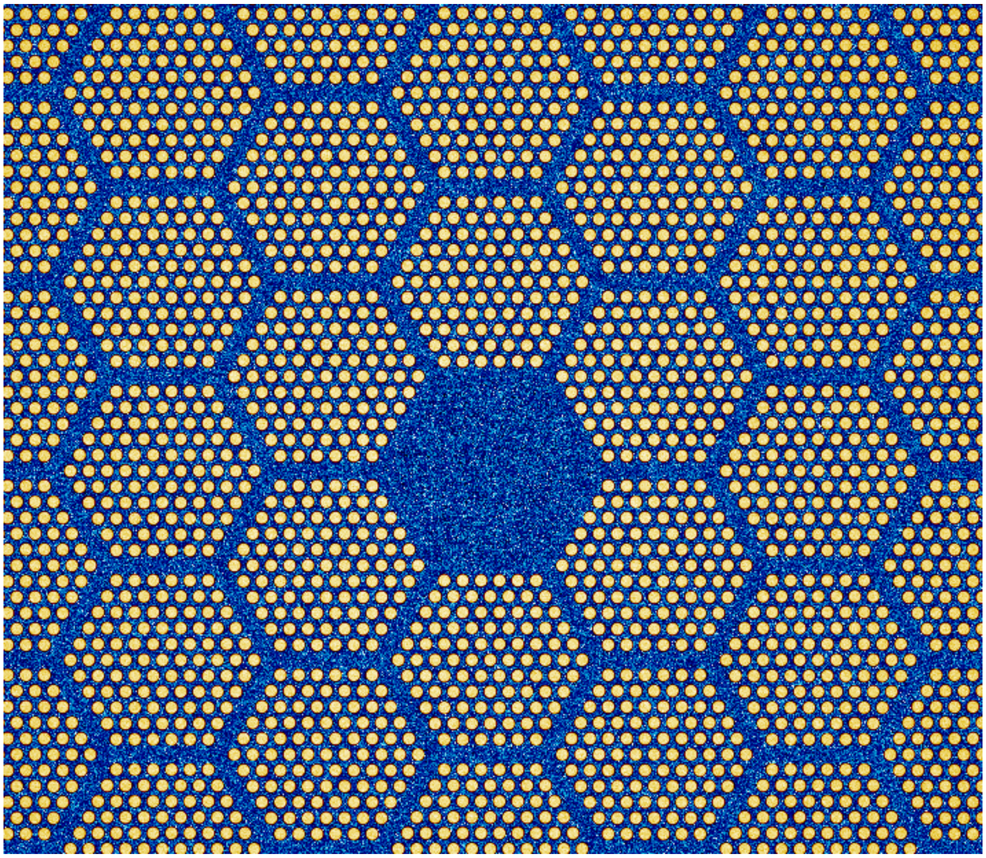

Figure 2.6 Close up of the central region.

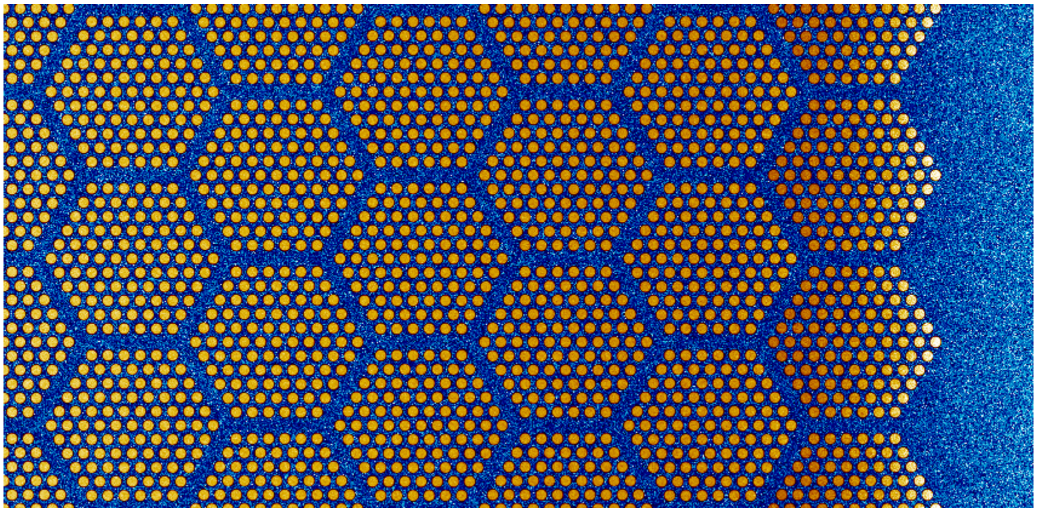

Figure 2.7 Close up of the outer driver.

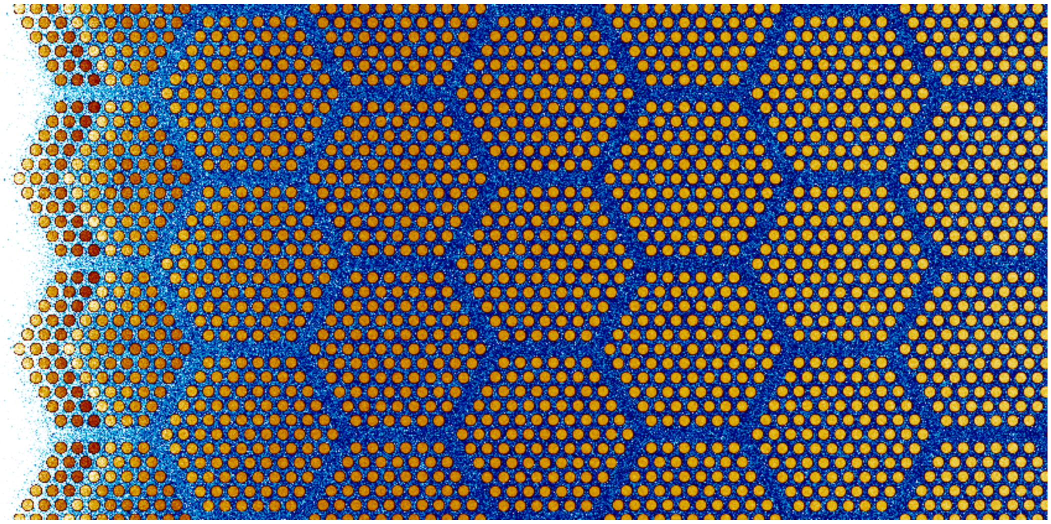

Figure 2.8 Close up of the outer driver and barrier assemblies.

The moderating region generates large quantities of thermal and epithermal neutrons. As ^{235}U is a 1/v absorber with a large resonance region, the path length of low energy neutrons is quite small in the fuel region. This leads to significant power peaking within the barrier assemblies. For this reason, the barrier assemblies had to be sharply zoned. 6% enriched fuel is located in the pins towards the moderating region, 12% enriched fuel in the center, and 15% enriched fuel towards the driver. These barrier assemblies use as many neutrons from the moderating region as possible to maintain criticality. The flux from the moderating region is sharply attenuated and 19.9% driver fuel can be used after it instead of 16% enriched fuel. Therefore, Zone 4 does not wrap around the whole core, just those parts that border the outer reflector. A burnup simulation of the base geometry with five radial zones and ten axial zones was performed to compare with the normal zoning procedure. Results will be presented later in this section. The base geometry is summarized in Section 6.1.

EBR-II has an average linear power of 230 W/cm, a peak linear power of 343 W/cm, and a power per driver assembly of 492 kW (Fast, 2006). The average linear power of the base geometry is 193 W/cm, so the average fuel temperature rise across the pins will be close to the EBR-II for a similar coolant temperature rise. The peak linear power in the inner driver is 270 W/cm, while the peak linear power in the outer driver is 320 W/cm. Power peaking in the 16% enriched outer driver (Zone 4), is due to the thermalization of MgO. The power per assembly is approximately 1754 kW, 3.6 times greater than in EBR-II. These values were calculated by assuming that all the core power was generated in the driver assemblies, none in the radial blankets. This is incorrect, but will not introduce significant error. To preserve coolant temperatures and structural temperatures, mass flow rate must be 3.6 times higher in the proposed reactor to match EBR-II. Higher mass rates mean higher velocities, which results in much higher pressure drops. Higher steady state pressure losses result in worse severe accident performance. Peak cladding temperature can be expected to increase for similar accident conditions and system dimensions. This result is an unintended consequence of a lower fissile content, as core size must be increased to maintain critically while linear power must be kept at a certain level to ensure high fluxes. A full exploration of this fact is beyond the scope of this project. Increasing the temperature rise across the core or having a taller system would improve severe accident performance.

2.2 The driver region

This section discusses two related topics; the choice of reflector and characterization of the driver region. The choice of reflector has a dramatic effect on the overall performance of the core, especially since the volume of reflector is limited by size constraints. The choice of reflector was guided by research performed by R. R. Macdonald and M.J. Driscoll and presented in their paper “Magnesium Oxide: An Improved Reflector for Blanket-Free Fast Reactors.” They examined the performance of several different reflectors for blanket free fast reactors. The ultimately concluded that MgO would be the best choice for a reflector, largely because Beryllium and BeO induced negative reactivity over the core lifetime, even if both materials performed better than MgO at the beginning of core lifetime. Beryllium has several high energy low probability reaction pathways that form ^{10}B, ^{7}Li, and ^{3}He (Tomberlin 2004). The buildup of these strong neutron absorbers inserts negative reactivity over time. Their research showed that Beryllium and BeO reflectors would have larger k_{eff}’s than cores with MgO reflectors at the beginning of core life. The small highly reflected geometry of the present investigation yielded a different conclusion from the large power reactor used in previous research. It will be shown that MgO is a better reflector than BeO. Beryllium was not simulated because of the large burnup induced reactivity effects demonstrated in previous research. Burnup simulations were not performed with alternate reflectors, but flux profiles were generated for the MgO, BeO, graphite, and PbO reflectors.

All reflectors replaced the axial and horizontal MgO reflector pins. The fast flux in each simulation was tallied in the middle 10 cm of the central irradiation position. Flux fraction, used throughout this section, is the flux in a bin divided by the total flux. Two general trends can be observed. Fast flux increases with decreases in k_{eff}, and fast fraction increases with decreases in k_{eff}. A perfect reflector would reflect all neutrons back at the same energy they streamed out of the core. A core with such a reflector would have a constant power density because the driver assemblies have a uniform composition. One of the hallmarks of the effectiveness of a reflector is the uniformity of flux and fission density within the core.

Table 2.1 k_{eff}, fast flux within the central region, and fast fraction within the central region with different reflectors.

Reflector	k_{eff}	Fast flux (n/cm^{2}s)	Fast fraction
MgO	1.08618	5.30E+15	0.742
Spinel ($MgAl_2O_4$)	1.08255	5.37E+15	0.746
BeO	1.08226	5.13E+15	0.746
PbO	1.07556	5.73E+15	0.745
Graphite	1.06998	5.39E+15	0.748
Steel	1.03221	6.59E+15	0.751
Nat. U.	1.02102	6.35E+15	0.751

The second is the similarity of the reflected flux to the incident flux. This cannot be so easily measured as power density, but some indication of reflected flux can be gleaned by the flux within the reflector itself. In the present work, thermal flux fraction, epithermal flux fraction, and fast flux fraction are shown throughout the core and reflector. Axial flux profile was measured in the central irradiation position. The central irradiation positon was divided into 36 axial positions of equal size and the four group flux tallied in each section. The fast group is the fast flux, while the slow group is the sum of the thermal and epithermal fluxes. The radial flux is tallied from the origin in the positive x direction. The bins are 4 cm by 4 cm by 10 cm (x by y by z). 26 such bins were used to tally from x=-2 cm to x=102 cm. The centers of each radial bin are 4 cm from each other in the x direction. Axial and radial flux tallies will be shown at the center of each bin. Fig 2.9 and Fig 2.10 show the radial flux profile and the radial flux fractions with the MgO reflector, respectively. The fast group is the flux above 0.1 MeV and the slow group is the flux below 0.1 MeV. The point at which the fast and slow group overlap is the approximate boundary between the driver and outer reflector. Flux on the y-axis is given in units of n/cm^{2}s.

Flux peaks towards the center of the core, but not the exact center. The loss of a fuel assembly in the center of the core shifts the flux peak approximately 8 cm outwards. The central irradiation position is not reflected by MgO assemblies, so there is more neutron leakage from those positions than from the fuel assemblies. Flux peaks in the axial profiles in the exact center because there is no axial gap in fissile material or reflector. The slow group follows the same trend as fast flux throughout most of the core, but peaks in the moderator. These epithermal neutrons, and some fast neutrons, are reflected back into the core. These neutrons have a shorter path length than fast neutrons and are absorbed in the outer assemblies.

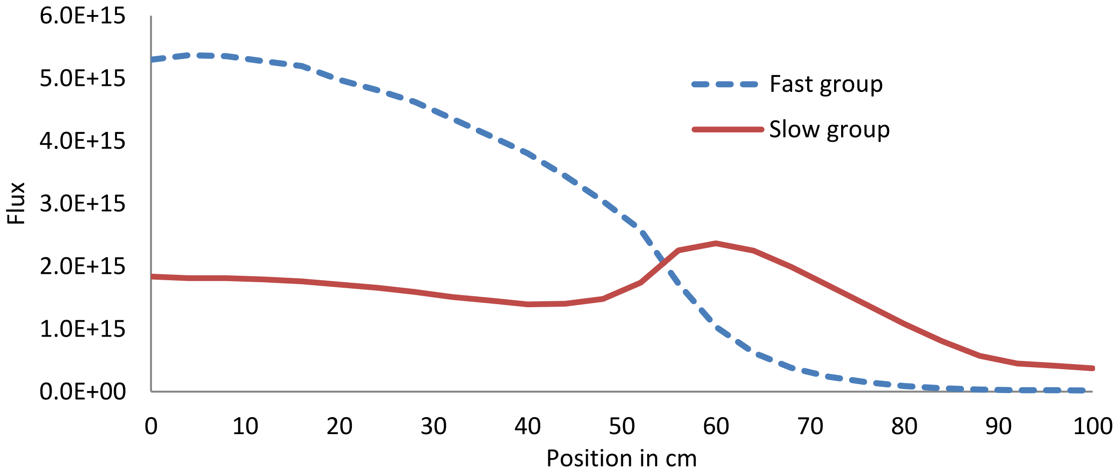

Figure 2.9 Radial flux with the MgO reflector

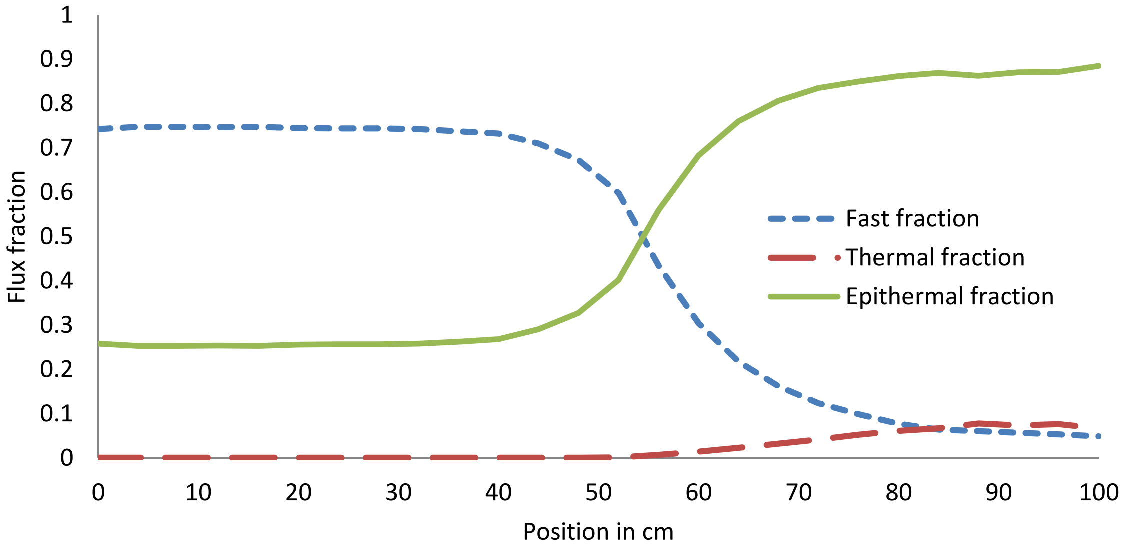

Figure 2.10 Radial flux fraction with the MgO reflector

Reflected neutrons increased the fission density, which increased flux in the outer periphery. MgO is an ineffective moderator; the thermal flux fraction within the outer reflector is low in comparison to the epithermal flux fraction. The peak epithermal flux is 2.37E15 n/cm^{2}s. The fast flux fraction does not drop below 0.7 until after 40 cm. This means that the maximum extent of epithermal neutrons into the driver is 15 cm. Fig 2.11 and Fig 2.12 show the axial flux and axial flux fractions. The position of the bin within the core is on the y-axis, while flux of flux fraction is on the x-axis. Flux is given in units of n/cm^{2}s. Fast flux and epithermal flux follow the same pattern as in the radial flux profile. Fast flux fraction drops below 0.7 after 30 cm from the origin. The bottom and top of the active fuel experiences a flux spectrum with significant epithermal neutrons from the reflector. This in contrast to the radial profile, which maintains the same flux spectrum for the 40 cm nearest the reflector. This discrepancy is most likely due to geometry. First, the flat to flat radius is close to 55 cm, 5 cm longer than the halves of the active core. The radial profile was generated at the flat to flat radius of the hexagonal core. Those sections of the active core that protrude into the reflector on the long edges face less fuel and more reflector and the epithermal flux from the reflector will undoubtedly protrude further into the core. In general, axial flux profiles follow the same behavior as the radial flux profiles so they will not be shown when comparing different reflector types. Increasing fast fraction with decreasing k_{eff} is a very slight effect, and is most likely due to the lack of epithermal neutrons generated in the reflector. Although a lower epithermal flux fraction is desirable, without the reflection of fast neutrons it is of little use. Similarly, it will be shown that reflectors which are effective moderators, like BeO and graphite, are not as useful as moderators that are ineffective moderators, like MgO. Fig 2.13 and Fig 2.14 show the radial flux fractions for the BeO and graphite reflectors, respectively.

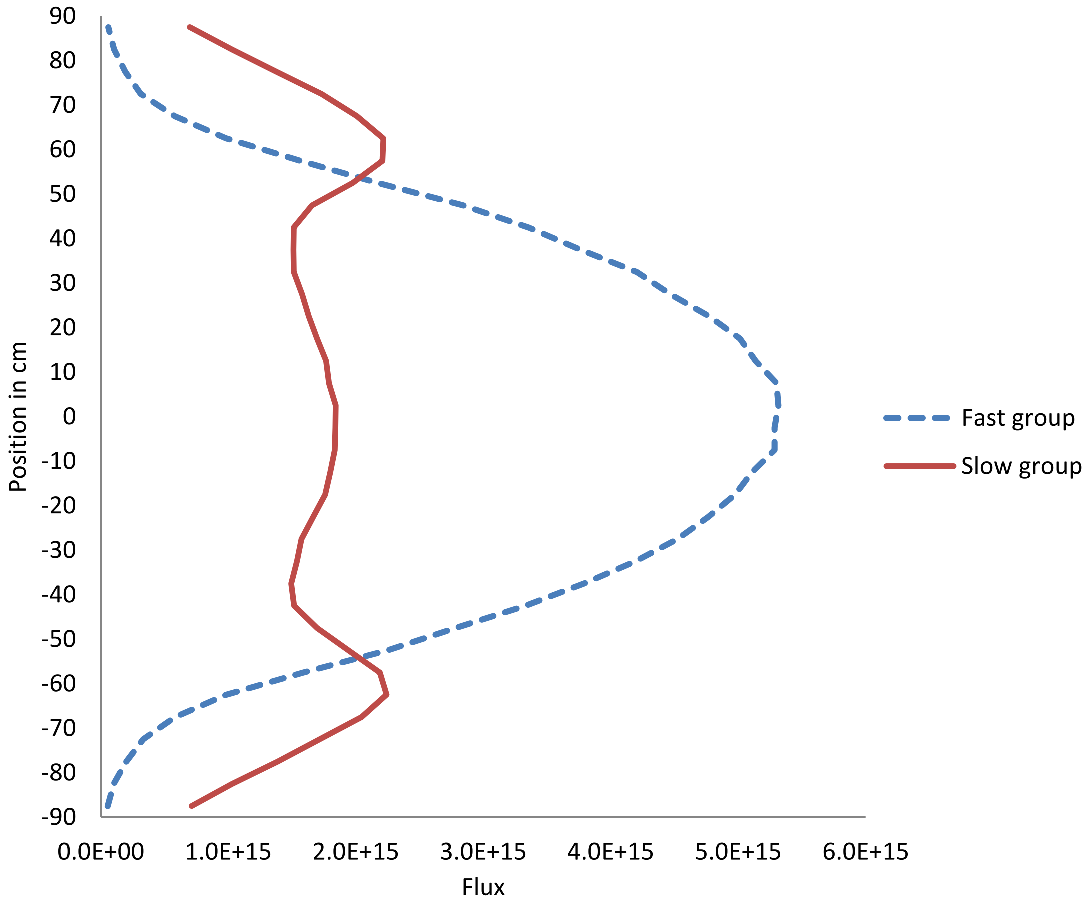

Figure 2.11 Axial flux with the MgO reflector

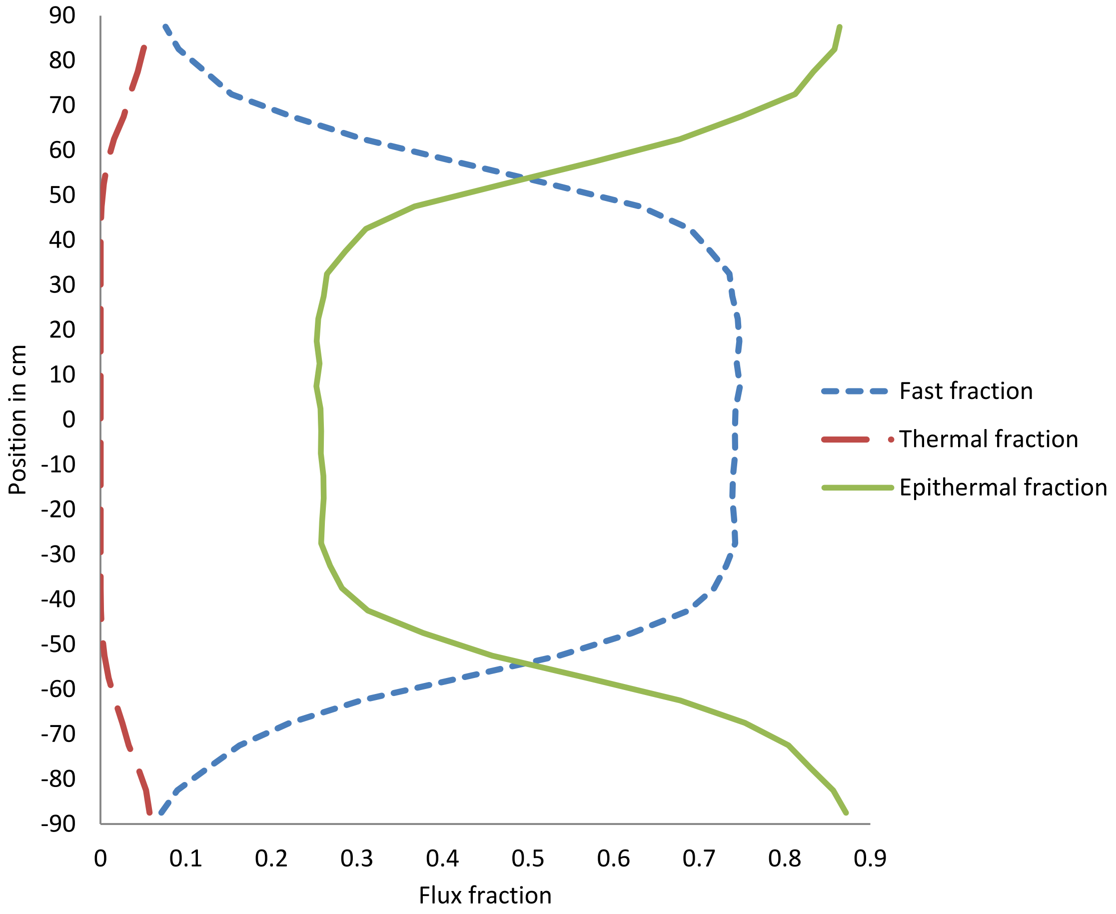

Figure 2.12 Axial flux fraction with the MgO reflector

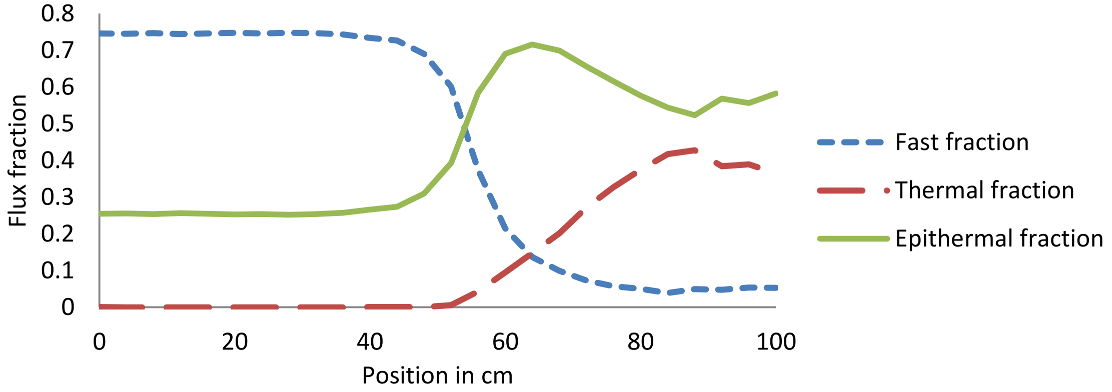

Figure 2.13 Radial flux fractions with the BeO reflector

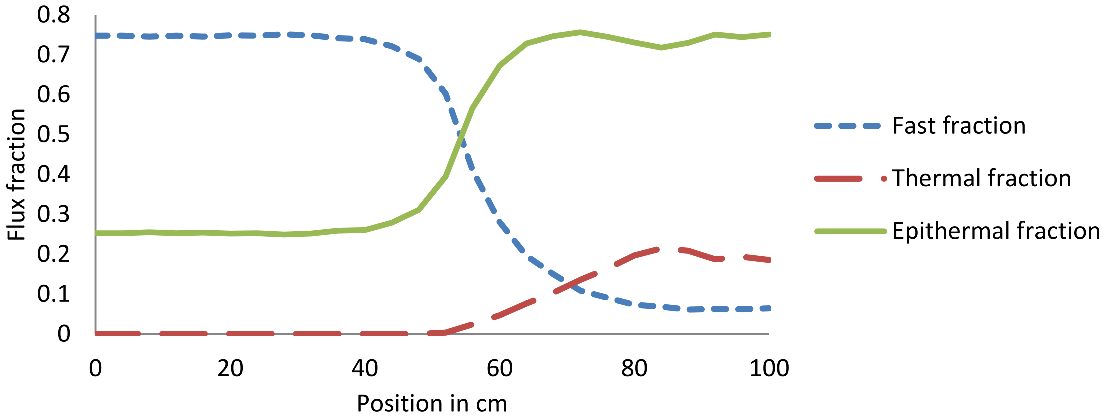

Figure 2.14 Radial flux fraction with the graphite reflector

The thermal flux fractions with the BeO and graphite reflectors are higher than those in the MgO reflector. Beryllium, with an atomic weight of 9 is a better moderator than carbon (atomic weight of 12). The next figure shows the relative slow group flux for different reflectors. Relative flux is defined as the flux in each bin divided by the flux at the center of the core. Radial relative slow group flux is shown in Fig 2.15 for the MgO, BeO, and graphite reflectors. The slow group caused by the BeO is higher in magnitude and its peak is shifted closer to the driver than with MgO. A greater slow group peak closer to the driver would seem to suggest that it is a more effective reflector. However, this peak is far more thermalized than the MgO peak. Indeed, the epithermal flux of the MgO reflector is slightly higher than that of the BeO reflector. Greater thermalization increases the fission density within the outer periphery despite the lower epithermal flux. This phenomenon will give the BeO reflector a nearly identical flux profile within the driver as the MgO core, but with lower magnitudes. Thermal neutrons are also more likely than epithermal neutrons to be absorbed in the sodium and steel than in the fuel. Fig 2.16 shows the radial flux fraction with the PbO reflector for comparison. PbO is a very ineffective moderator and has a far harder neutrons spectrum within the reflector than MgO, but ultimately reflects fewer neutrons. Fig 2.17 shows the radial relative fast flux for MgO, BeO, graphite, and PbO. The BeO and MgO reflectors have nearly identical fast flux profiles, but the greater thermalization caused by the BeO reflector results in a lower average flux. Fission cross sections increase with decreasing neutron energy. The total power of the core is related to the energy per fission, volume of the core, average flux, and average macroscopic fission cross section. BeO reduces neutron energies, increasing the average fission cross sections, and reducing the average flux. The core is optimized for fast neutrons, not thermal neutrons, which have a lower neutrons importance in fast reactors. The thermalization caused by BeO is ultimately a reactivity penalty.

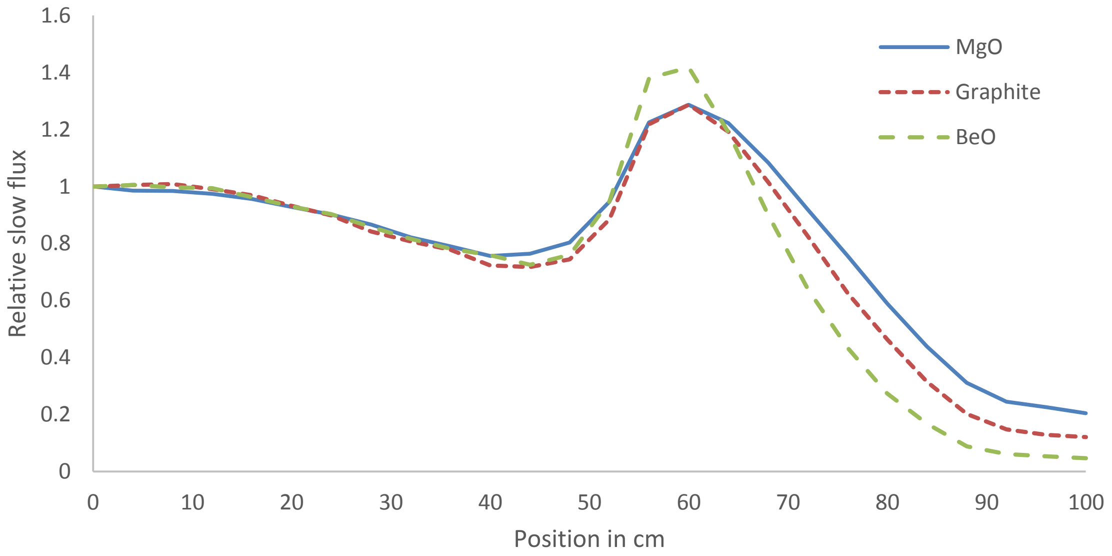

Figure 2.15 Radial relative slow group flux with MgO, BeO, and graphite reflectors

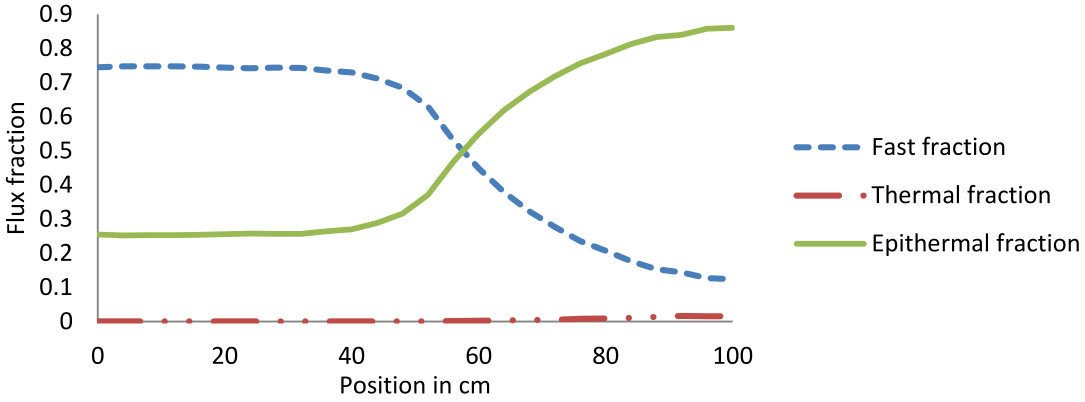

Figure 2.16 Radial flux fractions with the PbO reflector

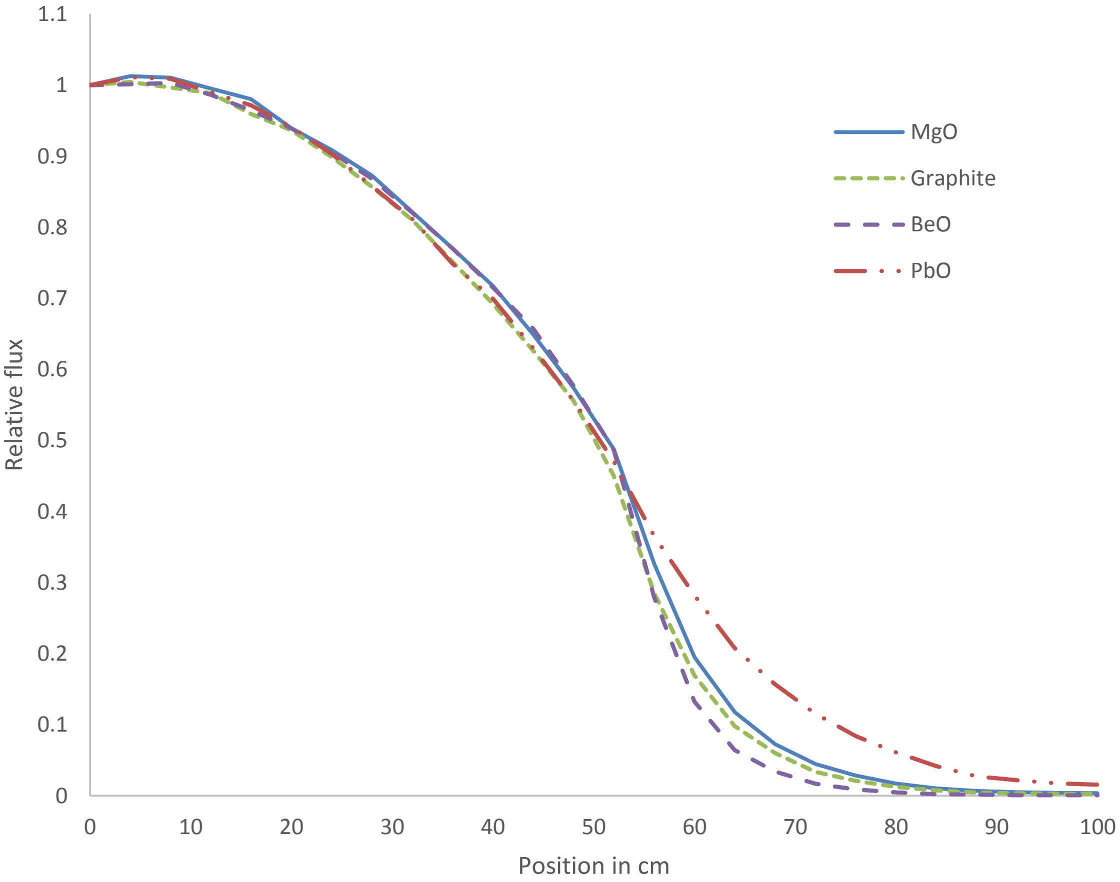

Figure 2.17 Radial relative fast flux with MgO, graphite, BeO, and PbO

The design of the outer reflected the design of the breeding blankets in the EBR-II. These blankets were designed to provide sufficient cooling for the buildup and depletion of fissile material over the assembly lifetime. However, the heat load associated with this should be less than the heat load associated with inelastic scattering and absorption resulting. Therefore, it was decided to replace the central region of the outer reflector with solid blocks of MgO. This decreases the sodium and steel in the outer reflector and increases the MgO content. As MgO is an effective reflector, this increases reactivity. The upper and lower reflectors were not changed because these reflectors must have sodium channels to transport sodium out of the core. The enhanced reflector increases k_{eff} to 1.10131 and causes the peak fast flux to decrease to 5.06E15 n/cm^2s. Lower peak fluxes and a greater initial k_{eff} will enhance the burnup behavior of the core. The potential benefits of this configuration will be stated in greater detail later in this section.

The central irradiation position provides a small irradiation area with an associated small penalty in k_{eff}, even if the central assembly has the greatest fission density and reactivity worth. The internal area of the assembly is 5.6134 cm flat to flat, for an effective diameter of 5.8945 cm. The volume of the whole assembly, including steel wall and sodium gap is 3007.5 cm^3. The design of the central irradiation position is a conjecture; it is possible to design an irradiation assembly that occupies the entire internal volume of the lattice position. One of the stated goals of the FMTR is to provide larger test volumes. Other reactors, like the ATR, MBIR, JHR, and MYRRHA, have greater test volumes and larger test volumes, especially the ATR. Therefore, different configurations of irradiation test volumes will be studied. Many of the reactors listed above included additional irradiation positions within the core between the main assemblies. These positions were smaller, and cannot be fitted into the FMTR because of differences in assembly geometry. Many of the reactors listed above included irradiation locations on the core periphery. These locations are not the focus of the present study, although it should be noted that with the increased size of the FMTR, more of the reflector is available for irradiation testing. As fast flux is highest in the center of the core and seven irradiation test assemblies would be radially symmetric within the inner driver, a study was conducted to see how best to orient the seven irradiation test assemblies within the inner driver. Three configurations will be examined. Each will be presented and Table 2.2 shows the essential characteristics. In each configuration, 7 fuel assemblies were removed in a radially symmetric pattern. Table 2.2 gives k_{eff} and flux data for each configuration. The column labeled “Central” gives the flux for the central position, while the column labeled “Surrounding” gives the flux for the 6 assemblies that surround the central position. The flux in each surrounding assembly was averaged together. The last column, titled “Average,” gives the average flux in all 7 assemblies.

Table 2.2 k_{eff} and fast flux within the central and surrounding flux traps for each configuration

Configuration	k_{eff}	Central	Surrounding	Average
1	1.07554	4.88E+15	4.91E+15	4.91E+15
2	1.07661	5.23E+15	5.02E+15	5.05E+15
3	1.07597	5.11E+15	5.08E+15	5.08E+15

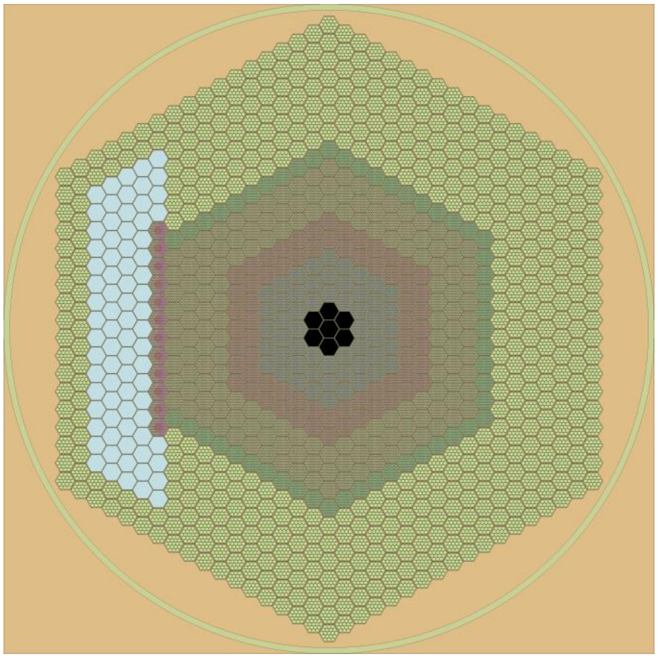

Figure 2.18 Configuration 1

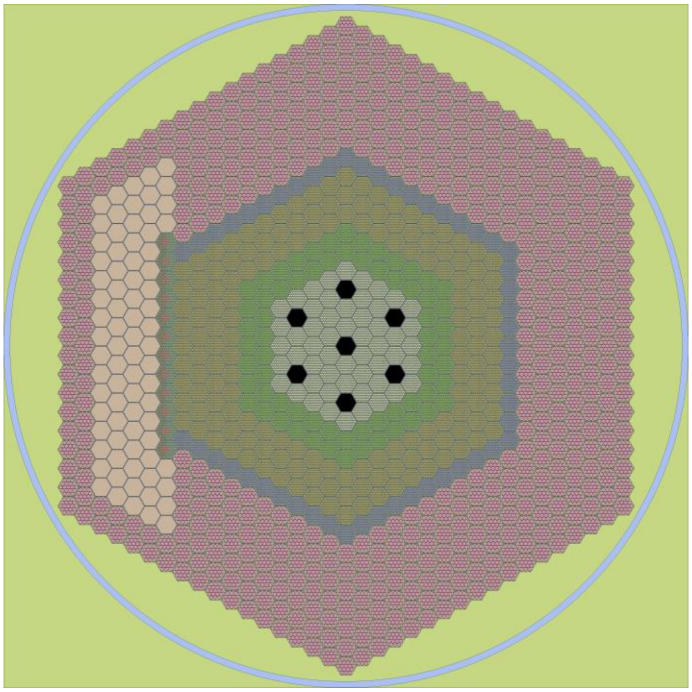

Figure 2.19 Configuration 2

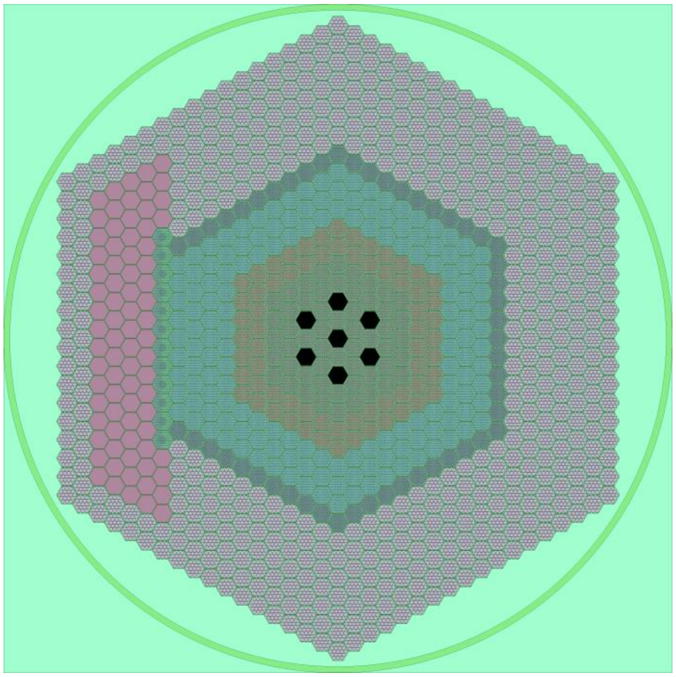

Figure 2.20 Configuration 3

Changes in k_{eff} were minor but greater than the standard deviations of the simulation. Configuration 1 provided a nearly uniform flux distribution within the large irradiation region, but at the cost of lower fluxes. There are two different flat to flat measurements for the large irradiation region which can be referenced as the internal dimension on the y axis and the internal dimensions on the x axis. The flat to flat measurements given here take the whole lattice element size into account, not just the internal area of the assemblies. The flat to flat distance along the y axis is 17.679 cm and the flat to flat distance along the x-axis is 13.609 cm. The effective diameter is 16.372 cm and the total volume is 21052 cm^3. The next two configurations did not incorporate the larger volume, but had lower fluxes. Configuration 2 had a greater peak flux than Configuration 3, but a lower average flux. Ultimately, it was decided to pursue Configuration 3 for the next studies into the proper locations of irradiation test assemblies. The large irradiation position was relocated to the outer driver. Different burnup simulations were performed with different fuel loadings. Fig 2.3 shows the locations of the large irradiation positions in the core. Note that the large irradiation positions remove 8 fuel assemblies from Zone 2 and 6 fuel assemblies from Zone 3. With the reduction in fissile material in the outer driver, flux shifted towards the core center and the fluxes within the central irradiation positions increased slightly. The loss of 14 fuel assemblies in the outer core significantly reduces k_{eff}. Values for this configuration are given in Table 2.3. Table 2.4 shows fast fluxes for a nearly identical core configuration as shown in Fig 2.21. The new configuration (shown in Fig 2.22) seeks to increase fluxes within the large irradiation volume by breaking up that large volume and spreading those irradiation assemblies throughout the outer driver. The same number of assemblies were removed from Zone 2 and Zone 3 as were removed in the core with large irradiation volumes. These assemblies were distributed in a way that was as radially symmetric as possible. The simulation worked as anticipated, with two additional benefits. Flux within the core redistributed itself, and the outer regions experienced a greater flux as anticipated. However, the fluxes within the central driver experienced a very slight increase. Flux was depressed within the large volumes and peaked far from them. By spreading the volumes more evenly throughout the core, flux is more evenly distributed throughout the core, increasing tallies within all the irradiation positions. Secondly, k_{eff} increased. This is most likely due to the elimination of a high leakage pathway through the large irradiation position and a more pronounced flux peaking within the center of the core. While potentially useful, large test volumes are deemed essential and this configuration is not recommended.

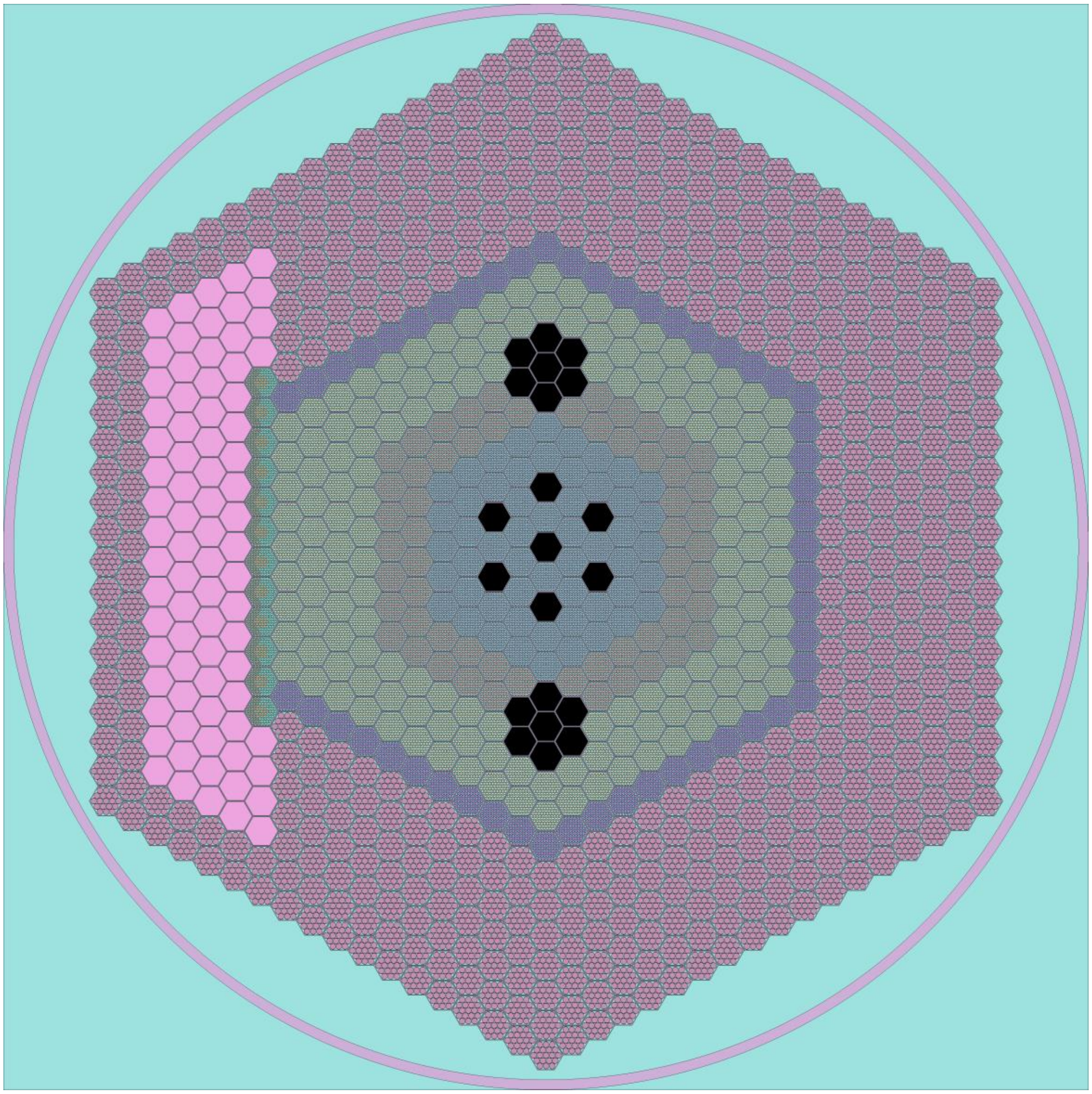

Figure 2.21 Core geometry with 7 small irradiation positions in the inner driver and 2 large irradiation positions in the outer driver.

Table 2.3 k_{eff} and fast fluxes within various irradiation positions with large outer irradiation positions

k_{eff}	Central	Surrounding	Outer
1.05618	5.20E+15	5.16E+15	3.91E+15

Table 2.4 k_{eff} and fast fluxes within various irradiation positions without large outer irradiation positions

k_{eff}	Central	Surrounding	Outer
1.05752	5.30E+15	5.20E+15	4.33E+15

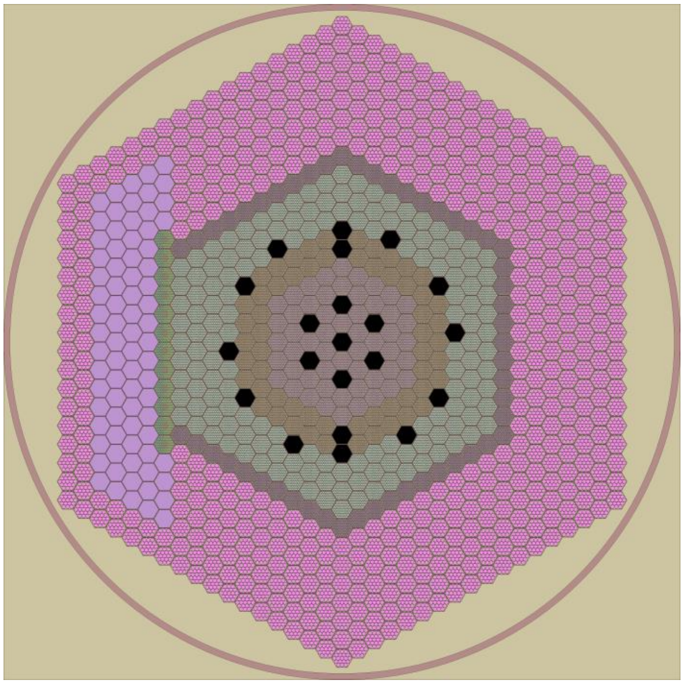

Figure 2.22 The core with the large irradiation positions replaced by an equivalent number of smaller irradiation positions.

Four different burnup simulations were performed. Burn up of the core will be studied in great deal in the next section and the burnup histories used here will be given in the next section. Here, results are presented for burnup of configuration 3, burnup of configuration 3 with large test volumes in the outer driver, and burnup of configuration 3 with large test volumes and two different core loadings. These will be called configuration 3, 4, 5, and 6. Configurations 5 and 6 have an increased fuel pin diameter such that the fuel volume fraction was increased by 10%. Configurations 5 and 6 also used the block MgO reflector presented earlier. In Configuration 5, Zone 2 is 17% enriched and Zones 3 and 4 are 15% enriched. In Configuration 6, Zone 1 and Zone 2 are 19.9% enriched, Zone 3 is 18% enriched, and Zone 4 is 16% enriched. Data is shown in Table 2.5. As fissile material in the core is depleted, fission cross sections must decrease and flux must increase to maintain core power. Core lifetime is measured in days. It was previously shown that inserting the large test volumes in the outer driver reduced fluxes in the central region. This is not the case here because of the loss in reactivity associated with removing the assemblies. Configuration 3 has a higher starting k_{eff} and a greater fissile mass; altogether it reaches an average core burnup ~80% greater than Configuration 4. The increase in flux due to burnup is a pronounced effect; it increases flux in the central position of Configuration 3 by 15% over the core lifetime. As Configuration 4 has a shorter lifetime, flux in the same position only increases by 9%. The loss in both flux and core lifetime associated with the large test volumes must be balanced against the increase in test volume. Similarly, Configuration 5 was zoned so as to increase the flux within the inner driver. The increase in flux must be weighed against the decrease in core lifetime. Configuration 6 was zoned so as to minimize the flux in the irradiation positions while increasing the core lifetime. The initial fast flux in the Center and Surrounding positions was 4.95E15 n/cm^{2}s in Configuration 6. Fluxes increased throughout the core lifetime, attaining average fluxes comparable to the other simulations for greater burnups and therefore greater fuel utilization.

Table 2.5 Core lifetime and fast fluxes for different configurations

Configuration	Core lifetime	Center	Surrounding	Outer
3	321	5.50E+15	5.42E+15	-
4	227	5.44E+15	5.37E+15	4.05E+15
5	169	5.76E+15	5.69E+15	4.08E+15
6	392	5.38E+15	5.34E+15	3.99E+15

2.3 Burnup simulations

This section will describe the results of burnup simulations. Burnup histories will be described, along with a benchmark for the zoning scheme. SERPENT 2 processes cross sections differently in burnup simulations than in static simulations; this effect is examined in connection with the benchmark. Various studies are performed that examine the relationship between core loading, flux within the central irradiation position, core average burnup, and core lifetime. The effectiveness of changing the fuel volume fraction is also studied, along with the use of the block MgO reflector. A simple fuel replacement scheme is examined wherein fuel assemblies in the outer driver have lower enrichments than those in the inner driver. In this refueling scheme, lower enriched assemblies in the outer driver are kept in the core while the inner driver fuel assemblies are replaced. The cost of fuel was not calculated for any of the cycles. More importantly, it is unknown how long a refueling or reshuffling interval is to be in this system. Without this metric, it is impossible to determine the optimum core loading from the standpoint of delivering a high fast flux over the reactor lifetime. It will be shown that cores with less fuel or lower enrichments have higher fluxes throughout the core. Such systems also have lower core lifetimes. Disregarding cost, it would be possible to give the optimum fuel cycle for simple refueling operations if the shutdown time were known. This would be done by finding the cycle that provides the highest fast flux within the irradiation positions over a set amount of time, perhaps a year. This would be tallied in terms of fluence within the irradiation position accounting for the shutdown time. This section will demonstrate the wide variety of core configurations and fuel loadings available and point out some general trends. In particular, the core is too small to function as a breed-burn core. However, if the fuel volume fractions were to be significantly, the core wide breeding ratio could be brought close to 1.0. Given the limitations on fissile mass, highly enriched fuel is the optimum fuel loading with respect to fuel utilization only. It is possible to attain fast fluxes as high as 7.5E15 n/cm^{2}s by changing enrichments throughout the core at the cost of shorter core lifetimes. Similarly, core lifetimes over 1 year are possible with fast fluxes close to 5.0E15 n/cm^{2}s.

Two burnup histories were used for the simulations; one where steps are given in terms of total average core burnup and the other were steps are given in terms of total irradiation time. The second sequence is derived from the first. The first sequence is copied from the SERPENT User's Manual as an example for burnup. This sequence comes from a high fidelity burnup simulation of a PWR assembly with gadolinium pellets. Each pin was modeled as a separate material. The units are MWd/kgU. The sequence is: 0.1, 0.5, 1.0, 1.5, 2.0, 2.5, 3.0, 3.5, 4.0, 4.5, 5.0, 5.5, 6.0, 6.5, 7.0, 7.5, 8.0, 8.5, 9.0, 9.5, 10.0, 10.5, 11.0, 11.5, 12.0, 12.5, 13.0, 13.5, 14.0, 14.5, 15.0, 20.0, 25.0, etc. The second sequence assumes a total core power of 200 MW_{th} and the units are days. The second sequence is: 1.0, 10.0, 20.0, 30.0, 40.0, 60.0, 80.0, etc. The first studies into the reactor's performance assumed a core power of 200 MW_{th}; as such, the first burnup simulations performed with the first sequence assumed that power. The base geometry was decided upon, but it was desired to perform simulations in terms of days because core lifetime was deemed a more important factor than core burnup. The second sequence closely approximates the first sequence for the base geometry at 200 MW_{th}. The first sequence takes smaller steps, but switches to larger steps after a certain point to minimize the number of steps taken. This characteristic was deemed undesirable in the study of core with shorter lifetimes. Greater precision was desired between 15 MWd/kgU and 25 MWd/kgU, so a more consistent scheme was used for short lifetime cores. Fig 2.24 shows k_{eff} versus time for the 20_12 core with both schemes. This core is described later in this section. Error bars give the absolute errors of k_{eff} at each step. The two simulations were deemed sufficiently similar to be used interchangeably. In general, schemes where the starting k_{eff} is 1.04 or below use the second sequence while schemes with a starting k_{eff} above 1.04 use the first sequence. Flux values and core lifetimes presented in this section assume a core power of 600 MW_{th}. Table 2.6 gives end of life isotopics for 20_12 calculated with both irradiation schemes. The end of life isotopics were calculated at a burnup of 21.4444 days after 500 days of irradiation at 200 MWth. The irradiation scheme based on burnup did not have a step at 21.4444 MWd/kgU, so the data was linearly interpolated between 20.0 MWd/kgU and 25 MWd/kgU. The two irradiation schemes did not differ in any meaningful way. Fig 2.23 and Fig 2.24 show a linear decrease in k_{eff} versus time. This trend was observed for every simulation performed. Therefore, simulations were tallied in terms of initial and final behavior. The last step were the reactor had a k_{eff} above 1.0 is the data point used when discussing final flux. However, this value is terms of reactivity varied widely between simulations, anywhere from 0.01$ to 1.0$. Therefore, the final burnup and core lifetime are actually extrapolations assuming a linear change in k_{eff} for these parameters.

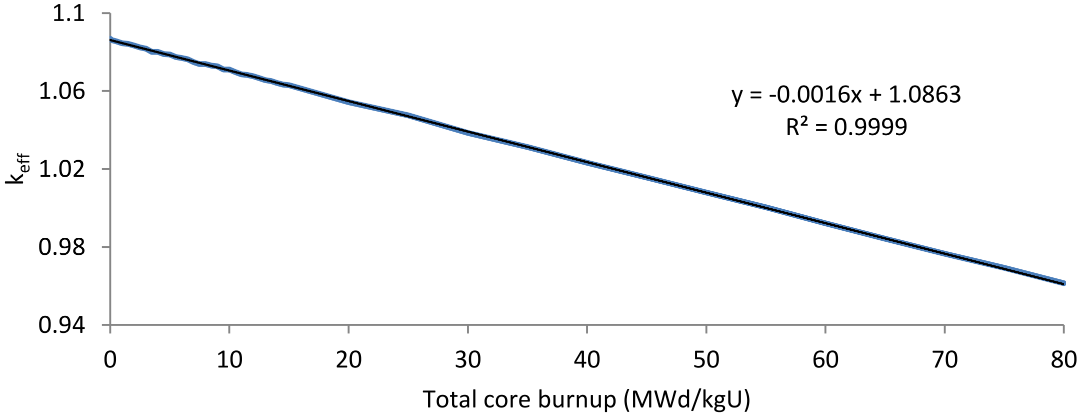

Figure 2.23 k_{eff} versus total burnup for the base geometry with linear best fit

Table 2.6 End of life isotopics for the same core with different irradiation schemes

Quantity	BU step	Time step
Pu mass (kg)	58.51415492	58.5425654
^{238}Pu mass fraction	0.000726467	0.000712856
^{239}Pu mass fraction	0.977045261	0.977264997
^{240}Pu mass fraction	0.020012064	0.019845218
^{241}Pu mass fraction	0.002216208	0.002176929
U mass (kg)	4499.823718	4499.79927
^{233}U mass fraction	9.01054E-09	9.23088E-09
^{234}U mass fraction	1.36177E-05	1.36291E-05
^{235}U mass fraction	0.129872933	0.129858904
^{236}U mass fraction	0.004986239	0.004990245
^{237}U mass fraction	5.27529E-06	5.28912E-06
^{238}U mass fraction	0.865121926	0.865131924
Total fissile mass (kg)	641.7059595	641.678043

These extrapolations use the initial excess k_{eff} (k_{eff} -1) divided by Δk_{eff} over the first and last steps and multiply this value, always greater than 1.0, by the burnup or core lifetime at the last burnup step. In actuality, cores are never run until k_{eff} is exactly 1.0, but the method of calculating final burnup and lifetime is consistent across all simulations. Fig

2.23 shows k_{eff} versus burnup for the base geometry. The linear fit and R^2 value are also presented. R^2 is nearly 1.

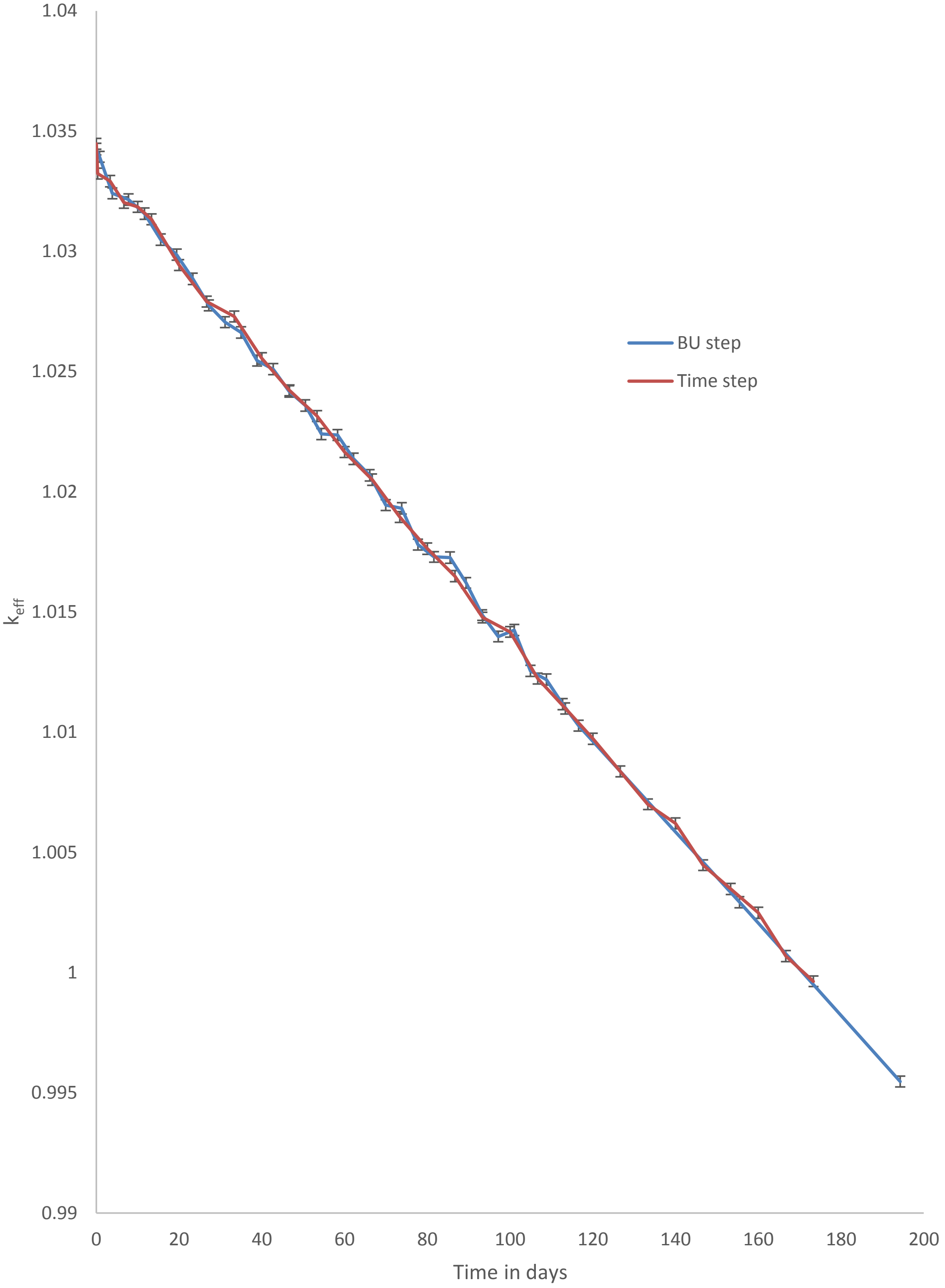

Figure 2.24 Comparison of the two burnup schemes

The benchmark used five radial zones and ten axial zones. The barrier assemblies were organized into the same burnable materials as before and were also divided into ten axial regions. However, no distinction was made between barrier assemblies near and far from the core centerline. In total, the benchmark included 80 burnable materials. The radial zoning scheme is shown in Fig 2.25. Zone 1 includes the inner three assembly rings, while Zones 2, 3, and 4 include two rings each. All burnup simulations used 2000 cycles of 5000 particles each. 20 inactive cycles are run per step. The predictor corrector algorithm was used along with all default SERPENT 2 burnup settings. This resolves k_{eff} to a relative error of 0.00021 to 0.00023, depending on the simulation. Table 2.7 gives the initial k_{eff} of each simulation, the final burnup in MWd/kgU, the core lifetime in days, the initial fast flux, it's absolute error, the final fast flux, and it's absolute error. These quantities are the essential characteristics for the reactor performance. They relate the effectiveness with which the fuel is used (burnup), the time until refueling, the average flux within the central irradiation position, and the degree to which control systems will have to compensate for the initial reactivity. The fuel isotopics were also investigated and were not found to differ in any meaningful way. The final burnup and core lifetime were within 2% of each other, which is sufficient for the purposes of this investigation. The mean plus standard deviation of the fluxes overlapped. The mean plus standard deviation of the initial k_{eff} also overlapped.

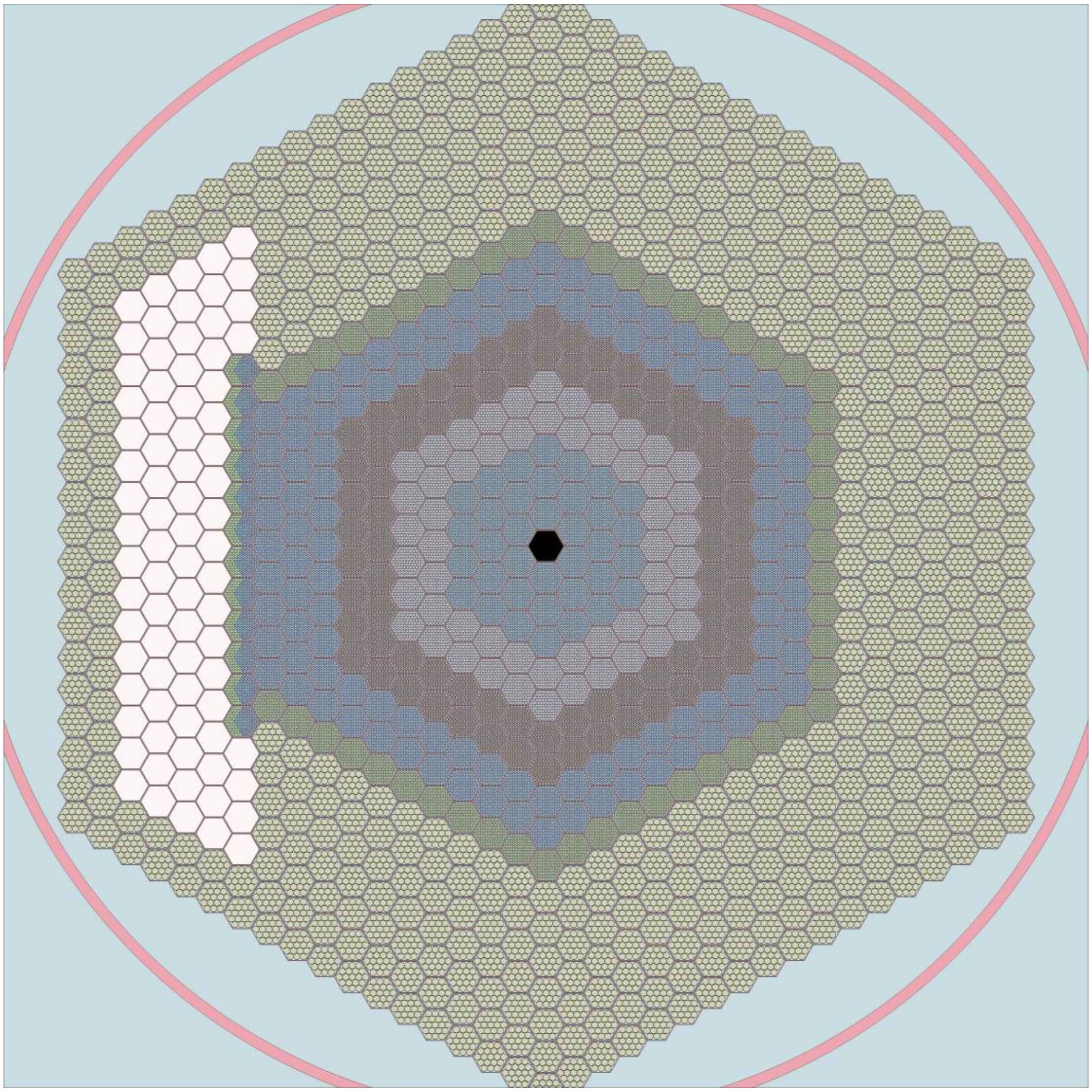

Figure 2.25 Benchmark of the base geometry performed with more materials

It would appear that the standard materials definition scheme and the higher fidelity scheme are appropriately similar. However, the initial k_{eff} of the simulations do not match the k_{eff} of the base geometry in static simulations. A total of 80E6 neutrons were simulated to obtain a k_{eff} of 1.08614 with a relative error of 7.7E-5 for the base geometry. The initial k_{eff} of the benchmark is over 5 standard deviations away from this value. The standard zoning scheme is approximately 4 standard deviations away as well, suggesting that the problem is common to both simulations. The answer stems from the manner in which SERPENT processes cross sections (Leppänen, 2013). To speed up computation time, SERPENT preprocesses the cross sections and stores them in the RAM. SERPENT does not calculate cross sections on the fly, as does MCNP. This feature does not pose a problem when dealing with the unburned core, but the sheer number of materials involved in a burnup simulation lead to very large grids.

Table 2.7 Initial keff, final burnup, core lifetime, initial fast flux, and final fast flux for the base and benchmark simulations. Burnup is in MWd/kgU, core lifetime is in days, and flux is in n/cm^{2}s.

Simulation	Initial k_{eff}	Final burnup	Core lifetime
Benchmark	1.08491	52.8	373
Base	1.08520	53.5	378

Simulation	Initial fast flux	Abs. err.	Final fast flux	Abs. err.
Benchmark	5.24740E+15	3.77086E+13	6.063102E+15	4.30382E+13
Base	5.29348E+15	3.82599E+13	6.015336E+15	4.22965E+13

SERPENT therefore uses a grid thinning technique to minimize the number of energy points (Leppänen, 2013). For example, the original grid of a burnup simulation had 1077498 points. Grid thinning reduced the number of points to 268378. 8.80MB of memory were allocated for grid data in this simulation. Therefore, a static simulation was performed using the initial unburned base geometry with the same grid thinning scheme that SERPENT uses for burnup simulations. The resulting k_{eff} was 1.08515 with a relative error of 7.7E-5. The initial k_{eff}'s of the standard and enhanced materials schemes now match the k_{eff} of the static simulation. This fact is common to all the burnup simulations performed in this investigation.

Table 2.8 Select whole core isotopics for the base and benchmark cases

Quantity	Base	Benchmark
Pu mass (kg)	96.122349	96.107378
^{238}Pu mass fraction	0.00212731	0.00215999
^{239}Pu mass fraction	0.95497042	0.95484969
^{240}Pu mass fraction	0.03774003	0.0376868
^{241}Pu mass fraction	0.00516224	0.00530352
U mass (kg)	3920.10059	3920.10973
^{233}U mass fraction	2.0209E-08	2.022E-08
^{234}U mass fraction	3.1484E-05	3.1489E-05
^{235}U mass fraction	0.14692353	0.14693517
^{236}U mass fraction	0.01186059	0.01185337
^{237}U mass fraction	2.7393E-05	2.7476E-05
^{238}U mass fraction	0.84115699	0.84115247
Total fissile mass (kg)	668.245207	668.279807

Burnup changed the neutron spectra within the core, in addition to increasing the absolute magnitude of the flux. The effect will be shown by comparing the flux in the center of the core at 0 MWd/kgU and at 50 MWd/kgU. To decrease the run time for the simulation, larger bin sizes were used. As explained previously, the flux peaks just outside of the central irradiation position. As the tally volume was larger than the central irradiation position, the neutron spectra presented here are 2.5 % greater in magnitude. The buildup of actinides and depletion of ^{235}U reduced the hardness of the neutron spectrum. Fig 2.26 shows the neutron spectrum for the core at different burnups. Relative flux is plotted. Flux fraction is the flux in each energy bin divided by the total flux. 120 energy bins were used. They are equal in lethargy from 1E-5 eV to 20 MeV. Flux fraction for each bin is plotted in y-axis and energy in MeV is plotted on the x-axis. Lower energy bins are omitted because they had few if any interactions at those energies. The spectral shift is slight but noticeable. The flux is shifted towards lower energies for higher burnups. Table 2.9 gives results for the shift. Flux is tallied in the standard four group scheme. The thermal fraction is negligible, but the epithermal fraction is not. The fast flux fraction within the core is approximately 0.746. The third significant figure varies somewhat between simulations depending on the exact definition of the tally volume, but this does not cause any significant change. The fourth row, entitled “Flux split,” gives the fast flux $E > 1.0$ MeV over the total fast flux $E > 0.1$ MeV. Both the flux fraction of $E > 0.1$ MeV and the flux fraction of $E > 1.0$ MeV decrease by 2.9% to 3.0 %. This change would become greater if the burnup was increased. No simulation presented in the present investigation exceeded 62 MWd/kgU, so the flux spectrum within the core is not expected to significantly change over the core lifetime. Fuel shuffling patterns were not studied; as a fuel shuffling scheme would increase the burnup, this investigation would have to be repeated for any advanced shuffling scheme.

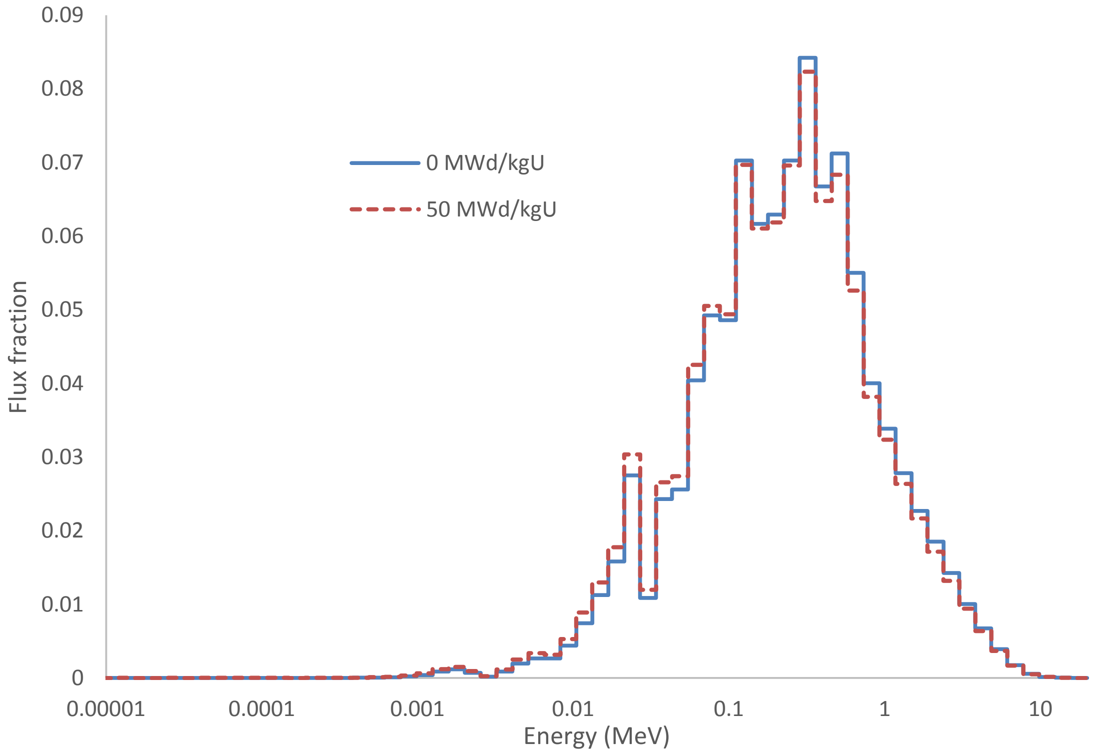

Figure 2.26 Neutron spectra of the base geometry driver region at 0 MWd/kgU and 50 MWd/kgU.

Table 2.9 4 group neutron spectra in the driver region of the base geometry.

Quantity	0 MWd/kgU	50 MWd/kgU
Thermal fraction	2.53E-06	1.46E-06
Epithermal fraction	0.254	0.275
Fast fraction	0.746	0.725
Fast split	0.172	0.167
Fast flux (n/cm^{2}s)	5.38E+15	6.17E+15

Reducing the enrichment will reduce the core lifetime and increase flux. The desire to increase flux was paramount; as a result the core was zoned in one of two ways. Either a uniform enrichment across the driver or with higher enrichments in the central core. The relative effects of concentrating fuel in the central driver versus spreading it out over the core are similar to heterogeneous versus homogeneous fast breeder reactor design. Heterogeneous breeder reactor typically have greater core wide breeding ratios than homogenous breeder reactors, but require more frequent change outs of the driver fuel. Additionally, heterogeneous breeder reactors must also have higher fluxes within the center of the core. Heterogeneous breeder reactors typically have more positive sodium void worth’s and less negative Doppler worth’s in the center of the core, but the high expansion coefficients of metallic fuel should ameliorate these concerns. The higher fast flux was the primary rationale for concentrating fissile material in the center of the driver and reducing the enrichment in the outer driver. As mentioned previously, fuel shuffling was not examined, but this method of zoning lends itself well to the relocation of the depleted driver assemblies to the outer driver and the addition of fresh assemblies to the inner driver. Table 2.10 gives data for three simulations. The first is the base geometry data, represented for ease of comparisons, while the second is the same geometry with Zones 2 and 3 at 18% enriched and the third with Zones 2 and 3 at 16% enriched. The core behavior is highly sensitive to enrichment, and the high enrichments necessary to maintain criticality are going to preclude any breeding ratio that approaches ~1.

Table 2.10 Burnup behavior of different core loadings with varying enrichments. Burnup is in MWd/kgU, core lifetime is in days, flux is in n/cm^{2}s, and Δflux/day is in n/(cm^2*s*d).

Simulation	Initial k_{eff}	Final burnup	Core lifetime	Initial fast flux	Final fast flux	Δflux/day	Average flux
Base	1.08520	53.5	378	5.29E+15	6.02E+15	2.04E+12	5.65E+15
Base_18	1.05559	36.0	255	5.75E+15	6.21E+15	1.83E+12	5.98E+15
Base_16	1.02337	15.2	107	6.20E+15	6.43E+15	2.13E+12	6.32E+15

There is a fairly large penalty associated with even modest changes in enrichments. The last two columns relate the change in flux per day and the average flux over the core lifetime. The change in flux is an operational concern. Many of the materials to be irradiated must experience constant temperatures. Higher fluxes yield higher temperatures, a phenomenon which will have to be accounted for but is not given further study in the present work. The average flux is the average flux that the central irradiation position experiences. The long core lifetime, in which significant depletion and buildup of fissile material occurs, raises the average flux of the base loading to a greater degree than the Base_16 loading. The initial flux of the Base_16 loading is 17% greater than the base loading, but the final flux of the Base_16 loading is only 7% greater than the base loading. This fact helps the base loading compensate for the initially lower fluxes. An increase of average flux by 12% requires a loss in core lifetime of 72%. This value of average flux does not account for shutdown times, which would be 3.5 times more frequent with reduced enrichments. In fact, a shutdown time of 18 days would results in the average fluxes for both loadings to be the same. With this shutdown time, the average flux for the Base_18 loading is higher, suggesting that this is the optimum core loading. It will be shown in subsequent sections that the addition of control systems reduces the core lifetime and initial k_{eff}. The insertion of control rods into the core increases flux within the central irradiation position. As control rods are withdrawn, flux decreases within the central irradiation position and increases near the control assemblies. In actual operation, this will compensate for the change in flux due to burnup. Burnup simulations were not performed in which control rods positions was varied. It will be shown in later sections that many of the additions to the outer reflector and moderating region to change fluxes to values more in line with other reactor types negatively impact core lifetime and initial k_{eff}. Therefore, an actual reactor in operation would have reduced performance relative to the simulations represented here. However, certain control systems are only useful for loading with minimal initial k_{eff}'s as outlined in later sections. While more fuel is required for the Base_16 loading, it is at a lower enrichment. However, the total amount of ^{235}U needed is significantly higher with the Base_16 loading because the lower enrichment does not compensate for the reduced core lifetime. Lower enrichments typically have higher breeding ratios. Reductions in enrichment do not stimulate breeding enough to compensate for the loss of ^{235}U for such a small core. Zoning schemes would have to be studied to examine the breeding of plutonium versus increasing enrichment.

Further decreasing enrichments to increase breeding ratio and fuel utilization would require a change to the base geometry. Increasing the fissile mass of the core would enable lower enrichments. However, making the pins larger would change the fuel assembly internal dimensions and increase the pressure drop while increasing the size of the core would violate the imposed size restrictions on the core. Both options will result in lower fluxes, which will be compensated with reduced enrichments. In order to minimize the perturbations from the base geometry, the increase in fissile mass was limited to 10%. An increase in fissile mass was affected in two ways. The first was to increase the fuel volume fraction by 10% by increasing fuel pin diameter. The second was to keep the fuel volume fraction the same and increase the core height by 10%. The change in fuel pin diameter will be described first. Fuel diameter increased to 0.3996 cm and the cladding thickness decreased to 0.0371 cm. The wrapper steel is modeled as an increase in cladding thickness. The cladding thickness is the same, so the amount of cladding steel within the core increases with increasing fuel diameter. However, the gap between the fuel pins decreases, so the volume of wrapper steel decreases. The two effects compensate for each other, and the steel volume fraction decreases. Larger pins increase the fuel volume fraction. The sodium volume fraction decreases slightly in response to the changes in steel and fuel volume. The sodium volume fraction and hydraulic diameter directly affect pressure drop within the assembly, which affects severe accident response. The change in sodium volume fraction is about 0.015, which should not cause pressure drop to increase beyond a few percent. Granted, a thorough fluid flow and heat transfer analysis would be required to prove this point. Increasing the core height by 10%, the other method to increase fissile mass, will increase pressure drop within the assemblies by 10% for a constant mass flow rate. Fuel volume fraction increases from 0.3450 to 0.3795, steel volume fraction decreases from 0.2399 to 0.0.2210, and sodium volume fraction decreases from 0.4151 to 0.3995 with a change in pin diameter. These values were measured over the active core only and include the assembly wall and sodium gap between assemblies. The increase in fissile mass could also be affected by adding more fuel assemblies. This was not recommend because the base geometry is slight flattened; the effective diameter is greater than the core height. Increasing the active height by 10% brings the core closer to a right cylinder with height the same height and diameter, the most reactive configuration for right cylinders. Table 2.11 gives data for three simulations. The enrichment scheme is the same in all three cases. Zones 1, 2, and 3 at 18% enriched while Zone 4 is 16% enriched. The first case is the base geometry, the second is with a 10% increase in fuel height and the third is with a 10% increase in fuel volume. Adding more fuel produces higher core lifetimes and reduces fluxes, but increasing the fuel volume fraction is clearly better than making the core taller. Increasing the fuel volume fraction increases both flux and core lifetime. There appear to be no tradeoffs associated with increasing fuel volume fraction versus increasing the core height.

Table 2.11 Burnup behavior of different core shapes. Flux is given in n/cm2s, burnup is in MWd/kgU, core lifetime is in days, and Δflux/day is in n/(cm2s*d).

Simulation	Initial k_{eff}	Final burnup	Core lifetime	Initial fast flux	Final fast flux	Δflux/day	Average flux
Base	1.04180	27.5	195	5.57E+15	5.98E+15	2.34E+12	5.77E+15
Tall	1.05339	35.4	275	5.08E+15	5.68E+15	2.22E+12	5.38E+15
More_fuel	1.07608	51.3	399	5.32E+15	6.08E+15	1.95E+12	5.70E+15

Keeping the same fuel type and increasing the fuel volume fraction more than doubled core lifetime while reducing flux by 1.2% versus the base geometry. Therefore, it was decided to attempt to increase breeding by decreasing outer driver enrichment. 14% enriched fuel was used in Zones 2 and 3. Table 2.12 shows results, tallied under 20_14. The initial k_{eff} is similar to Base_16, but the average flux and core lifetime are larger. Further decreases in enrichment would come at the cost of increasing the size of the inner driver. Therefore, Zones 1 and 2 contained 19.9% enriched fuel and Zone 3 was decreased in enrichment even further. The next two simulations, 20_12 and 20_11, give data for these simulations with Zone 3 at 12% and 11% enriched, respectively. 20_14 has an average enrichment of 15.3%, 20_12 has an average enrichment of 15.6%, and 20_11 has an average enrichment of 15.0%. This was tallied over the first three fuel zones. There does not appear to be any loading that is clearly better than the others.

Table 2.12 Burnup behavior of different core loadings, all with greater fuel volumes. Flux is given in n/cm2s, burnup is in MWd/kgU, core lifetime is in days, and Δflux/day is in n/(cm2s*d).

Simulation	Initial k_{eff}	Final burnup	Core lifetime	Initial fast flux	Final fast flux	Δflux/day	Average flux
20_14	1.02295	15.7	122	6.49E+15	7.47E+15	8.42E+12	6.98E+15
20_12	1.03421	21.9	170	6.79E+15	7.09E+15	1.87E+12	6.94E+15
20_11	1.02218	13.8	107	7.13E+15	7.38E+15	2.46E+12	7.26E+15

However, such low enrichments do open the possibility of a simple fuel reloading scheme. The central driver assemblies could be replaced with fresh fuel while the outer assemblies are kept in the core. This strategy was studied for 20_12 and 20_11. Fig 2.27 shows a graph of k_{eff} versus time for 20_11. 20_12 followed the same behavior. The initial k_{eff} after the second reloading was 86% of the first. The initial k_{eff} after the third reloading was 94% of the second. This relatively small drop in initial k_{eff} for the third loading suggests that the combination of 19.9% enriched fuel in Zones 1 and 2 and 10% enriched fuel in Zone 3 would be sustainable. Zone 3 was estimated at 10% enriched by comparing the amount of ^{239}Pu, ^{241}Pu, ^{235}U, and ^{238}U at the end of the second loading. However, this configuration would only have a lifetime of 80 days, which may not be useable from an operations perspective. The fast flux for this configuration and scheme would be 7.57E15 n/cm^{2}s at the point of refueling. As noted previously, long shutdown times would ameliorate many of the benefits of this scheme.

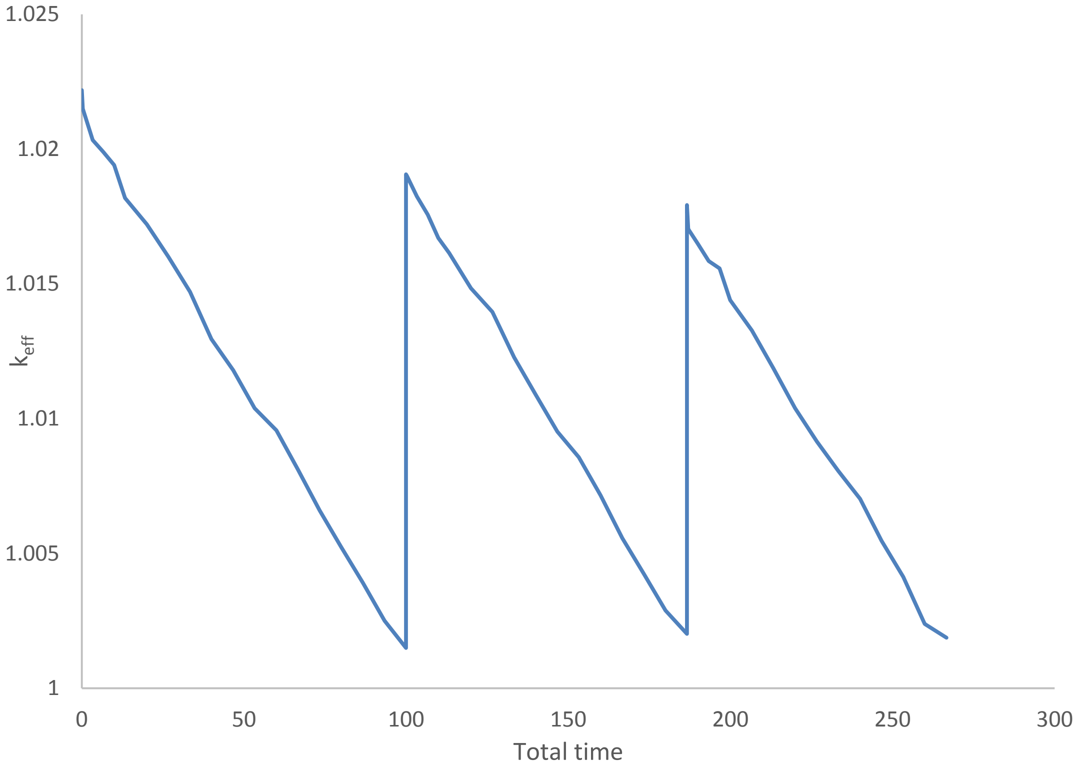

Figure 2.27 k_{eff} versus time for the 20_11 core and refueling scheme

The block MgO reflector mentioned earlier was revisited in the search for lower enrichments within the core. The block MgO reflector increases k_{eff} by reflecting more neutrons back into the core. A burnup simulation was performed with this reflector around the base geometry. An average flux of 5.54E15 n/cm^{2}s was attained over 433 days. Initial k_{eff} was 1.1013 and the final burnup was 61.3 MWd/kgU. The MgO reflector increases the neutrons flux within the outer reflector, which shifts the power density. Zoned cores where fissile material is concentrated in the center would not experience flux values so heavily peaked in the center. The central region would not deplete as quickly, maintaining k_{eff} for longer. However, fewer neutrons enter the reflecting region when the core is heavily zoned, so the block reflector will not have as strong an effect on the initial k_{eff}. The block reflector has an estimated reactivity worth of $2.11 for the base geometry. The block reflector was placed around 20_11 where it had an estimated reactivity worth of $1.63. The core lifetime increased to 162 days and flux dropped to 7.01E15 n/cm^{2}s. The block reflector appears to affect heavily zoned core with short lifetimes to a greater degree than uniformly 19.9% enriched cores. The block reflector increased the core lifetime by 54 to 55 days in both geometries. However, this is more noticeable with heavily zoned cores as a percentage of core lifetime.

It was desired to more precisely state the degree to which enrichment changes the breeding ratio in the core. Two simulations were performed, one with a higher enrichment and one with a lower enrichment. Decreasing the enrichment for the same size of fuel pin decreases the ^{235}U mass within the system. Differences in burnup behavior are going to be driven by loss of ^{235}U and by the change in breeding. However, it is only desired to study the relationship between breeding ratio and enrichment, not fissile mass. Therefore, the fissile mass of the two simulations must be keep the same with different enrichments. The only option is to change the fuel volume fraction. The fuel volume fraction of the lower enriched core must be higher than the higher enriched core. Decreasing the fuel volume fraction was examined towards the beginning of the research for this project. It was quickly disregarded because of the substantial penalty in both initial k_{eff} and core lifetime. Enrichment is the limiting quantity; smaller pins with the same enrichment results in a lower fissile mass. However, the flux does increase. In fact, the 19.9% enriched core with a fuel volume fraction of 0.3105 would have the same fluence as the base geometry with a shutdown time of 11 days. It would require refueling nearly twice as often but less fuel is present in the core. However, the reduction in fuel volume does not counteract the reduction in core lifetime, and 77% more fuel is required for the reduced fuel volume fraction presented here than without it. The lower enriched core with 10% greater fuel volume follows the standard fuel loading for the barrier assemblies and utilizes 16% enriched fuel in Zone 4. Zones 1, 2, and 3 are 16.281% enriched to match the fissile content in the higher enriched core. The higher enriched core is 19.9% enriched in Zones 1, 2, and 3, 16% enriched in Zone 4 and follows the standard zoning scheme in the barrier assemblies. To preserve the fissile content at the core periphery, the pins in the barrier assemblies and Zone 4 are 10% larger than the base geometry. The pins in Zones 1, 2, and 3 are 10% smaller than the base geometry. The fuel diameter is 0.36144 cm and the cladding thickness with the smeared wrapper volume is 0.4333 cm. The fuel volume of Zones 1, 2, and 3 in the lower enriched core is 22.23% greater. Because of rounding, the fissile mass of the lower enriched core is 0.00174% greater than the higher enriched core, a difference considered negligible.

Table 2.13 Burnup behavior for two cores with the same fissile mass but different enrichments and fuel volume fractions. Burnup in MWd/kgU, core lifetime in days, flux in n/cm2s, and Δflux/day in n/(cm^2*s*d).

Simulation	Initial k_{eff}	Final burnup	Core lifetime	Initial fast flux	Final fast flux	Δflux/day	Average flux
Higher	1.05671	34.0	225	5.37E+15	5.93E+15	2.81E+12	5.65E+15
Lower	1.03298	23.6	183	5.43E+15	5.85E+15	2.47E+12	5.64E+15

Both cores contain 748.8 kg of ^{235}U, while the higher enriched core contains 3222.5 kg of ^{238}U and the lower enriched core contains 3914.4 kg ^{238}U. Table ??? shows essential characteristics for the two simulations. The row labeled “Higher” presents data for the higher enriched core.

The average fluxes for the two systems are nearly identical but the core lifetime for the higher enriched core is 23% greater than for the lower enriched core. The breeding ratio, measured as the number of atoms of ^{239}Pu and ^{241}Pu generated divided by the number of atoms of ^{235}U lost, for the lower enriched core is 20% greater than for the higher enriched core. Breeding ratio for the two cores is plotted in Fig 2.28. The breeding ratio is nearly constant at the end of core life. ^{239}Np, produced by the absorption of a neutron by ^{238}U, beta decays into ^{239}Pu with a half-life of 2.356 days. Secular equilibrium between ^{239}Np and ^{239}Pu takes a few weeks, but after that the breeding ratio is stable. ^{238}U is a more significant absorber than steel or sodium, and the higher breeding ratio cannot compensate for its presence. However, further increases in fuel volume with the addition of the outer block reflector will cause the breeding ratio to approach 1.0, at which the lower enriched fuel loading would be favored over the higher enriched fuel loading. Further changes to the fuel volume ratio would alter the assembly internal geometry too much, and detailed calculations would be needed to study the effects. At the minimum, the pressure drop across the assembly would have to be compared to the EBR-II.

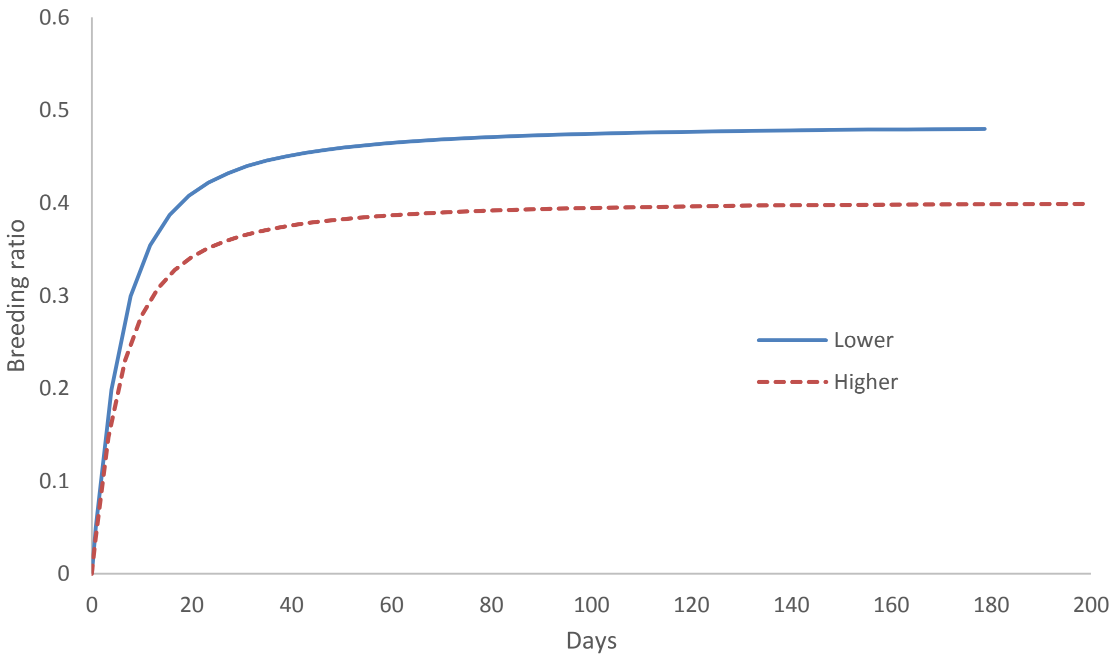

Figure 2.28 Breeding ratio for cores with different enrichments and fuel volume fractions but the same amount of fissile material

End of life isotopics for the two simulations were calculated. The estimated end of life burnup (34.0) for the higher enriched core was between the burnup steps (30.0 and 35.0). Fuel compositions are given as linear interpolations between the two data points.

The estimated end of life burnup was very close to the last burnup step for the lower enriched core and no linear interpolations was necessary. The higher enriched core attains greater burnups than the lower enriched core, so more plutonium is produced with the higher enriched core but the fuel is used more effectively with the lower enriched core. The end of life total fissile mass is 29.3 kg higher for the lower enriched core; ^{238}U has an larger negative effect on reactivity than the sodium and steel it replaced in the higher enriched core. Larger fissile masses are required to cause the presence of ^{238}U to have a positive effect of reactivity through the production of plutonium. The fuel loadings used here are something of a proliferation risk, as they contain greater than significant quantities of weapons grade plutonium. Over 100 kg of weapons grade plutonium would be produced by these fuel loadings per year, depending on the shutdown time. The total fissile mass associated with the base geometry is approximately the same as the fissile mass at the end of core lifetime for the core with reduced fuel volume fraction. The fissile mass of the base geometry is less than the fissile mass at the end of core lifetime for the core with reduced enrichment. The internal driver fuel geometry and overall core size impose restrictions on fissile mass. For a given amount of fissile material per cycle, it is more effective to increase enrichment and decrease fuel volume fraction. However, it is more effective overall to increase fissile mass and maintain a reasonably high enrichment. The same enrichment will attain a higher burnup with larger fuel volume fractions. Cores with low enrichments and higher breeding ratios will consume less fissile material. While they have shorter lifetimes, the increase in breeding ratio may result in fuel savings with an extensive reprocessing scheme. As less fissile material is consumed, less fissile material would be needed over the core lifetime for increases in flux. This would have to be balanced against the cost of an extensive reprocessing scheme and the loss in fluence associated with the shutdown time.

Table 2.14 End of life isotopics for two core with different enrichments and fuel volume fractions but the same fissile mass.

Quantity	Higher	Lower
Pu mass (kg)	63.30669	59.1078
^{238}Pu mass fraction	0.001189	0.00072
^{239}Pu mass fraction	0.966535	0.975303
^{240}Pu mass fraction	0.028511	0.021591
^{241}Pu mass fraction	0.003766	0.002387
^{235}U mass (kg)	597.4396	630.371
^{233}U mass fraction	1.4E-08	9.63E-09
^{234}U mass fraction	2.13E-05	1.43E-05
^{235}U mass fraction	0.158643	0.140368
^{236}U mass fraction	0.008354	0.005477
^{237}U mass fraction	2.19E-05	1.59E-05
^{238}U mass fraction	0.83296	0.854125
Total fissile mass (kg)	658.8607	688.1601

3. TRANSIENT TESTING LOOPS

While time invariant materials testing has enormous benefits, it is frequently desired to subject nuclear materials to time varying conditions. Time invariant behavior will be implemented by using transient testing loops, with a similar design and purpose as those in the ATR (FY, 2009). These transient testing loops are intended to replicate thermal hydraulic conditions of reactors in test assemblies. Test assemblies are sections of assemblies that are prototypic of assemblies in a given reactor. They are used to acquire assembly level behavior of the reactor they represent. The transient testing loop comprises the test assembly itself, which is inside the core, along with the associated piping, pumps, heaters, condensers, heat exchangers, etc. to achieve the necessary thermal hydraulic conditions. The transient testing loops are quite complicated (Gerstner and Davis, 2012) and will not be outlined here. As they have been successfully implemented in the ATR (FY, 2009), it is assumed that they can be implemented in this reactor. To provide some context, a schematic of the reactor is shown in Fig 3.1 with the locations of the neutron flux trap and transient test assembly highlighted.

Transient testing in this reactor poses special concerns. The first is that transient testing using light water raises the possibility of water-sodium chemical reactions. Such reactions are potentially dangerous, but this hazard will not be addressed here. It is assumed that the system can be designed so as to reduce the likelihood of a water-sodium reaction and mitigate the consequences should that reaction occur. The second major issue relates to neutronic effects that the loop will have on the core, and will be discussed in great deal. The in core portion of the transient testing loop, where the test assembly is located, is inside a neutron flux trap. The purpose of this flux trap is isolate the test assembly from the rest of the core. This is important for two reasons.

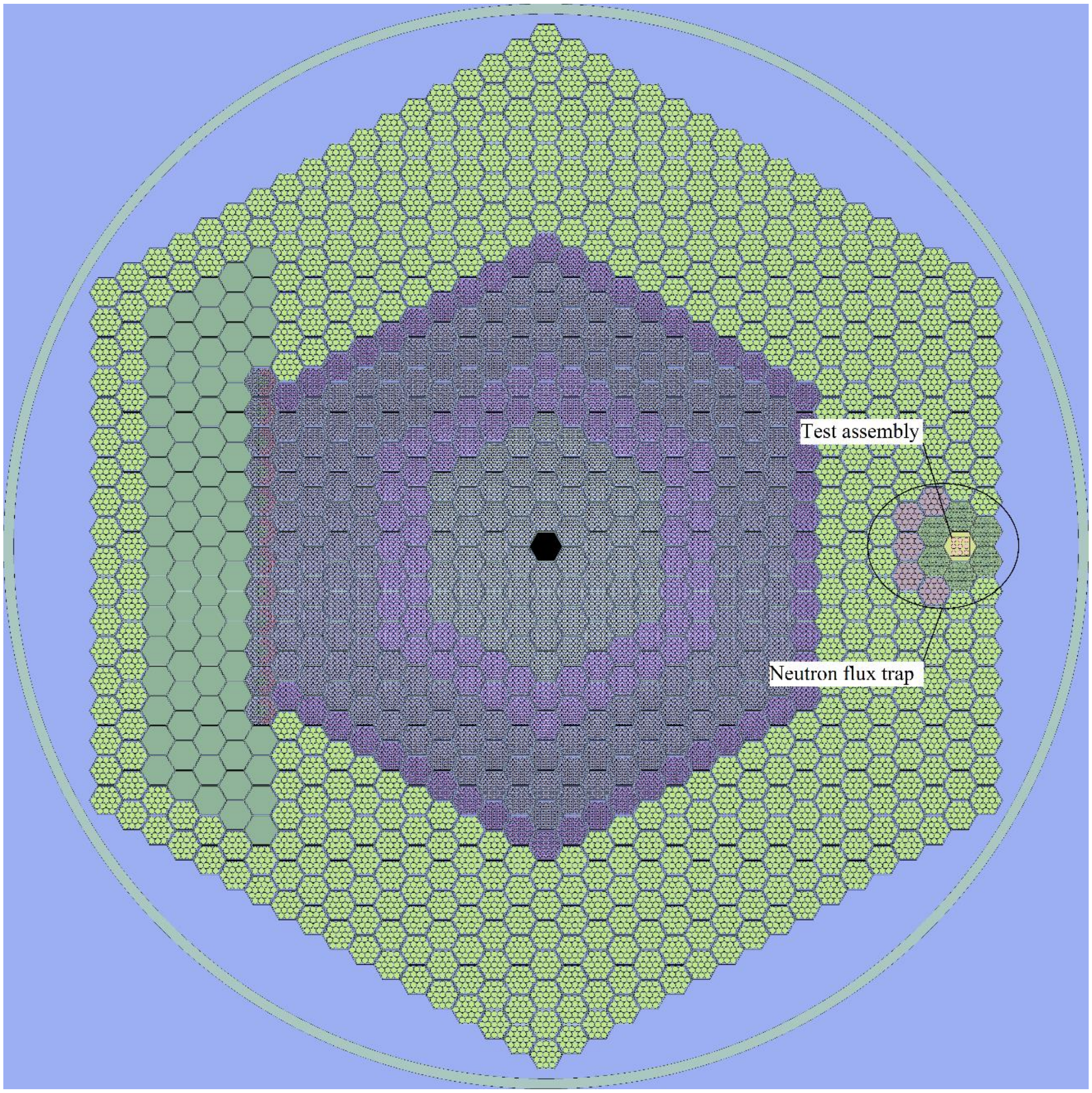

Figure 3.1 Locations of flux trap and transient test assembly

As this is a materials test reactor, there will be other samples within the core. These samples are irradiated at time invariant conditions; it is undesirable to subject them to changing conditions. Similarly, changing cladding and structural temperatures in the driver fuel causes the elements to expand and contract. Over time, this causes fatigue. For these reasons, changing conditions in the test assembly should not affect the core.

Test assemblies are subjected to a wide variety of potential scenarios. It is not the purpose of this work to detail how these scenarios are to be performed; rather it will be shown that if some of these scenarios are performed, the expected effects on the core can be easily offset with appropriate movements of the regulating control elements. Specifically, it will be shown appropriate movements of the regulating control assemblies in the core can offset the reactivity effects of changing the power in the test assemblies and the reactivity effects of voiding a PWR test assembly. The effect on the core of voiding a test assembly and inserting control rods to change the test assembly power is tallied in terms of reactivity. Explaining these reactivity values constitutes a large portion of the present work. The other portion of the present work concerns the power levels and profiles within the test assemblies. As these test assemblies are meant to represent actual reactors, they should be irradiated at power levels and with power profiles similar to those experienced in the reactors they are meant to replicate.

The neutronic isolation in the flux trap is affected by thermalizing neutrons in the trap. Neutrons streaming from the core are primarily fast. As they interact with the outer reflector they lose energy, becoming epithermal. Some do eventually thermalize, but most stay above thermal energies. The degree of thermalization depends on the distance from the core, as previously demonstrated. Neutrons streaming directly from the core towards the flux trap should be epithermal, whereas neutrons streaming from the sides (i.e. further from the core) are going to be more thermal. For this reason, reflector assemblies doped with cadmium are placed between the test assembly and the core. Cadmium has a very high thermal absorption cross section and a comparatively low epithermal cross section. The flux trap itself contains a great deal of light water. It is intended that neutrons streaming directly from the core enter the flux trap and thermalize. Neutrons that stream from the trap directly towards the core will be absorbed by the cadmium. Thermal neutrons that enter from the sides are not absorbed. It is intended to make the flux trap as “black” as possible from the perspective of the driver, while not actually losing any neutrons that enter the trap. The cadmium allows epithermal neutrons to enter the trap, while preventing thermal neutrons from leaving. The light water in the trap helps to ensure that any neutrons that enter the trap or are generated in the trap are absorbed before they can reach the core. This methodology minimizes the effect the neutrons trap has on the core. The transient testing region should be as far from the driver as possible and take up as little space as possible. Neutrons that enter the region do not escape; the reflector is essential to maintain criticality of the core and this trap reduces its effectiveness. Placing the trap as far as possible from the core is not an issue with respect to providing a high enough flux in the trap itself, as will be demonstrated in this section.

The (n,γ) cross section of ^{113}Cd is shown in Fig 3.2. The neutron absorption cross section below approximately 0.5 eV is very large; any neutrons below 0.5 eV passing through the material are captured. However, far more neutrons above this energy will pass through the materials unimpeded. To provide more clarity, the Maxwell averaged absorption cross section at 0.0253 eV is 24388 barns, while the Resonance Integral is 393.6 barns (Chang, 2015). By doping the reflector pins around the test assembly with this material, thermal neutrons would be absorbed while fast and epithermal neutrons would not be absorbed.

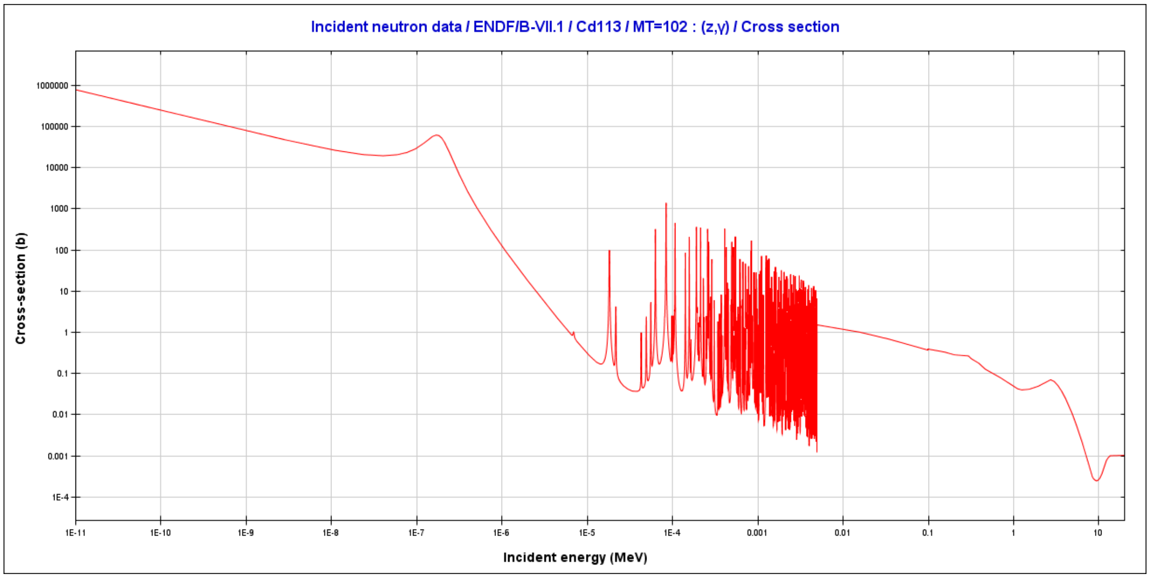

Figure 3.2 ^{113}Cd absorption cross section. Generated with JANIS 4.0 (Soppera, 2014)

Regulating the power of the transient testing assembly is done by surrounding it with boron control assemblies. These assemblies contain 61 unenriched B_4C graphite followed rods cooled by light water. ^{10}B, shown in Fig 3.3 has a significant absorption cross section and is used in current LWRs. It's most common form is as B_4C, used in control rods. ^{10}B has an abundance of 19.9%, and is used here in its unenriched form.

The Maxwell averaged cross section is 3400 barns at 0.0253 eV, with a resonance integral of 1719 barns (Chang, 2015).

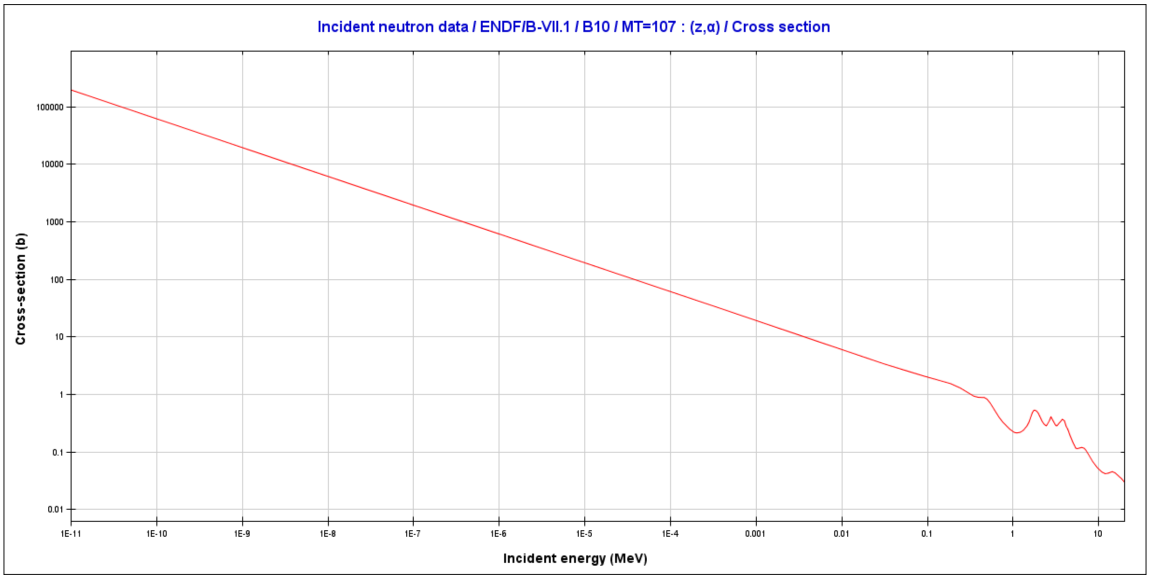

Figure 3.3 ^{10}B absorption cross section. Generated with JANIS 4.0 (Soppera, 2014)

This material is capable of absorbing both thermal and epithermal neutrons. Considering the distance from the core and the presence of so much moderator, few fast neutrons are present. Although liquid sodium is a more effective coolant, light water is used so as to provide additional moderation. Light water cooling in the control assemblies increases the reactivity worth of the rods by slowing down the neutrons. ^{10}B is a 1/v absorber; the cross section below the resonance region varies inversely with the velocity of the neutrons. Slowing down the neutrons therefore increases the likelihood that they will be absorbed by the rods. The control rods must be rapidly moved to control power changes. The rods are moved from above and are followed by graphite, which provides additional moderation. Therefore, insertion of the rods both decreases moderation and increases capture.

The insertion of control rods from above will perturb the power profile in the test assembly. In some transient testing scenarios, this may be desirable; in others, this is undesirable. It is intended that the control rods are rapidly individually movable (all 366 of them). They must be able to move 1.8 meters in a few seconds. The control assemblies towards the outside of the system matter less than those between the driver and testing assembly, and it may be possible to group rods together in banks for those assemblies only. The rods will be either fully inserted or fully withdrawn at all times. The presence or absence of individual rods regulates how many neutrons from the driver fission in the transient testing assemblies, affecting power in the assembly. While not proved in this research, it should be possible to modify the power in the test assembly to any power between the minimum and maximum power (all rods fully inserted and withdrawn, respectively). As stated previously, there are many rods with which to modify assembly power. However, the neutron flux spectrum that each rod is exposed to is different in both magnitude and shape. This is because neutrons entering the trap from the core are not fully thermalized. As they slow down, they are more likely to be absorbed by the rods. Therefore, rods closer to the test assembly are more likely to absorb neutrons, while rods closer to the core have lower effective cross sections but have a greater flux. Similarly, the withdrawal of a rod will increase the amount of graphite at that position. This increases moderation, slowing the neutrons, and increasing the effective cross sections of the control rods that have not been withdrawn. Given the complexity within the control assemblies, it should be possible to mimic any power level between the power levels associated with all of the rods full withdrawn and fully inserted.

Three different transient testing assemblies were simulated in the system: a 3 by 3 PWR assembly, a 19 pin SFR bundle, and a prismatic VHTR assembly. The reactivity worth of the control rods and assembly itself were tallied, along with the power profile for the rods fully inserted and withdrawn. The amount of power produced from fission at different neutron energies was tallied as well, along with the power per pin for the PWR and SFR. These three reactor types were chosen because they represent the three different strains of current and proposed reactor types. The PWR is the most common reactor type today, and will be for some time in the future. The SFR represents the most established fast reactor technology. The lead cooled fast reactor and gas cooled fast reactor do not substantially differ from the SFR in terms of assembly design. The VHTR is one of the candidate advanced reactors which received significant attention in 2000s for its ability to support Hydrogen Economy and power cycles with a high thermodynamic efficiency (Next, 2007). The analysis presented here will show that transient testing can be performed in the proposed reactor for the PWR, SFR and VHTR.

3.1 PWR transient testing

Fig 3.4 shows the PWR transient testing assembly and the flux trap. Twelve MgO reflector assemblies are removed and replaced by five cadmium doped MgO reflector assemblies, six control assemblies, and one PWR testing assembly. The testing assembly is in the center of Fig 3.4 and is composed of a 3 by 3 representative PWR assembly.

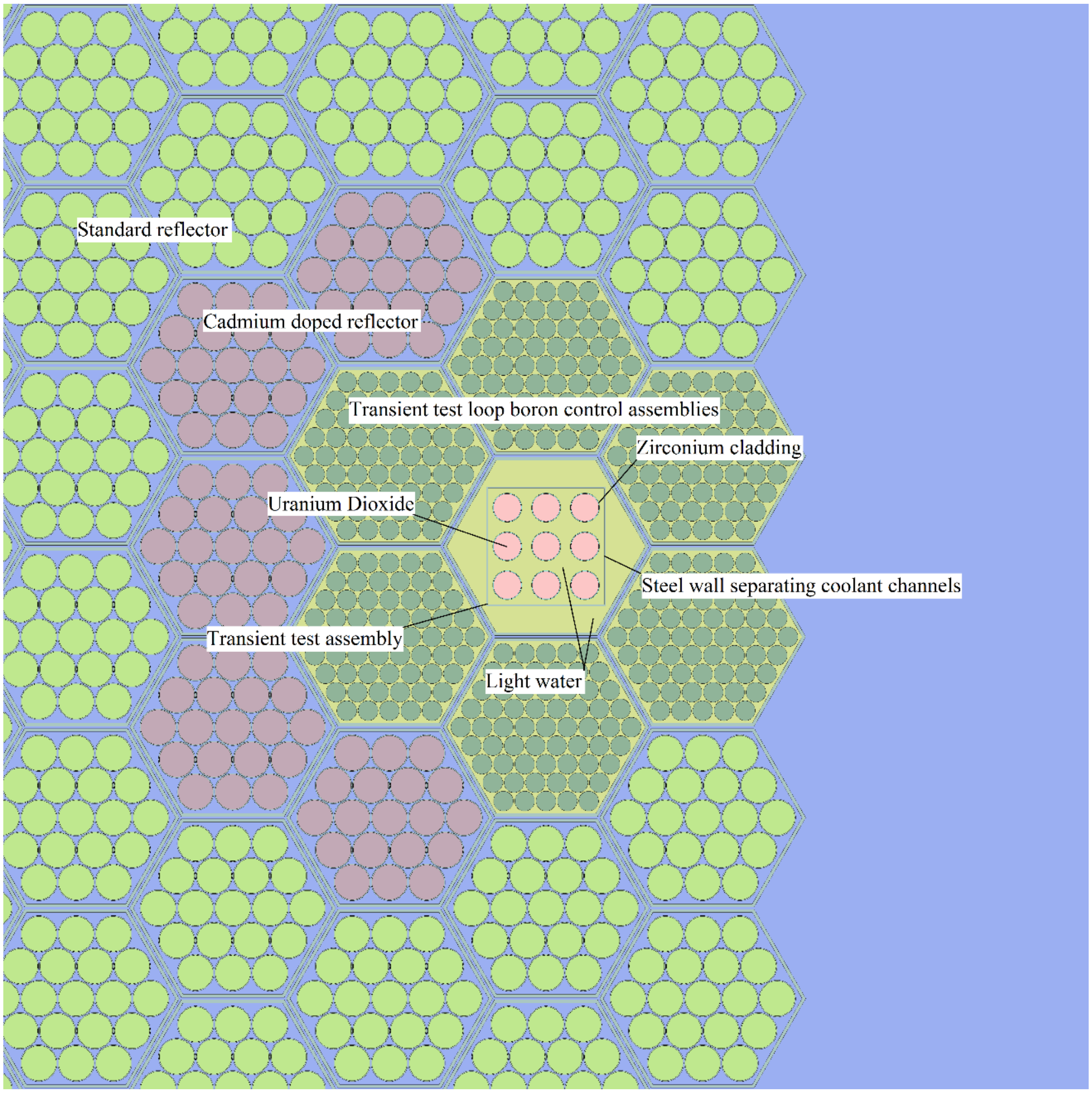

Figure 3.4 PWR test assembly in the transient test trap. The cadmium doped reflectors assemblies and boron control assemblies are highlighted.

Pin pitch is 1.265 cm and the pin outer diameter is 0.95 cm. The fuel is uranium dioxide with a density of 10.475 g/cm^3. Cladding, modeled as pure zirconium, is 250 μm thick. No gas gap is modeled. Light water, modeled with 600 K cross sections at a density of 660 g/cm^3, surrounds the pins. A 250 μm thick steel wall surrounds the testing assembly. Water, modeled at the same conditions as the testing assembly, is outside the thin steel wall. A wall of standard dimensions separates the outside loop water from the sodium outside the assembly. The boron control rods are 0.65 cm in diameter with a cladding thickness of 25 μm. The cadmium doped MgO assemblies contain 0.5% cadmium by atom percent. These dimensions are similar to dimensions presented in the AP1000 Design Control Document (Westinghouse 2011).

Table 3.1 Reactivity's associated with PWR transient testing

Geometry to be measured	Reactivity in dollars	Absolute error
Testing assembly with rods fully withdrawn	0.00783491	0.01819
Control rods without testing assembly	-0.0653247	0.0182
Control rods with testing assembly	-0.0731596	0.01431

The given reactivity worth's, presented in Table 3.1, assumed β_{eff} to be 0.0065. This value will be lower at the end of core lifetime. Inserting the testing assembly slightly increases the reactivity of the core. However, the effect is far less than the statistical error of the calculation. Inserting all the rods inserts about 0.065$ with no testing assembly present, while inserting all the rods with the assembly present insert

0.073$. It should be noted that the absolute errors of those reactivity estimates are greater than the difference between the two measurements. The absolute errors of the reactivity estimates are much smaller than the reactivity estimates themselves. The estimate of control rod worth without the testing assembly is approximately 3.5 standard deviations from 0.0$ and the estimate of control rod worth with the testing assemblies is approximately 5.2 standard deviations from 0.0$. Based on the control rod worth data previously presented, the rods in x control assemblies would have to be moved from position y to position z to maintain a constant core power.

Fig 3.5 shows the axial power profile in the test assembly with the rods fully withdrawn. Uranium dioxide at 0.4% enrichment was used to generate this plot. The 1 meter tall rod was broken into 20 axial sections, each 5 cm tall. The points on the figure are the midpoints of the sections. 40 cm of graphite is located above and below the fuel portion. This reflector flattens the power profile.

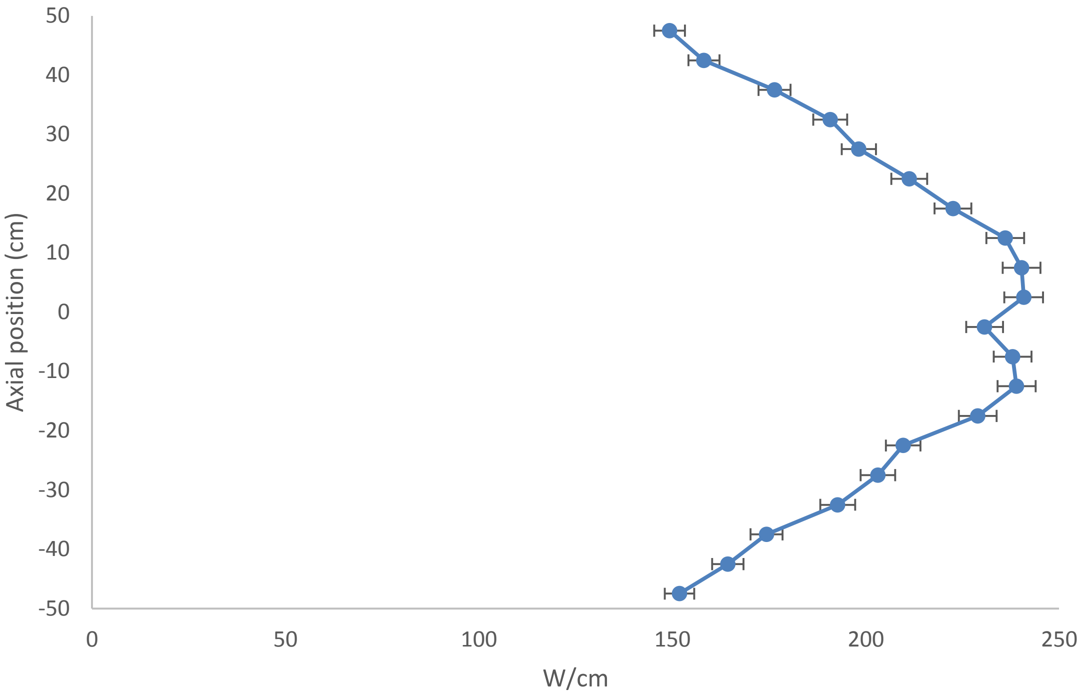

Figure 3.5 Axial power profile of a PWR test assembly at full power

The power in the axial sections from 0 to -5 cm centered at -2.5 cm dips compared to the other sections in the center. It should be noted that the error bars of those sections overlap, meaning that that dip is not statistically significant.

Table 3.2 shows the average linear power for the whole assembly as well as the power generated by neutrons in different energy groups. The column titled “Relative error” gives the statistical error associated with the linear power. The column titled “Relative power” gives the fraction of power produced in each energy bin divided by the total power. As can be seen, over 90% of the fissions are thermal fissions in this configuration. The average linear power is approximately 203 W/cm, slightly higher than the average linear power for the AP1000 (187.7 W/cm) (Westinghouse, 2011).

Table 3.2 Power per energy group for a PWR test assembly at full power

Flux bin	Linear power in W/cm	Relative error	Relative power
E < 0.625 eV	185.565	0.00602	0.914848
0.625 eV < E < 0.1 MeV	11.893	0.00875	0.058633
0.1 MeV < E < 1 MeV	0.109185	0.01679	0.000538
E > 1 MeV	5.26991	0.02202	0.025981
Total linear power	202.8371	0.000146	1.0

The axial power profile for the same configuration except with the rods fully inserted will not be shown. So few fissions occurred within the assembly that the resulting profile has very large error bars. Table 3.3 shows the effect on spectrum that inserting the rods caused. The same group structure was used as in Table 3.2. Assembly power was reduced to 2.88% of its original value. This dramatic reduction in power caused by a reduction in neutron flux means that the simulation would have to be run for a prohibitively long time to resolve statistical error with each axial section to as great a degree as previously. The column titled “Power drop fraction” relates how the power in each bin changed with the insertion of control rods. It is the linear power per bin with rods withdrawn divided by the same quantity with the rods inserted. The addition of boron rods had the greatest effect on the thermal group; the power contribution of the thermal group dropped to 1.8% of its previous value. This is to be expected as boron is a 1/v absorber. Now, just 56% of fissions are due to thermal neutrons.

Table 3.3 Power per group with rods fully inserted

Linear power in W/cm	Relative error	Relative power	Power drop fraction
3.28208	0.02072	0.5618226	0.017686956
1.39117	0.01187	0.2381388	0.11697385
0.051485	0.01151	0.0088132	0.471540047
1.11712	0.02205	0.1912273	0.21198085
5.841855	0.005902	1.0	0.028801

The importance of thermal neutrons will be more explicitly shown with a flux profile, Fig 3.6. This uses the 120 equal lethargy group structure. The lack of appreciable amounts of ^{235}U in the system, necessary to keep linear power to a reasonable value, reduces the fast portion of the spectrum. The presence of such a large body of thermal neutrons without the characteristic fast portion hints at the thermalizing effect of the moderating control assemblies. This thermalizing effect is the reason the cadmium reflector assemblies neutronically isolate the core. When this thermalizing effect is reduced, the cadmium reflector assemblies are not as effective, as will be shown when examining the SFR test assembly.

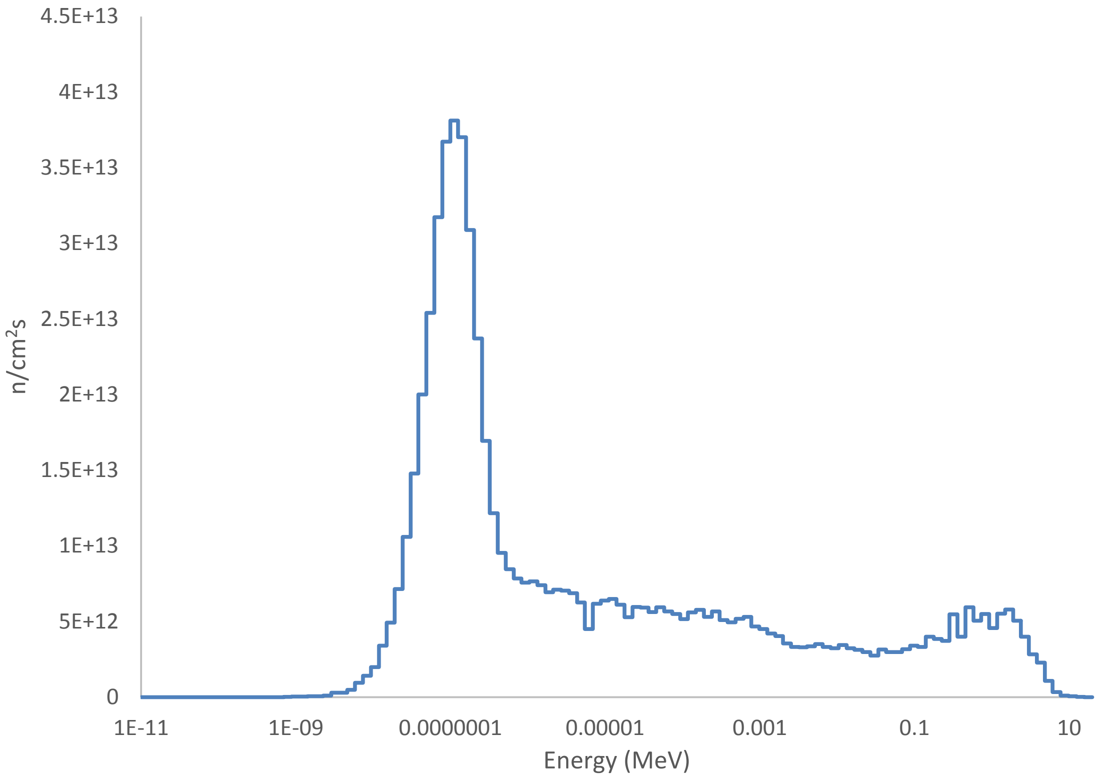

Figure 3.6 PWR test assembly neutron spectra at full power

The last bit of analysis relevant to the PWR test assembly is the power produced per pin. Pin power will be shown on a line chart. Each point on Fig 3.7 represents the pin power. Continuous lines are used on the graph so that general trends are easier to visually see, although pin power is a discrete, not continuous quantity. Ideally, pin power should be represented on a 2D plot, but it is here represented on a 1D chart.

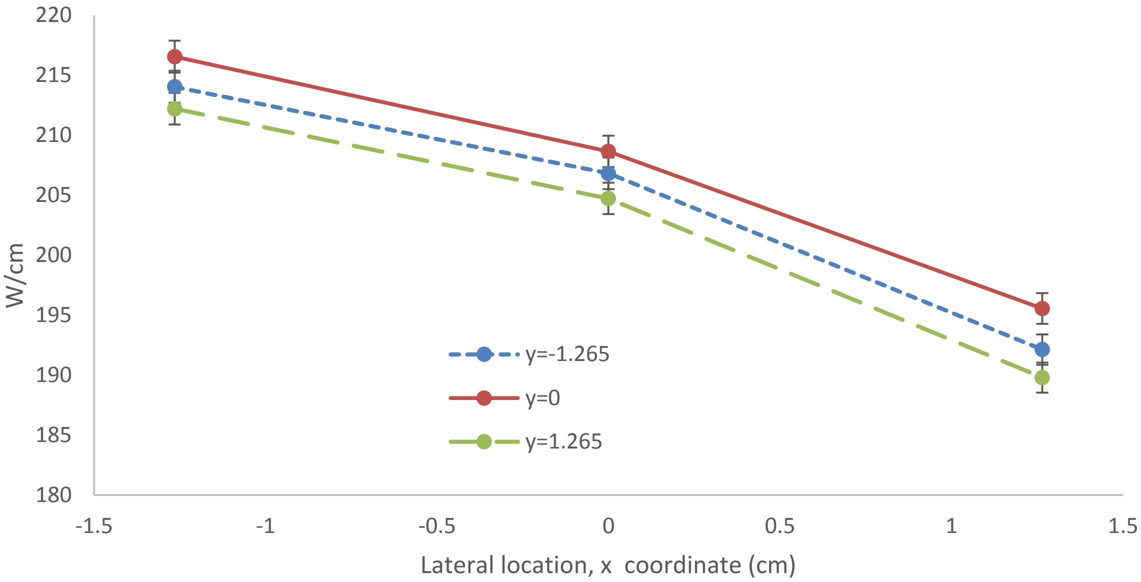

Figure 3.7 Pin power of the PWR test assembly. The square lattice has three rows and three columns. Each line gives pins power for constant horizontal pin rows. The x-axis gives the x-coordinate of the pins, while each line gives the y-coordinate of the pin. The y-axis gives average pin power.

There are three different lines with three points per line. Each line is for a different “y” coordinate. The 3 by 3 pin lattice has its origin at (0,0) in the center of the assembly and is laid out on the (x,y) plane. The upper most line is through the center of the assembly, the next line is the bottom of the assembly and the lowest line is through the top of the assembly. While it is expected that the center pins would have the greatest flux and correspondingly greater power, it was not expected that there would be a difference between the two boundary assemblies. The error bars between the two lines overlap, so this observed discrepancy is not statistically significant. As can be expected, pin power decreases further from the driver. More neutrons stream directly from the driver than stream into the reflector and are scattered in from the sides.

Analysis so far has restricted itself to manipulating power in the test assembly and how to offset that manipulation with appropriate movements of the control rods. However, as pointed out previously, there are other transient scenarios besides those regulated by power. An example scenario could involve boiling in a PWR. This scenario is mimicked in the present analysis by reducing the density of the inner water coolant channel from 660 g/cm^3 to 186 g/cm^3. This represent a mass quality of 20%. The outer coolant channel is unchanged. With this modification, the average linear power is now 211 W/cm. The k_{eff} of the reactor increases, inserting 0.0379$ of reactivity with a standard deviation of 0.0157. Increases in both the power of the assembly and reactivity of the reactor suggest that the test assembly is over moderated. Although the insertion of positive reactivity is a potential safety concern, the magnitude of the insertion is less than the magnitude of the negative insertions associated with reducing the test assembly power.

While using 0.5% cadmium in the barrier reflector assemblies brought about favorable results, it would be a worthwhile investigation to see what would result from changing the cadmium concentration in those assemblies. Full data sets like the one presented above were generated for barrier assemblies with 0.0% cadmium and 1.0% cadmium, but for the sake of brevity, only the reactivity worth’s and average linear power will be presented. The PWR test assembly shown above was used to test the effect of changing the cadmium concentration. First, the effects of 0.0% cadmium are analyzed and presented in Table 3.4.

Table 3.4 Reactivity's associated with a PWR transient test assembly with no cadmium in the reflector assemblies surrounding the flux trap.

Geometry to be evaluated	Reactivity ($)	Absolute error
Testing assembly with rods fully withdrawn	-0.0065267	0.012738
Control rods without testing assembly	-0.1045002	0.012747
Control rods with testing assembly	-0.0927448	0.011052

The average linear power was calculated to be 237.2 W/cm with an absolute standard deviation of 0.781. Removing the cadmium increased the linear power, but not so much as to significantly differ from typical PWR average linear powers. The more interesting effects stemmed from the reactivity worth's of the assembly and control rods. In this case, the reactivity worth of the assembly was negative, but this result is not statistically significant. However, the reactivity worth of the rods was greater with 0.0% cadmium than with 0.5% cadmium. The difference between the two values was greater than the combined standard deviations when measuring the reactivity worth of inserting the rods without a test assembly present. The difference in worth's was approximately 0.0392$ with combined standard deviations of 0.0309$. The difference between the reactivity worth's of the control rods for the two cadmium concentrations with the test assembly present was less than the difference without the assembly present. The difference in worth’s with the assembly present is approximately 0.0196$ while the combined standard deviation is 0.0254$. The cadmium in the barrier assemblies reduces both the linear power of the test assembly and the effect of the control rods on core power.

Increasing the cadmium concentration from 0.0% to 0.5% reduced the effect of the rods while not having a deleterious effect on assembly power. Would increasing the concertation further reduce the rod worth’s while not affecting assembly power? The results are inconclusive. Table 3.5 shows the reactivity worth’s of the assembly and control rods with 1.0% cadmium. Average linear power for this scenario is 200.9 W/cm with a standard deviation of 0.715 W/cm. Increasing cadmium concentration reduced assembly power by only a few percent, a favorable outcome.

Table 3.5 Reactivity’s associated with a PWR transient test assembly with 1.0% cadmium in the reflector assemblies surrounding the flux trap.

Geometry to be evaluated	Reactivity ($)	Absolute error
Testing assembly with rods fully withdrawn	0.00391785	0.012836
Control rods without testing assembly	-0.0914781	0.012752
Control rods with testing assembly	-0.0823204	0.011163

However, the reactivity worth’s of the rods increased. Their increase is not enough to draw meaningful conclusions. The difference in reactivity worth’s without a test assembly present is 0.0262$ while the combined standard deviation is 0.0310$.

Similarly, the difference in reactivity worth's with a test assemble present is 0.0091$ while the combined standard deviation is 0.0255$. Changing the cadmium concentration by this small amount did not bring about a desirable effect on reactivity worth, so further increases in cadmium concentration were not affected. Suffice it to say, analyses of the SFR and VHTR test assemblies were performed with a cadmium concentration of 0.5% by atom fraction.

3.2 SFR transient testing

The SFR test assembly here modeled is not based on any specific reactor, but is meant to be representative of typical fast reactor assembly dimensions (Fast, 2006). The fuel diameter is 0.6 cm with a cladding thickness of 0.0305 cm. A pin pitch of 0.9658 cm gives a fuel volume fraction of 0.35 within the assembly. 19 such pins are enclosed in a steel wall 0.05 cm thick. As in the driver, the wrapper is not explicitly modeled, but the wrapper steel is instead wrapped around the pin, increasing the cladding thickness. The reactor uses metallic fuel, but most SFR design uses UO_2 as their fuel. As such, 4.0% enriched UO_2 fuel is used in this analysis. The SFR test assembly and the flux trap are shown in Fig 3.8. The neutron spectrum within the SFR test assembly with the rods fully withdrawn is shown in Fig 3.9.

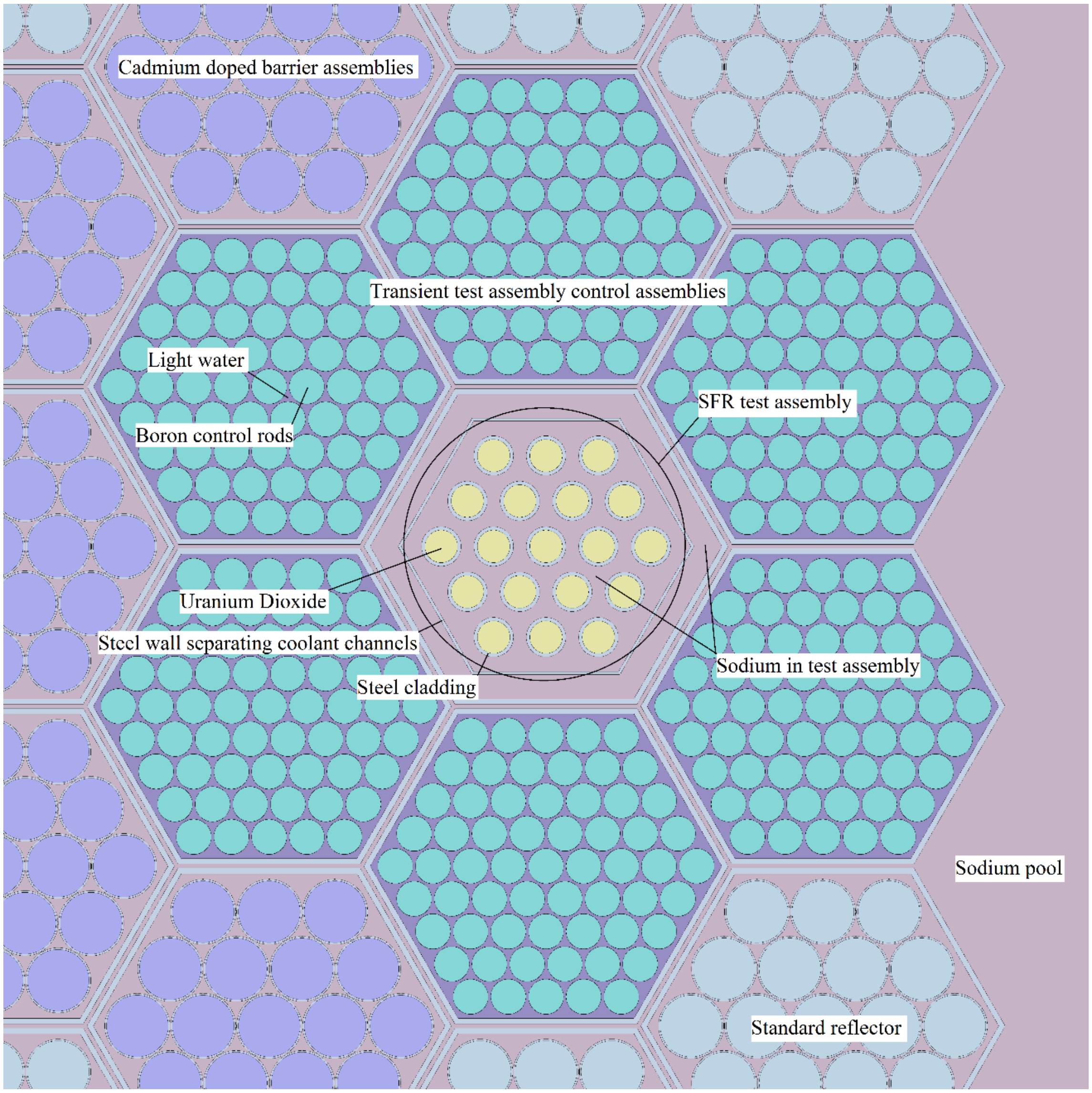

Figure 3.8 SFR test assembly and flux trap. The flux trap is the same configuration as presented in the PWR section. The SFR test assembly uses a hexagonal lattice with dimensions derived from a generic oxide fueled sodium fast reactor (Fast, 2006).

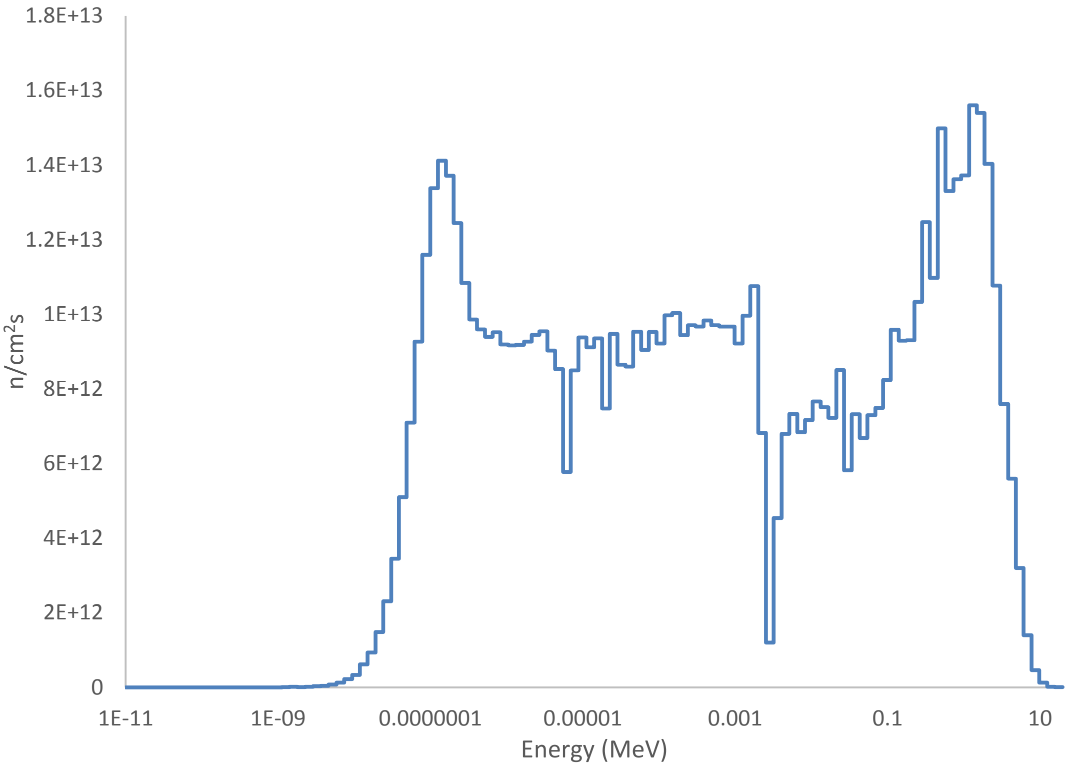

Figure 3.9 SFR transient test assembly neutron spectrum as full power.

In order for the trap to be neutronically isolated from the driver, neutrons inside the trap must be thermalized. However, neutrons generated inside the test assembly itself do not moderate. Some of the neutrons that escape are moderated and reflected back into the assembly. Neutrons streaming from the driver are also moderated before fissioning in the test assembly. The performance of the flux trap requires extensive thermalization; as the SFR test assembly does not thermalize as effectively as the PWR test assembly, the reactivity worth's of the control rods are larger in magnitude than the worth's for the PWR test assembly. The control rod worth's both with and without the test assembly present are approximately 0.1$, an amount which can be successfully offset by shim movements, presented in Table 3.6. The difference in rod worth without the assembly present is less than the sum of the standard deviations. The difference is rod worth with the assembly present is greater than the sum of the standard deviations.

Table 3.6 Reactivity's associated with SFR transient testing

Geometry to be measured	Reactivity in dollars	Absolute error
Testing assembly with rods fully withdrawn	0.00522241	0.014189
Control rods without testing assembly	-0.0979915	0.018109
Control rods with testing assembly	-0.1032139	0.014321

The power profiles of the SFR test assembly are shown in Fig 3.10. Power peaks at the center of the assembly. As in the PWR test assembly, 40 cm of graphite is located inside the pins above and below the active fuel region, flattening the power profile. This flattening is most noticeable when examining those points adjacent to the upper and lower reflector. The section of fuel occupying the region from ± [40, 45] cm is nearly the same power as the section from ± [45, 50] cm. The average linear power is 334.98 W/cm with a standard deviation of 0.77825. The table following the power profile shows how much power was generated from neutrons at different energies.

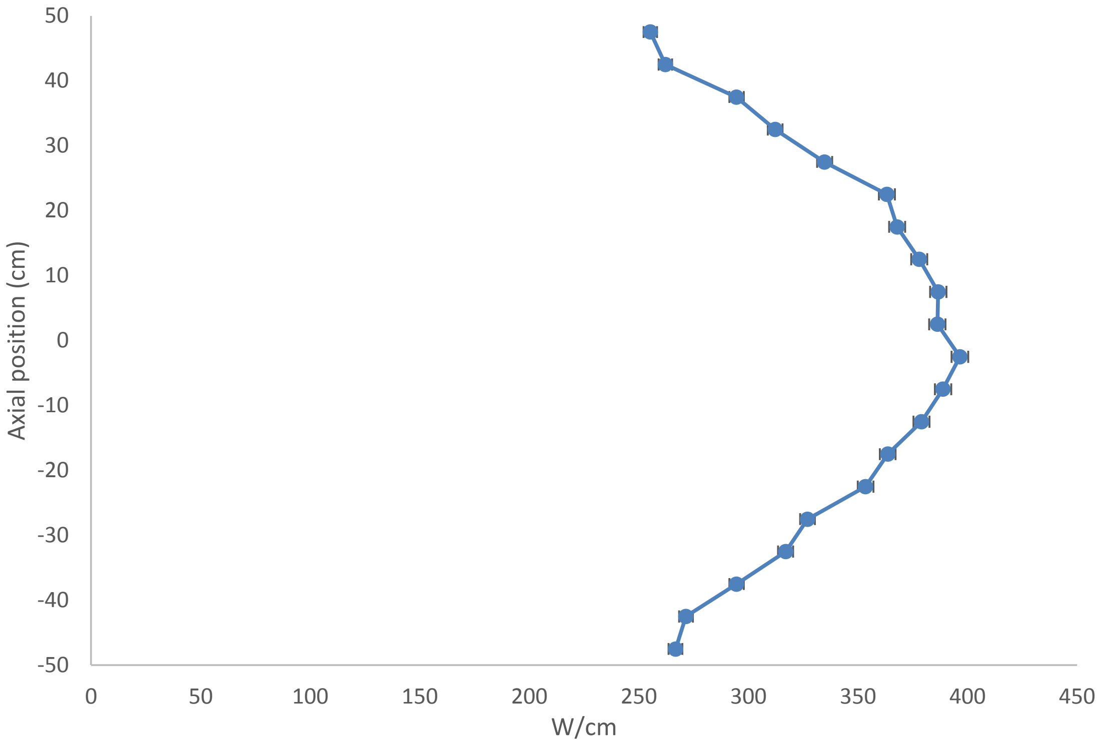

Figure 3.10 Axial power profile for a SFR test assembly at full power

Table 3.7 shows the power per energy group with the rods withdrawn. With the rods withdrawn, 76% of fissions are due to thermal neutrons, while 21% are due to epithermal neutrons. Despite the prevalent fast flux, just 2% of fissions are due to fast neutrons, very atypical behavior for a fast reactor. The average linear power is typical of SFR's (Fast, 2006). The average linear power with rods fully inserted is 3.36574 W/cm with a standard deviation of 0.056771. This corresponds to a 99% drop in power. Table 3.8 shows the fission power for each energy group with the same group structure as used previously. Thermal fissions are virtually nonexistent, while the majority of fissions are due to epithermal neutrons. The test assembly itself does not thermalize neutrons, which must be performed in the control assemblies. When thermal and epithermal neutrons are absorbed in those assemblies, the power must drastically reduce to a degree greater than in the PWR test assembly, where the test assembly itself performed a great deal of moderation.

Table 3.7 Power per energy bin for a SFR test assembly at full power

Flux bin	Linear power (W/cm)	Relative error	Relative power
E < 0.625 eV	255.705	0.00314	0.763344
0.625 eV < E < 0.1 MeV	71.0656	0.00325	0.212149
0.1 MeV < E < 1 MeV	0.947757	0.00528	0.002829
E > 1 MeV	7.26148	0.00646	0.021677

Table 3.8 Power per energy bin for a SFR test assembly with rods fully inserted

Linear power (W/cm)	Relative error	Relative power	Power drop fraction
0.053739	0.43803	0.015967	0.00021016
2.33756	0.0204	0.694517	0.03289299
0.289891	0.01783	0.08613	0.3058706
0.684544	0.03827	0.203386	0.09427059

The neutron path length inside a PWR is about 1 to 2 cm, similar to the pin pitch in a PWR. Thus, most neutrons generated in the core will only interact with pins immediately around them. As such, effects due to proximity to the inter-assembly water space, plutonium concentration in MOX fuel, burnable absorber concentration, proximity to control rods, and burn up are going to have a very localized effect, often on the individual pin level. For these reasons, it is not atypical for there to be different linear powers for pins in the same assembly. In the SFR, neutron path lengths are in the tens of centimeters. Neutrons will travel through many fuel pins, a great amount of wrapper and assembly steel, and a great deal of sodium before being absorbed. Neutrons often interact with other assemblies. For these and other reasons, the linear power per pin is fairly constant within an assembly, and it is expected that pins near each other will have the same linear power, in contrast to a PWR. While the pin powers in the PWR test assembly did show some variation, such a variation is not atypical. However, such variation would be atypical in a SFR assembly. Unfortunately, pin power does vary in the SFR test assembly. The most obvious solution to solve this problem is to vary the enrichment of the pins, but another method is also proposed. Pin power is shown in the Fig 3.11.

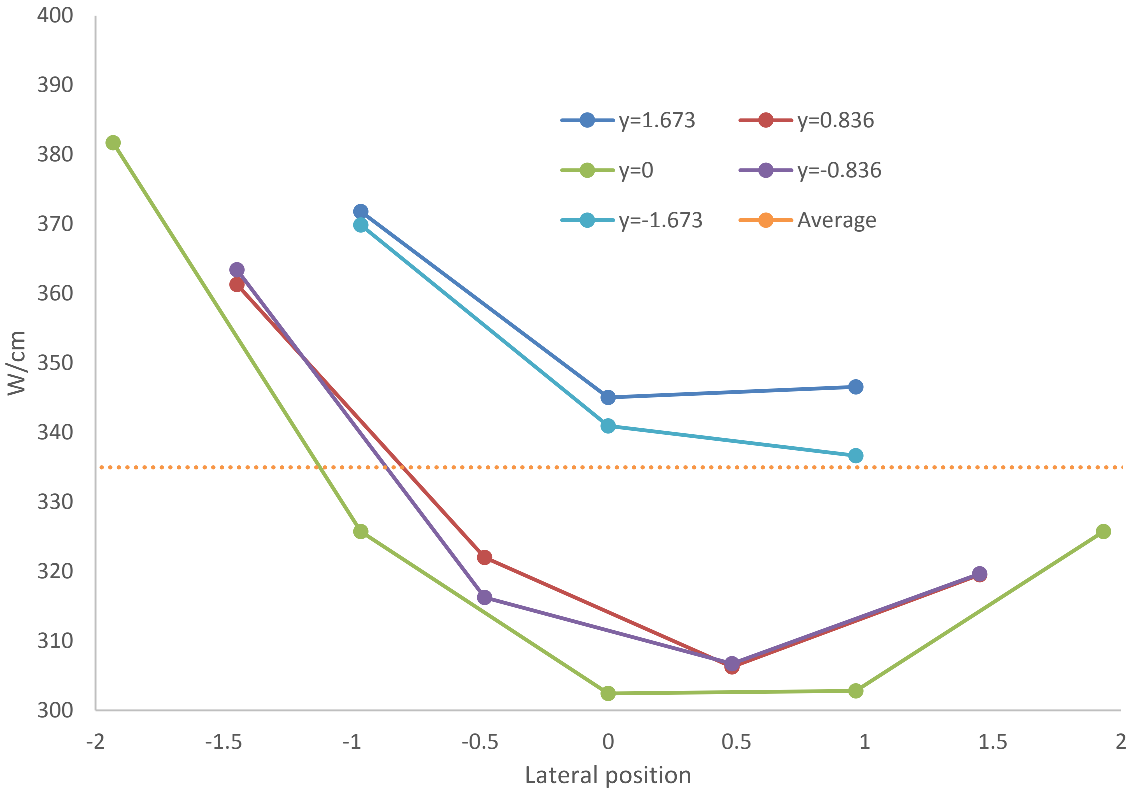

Figure 3.11 Pin power of the SFR test assembly at full power. The y-axis gives linear power of each pin and the x-axis gives the x-coordinate of each pin. The lines are for constant y-coordinate.

This 19 pin assembly is hexagonal. There are three radial rings of fuel pins and five horizontal rows of fuel pins. The center pin is at coordinates (0,0) while the pin to its immediate left is at coordinates (-0.9658,0) and the pin to the upper left of the central pin is at coordinates (-0.4829,0.8364). Generally, the pin powers follow the expected distribution of the thermal flux. Thermal flux is highest in those moderating assemblies closest to the driver. The flux at the center of the assembly is not as thermalized as the outside because sodium is a poor moderator. There is a corresponding decrease in power for the central pins. The pin at the very center (0,0) and the pin to its immediate right (0.9658,0) produce the least power while the pin surrounded by moderator on four sides (-1.9316,0) towards the driver produces the most power. The standard deviation of linear pin power for this configuration is 24.5 W/cm. An increase in thermal flux for those pins towards the center of the assembly would decrease the standard deviation. While decreasing the enrichment of the outer ring of pins would also decrease the standard deviation, adding water to the inside of the assembly would increase the thermal flux. This was implemented by replacing the fuel in the pin to the immediate right of the central pin with light water modeled at saturation conditions for 300 °C. The pin outer diameter was not increased, which would perturb the sodium flow pattern of the assembly. The standard deviation of pin power with the water rod is 20.9 W/cm and the average linear power is 347.1 W/cm. This is shown in Fig 3.12.

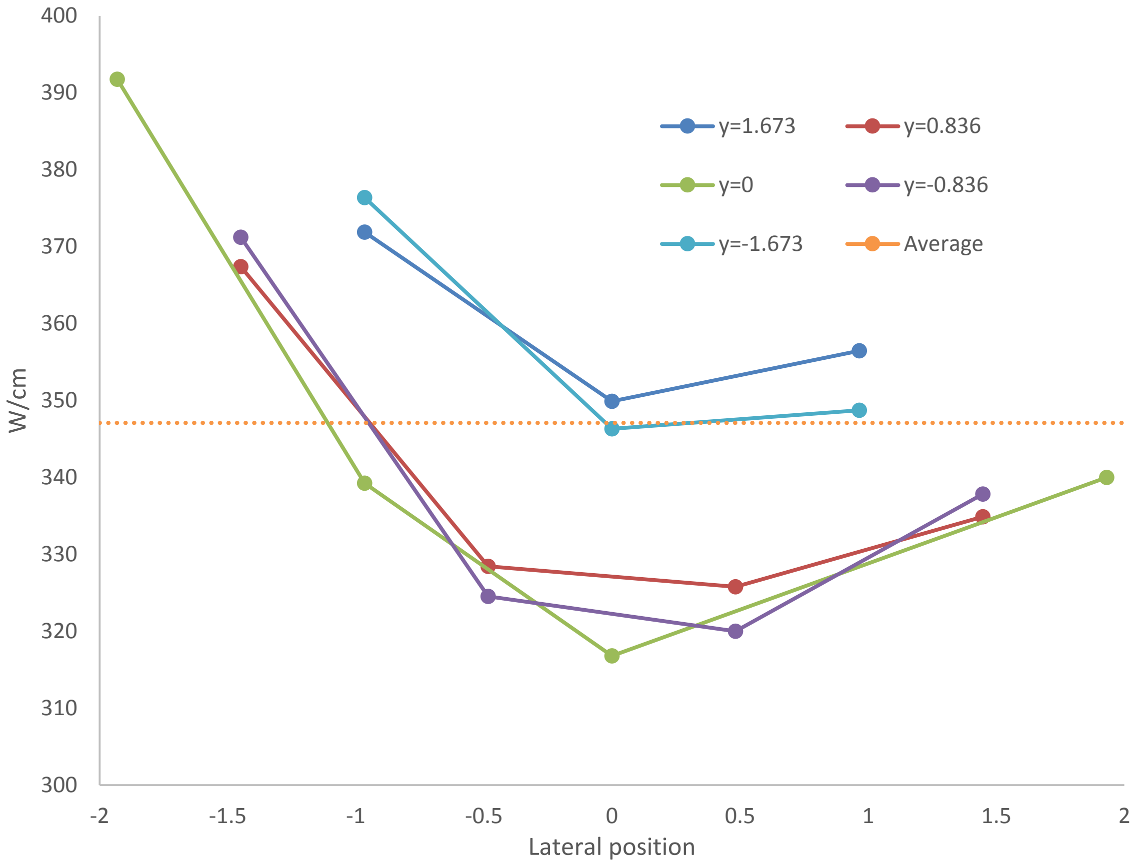

Figure 3.12 Pin power for a SFR test assembly with one fuel rod replaced with a fuel rod.

Performing SFR transient testing in the proposed reactor poses special challenges when compared to PWR and VHTR transient testing. The lack of thermalization within the assembly itself has several consequences, both favorable and unfavorable. Most fissions are due to thermal neutrons, meaning that assembly power is heavily dependent on fast neutrons streaming outside the assembly and scattering back in addition to neutrons streaming directly from the driver. Inserting the boron rods and absorbing essentially all thermal and epithermal neutrons streaming outside the assembly drastically reduces power, to greater degree than for the PWR and VHTR test assembly configurations. The overall lesser degree of thermalization when compared to the PWR and VHTR also translates into a greater neutronic coupling of the driver and flux trap, as the cadmium barrier assemblies have much higher thermal cross sections than non-thermal cross sections. However, it should still be possible to offset the negative reactivity insertion with appropriate shim movements. Linear power for the SFR assembly is not constant from pin to pin due to the variable thermal flux shape throughout the system. Two methods are proposed for flattening the power generated per pin. The first is simply to vary the enrichment while the second is to replace rods towards the center of the assembly with water. All things considered, SFR transient testing is viable in the proposed reactor.

3.3 VHTR transient testing

The VHTR configuration, modeled in this investigation, is based on the HTTR (Tsvetkov, 2010), and is shown in Fig 3.13. It is in the same location as the PWR and SFR test assemblies. Material compositions and dimensions of the fuel particle are given in Table 3.9. The fuel compact, helium, and inner graphite were modeled with 900 K cross sections, while the moderating graphite outside the helium channel was modeled with 600 K cross sections. Four concentric radii determine the radial divisions of the assembly. The first section, from 0 cm to 0.5 cm, is composed of helium with a density of 0.0001604 g/cm^3. The fuel compact, modeled as a regular square lattice of fuel particles, occupies the region from 0.5 cm to 1.3 cm. The pitch of the fuel particles is 0.110716 cm for a packing fraction of 0.31. Graphite is modeled from 1.3 cm to 1.7 cm at a density of 1.77 g/cm^3. Helium occupies the region from 1.7 cm to 2.05 cm, while standard graphite at a density of 2.2 g/cm^3 occupies the region from 2.05 cm to the inner steel wall. The active fuel portion is 100 cm tall, and 40 cm of standard graphite forms a reflector above and below it. The reflector is solid except for the outer helium channel annulus, which flows outside of the core to be cooled.

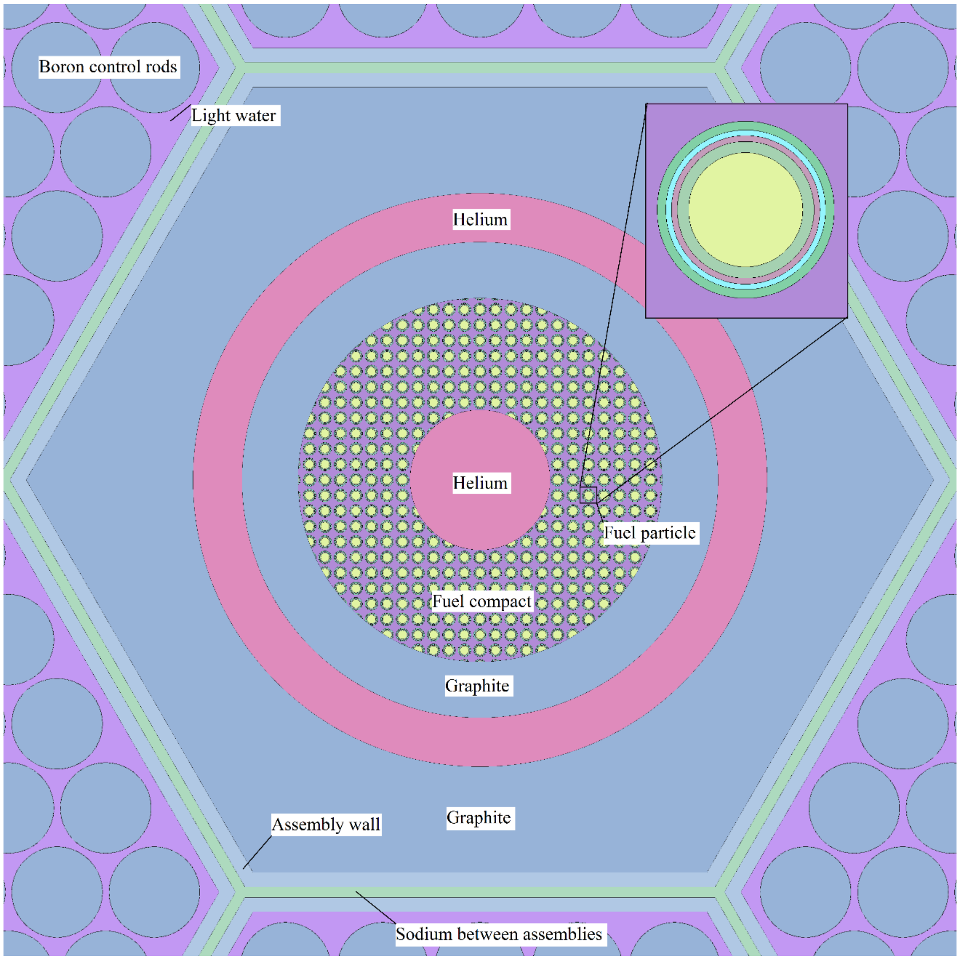

Figure 3.13 A VHTR test assembly with a close up of a fuel particle

Table 3.9 Dimensions and compositions of the fuel particle

Material composition	Outer spherical radius in cm	Density in g/cm^3
Uranium dioxide, 0.2% enriched	0.03	10.41
Graphite	0.0359	1.14
Graphite	0.039	1.89
Silicon Carbide	0.0419	3.2
Graphite	0.0465	1.87
Graphite	Between pebbles	1.69

The VHTR assembly has a negative reactivity worth, but this result is not statistically significant. The reactivity worth of inserting the control rods without an assembly present is 0.101$ and the worth with an assembly present is 0.081$, a value low enough that it can be offset with shim movements. Table 3.10 shows the reactivity's of the assembly and rods.

Table 3.10 Reactivity's associated with a VHTR test assembly

Geometry to be measured	Reactivity in dollars	Absolute error
Testing assembly with rods fully withdrawn	-0.0104464	0.021852
Control rods without testing assembly	-0.1006102	0.009054
Control rods with testing assembly	-0.0810115	0.021389

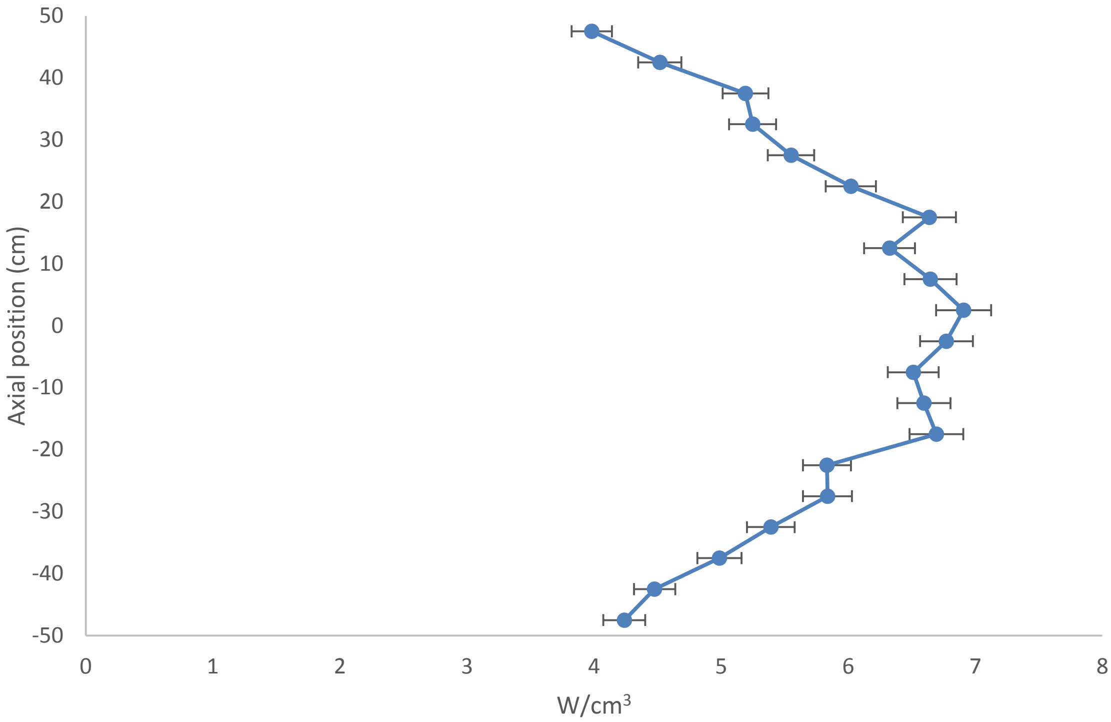

Figure 3.14 Axial power profile of VHTR test assembly at full power

Figure 3.14 shows the axial power profile. Twenty 5 cm axial sections were used. Although the shape of the profile is not very smooth, the error bars indicate that this feature of the graph does not stem from any physical cause, merely the number of neutrons simulated. The average power density is 5.719 W/cm^3 with a standard deviation of 0.0427. This value was measured over the fuel compact; if measured over the region defined by the fuel compact, helium channels, and graphite sleeve, the average power density is 1.96 W/cm^3.

The contributions of the various flux groups to heat generation are tallied and presented in Table 3.11. 86.5% of the fissions inside the VHTR assembly are thermal fissions, while 11.5% of fissions are epithermal fissions. These values change when the rods are inserted, data shown in Table 3.12. Now, the average power density is 0.110 W/cm^3 with a standard deviation of 0.0043. This corresponds to a 98.1% drop in assembly power. The drop in power is greater than in the PWR test assembly, reflecting the greater coupling between assemblies in a VHTR.

Table 3.11 Power per energy group in a VHTR test assembly at full power

Flux bin	Power density in W/cm^3	Relative error	Relative power
E < 0.625 eV	4.94861	0.0086	0.86534
0.625 eV < E < 0.1 MeV	0.655102	0.0118	0.114555
0.1 MeV < E < 1 MeV	0.003717	0.03178	0.00065
E > 1 MeV	0.111262	0.0625	0.019456

Neutron path lengths in graphite systems are much longer than in system cooled by light water due to graphite’s longer diffusion length, stemming from its lower absorption cross section and greater atomic mass (which means more collisions are necessary to thermalize neutrons). The coupling between the VHTR test assembly and the graphite control assemblies surrounding it is clearer when examining the fission power per energy group.

Table 3.12 Power per energy group for a VHTR test assembly with rods fully inserted

Power density in W/cm^3	Relative error	Relative power	Power drop fraction
0.000580	0.38981	0.0052774	0.000117284
0.025227	0.02771	0.2293816	0.038507896
0.002912	0.02480	0.0264816	0.783530671
0.081257	0.05196	0.7388592	0.730323021

With the rods fully inserted, only 0.5% of fissions are induced by thermal neutrons. 73.9% of fissions are due to fast neutrons, a situation only attainable if the majority of neutrons have to leave the assembly to moderate and then be reflected back into the assembly to fission. Neutrons that leave the test assembly are overwhelmingly likely to be absorbed by the boron, so only those neutrons that fission before they escape the assembly will generate heat. Given the short distance between fuel particles in the fuel compact, those neutrons are fast, although some are epithermal.

Neutron flux within the VHTR test assembly is shown in Fig 3.15. Two spectra are shown: the first shows flux averaged over the fuel compact while the second shows flux averaged over the entire test assembly. The fuel compact is only a small portion of the test assembly; the whole test assembly contains more graphite than the fuel compact. As a result, the flux spectrum for the whole assembly is more thermalized than the flux averaged over the fuel compact only.

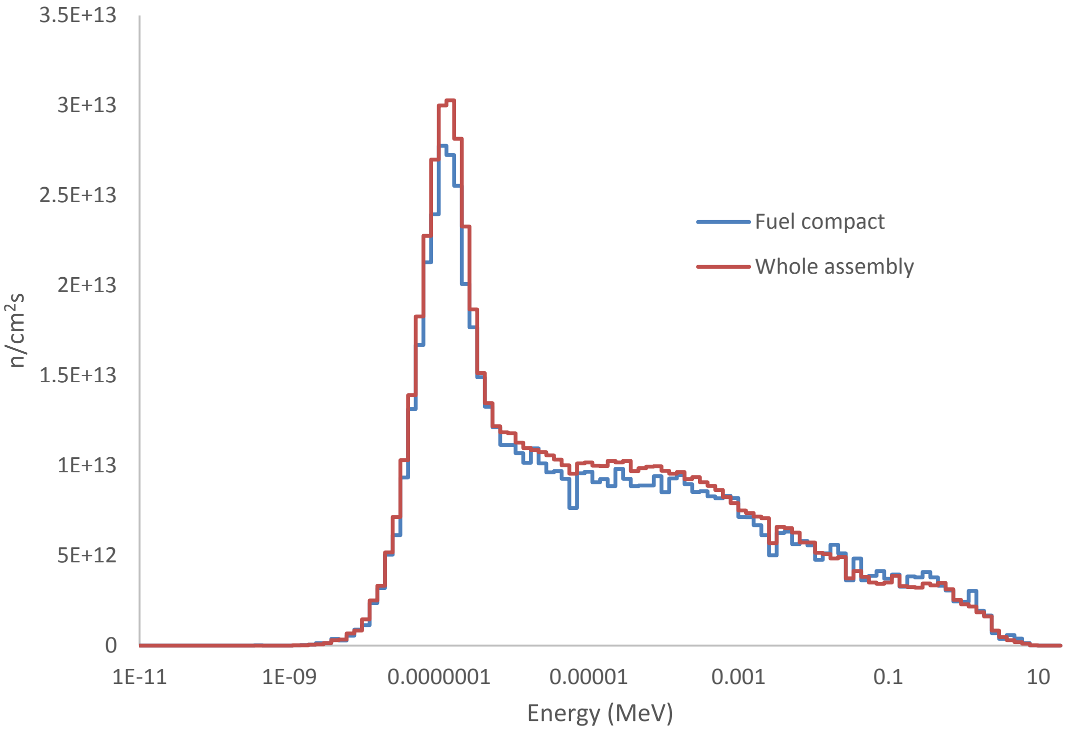

Figure 3.15 Neutron spectra in a VHTR test assembly at full power

The data presented in this section support the assertion that a VHTR test assembly can be subjected to transient testing in the reactor without negatively affecting the driver. A test assembly within a thermal flux trap has an average power density, measured over the fuel compact, of 5.719 W/cm^3 using only 0.2% enriched fuel. Fully inserting the control rods reduces assembly power by 98.1% while only inserting -0.09$ of reactivity. This amount of reactivity can be offset by appropriate movements of the shims.

4. THE MODERATING REGION

The purpose of the FMTR is to provide a platform for materials irradiation that accommodates a wide variety of reactor types. The central driver has a hard spectrum while the moderating region provides epithermal and thermal fluxes. The driver region and fast reflector have been characterized; the purpose of this section is to characterize the moderating region. The moderating region will be characterized with respect to the stated role of providing variable neutron spectra; particularly with respect to the PWR and VHTR. The whole moderating region will be characterized without reference to any form of irradiation assembly first. This unperturbed case will provide a general overview of the entire region. Different material compositions and configurations of the moderating region will be considered in the first section. The second section examines the relative effects of graphite versus light water in the moderating region. Irradiation conditions for PWR and VHTR test assemblies located in the graphite moderating region will be presented next. Static irradiation capsules meant to mimic PWR and VHTR neutron spectra will be presented last.

The PWR is the most common reactor type in the world, while the VHTR is given serious attention both in the US and in the rest of the world (Next 2007). Characterizing the PWR spectra was done with the 120 group and 4 group arrangements used previously. Characterizing the VHTR spectra was done with the 120 group arrangement and a new 3 group arrangement. The 3 group arrangement was necessary for direct comparison to results obtained from an analysis of a prismatic VHTR performed at INL using MCNP (Sterbentz 2008). The 3 group arrangement has the following energy bounds: 1E-5 eV, 2.203 eV, 0.18 MeV, and 20 MeV. The research presented in the INL report sought to characterize the neutron and gamma spectra in different regions of the High Temperature Test Reactor, abbreviated as the HTTR (Tsvetkov, 2010). The HTTR contains 3 rings of fuel assemblies surrounded by an inner and outer graphite reflector. The flux bins used here for comparison stem from the middle ring, which had the highest fast flux in proportion to the total flux. The HTTR does not exactly correspond to the VHTR proposed as part of the NGNP (Next 2007). Similarly, the prismatic fuel assembly used in this research does not exactly correspond to either design. These discrepancies should not denigrate the results of the present research. To fit inside the core lattice on which the reactor is designed, the actual VHTR assembly must be smaller than the assemblies described as part of the NGNP program. For example, the standard prismatic fuel assemblies are approximately 74 cm tall and 36 cm flat to flat for a total volume of 83055 cm^3 (Next 2007). By contrast, the volume available to insert a VHTR assembly is just 2728.9 cm^3, 3.3% of the total assembly volume. With such a small assembly volume, it is untenable to insist on matching exact spectral conditions in the test assembly. The INL report provided sufficient results to compare the neutron spectra in the VHTR test assembly modeled here and a generic VHTR assembly.

4.1 Unperturbed behavior of the moderating region

In this section, the whole unperturbed moderating region is characterized. This research was performed chronologically first and the results presented here informed decisions about where to locate test assemblies in the moderating region and the relative use of light water and graphite to control the thermal and epithermal fluxes. The spectra presented here did not match PWR and VHTR spectra as closely as with the test assemblies and static capsules. This section will provide general information about the moderating region and highlight the use of specific materials in this region. Later sections assume the graphite moderator and show how permutations of the base geometry will more closely mimic PWR and VHTR spectra. In this section, graphite and light water will be used in the moderating region, but beryllium and cadmium will also be used in the barrier assemblies. Beryllium is a common reflector material in research reactors because of its low mass and (n,2n) reaction for neutrons above 2 MeV (Tomberlin 2006). Beryllium has other absorption reactions that cause the buildup of neutron poisons over time (Tomberlin 2006). Over time these poisons will introduce negative reactivity into the system. As previously mentioned, cadmium is a thermal absorber and has a low epithermal cross section. This material can be used to decrease the thermal flux streaming from the moderating region into the driver, which would decrease the power density in those fuel assemblies near the driver. Six cases will be analyzed and the first four are: graphite comprising the entire moderating region, light water comprising the moderating region, beryllium in the barrier assemblies, and cadmium in the barrier assemblies. The last two cases are very similar to the first two cases except they abandon the standard assembly structure used throughout this project. No steel or sodium is used; the reflector is assumed to be a solid block of graphite or light water. These simulations will highlight the relative effect of diffusions versus absorption within the moderating region and estimate the theoretical highest fluxes within the region.

The moderating region was characterized in the same manner for all the cases. The moderating region consists of a central region with two tails. The central region directly borders the driver and experiences peak fluxes. The tails are further from the driver, and had correspondingly lower fluxes. The central region comprises 75.2% of the total moderating region, so it was characterized more heavily than the tails. The central region is of greater importance than the tails because of its larger volume, so this region was characterized in greater detail than the tails. The central region is rectangular in shape. It was subdivided into 64 rectangular sections; 16 vertical slices and 4 horizontal slices. The thickness of each vertical slice was 4.6775 cm while the thickness of each horizontal slice was 5.8925 cm. Fig 4.1 shows the entire core with the central region and tails pointed out while Fig 4.2 focuses on the central region. The sections on the very top and bottom of the central region on the furthest right are in the center of the tails. These sections will be used to characterize the tails. The moderating region contains a great deal of steel and sodium so that the assemblies can be easily replaced. This makes the moderating region very operationally flexible, but lowers flux values throughout the region because steel and sodium will absorb neutrons. The parasitic losses of neutrons and the moderating powers of the materials within the moderating region shape the thermal and epithermal fluxes. Similarly, the materials present in the barrier fuel assemblies between the driver and moderating region affect the moderating region.

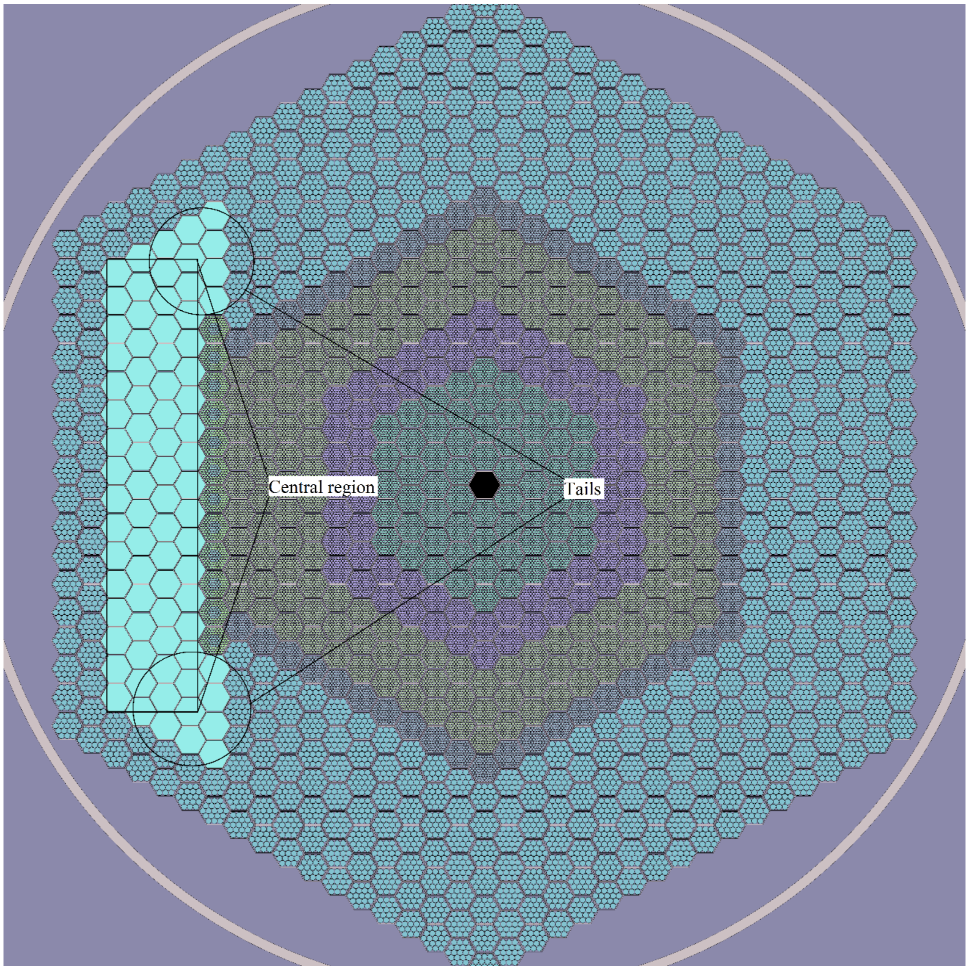

Figure 4.1 Location of central region and tails within core

It will be observed that thermal flux exhibits a sharp peak with the moderating region. It is conjectured that this thermal peak is caused by a balance between the creation of thermal neutrons by down scattering from epithermal energies and the loss of thermal neutrons due to diffusion and absorption in the moderator. It will be shown that diffusion is the most likely cause for the flux shape.

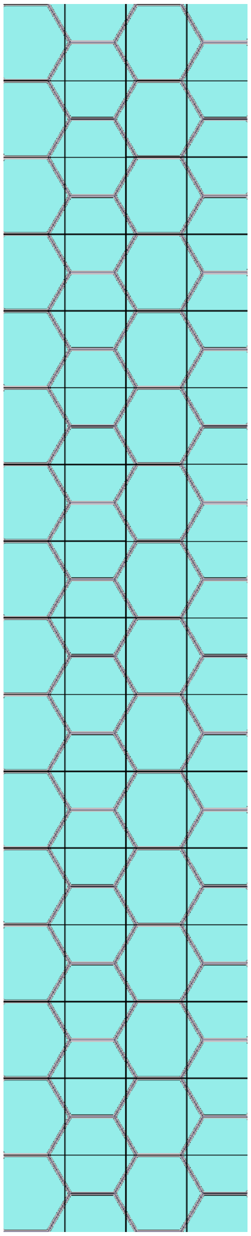

Figure 4.2 Central region with each smaller section outlined

Within each section, three energy groups were tallied: thermal, epithermal, and fast. This grouping followed the 4 group structure outlined previously, except the fast group included all neutrons with energies above 0.1 MeV. The fluxes presented in this section were tallied from z=-5.0 cm to z=5.0cm, representing the peak flux in that section.

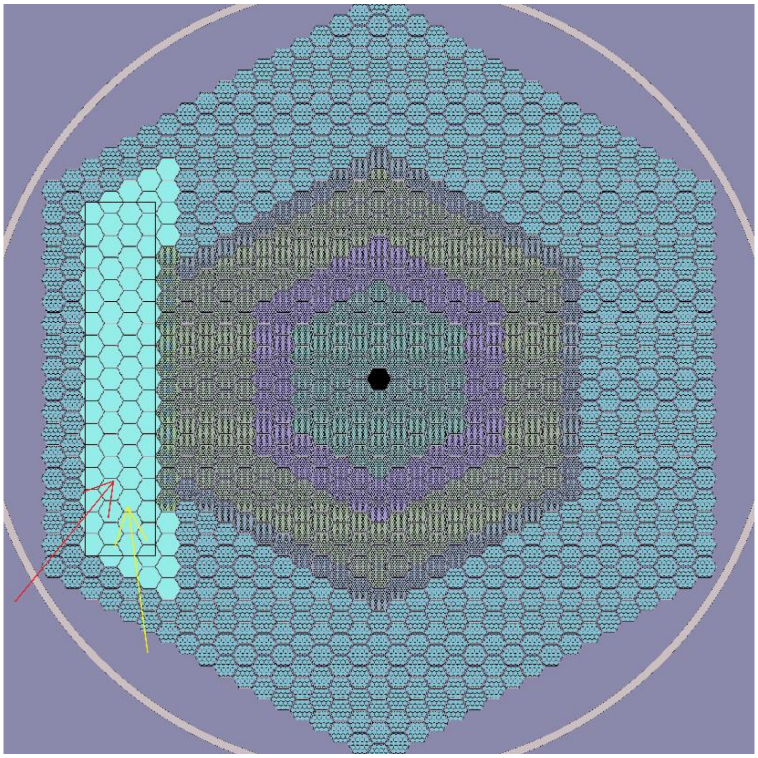

Figure 4.3 The red arrow represents the orientation of the fast and epithermal flux maps while the yellow arrow represents the orientation of the thermal flux map

The first case to be analyzed is that of a moderator composed entirely of graphite with the barrier fuel assemblies composed of fuel at different enrichments. The fuel pins towards the graphite are 6% enriched, those in the center of the assembly are 12% enriched, and those near the driver are 15% enriched. This represents the base geometry. 3D plots of each flux group will now be shown. Fig 4.3 shows the directions these 3D plots were made. The red arrow represents the orientation of the fast and epithermal fluxes while the yellow arrow represents the orientation of the thermal flux.

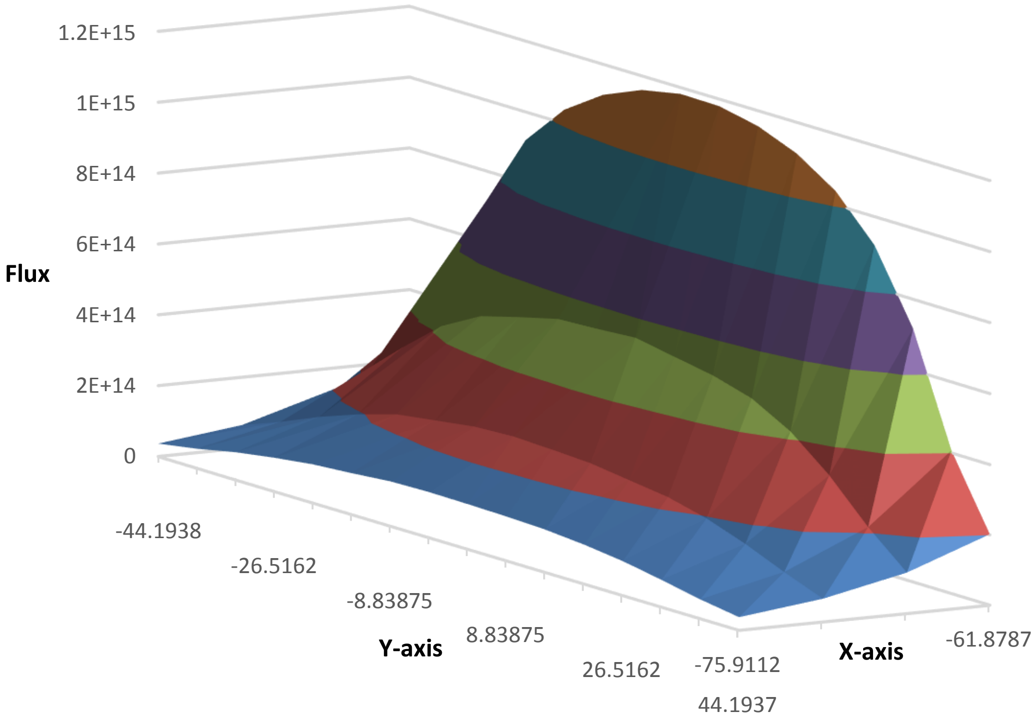

Figure 4.4 Fast flux in the moderating region with graphite

Fast flux, shown in Fig 4.4, peaked towards the driver and quickly dropped off further into the moderating region. Fig 4.4 is shown looking from the outside of the moderating region towards the driver. Flux height is tallied on the z axis. Peak fast flux was calculated to be 1.18E15 n/cm^{2}s. Fast fluxes reported for static capsule irradiation with graphite moderation are higher. This is to be expected as the sections used in the present investigation are both larger and further from the driver. Epithermal flux, shown in Fig 4.5, is presented in the same orientation as fast flux. Epithermal flux follows the same general pattern as fast flux, except it does not drop off as quickly as fast flux. Peak epithermal flux is 2.28E15 n/cm^{2}s, next to the driver. Thermal flux, shown in Fig 4.6, follows a different pattern from the fast and epithermal fluxes. Few thermal neutrons are present near the driver; thermal flux peaks towards the center of the moderating region. Diffusion and absorption in the moderating region absorbs thermal neurons, reducing the thermal flux and shaping the peak. Thermal flux drops off far from the driver, especially towards the corners of the moderating region. The peak thermal flux is 4.51E14 n/cm^{2}s.

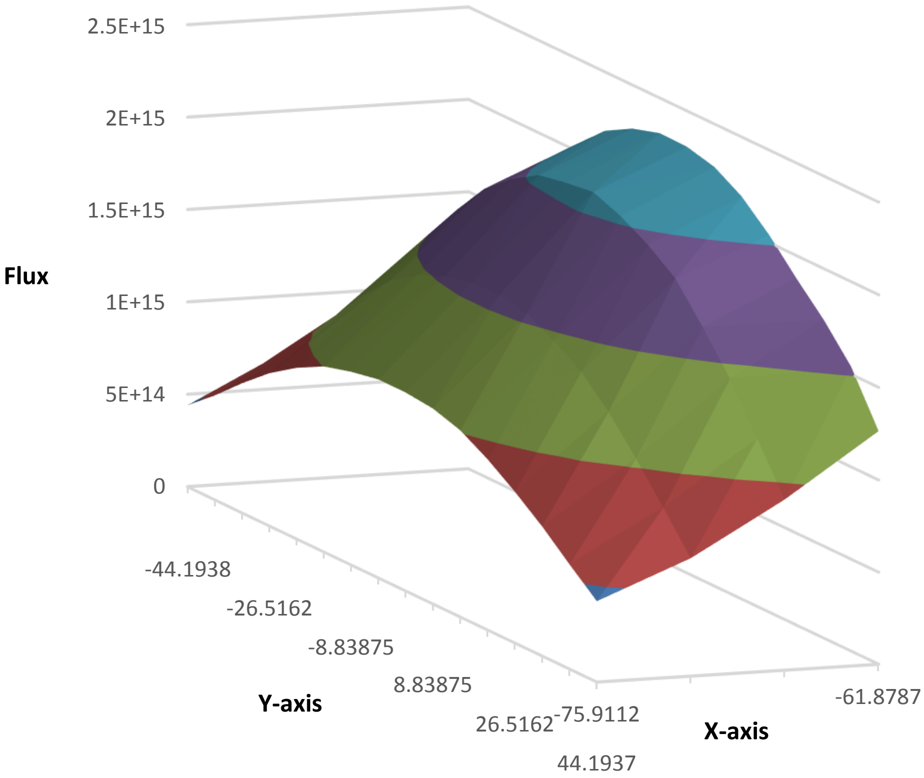

Figure 4.5 Epithermal flux in the moderating region with graphite

Thermal flux is shown in a different orientation from the fast and thermal fluxes: tangential to the moderating region shifted so that the moderating region is viewed from the driver. The peak in the center of the moderating region is prevalent along with the depressions towards the driver and in the corners. The complex shape of the thermal flux means that the flux fractions will also exhibit a complex shape. Flux fractions at various places within the moderating region are presented in Table 4.1. Fig 4.7 shows the locations of the sections shown on Table 4.1.

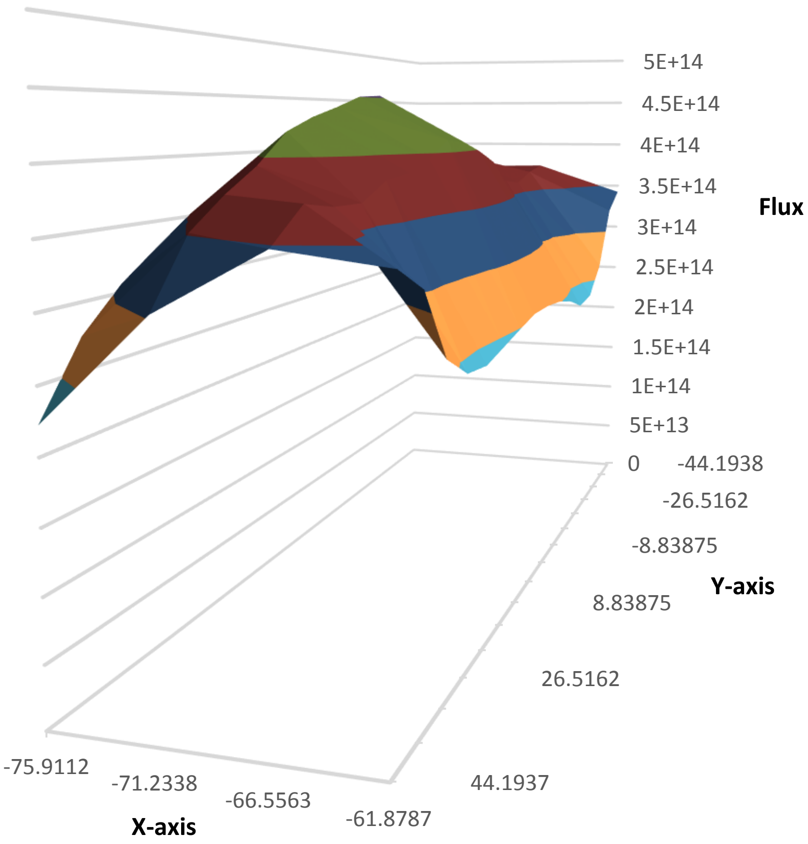

Figure 4.6 Thermal flux in the moderating region with graphite

Table 4.1 Flux fractions and total fluxes in different sections of the moderating region with graphite.

Flux fraction	Peak fast	Peak thermal	Tail	Corner
Thermal	0.068	0.198	0.189	0.319
Epithermal	0.616	0.688	0.699	0.629
Fast	0.315	0.115	0.112	0.053
Total flux	3.74E+15	2.28E+15	1.80E+15	7.00E+14

The flux fractions presented in Table 4.1 do not correspond to the PWR and VHTR spectra. Some degree of flux shaping within the irradiation assemblies is warranted. However, if this is unneeded, then most of the moderating region will be useful for general purpose irradiation. The tails do have high enough fluxes for general purpose irradiation, even if they are below those near the center of the moderating region. This is because of the layout of the barrier assemblies. The barrier assemblies extend into the tail region slightly so as to minimize the number of neutrons that stream from the moderating region into the driver around the barrier assemblies. The corner regions provide the highest thermal flux fractions; passive materials assemblies with only light water would provide a strong thermal flux without any higher energy neutrons, which could be useful for general purpose irradiations. Total fluxes in every part of the moderating region are several times those of a prototypical PWR and VHTR, even if the spectra do not entirely match. Irrespective of the distance from the driver, the epithermal flux fraction stayed between 0.6 and 0.7 while the fast and thermal flux fractions varied widely. This large epithermal fraction favors irradiation under conditions similar to a PWR.

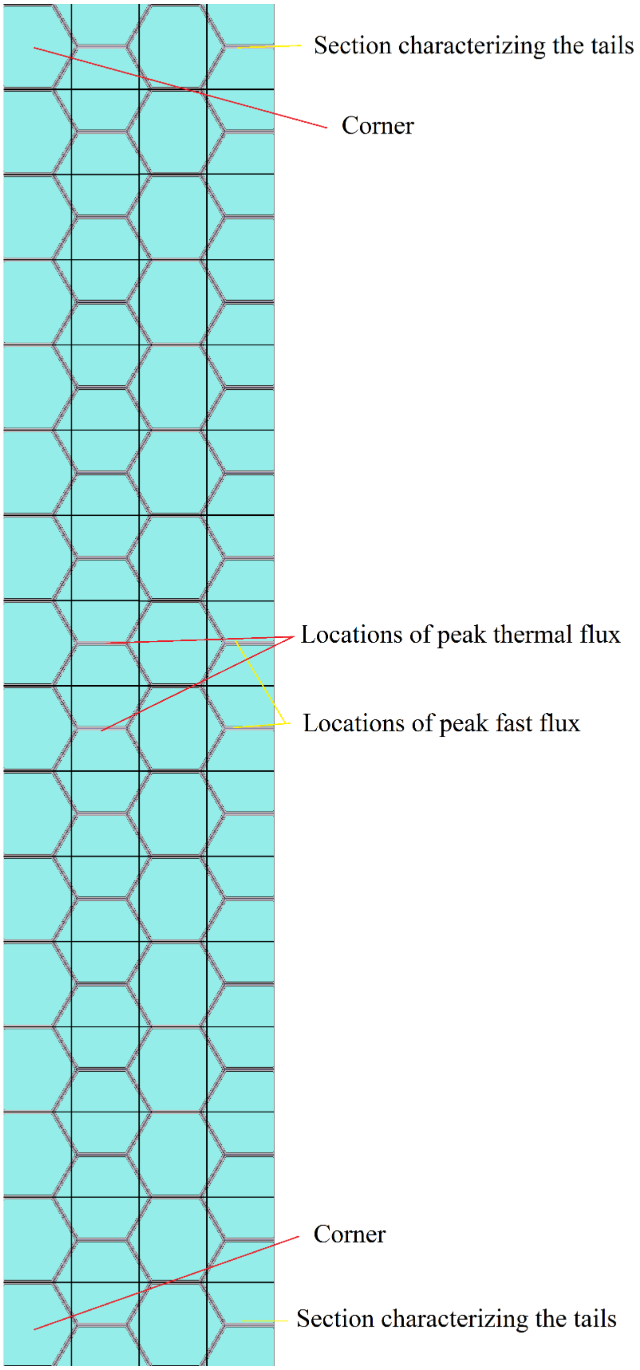

Figure 4.7 Locations of regions in Table 4.1. Graphite moderator

The second case to be analyzed uses light water instead of graphite in the moderating region. Flux exhibited the same general shapes for each group as with a graphite moderator. Peak fast flux with the light water moderator was 5.21E14 n/cm^{2}s, while the peak epithermal flux is 7.56E14 n/cm^{2}s. These values are lower than in the graphite moderator due to the higher moderating power of light water as compared to graphite. The greater energy loss per elastic scatter of fast and epithermal neutrons results in a greater abundance of thermal neutrons nearer to the core. Peak thermal flux is 1.17E15 n/cm^{2}s, higher than in the graphite moderator. Fig 4.9 shows a 3D plot of thermal flux viewed from the lower corner of the moderating region towards the driver. Thermal flux peaks closer to the core but not immediately next to it. Flux also exhibits local maxima in the tails. Table 4.2 gives total fluxes and flux fractions in the regions of fast and thermal flux and in the corners and tails. In contrast to the graphite moderator, thermal flux is the largest flux group in all sections of the moderator. Total fluxes for this region are lower than with graphite, but the greater fraction of thermal neutrons coupled with the fact that most materials exhibit 1/v absorption cross sections means that absorption reaction rate densities for a material such as ^{235}U are greater with a light water moderator than with a graphite moderator. The flux fractions near the core resemble flux fractions associated with a VHTR, which will be discussed in detail in later sections. The greatest drawback associated with a light water moderator is the reactivity penalty. Light water is a not as effective a reflector as graphite, and inserts -1.92$, a fairly steep penalty. For this reason, a moderator composed entirely of light water was not used in any further simulations. Additionally, the amount of light water for the test assembly and static capsules simulations was minimized to reduce the reactivity penalty associated with materials irradiation. Fig 4.10 shows the locations of the peak thermal flux, peak fast flux, corners and tails. Fig 4.8 shows the orientation of the 3D thermal flux plot. The red arrow is the orientation of the thermal flux plot.

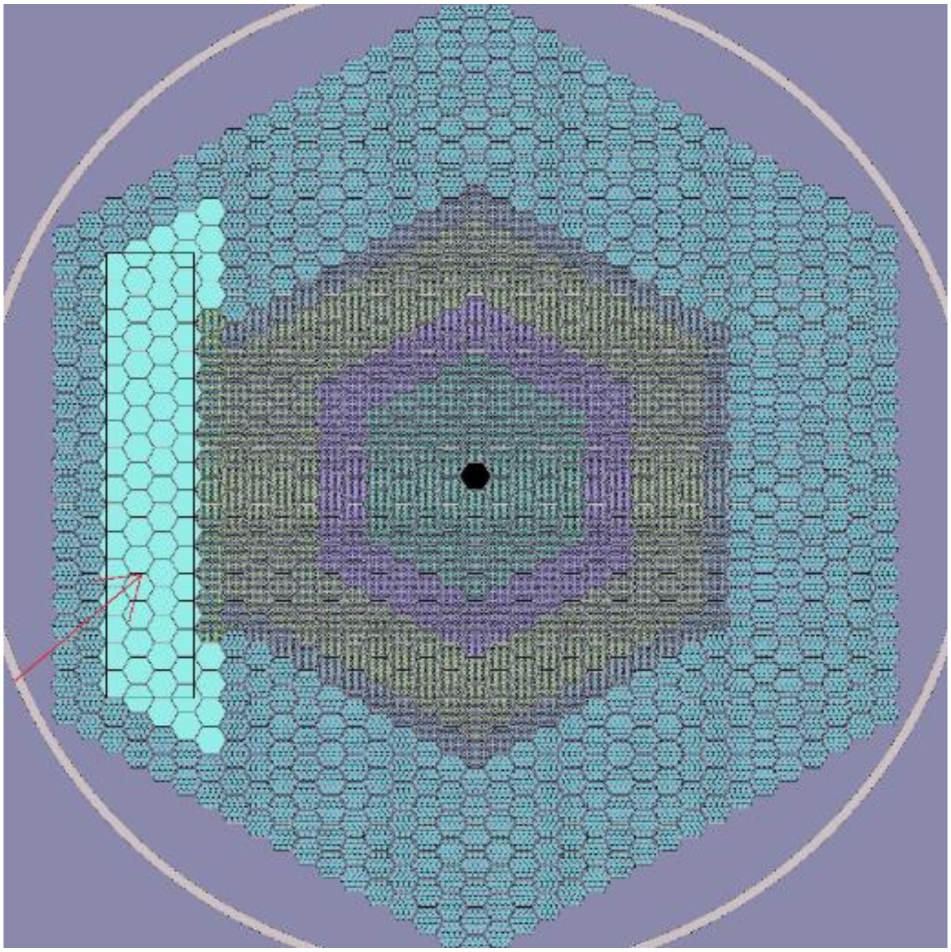

Figure 4.8 Orientation of Figure 4.9

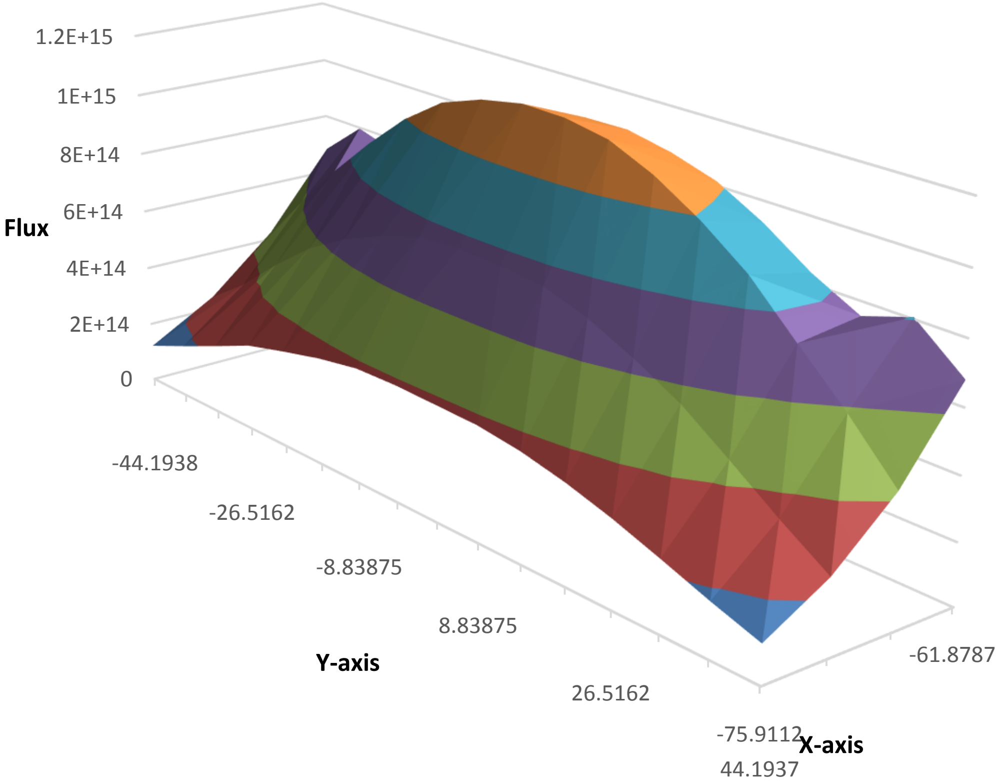

Figure 4.9 Thermal flux in the moderating region composed of light water

Table 4.2 Flux fractions and total flux with light water

Flux fraction	Peak fast	Peak thermal	Tail	Corner
Thermal	0.459	0.678	0.755	0.752
Epithermal	0.320	0.211	0.171	0.160
Fast	0.221	0.111	0.073	0.088
Total flux	2.36E+15	1.72E+15	9.02E+14	1.63E+14

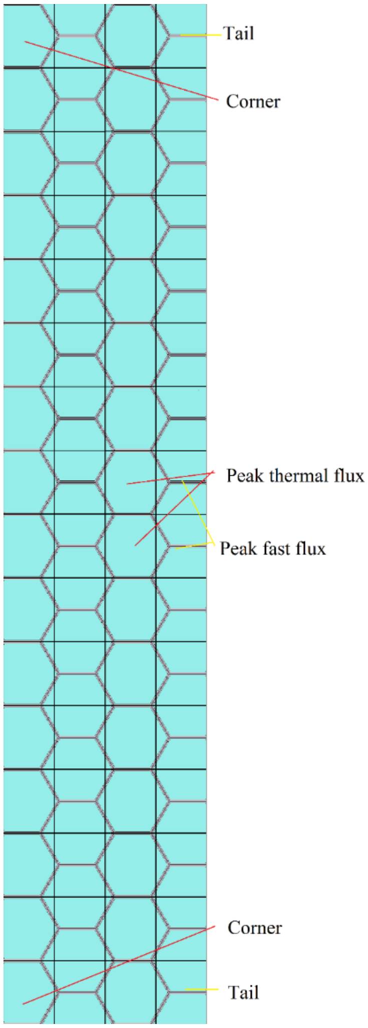

Figure 4.10 Locations of sections for Table 4.2

As mentioned previously, beryllium has a significant (n,2n) cross section for neutrons above 2 MeV and an even larger cross sections for parasitic absorption of neutrons at thermal energies. The excess energy for this reaction is 1.666 MeV, meaning that the two neutrons kicked off from the nucleus share the difference of the incident neutron kinetic energy minus 1.666 MeV. For these reasons, beryllium is placed in a location of a high fast flux where thermal neutrons are unwanted. Additionally, thermal scattering cards for beryllium were not used in this simulation. The thermal flux is low in this region, minimizing the error associated with unbound scattering cross sections. Thermal and epithermal neutrons from the graphite cause fissions in the barrier assembly. This fact cause’s power peaking for the barrier assemblies at certain enrichments, as mentioned in a previous section. The beryllium would absorb some of these neutrons, reducing the power peaking with the assembly. Though the (n,2n) cross section is far greater than the parasitic cross sections, parasitic absorptions produce ^{10}B, ^{6}Li, and ^{3}He. These nuclides possess very large thermal absorption cross sections and the absorption of neutrons will increase under irradiation. Simulations associated with this behavior were performed, and these strong absorbers did cause the negative reactivity worth of the beryllium to increase over time. Fig 4.11 shows the location of the beryllium and the enrichment of the fuel assemblies within the barrier assemblies. Graphite was used in the moderating region.

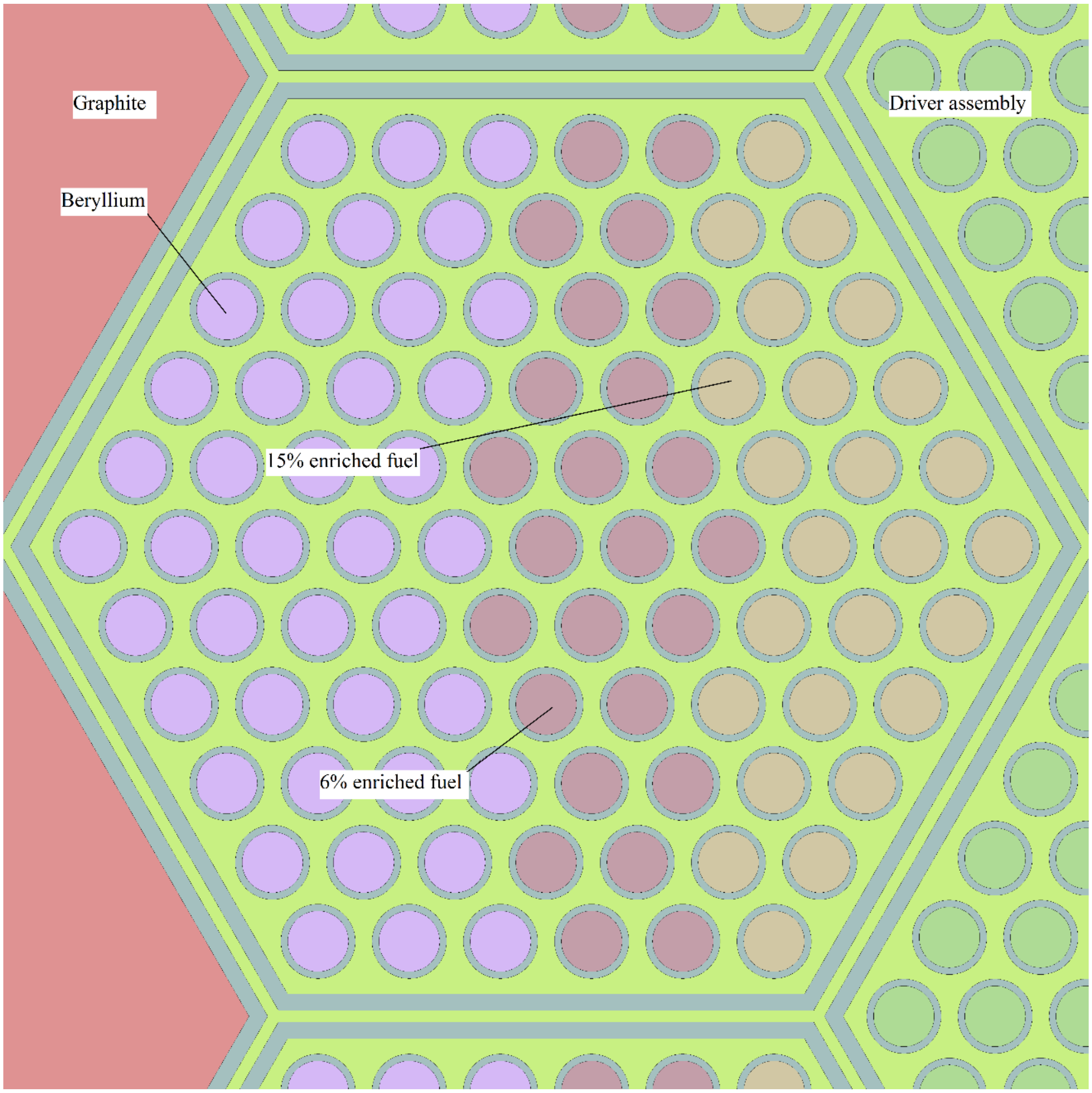

Figure 4.11 Location of beryllium in barrier assemblies

Peak fast flux was calculated to be 9.61E14 n/cm^{2}s, less than without beryllium. This characteristic is to be expected, as neutrons above 2 MeV are reduced in energy and doubled when striking beryllium. Peak epithermal flux was calculated to be 2.37E15 n/cm^{2}s, higher than without beryllium. A greater epithermal flux generated near the driver causes the thermal peak to shift towards the driver. This effect is visible in Fig 4.13, which shows thermal flux. Thermal flux is shown tangential to the moderating region, slightly tilted so that the moderating region is viewed from the driver. While thermal flux does shift towards the driver, the effect is not great enough to cause the thermal peak to shift to a completely different section. With beryllium in the barrier assemblies, the thermal flux exhibits greater values over larger sections of the moderating region, which would enable faster degradation with more materials testing locations. Peak thermal flux is 4.90E14 n/cm^{2}s, higher than without the beryllium. Table 4.3 shows the flux fractions and total fluxes for select sections of the moderating region. The red arrow in Fig 4.12 gives the orientation of Fig 4.13.

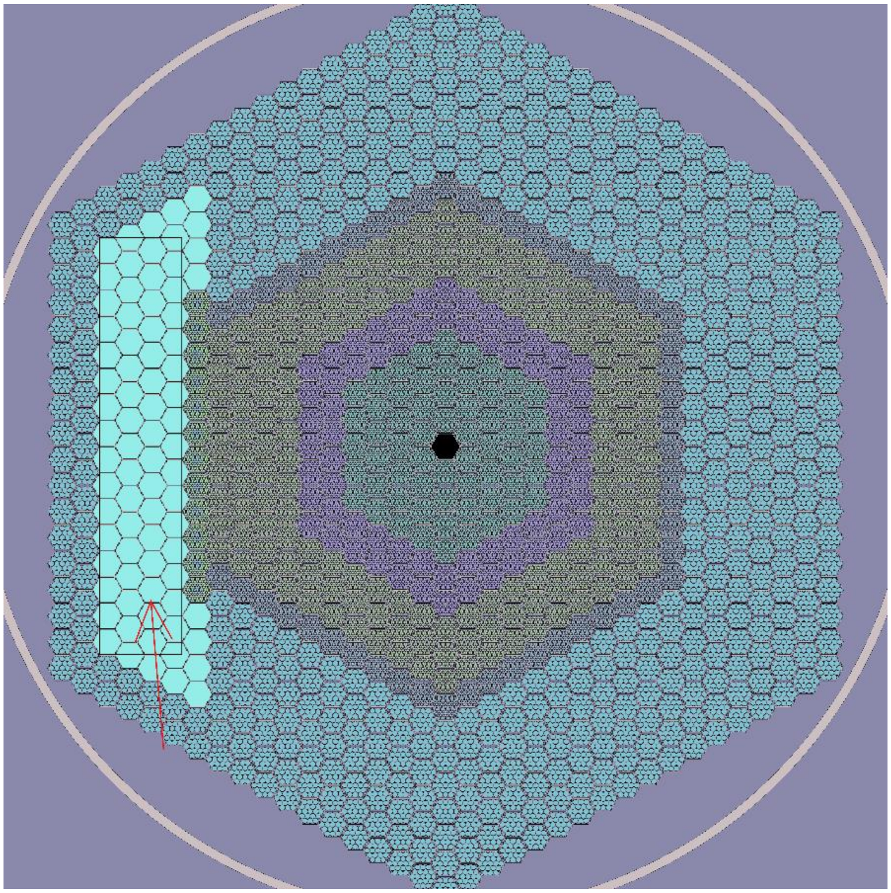

Figure 4.12 Orientation of Figure 4.13.

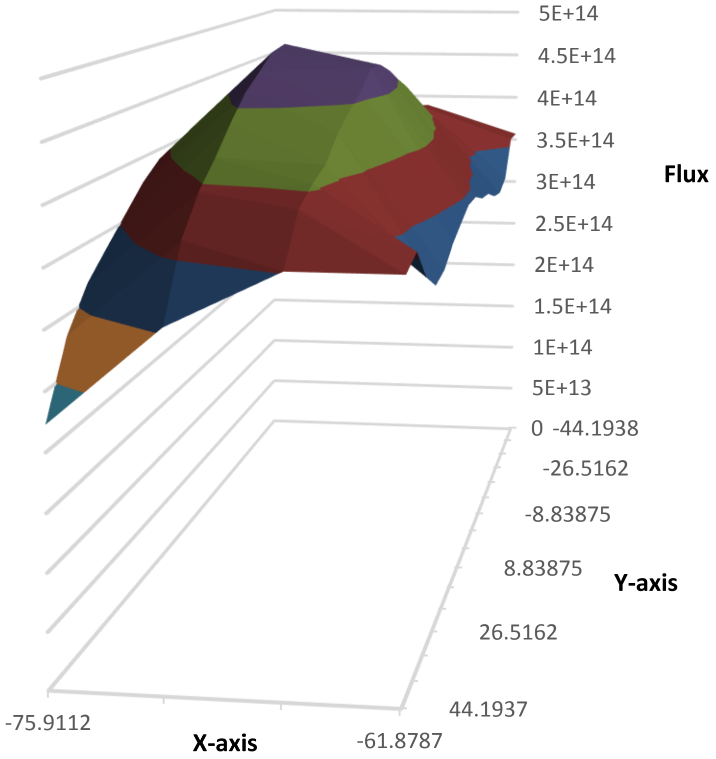

Figure 4.13 Thermal flux with graphite moderator and beryllium in the barrier assemblies.

Table 4.3 Flux fractions and total fluxes with graphite moderator and beryllium in the barrier assemblies

Flux fraction	Peak fast	Peak thermal	Tail	Corner
Thermal	0.093	0.229	0.205	0.341
Epithermal	0.646	0.674	0.695	0.611
Fast	0.261	0.098	0.100	0.048
Total flux	3.68E+15	2.15E+15	1.73E+15	6.52E+14

Flux fractions with beryllium in the barrier assembly are shifted towards the thermal region for a reactivity penalty of -0.25$. A burnup simulation was performed to study the effect of the buildup of strong absorbers within the assembly. The core reached an average burnup of 50 MWd/kgU in approximately 1043 days, slightly shorter than without the beryllium. This small change is most likely due to the replacement of fissile fuel with beryllium. The end of life reactivity barrier assembly reactivity worth was estimated at -0.29$, meaning that the beryllium burnup induced reactivity was -0.04$. The barrier assemblies initially contained 10.377 kg of beryllium. At the end of life, the beryllium mass had decreased by 0.107%. ^{10}B was present in trace amounts, along with 0.900 grams of ^{6}Li and 0.007 grams of ^{3}He. The assemblies also contained 0.620 grams of tritium, which diffuses through steel and could be present in the sodium. This is a potential radiological hazard, and the consequences of the tritium were not analyzed.

Having different enrichments within the barrier assembly is in response to the power peaking factor caused by the large flux of thermal and epithermal neutrons from the graphite. Directly changing the enrichment of the barrier assembly is perhaps the most direct method to control power peaking, but this does pose a few problems. An assembly loaded incorrectly could cause severe power peaking. If a barrier assembly would be rotated, power in some of the pins may be enough to increase cladding temperatures beyond safety limits. This effect would be highly localized because of the high thermal absorption cross sections of the fuel, so it may be difficult for operators to notice dramatically increased pin temperatures within an assembly. For this reason, the enrichments within the assembly should be as constant as possible while still minimizing the power peaking within the assembly. Perhaps the simplest way would be to add a thermal and epithermal absorber to the barrier assembly to absorb the thermal and epithermal neutrons before they fission within the barrier assembly. Cadmium has a high thermal (n,γ) cross section and a reasonable epithermal (n,γ) cross section, as demonstrated in the section concerning transient test assemblies. 1.0% cadmium by weight was added to the steel wall surrounding the barrier assemblies. Fig 4.14 shows the enrichments of the fuel located in this assembly.

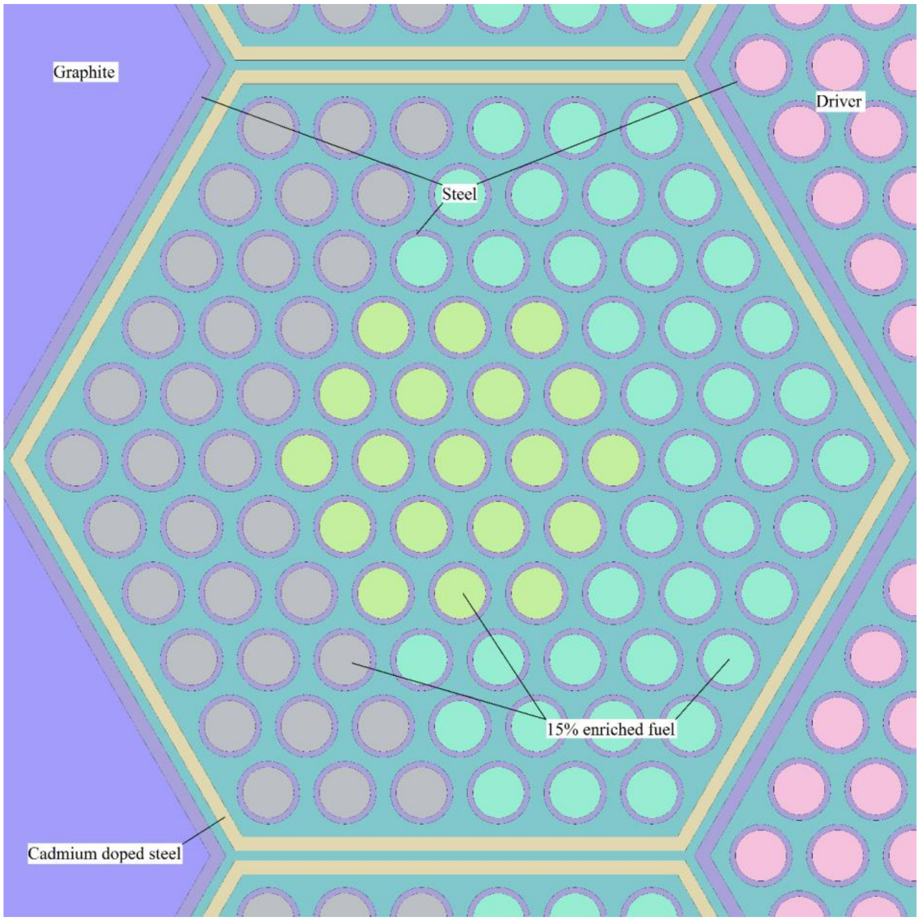

Figure 4.14 Cadmium doped barrier assembly

As demonstrated previously, peaking power can be estimated from the fission mesh, where the color of individual pins denotes power. The pins in this configuration did exhibit a great deal of power peaking. This is to be expected, as epithermal neutrons are not as attenuated as thermal neutrons by cadmium and would induce fissions within the fuel. A 15% enrichment was still too high, and those pins nearest the graphite were lighter in color than pins in the center of the driver. Switching to a different absorber such as boron, which absorbs thermal and epithermal neutrons, might be worthwhile. Reducing the enrichment would also decrease power production in those pins. By absorbing neutrons, negative reactivity is introduced; this is offset by adding more fissile material. Neutrons reflected back into the core by scattering off of a light water moderator will be preferentially absorbed. For this reason, the reactivity worth of the light water moderator with the cadmium doped assemblies is -2.24$, a greater reactivity worth than without cadmium doped barrier assemblies. Ultimately, this configuration inserts 0.10$ of reactivity at increased fuel costs. Increasing the enrichment and adding an absorber increased the fast flux and decreased the epithermal flux from the driver. The peak thermal flux did not change, but the peak fast flux increased to 1.27E15 n/cm^2s. Placing absorber around the barrier assembly might be worthwhile, but it comes at increased fuel costs and increased reactivity worth's of light water within the moderating region. Neither result is favorable. Designing the barrier assemblies such that they can only be placed in the correct orientation near the core would be the best option to reduce the consequences of accidentally rotating a barrier assembly when loading the core.

Removing sodium and steel from the moderating region generally increases fluxes throughout the region because sodium and steel are absorbers. However, it will have the greatest effect on the thermal flux. This moderator configuration represents a permanent moderator that would be placed in the core and used in a manner similar to the beryllium reflector in HFIR (Tomberlin 2006). The flux shapes in the moderating region are generally the same as with canned assemblies. Replacing the sodium and steel with graphite increases moderator volume by 10.2%. Thermal flux is shown in Fig 4.15 and is presented in the same orientation as Fig 4.13. Peak thermal flux is 1.02E15 n/cm^{2}s.

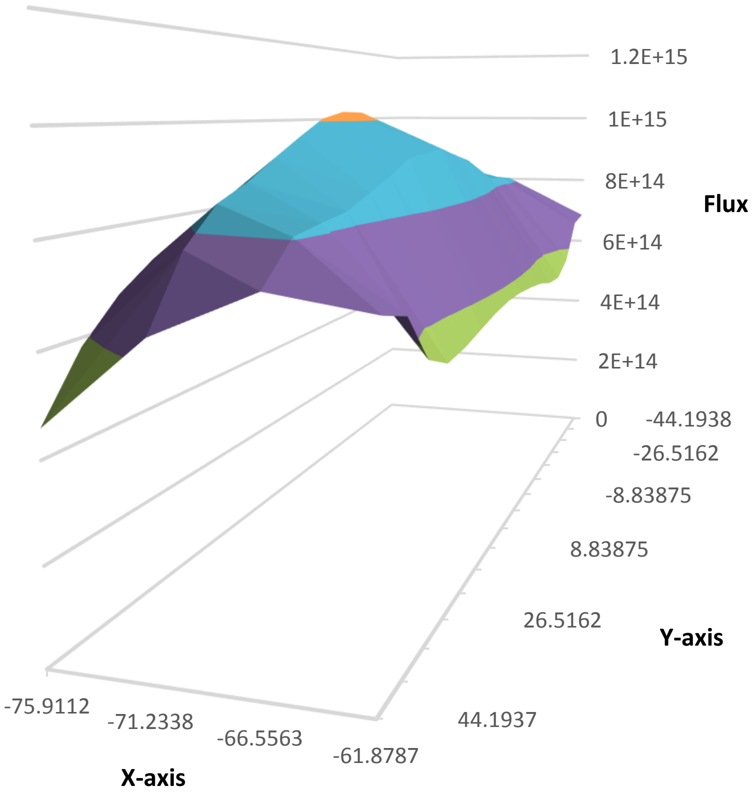

Figure 4.15 Thermal flux in graphite without canned assemblies

Table 4.4 Flux ratios for the graphite moderator without canned assemblies

Flux fraction	Peak fast	Peak thermal	Tail	Corner
Thermal	2.240	2.263	2.031	2.036
Epithermal	1.141	1.120	1.094	1.092
Fast	1.149	1.109	1.092	1.132
Total flux	1.218	1.345	1.271	1.395

Table 4.4 shows the flux ratios for the graphite moderator without canned assemblies. This is the flux in each energy bin and position without canned assemblies dividing by the appropriate value for the graphite moderator with canned assemblies. Peak thermal flux was in the same location with and without canned assemblies. Steel and sodium are largely 1/v absorbers, so the absence of steel and sodium will reduce parasitic absorption in the thermal groups more than in the faster groups. Adding more moderator will increase scattering from fast to epithermal energies and from epithermal energies to thermal energies. Indeed, the flux fractions throughout the region are more thermalized without cans. Fast and epithermal flux ratios are similar throughout the region. The thermal flux ratio for the peak thermal location is higher than for the tails and corners. Epithermal and fast neutrons will be more concentrated in the center of the region near the core. Therefore, the increase in moderation will cause more of these neutrons to down scatter, increasing the population of thermal neutrons. Far from the center, in the tails and corners, fewer high energy neutrons are present and the fewer neutrons down scatter to thermal energies. With the near elimination of absorption

within the moderating region, flux has the same general shape as without cans but at greater flux magnitudes. Diffusion of neutrons out of the region, presumably vertically, is shaping flux within the moderating region as strongly as parasitic absorption. Increases in flux within the moderating region increase the flux that streams back into the driver. Power peaking within the barrier assemblies increases. If more sodium cannot be directed into those assemblies, then enrichment will have to be decreased which will decrease flux within the moderating region. 0.92$ of reactivity are inserted by removing cans from the graphite.

The same effects noted with graphite in the moderating region without cans are observed with light water without assembly cans. Thermal flux is shown in Fig 4.16. It is presented in the same orientation as Fig 4.15. Thermal flux is the same general shape as with assembly cans. Thermal flux peaks at 2.02E15 n/cm^{2}s. -1.47$ of reactivity are inserted by removing cans with light water. Table 4.5 shows the flux ratios for the light water moderator with and without assembly cans.

Table 4.5 Flux ratios comparing light water in the moderating region with and without assembly cans.

Flux fraction	Peak fast	Peak thermal	Tail	Corner
Thermal	1.599	1.731	1.636	1.860
Epithermal	1.067	1.051	0.981	1.001
Fast	1.117	1.106	1.072	1.123
Total flux	1.323	1.518	1.483	1.658

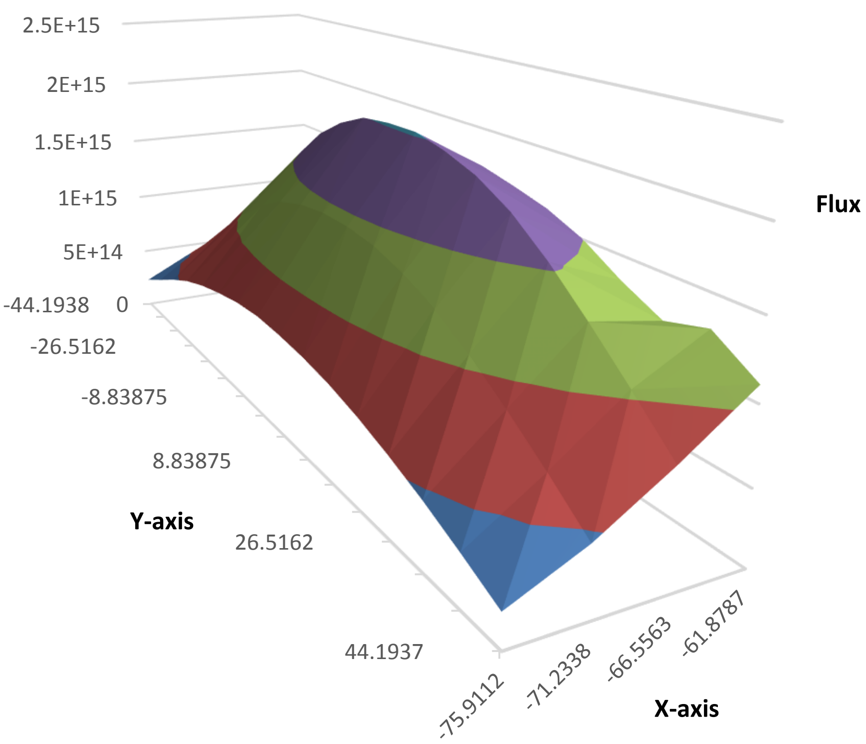

Figure 4.16 Thermal flux with light water without assembly cans

Fast ratio is relatively constant throughout the region. The increase in scattering and decrease in absorption will affect fast flux consistently throughout the region as there is no source of fast neutrons. The source of epithermal neutrons is fast neutrons. Far from the center of the moderating region fast flux will be suppressed and there will be fewer neutrons scattering into epithermal energies. The removal cross section for epithermal neutrons in light water is higher than for graphite, translating into lower flux ratios for epithermal neutrons in certain parts of the moderating region. Longer path lengths in graphite counteract this effect, but it would be observed if the graphite moderating region were to be increased in size. In general, thermal flux ratios are lower for light water than for graphite. Light water has a greater absorption cross section than graphite but still far less than steel and sodium. The moderating region was already heavily thermalized with cans; replacing them with additional light water produced less of an effect than replacing steel and sodium with graphite.

4.2 The effects of graphite and light water

Before considering irradiation conditions meant to closely mimic PWR and VHTR conditions, it is useful to consider the effects of graphite and light water by themselves. In these simulations, two irradiation test assemblies of the same design as the irradiation test assemblies in the driver are located in the core. In the last section, they are modified slightly. These irradiation assemblies are surrounded by flux shaping assemblies, six per irradiation test assembly, twelve in total. The results of twelve simulations are presented first. In these simulations, the relative amounts of graphite and light water are varied in two different ways. The first is to begin with only light water present in the flux shaping assemblies and gradually add graphite in 61 pins. The pin size is gradually increased. The second is to begin with only graphite, and gradually increase the size of light water holes. The volumes of light water and graphite are preserved in the simulations except in those simulations that are entirely composed of one substance. The largest graphite pin used was 0.68 cm in diameter with a pin pitch of 0.6945 cm. Pin diameter was varied so that area of these pins was changed linearly.

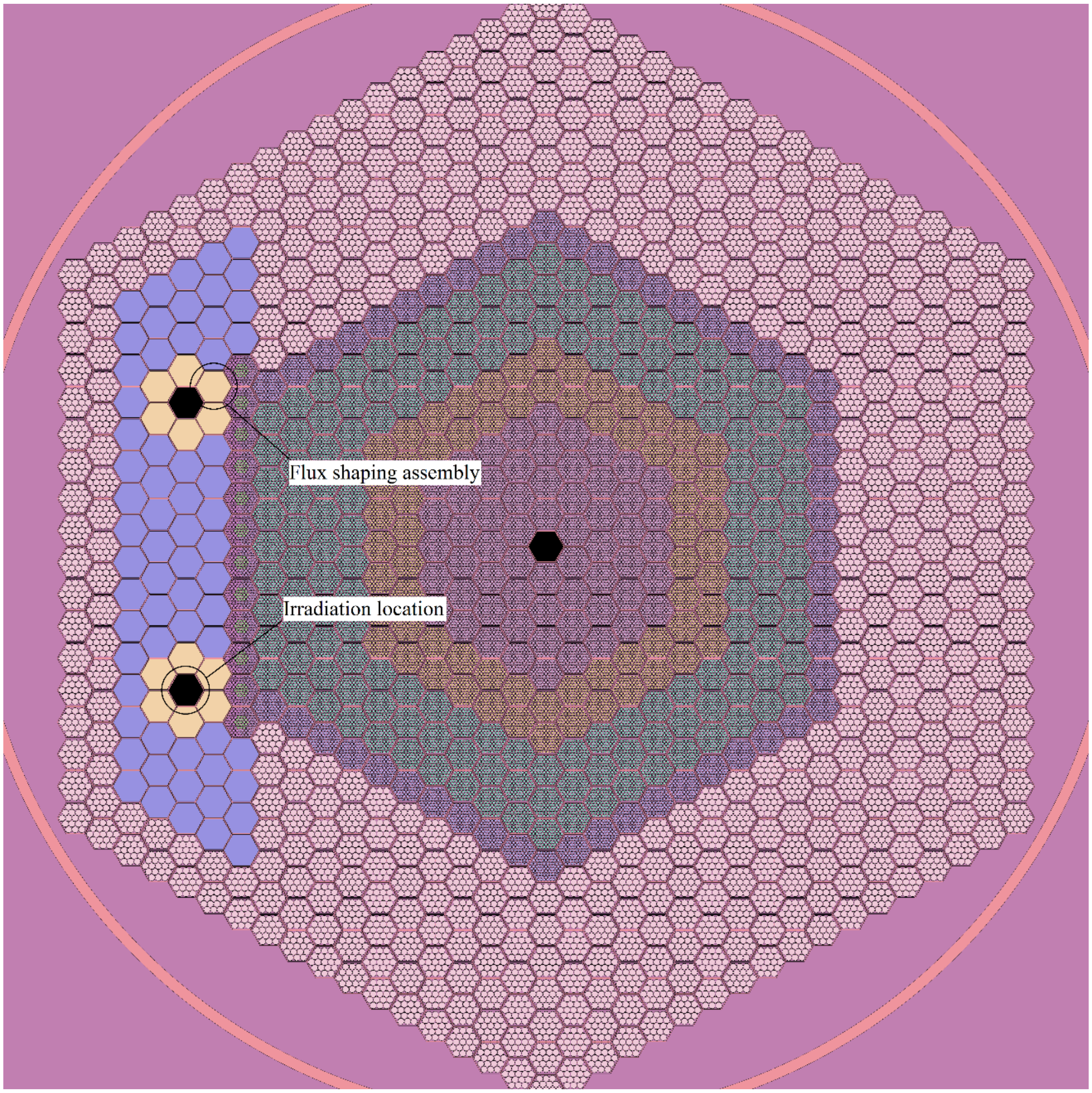

Figure 4.17 Picture of the core with two irradiation test assemblies and twelve flux shaping assemblies around it.

The percentages of graphite pin volume are: 0% (only water), 20%, 40%, 60%, 80%, and 100%. Therefore, pin radius of each was calculated as 0.34 cm times the square root of 0.2. This was repeated for 0.4, 0.6, and 0.8. Light water hole radii are calculated to preserve the volumes in these simulations. In order to increase thermal and epithermal flux, beryllium was used in the barrier assemblies. The locations of the flux shaping assemblies and irradiation locations are shown in Fig 4.17.

Table 4.6 Comparison of the graphite pins in light water versus light water holes in graphite for the same volume fraction. Greatest difference between the two.

Graphite pins in light water			Light water holes in graphite		
Flux	Rel. err.	Flux fraction	Flux	Rel. err.	Flux fraction
8.8274E+14	0.00244	0.549035	8.86847E+14	0.00245	0.545895
5.1446E+14	0.00249	0.31998	5.23533E+14	0.00250	0.322258
1.4293E+14	0.00417	0.088899	1.45737E+14	0.00416	0.089708
6.7667E+13	0.00583	0.042087	6.84586E+13	0.00590	0.042139
1.6078E+15	0.00162	1.0	1.62458E+15	0.00162	1.0
k_{eff} and rel. err.	1.08140	0.00011	k_{eff} and rel. err.	1.08148	0.00011

Fluxes were very similar between the two sets, graphite pins in light water and light water holes in graphite. Standard deviation was calculated between two simulations with the same volume fractions as the square root of the sum of the differences squared between the fluxes in each energy bin. The greatest standard deviation was with the graphite volume fraction at 0.1624. Total flux measured at this position was approximately 1.6E15 n/cm^{2}s. The standard deviation was 1.04E15. Fluxes in each position, relative error of each bin, flux fractions, k_{eff}, and the relative error of k_{eff} are shown for the two simulations in Table 4.6. The third through seventh rows give data for each energy bin and the total flux. The last row gives k_{eff} and its relative error, which match very well between the simulations. Flux in each energy group was consistently higher with light water in graphite than with graphite in light water. However, the flux fractions matched very well, differing in the third significant figure. Again, the fluxes differed the most at this volume fraction between the two methods of using graphite and light water. Given the similarity of flux fraction, flux fractions for each group are given in Fig 4.18 as a function of graphite fraction. The data for graphite pins in light water was used to create Fig 4.18, except the last data point with pure graphite.

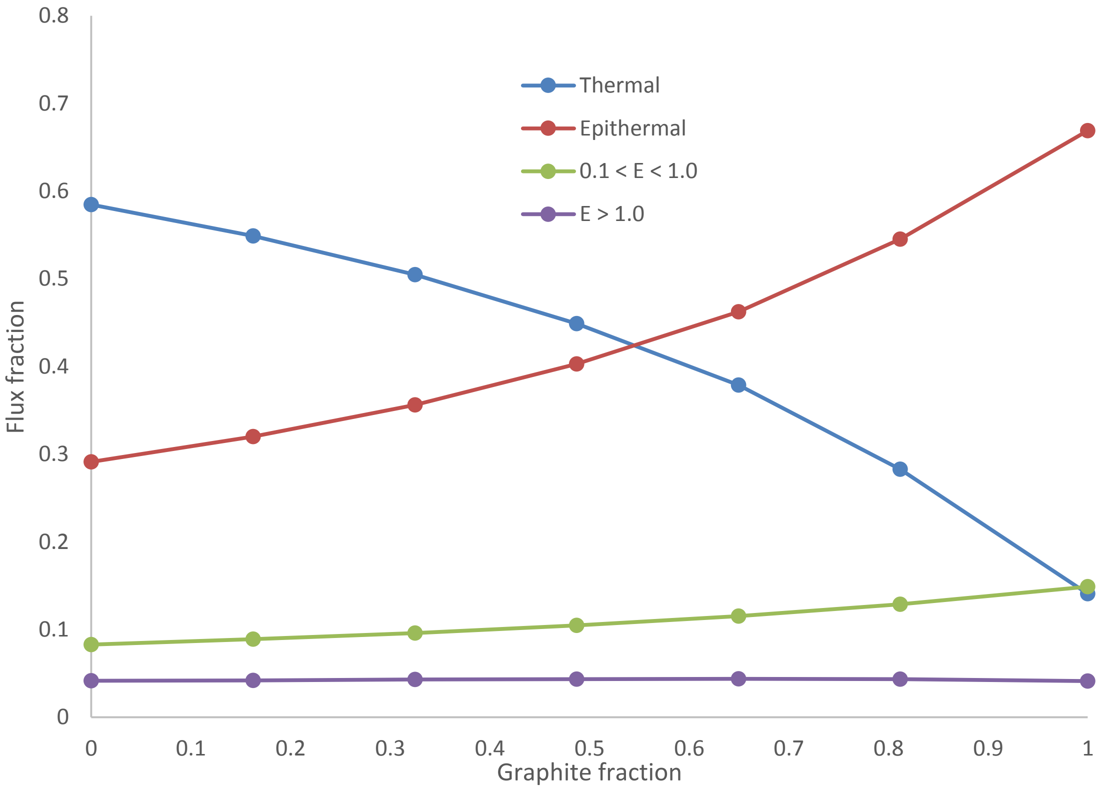

Figure 4.18 Flux fraction versus graphite fraction

Fast flux E > 1.0 MeV exhibits a very slight decrease for graphite fractions near 1.0. This is an artifact of increasing total fluxes. Fast flux E > 1.0 MeV increases with increasing graphite fraction from 6.56E14 to 8.36E14 n/cm2s. Graphite fraction and flux values follow the same trends for the other three groups. Predictably, a decrease in graphite fraction increases thermal flux and decreases epithermal flux and fast flux. A wide variety of flux fractions are attainable from only varying graphite and light water. PWR spectra will use more graphite while VHTR spectra will use more light water as outlined in the following sections. Fast flux in these area is suppressed. The following sections will examine two different ways to increase fast flux. As outlined in the last section, light water is a less effective reflector than graphite. Therefore, reactivity decreases with increasing light water fraction as shown in Fig 4.19. The addition of two irradiation assemblies without any light water causes a small decrease in reactivity because of the removal of graphite from the moderating region.

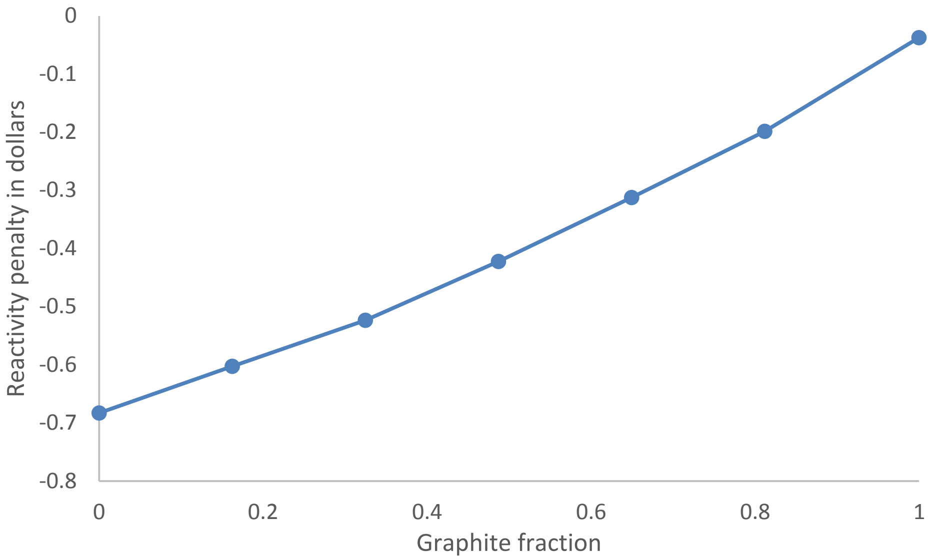

Figure 4.19 Reactivity penalty of graphite fraction with two irradiation assemblies

Lattices of graphite and light water yielded consistent results. However, it is also useful to consider heterogeneous effects of the two moderators. Therefore, it was decided to include graphite and light water occupying different sides of the same assembly and to rotate all the assemblies so that only light water or graphite faces the irradiation assembly. The next two figures shows close-ups of the moderating region with these configurations. To fit better on the page, the figures are rotated 90 degrees. Fig 4.20 shows light water near the irradiation position and Fig 4.21 shows graphite near the irradiation position.

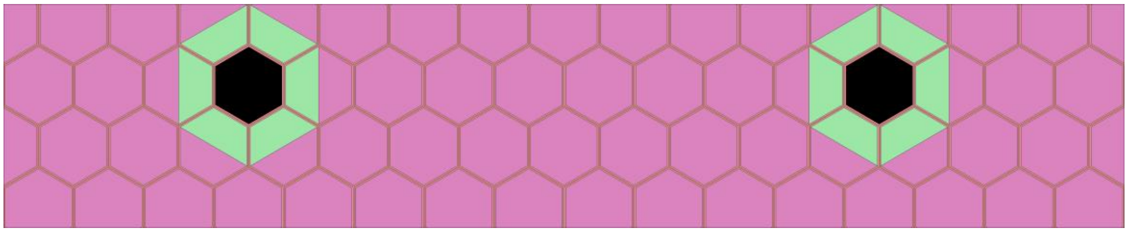

Figure 4.20 Simulation 13, light water near the irradiation positions

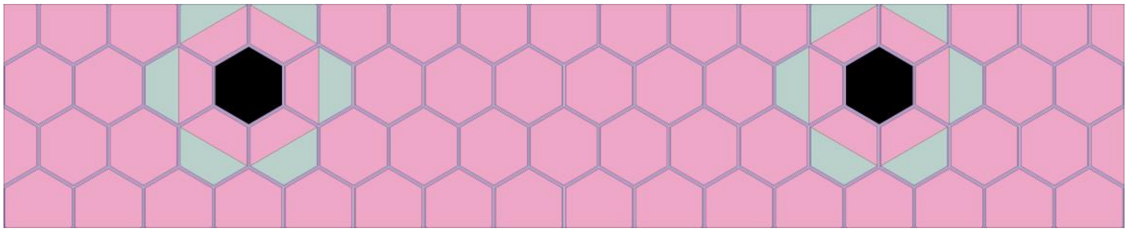

Figure 4.21 Simulation 14, graphite near the irradiation positions

None of the pin simulations were conducted with a graphite fraction of 0.5, so Simulation 15 was performed, with graphite pins in light water at a graphite fraction of 0.5. Fluxes and flux fractions for each simulation and the associated k_{eff}'s and relative error are presented in Table 4.7.

Table 4.7 Fluxes, flux fractions, k_{eff} and relative error for simulations 13, 14, and 15.

Simulation 13		Simulation 14		Simulation 15	
Flux	Fraction	Flux	Fraction	Flux	Fraction
8.43E+14	0.495	6.47E+14	0.370	7.64E+14	0.446
6.31E+14	0.371	7.95E+14	0.454	6.95E+14	0.406
1.61E+14	0.094	2.26E+14	0.129	1.81E+14	0.105
6.78E+13	0.040	8.23E+13	0.047	7.43E+13	0.043
k_{eff}	Rel. err.	k_{eff}	Rel. err.	k_{eff}	Rel. err.
1.08276	0.00011	1.08333	0.00011	1.08273	0.00011

Flux fractions for Simulation 15 are between those of Simulation 13 and 14 in each group. Light water near the irradiation assemblies shifts the spectrum towards thermal energies. By concentrating light water around the irradiation assembly, it increases the chances that neutrons will undergo multiple interactions with light water. The distance from the center of an assembly to the nearest steel wall is 2.8067 cm. This is far lower than the fuel pin pitch in a LWR. All neutrons that enter the irradiation assembly must pass through this layer of light water. However, in Simulation 14, neutrons can enter the irradiation assembly do not have to pass through layer of light water or can pass through a shorter layer. This is the most likely reason for the discrepancy between the two values. Concentrating light water near the irradiation assembly causes the flux fractions to resemble those associated with a graphite fraction of 0.30. As k_{eff} decreases with decreasing graphite fraction, utilizing light water more effectively within the assemblies would reduce the reactivity penalty associated with light water.

Heterogeneous effects of light water and graphite were examined from a different angle in the last four simulations, Simulations 16, 17, 18 and 19. In this, the effect of equal volume fraction versus equal thickness of moderator is studied. As noted previously, with graphite near the irradiation assembly neutrons could enter the assembly without passing through a meaningful thickness of light water. With concentric cylinders of moderator, this effect is minimized. The irradiation test assemblies and flux shaping assemblies were redesigned in concentric cylinders. Fig 4.22 shows Simulation 19, with graphite close to the irradiation locations and equal volumes of light water and graphite. Flux shaping assemblies and the volume over which they are averaged are different in these simulations.

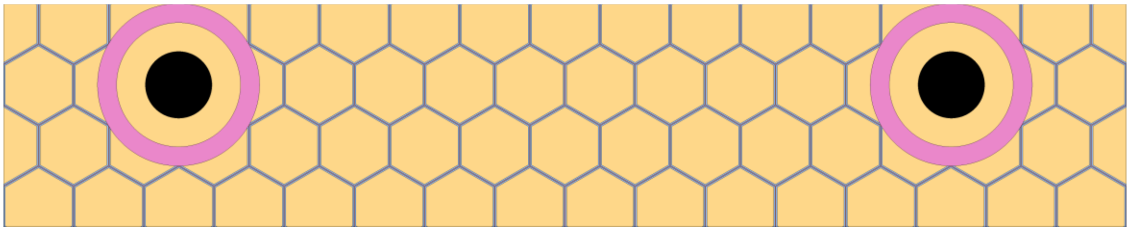

Figure 4.22 Simulation 19, graphite near the irradiation locations.

The flat to flat distance inside 7 assemblies is 17.679 cm. However, a cylinder of this diameter would encompass assemblies outside the testing location, so the interior diameter of 13.6093 cm is used. When studying equal thicknesses of moderator, it was decided to balance the thickness of the moderator versus the size of the irradiation position. Therefore, the moderator thicknesses were limited to 2 cm each, and the diameter of the irradiation positon was 5.6093 cm. Graphite volume fraction, whether water or graphite are near the irradiation position, the thickness of the water slab, and the thickness of the graphite slab are given for each simulation in Table 4.8. Table 4.9 shows the flux in each group, flux fractions for each simulation, k_{eff}, and relative error for Simulation 16, 17, 18 and 19.

Table 4.8 Graphite fraction, material near irradiation position, and the thicknesses of the light water and graphite in Simulations 16, 17, 18, and 19

Simulation	Graphite fraction	Material near assembly	Light water thickness	Graphite thickness
16	0.60407	Light water	2.0 cm	2.0 cm
17	0.39593	Graphite	2.0 cm	2.0 cm
18	0.5	Light water	2.39965 cm	1.60035 cm
19	0.5	Graphite	1.60035 cm	2.39965 cm

Simulation 16 with more graphite had the highest k_{eff} but k_{eff} was very similar between the simulations. Simulation 18 had the second highest k_{eff} because the graphite was closest to the driver. Simulations 18 and 19 followed the same pattern as Simulations 13 and 14, where the same volumes of graphite and light water distributed within the assemblies have different fluxes. Light water near the assembly thermalizes more than graphite near the assembly. Neutrons traveling directly towards the moderating position will travel through 50% more of whatever material is closest to the driver. However, neutrons traveling at different angles or scattering within the volume will experience the two volumes in more equal amounts. Simulations 16 and 17 have far more equal flux fractions, but Simulation 16, with light water on the inside and 53% more graphite than light water still had a more thermalized spectrum. Elastic scattering is highly isotropic for light water and graphite at energies below 1 MeV. This means that the probability of backscatter and forward scatter are the same. Neutrons may be backscattering off of the material immediately surrounding the irradiation assembly, which would cause neutrons to be more thermalized in Simulation 16 than in Simulation 17. Although the results of these demonstrate the minimization of light water, which increases k_{eff}, such heterogeneous assemblies were not used to shape flux when testing prototypic PWR and VHTR assemblies. Flux fraction only varies with graphite fraction for pins in media, which will greatly simplify optimization processes. However, more detailed optimization processes, especially relating to minimizing light water in the core as it is safety risk, should make use of the information presented in this section.

Table 4.9 Flux in each group, flux fraction, k_{eff}, and relative error for each Simulations 16, 17, 18, and 19.

Simulation 16		Simulation 17		Simulation 18		Simulation 19	
9.83E+14	0.533	9.24E+14	0.511	1.04E+15	0.567	8.54E+14	0.469
6.71E+14	0.364	6.66E+14	0.368	6.14E+14	0.334	7.33E+14	0.402
1.35E+14	0.073	1.57E+14	0.087	1.28E+14	0.070	1.71E+14	0.094
5.65E+13	0.031	6.25E+13	0.035	5.47E+13	0.030	6.44E+13	0.035
k_{eff}	Rel. err.	k_{eff}	Rel. err.	k_{eff}	Rel. err.	k_{eff}	Rel. err.
1.08495	0.00011	1.08462	0.00011	1.08479	0.00011	1.0848	0.00011

4.3 PWR test assemblies in the moderating region

This section will describe the attempt to mimic the PWR neutron spectra in the FMTR. The first step was to provide some kind of benchmark for the neutron spectra in a PWR. Many examples of PWR spectra exist. Rather than adopt one, it was decided to simply create a PWR neutron spectrum using specific group structures and to create an associated power profile. This allows direct comparison of neutron groups and power profiles between different geometries. A single pin and its associated square unit cell was simulated. The axial power profile, power energy spectra, 4 group spectrum, and 120 group spectrum for the single pin and its surrounding coolant were tallied. Power energy spectra tallies how much power was generated by neutrons that fission in a given energy bin. The fuel pin was simulated with an average linear power of 187 W/cm. The neutron spectra was tallied over the whole active core height; this did not include the light water reflector above and below the core. Pin pitch was 1.265 cm and pin diameter was 0.95 cm. Cladding was 0.025 cm thick. No gas gap was modeled. The light water and cladding were modeled with 600 K cross sections and the fuel was modeled with 900 K cross sections. The light water was at a density of 660 g/cm^3, which is the approximate density of water at saturation conditions between the temperatures of 320°C and 325°C. The fuel was uranium dioxide at 10.475 g/cm^3. The pin was 330 cm tall and an infinite light water reflector was modeled above and below the pin. The results of this simulation will be provided later when comparing different features of the PWR test assembly and moderating region in general. The Design Control Document for the AP1000 lists slightly different values for the pin pitch, fuel density, cladding thickness, and linear power, but these differences should not result in a neutron spectra significantly different from that of a large PWR. Pin pitch is 1.25984 cm, cladding thickness is 0.0572 cm, and fuel density is 95.5% theoretical. Assuming a theoretical density of 10.963 g/cm^3, this corresponds to a fuel density of 10.470 g/cm^3 (Thermophysical 2006). Average linear power is 187.7 W/cm, but the peak linear power for normal operations is 488.8 W/cm. In simulations, the linear power is maintained between these two values.

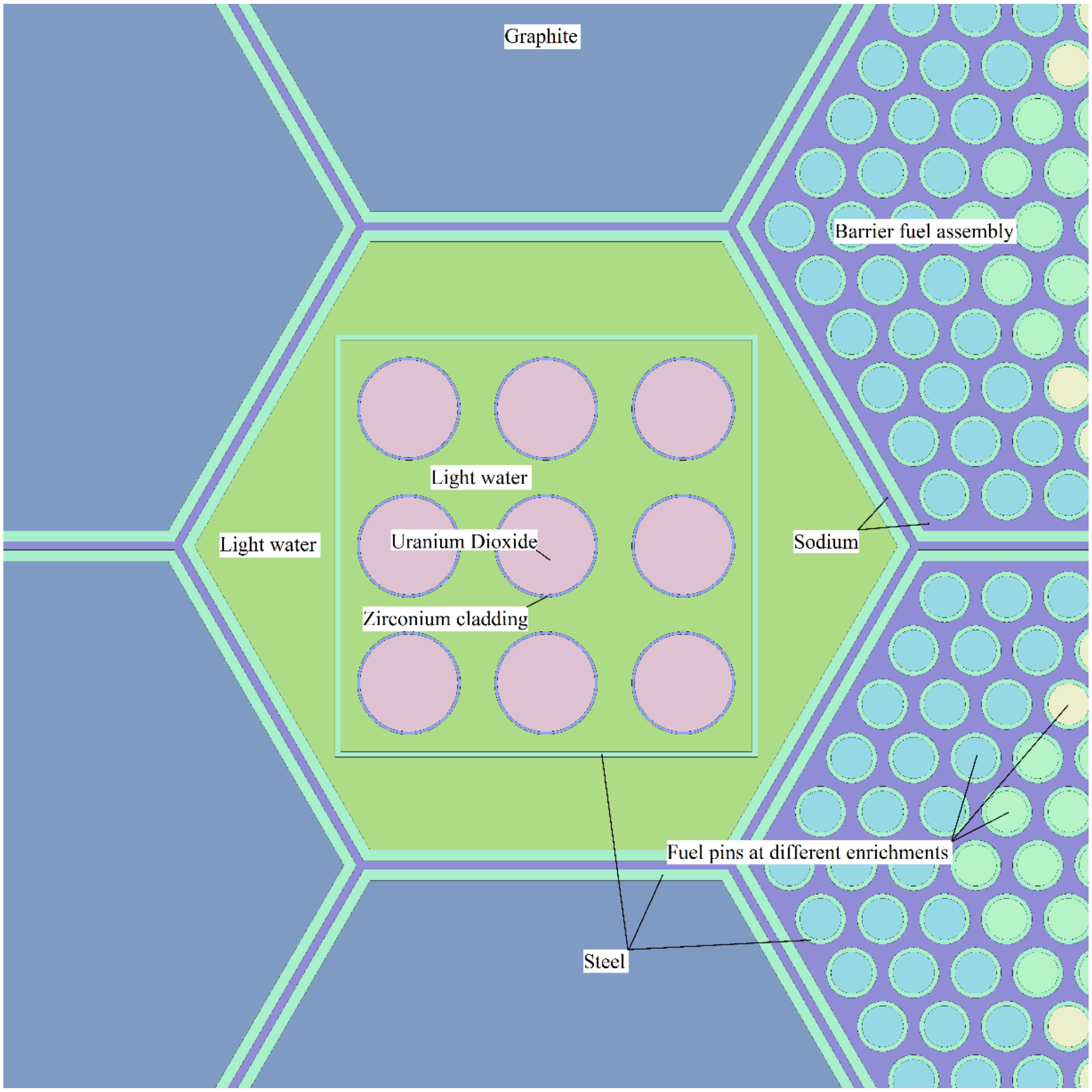

Figure 4.23 PWR test assembly

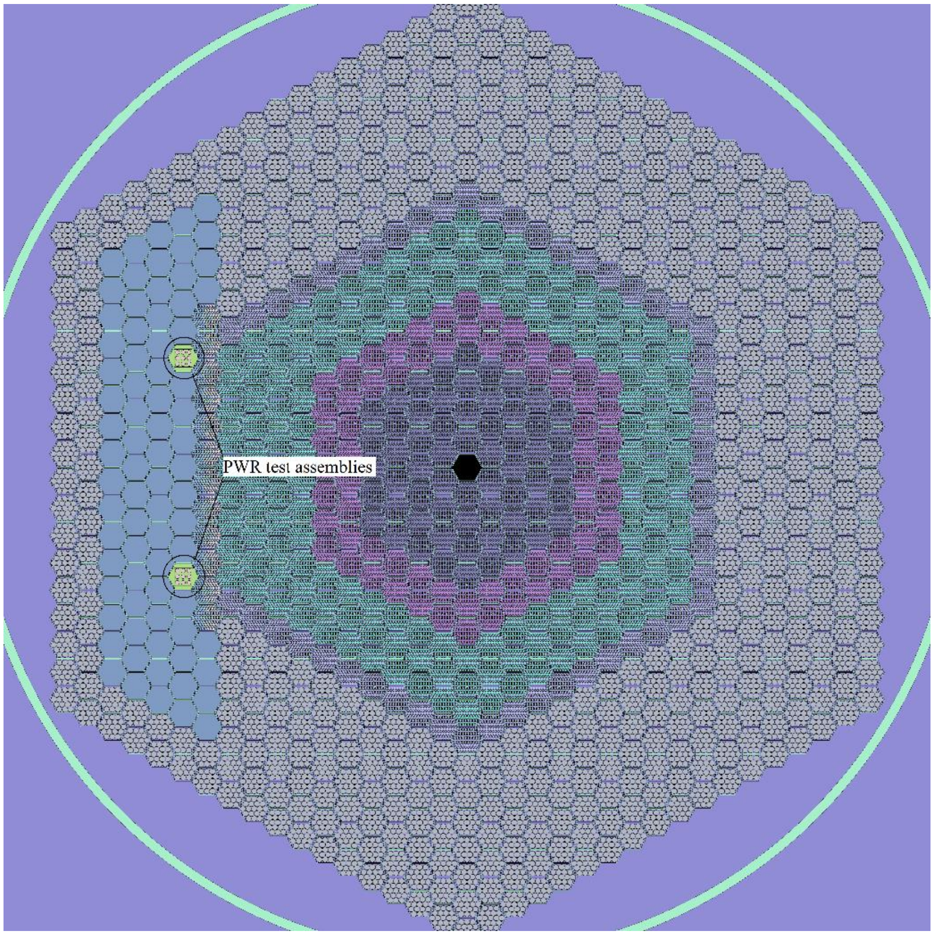

Figure 4.24 Location of PWR test assemblies near core

A 3 by 3 lattice of the single reflected pins was created. This lattice was surrounded by a thin steel wall (0.05 cm thick) and placed inside the standard assembly configuration. The pins are 180 cm tall; only the middle 100 cm is filled with fuel. The upper and lower 40 cm sections contain graphite. The thin steel wall separates inner and outer light water coolant flow paths. Fig. 4.23 shows the test assembly immediately adjacent to the barrier fuel assemblies. Fig 4.24 shows where the PWR test assemblies were located within the core. The locations of the test assemblies are symmetric through the x-axis. The spectra and power profiles for the two assemblies were averaged together for better statistics. This test assembly is identical to the one used in transient testing. It was calculated that placing two assemblies in those positions would insert approximately -0.153$ of reactivity, assuming a β_{eff} of 0.0065. With an enrichment of 0.2%, these test assemblies produced an average linear power of 229.3 W/cm next to the core for a total flux 8.7 times that of the prototypical pin. Such an increase in flux would enable accelerated materials degradation. However, the neutron spectra that the test assembly experiences is different from the neutron spectra experienced by the prototypic pin, an effect that will now be analyzed. Fig. 4.25 shows the neutron flux in the prototypic pin and in the test assembly. The neutron flux in the test assembly near the core is clearly larger than the neutron flux of the prototypic pin, but the neutron spectra of the test assembly is more weighted towards the thermal than the single pin, an effect than can be seen by plotting the fractional spectra, shown in Fig. 4.26.

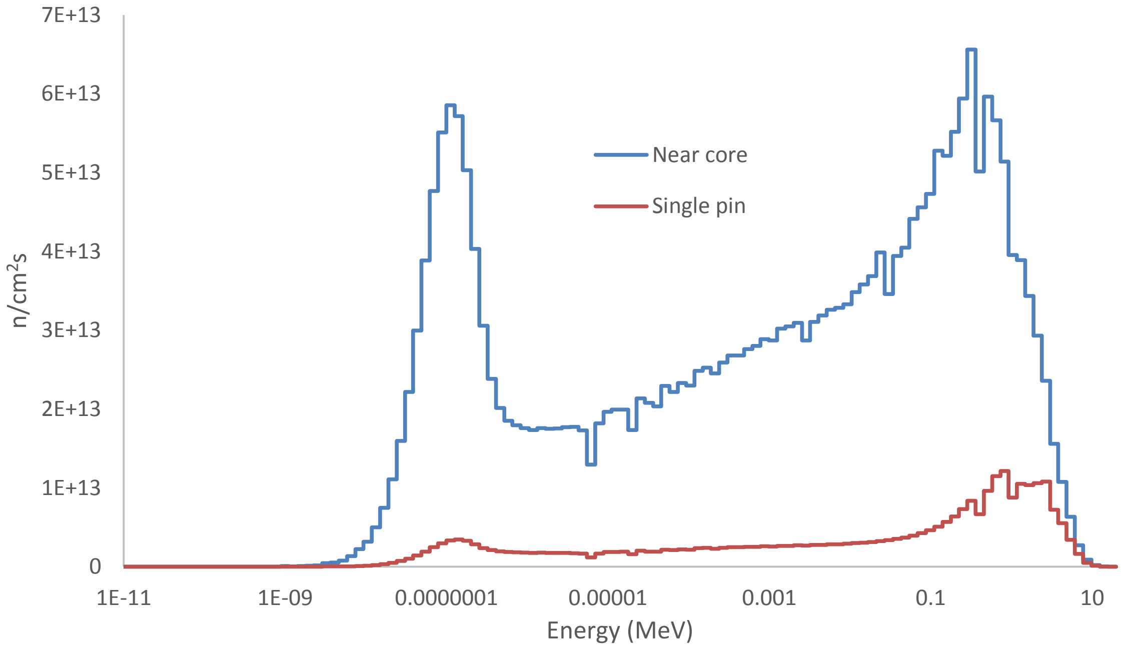

Figure 4.25 Flux in the PWR test assemblies near the driver with the flux a prototypic PWR pin.

Flux fraction is the flux in each energy bin divided by the total flux, such that the sum of all 120 energy bins comes to 1. The spectrum of the test assembly is clearly weighted towards the thermal and epithermal. The thermal peak of both spectra occurs of the same energy. This is to be expected, as the light water is both simulations is simulated at 600 K. However, the fast spectrum peak is shifter to lower energies. This happens because the fast spectrum in the fast region is shifted towards the lower portions of the fast group, a feature discussed previously. These effects are shown more clearly by comparing the four group spectra.

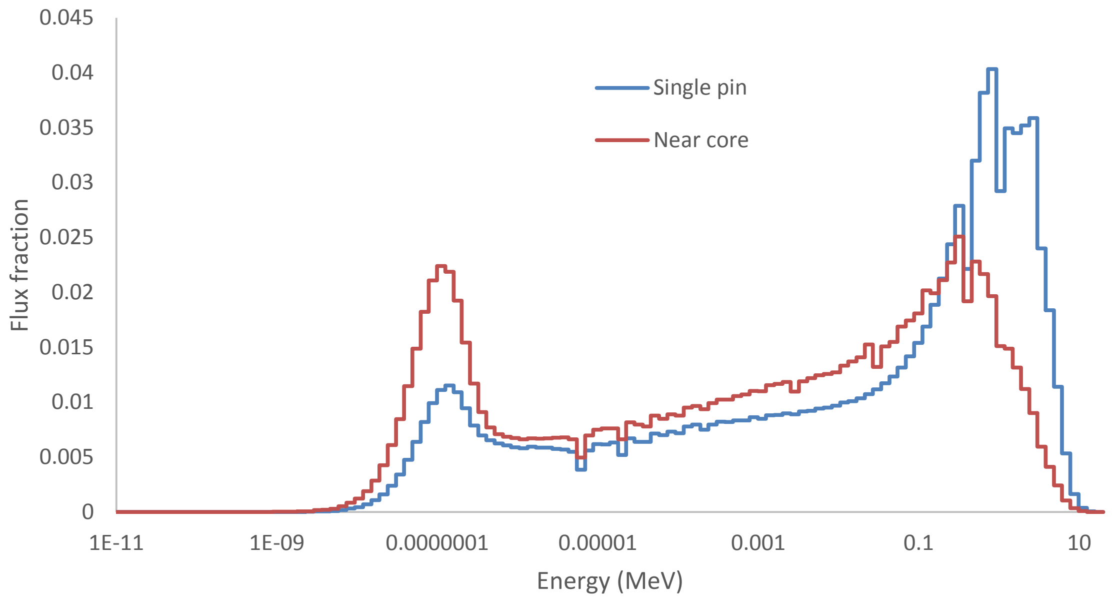

Figure 4.26 Relative flux of the PWR test assemblies near the driver and a prototypic PWR pin

Table 4.10 shows the 4 group flux tallies for the single pin and the test assembly. The column entitled “Flux ratio” is the value of the “Single pin” flux divided by the “Near core” flux for each bin. The flux ratio relates how the flux is weighted. As expected, the test assembly is far more thermal than an actual PWR. Similarly, the fast flux in the test assembly more closely resembles the fast spectrum in the driver region than in a PWR. The flux between the energies 0.1 MeV and 1 MeV is nearly the same as the flux between the energies between 1 MeV and 20 MeV for the PWR spectra. In a previous section it was shown that the group from 1 MeV to 20 MeV makes up only 21% of the fast flux in the driver region. In this test assembly, the group from 1 MeV to

20 MeV makes up 26% of the fast flux. This is because the fast flux in the test assembly comes primarily from the driver, not the test assembly itself.

Table 4.10 Fluxes and flux ratios within a PWR test assembly near the core

Energy group	Single pin	Near core	Flux ratio
E < 0.625 eV	3.27E+13	5.38E+14	16.44
0.625 eV < E < 0.1 MeV	1.24E+14	1.35E+15	10.93
0.1 MeV < E < 1 MeV	7.74E+13	5.37E+14	6.95
E > 1 MeV	6.69E+13	1.90E+14	2.84
Total	3.00E+14	2.62E+15	8.70

By placing the test assembly so near the core, the fast flux in the test assembly is primarily that of the fast flux stemming from the driver. By placing the test assembly further from the core, where the flux is heavily moderated, the test assembly is moved to a location with few fast neutrons. Placing a fissile material in this region will help correct the discrepancy in fast fluxes between the prototypic PWR pin and the test assembly by ensuring that the only fast neutrons present in the test assembly were generated inside the test assembly. However, in a region of such thermal and epithermal fluxes, little fissile material is needed to generate enough power for the test assembly. However, a great deal more fissile material is needed to generate enough fast neutrons to approach the fast fluxes in a PWR. Thus, it is necessary to include a great deal of absorber materials surrounding the test assembly to suppress the thermal flux and lower the power in the test assembly. Fig 4.27 shows the test assembly and Fig 4.28 shows the locations of the test assemblies in the moderating region. Six graphite assemblies around the test assembly are removed and replaced with moderating and absorbing assemblies. The absorber assemblies are filled with light water to both moderate neutrons and cool the absorber pins. 61 Er_2O_3 pins 0.6 cm in diameter are located inside the absorbing assembly. The Er_2O_3 had a density of 8.64 g/cm^3.

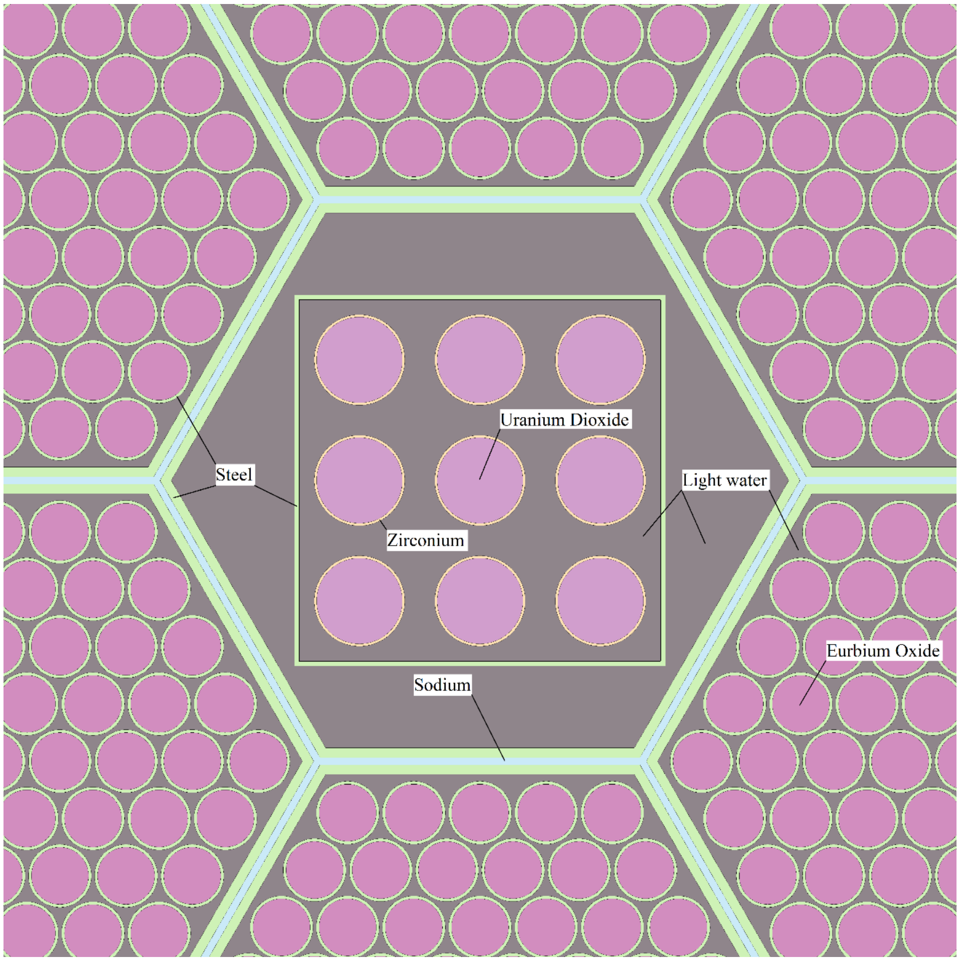

Figure 4.27 PWR test assembly far from driver with Er_2O_3 absorber and light water in the flux shaping assemblies.

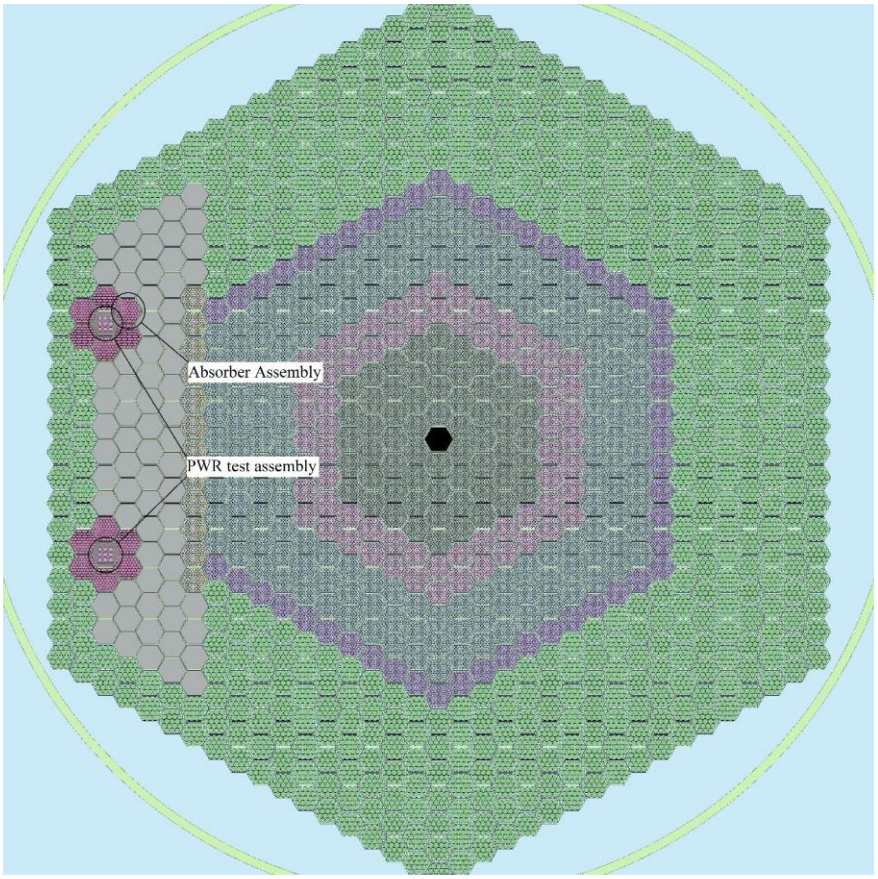

Figure 4.28 Location of PWR test assemblies and flux shaping assemblies in driver

Average linear power was 202.1 W/cm with an enrichment of 6% for a total flux 80% that of that of a prototypic PWR. This configuration inserts -0.396$ of reactivity, a fairly hefty penalty in comparison to placing the test assemblies near the core. It should be stressed that the presence of so much absorber adversely effects reactivity. Without those assemblies, the reactivity penalty would be far lower but there would be little fast flux. The absolute flux for the prototypic pin and test assembly is shown in Fig 4.29. Both plots demonstrate the expected behavior of relatively high enrichment and significant absorber around them. Table 4.11 gives the 4 group fluxes for the two simulations.

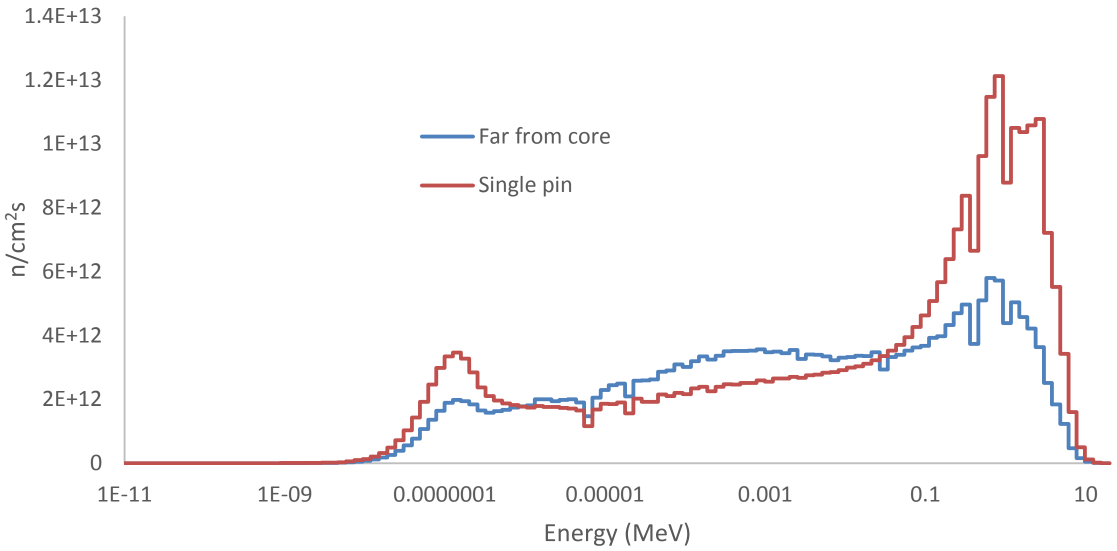

Figure 4.29 Flux of the PWR test assemblies far from the driver with Er2O3 and light water flux shaping assemblies with a prototypic PWR flux.

The presence of an absorber skews the spectrum towards the epithermal. Depleted uranium and pure gold were also used in this configuration but did not produce results that were less skewed. Pure gold is also expensive, the raw material costing more than 30,000$ per kilogram as of from August 2014 to August 2015 (Gold 2015). Depleted uranium was also considered, but did not produce substantially better results. Additionally, the depleted uranium pins would generate heat and breed plutonium. The test assembly spectrum far from the core spectrum is closer to the PWR spectra than the spectrum near the core, but at the cost of lower fluxes. Further analysis should be able to more closely mimic the PWR spectra, but such shaping will always come at the expense of lower fluxes than the heavily skewed spectrum next to the core.

Table 4.11 Flux data for a PWR test assembly far from the core surrounded by moderating and absorbing flux shaping assemblies.

Energy group	Single pin	Near core	Flux ratio
E < 0.625 eV	3.27E+13	2.04E+13	0.62
0.625 eV < E < 0.1 MeV	1.24E+14	1.47E+14	1.19
0.1 MeV < E < 1 MeV	7.74E+13	4.52E+13	0.58
E > 1 MeV	6.69E+13	2.68E+13	0.40
Total	3.00E+14	2.39E+14	0.80

Lastly, the power profile associated with the single pin and the test assembly is shown in Fig 4.30. This profile was acquired without varying the enrichment axially along the pin, so the power profile for the single pin takes on the expected chopped cosine. Light water, which is above and below the core, is a less effective moderator than graphite, which is above and below the test assembly. The profile for the test assembly is flatter than the single pin. The relative flux is shown per unit of relative pin length. Relative flux is the flux in each position divided by the total flux. This means that the average of the relative fluxes is 1.0. However, relative pin length is the location of each axial location divided by the total pin length. The active length of the test assembly is 1.0 meters, extending from -50 cm to 50 cm. This is divided into 20 equal sections. The power associated with each 5 cm section is shown in the plot at the center of each bin. The power associated with the topmost bin, from 45 cm to 50 cm, is therefore shown at 47.5 cm. The relative pin length associated with this position is therefore 0.475. The 3.3 meter pin was also divided into 20 equal section. The relative pin lengths for the two scenarios are identical. If it was desired to mimic the power peaking shown in the single pin, it would be sufficient to simply replace the graphite reflector with light water. The jaggedness of the test assembly profile is caused by statistical error and has no physical meaning.

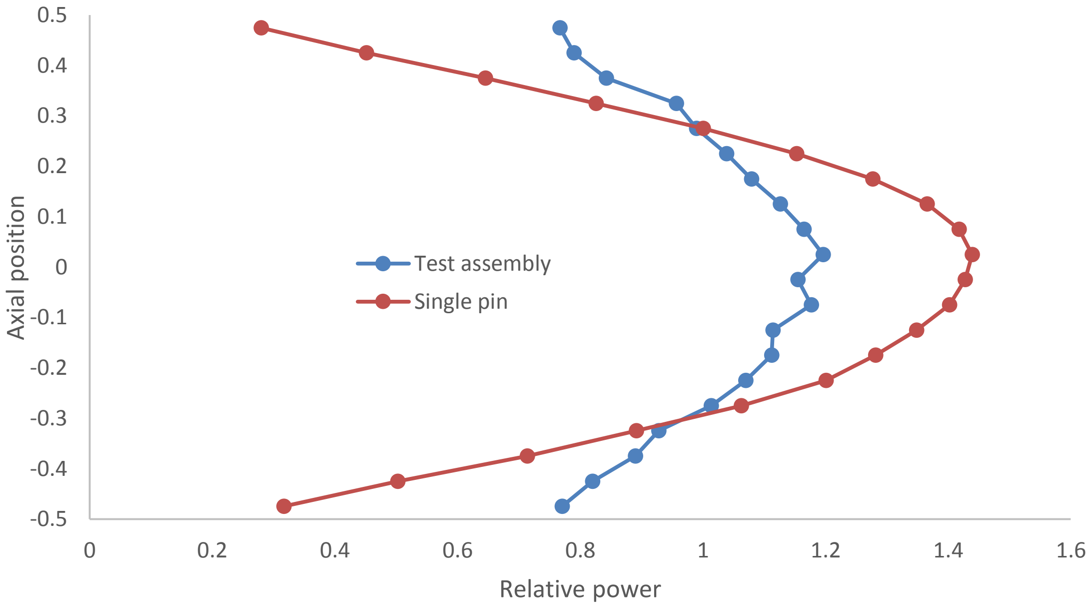

Figure 4.30 PWR test assembly and prototypic PWR axial power profiles

4.4 VHTR test assemblies in the moderating region

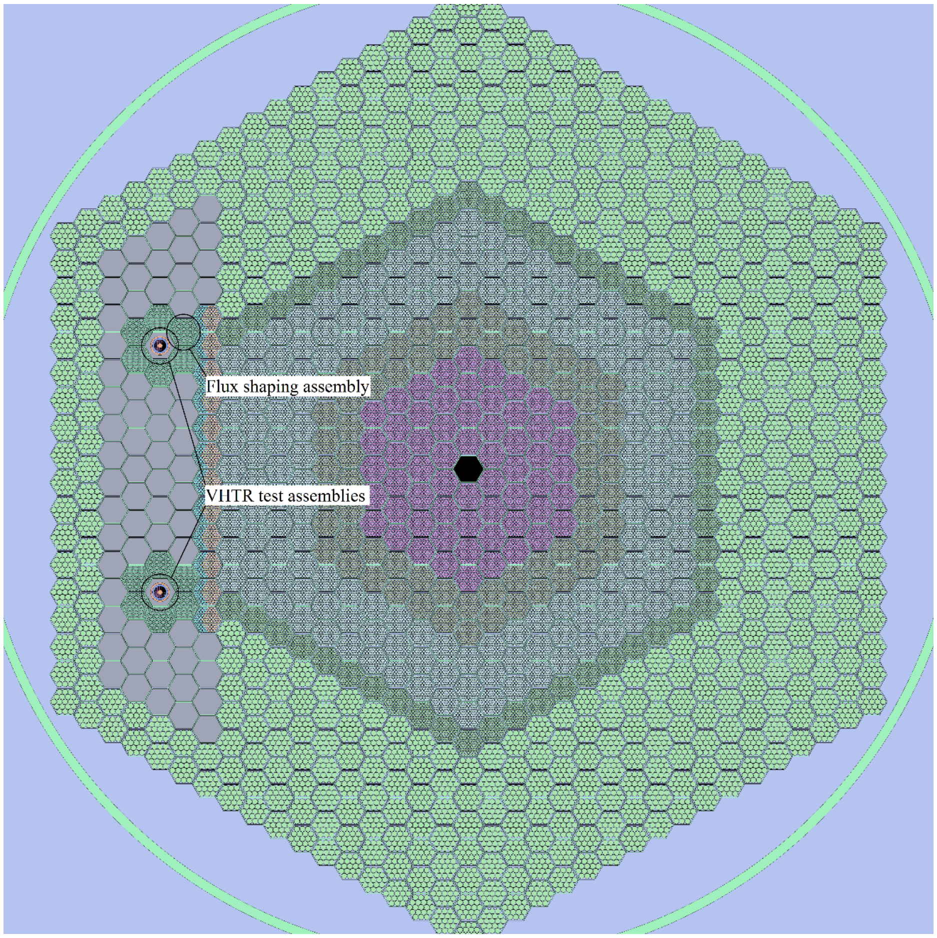

Figure 4.31 Location of VHTR test assemblies near driver

An infinite lattice of the VHTR test assembly used in this investigation did not yield 3 group fluxes similar to the values stemming from the INL report. This is to be expected, as VHTR's are heavily reflected by graphite. For this reason, the 3 group fluxes will be the only metric of comparison of the test assemblies. As in the PWR test assemblies, the test assemblies placed near the core are described first. However, the amount of graphite within the test assembly was insufficient to thermalize the spectrum. Therefore, the test assembly is surrounded by six assemblies that attempt to mimic a VHTR spectrum using two different philosophies. The first method uses a mixture of graphite and light water to control the epithermal and thermal fluxes that enter the test assembly. The second method used light water and Er_2O_3 to moderate and absorb thermal and epithermal neutrons. The advantages and disadvantages of both methods will be demonstrated. Fig 4.31 shows the locations of the test assemblies near the core. Fig 4.32 shows the test assembly itself and the flux shaping assemblies that surround it. The test assembly is identical to the one used in transient testing. Only general dimensions and compositions of the test assembly are provided here. The fuel compact is composed of bands of SiC and graphite surrounding a kernel of UO_2. The kernel is 0.06 cm in diameter and the whole fuel particle is 0.093 cm in diameter. The packing fraction of the particles was 0.31. 0.2 % enriched fuel was used with graphite flux shaping assemblies, while 0.4% enriched fuel was used for the Er_2O_3 flux shaping assemblies. The graphite pins were 0.42 cm in diameter with a cladding thickness of 0.0305 cm whereas the Er_2O_3 pins were 0.08 cm thick with 0.0305 of cladding. Pins of these diameters may be too thin to be feasible. Concentrating the materials in a few larger pins should not significantly affect the results. The configuration with the Er_2O_3 pins is identical to the configuration with graphite pins, save the aforementioned different enrichments and pin diameters. For these reasons, the Er_2O_3 configuration will not be shown.

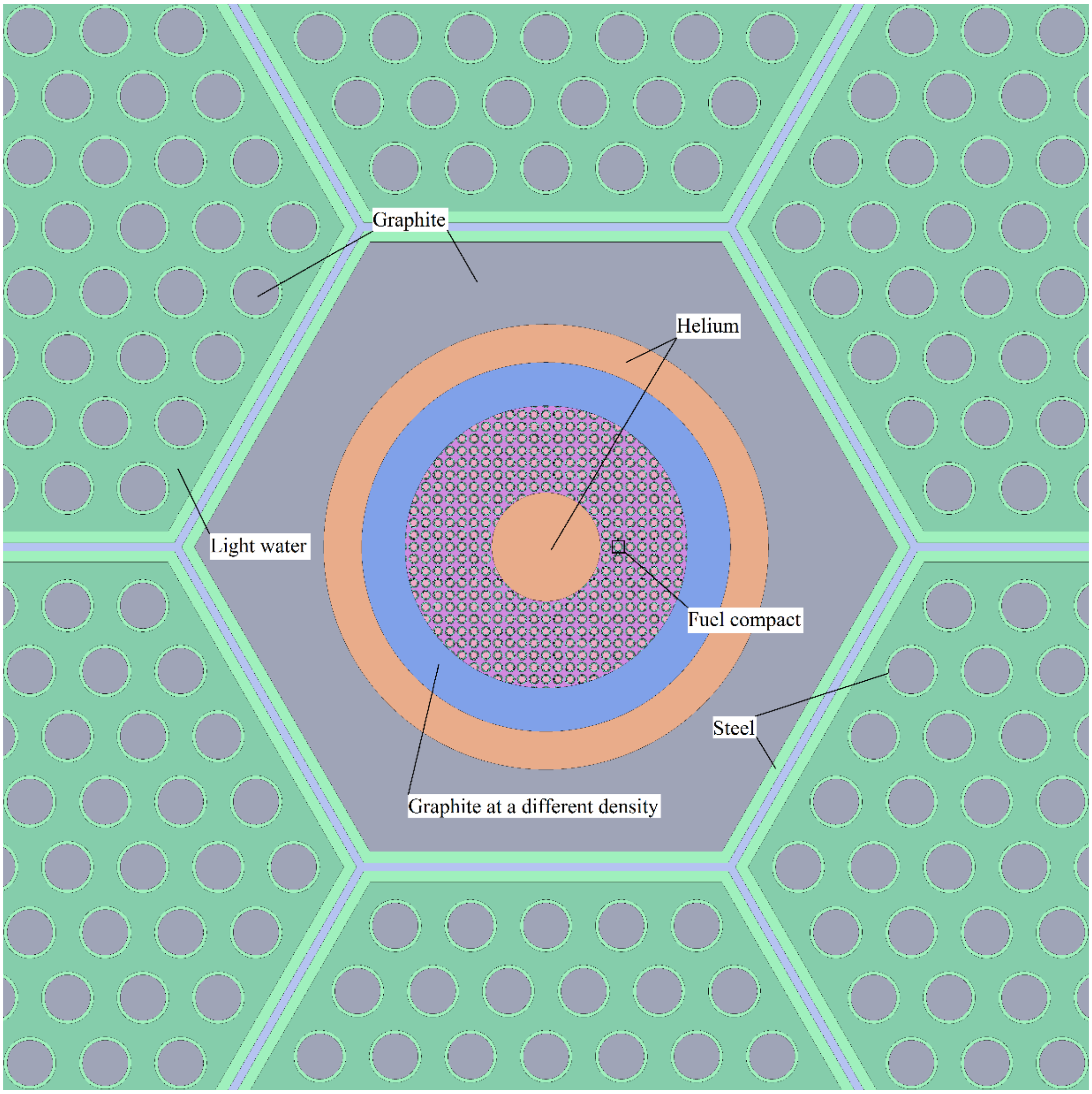

Figure 4.32 VHTR test assembly and flux shaping assembly

The graphite configuration inserted -0.572$ of reactivity, but the Er_2O_3 configuration inserted -0.996$ of reactivity. Light water is a less effective reflector than graphite, and causes a loss of reactivity. The Er_2O_3 configuration contains more light water than the graphite configuration and the absorber pins, which cause an even greater loss of reactivity. The insertion of absorber will reduce the total flux while also shaping it. However, the greater enrichment of the Er_2O_3 configuration results in a higher power density that the graphite configuration (33.4 W/cm^3 versus 26.7 W/cm^3). Power density was defined over the fuel compact only, not the whole test assembly. The flux spectrums for both configurations are shown in Fig. 4.33. The greater total flux for the graphite configuration is clearly visible. What is more difficult to see is the different flux fractions between the two configurations. The Er_2O_3 configuration had a greater portion of its flux in the fast region than the graphite configuration. The graphite pin and Er_2O_3 pins were sized such that the thermal flux was larger than the epithermal flux. Table 4.12 and Table 4.13 show the flux in each energy group for the two configurations.

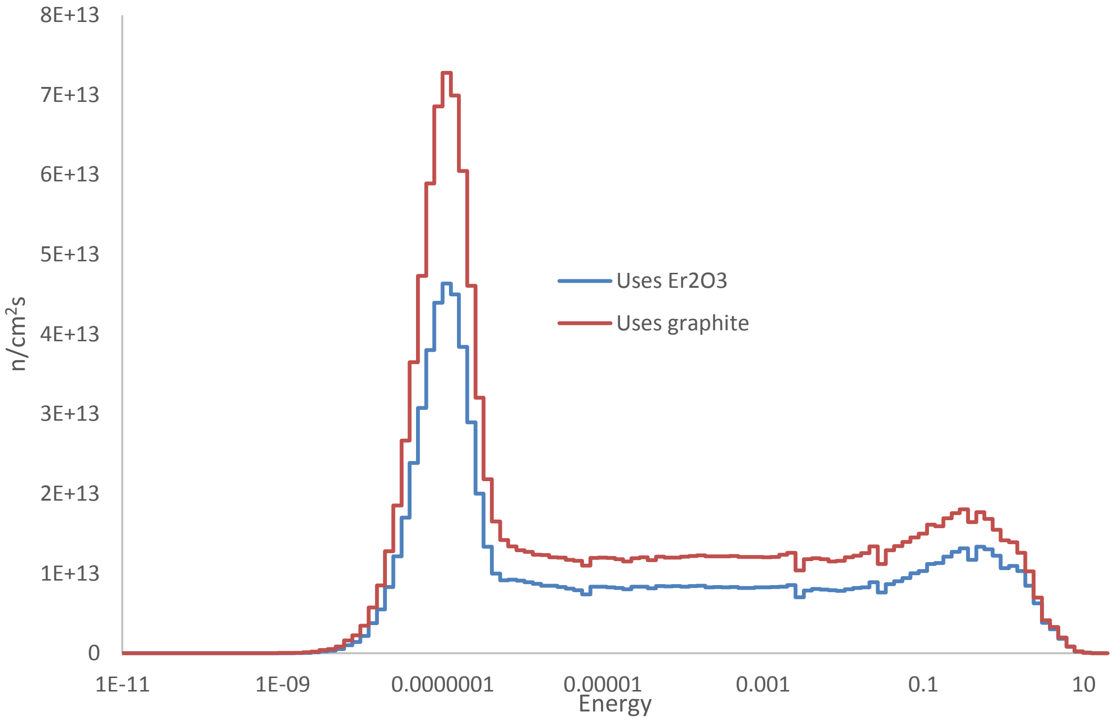

Figure 4.33 Flux of VHTR test assemblies with Er2O3 pin and graphite pins in light water flux shaping assemblies

Five columns and rows are shown in Table 4.12 and Table 4.13. The rows of data are for each energy group; E > 2.023 eV, 2.023 eV < E < 0.18 MeV, E > 0.18 MeV, and the total flux in descending order. The first column gives the absolute flux values presented in the INL report. The next column shows the proportion of each flux bin to the total flux. It is a flux fraction, because the bins sum to 1.0. The third and fourth columns are the absolute flux values and flux fractions for the test assembly. The last column gives the flux ratio, the test assembly flux divided by the INL report flux. This gives an idea of how quickly a material would experience neutron damage in this reactor. Higher values of neutron flux mean faster neutron induced damage. Ideally, the flux fractions for the test assembly and from the INL report would be the same, with the flux ratios for each bin being as large as possible and the same value. Naturally, this is not the case.

Table 4.12 Flux fractions and ratios for a VHTR test assembly near the core surrounded by graphite and light water flux shaping assemblies.

INL report	Fraction INL	Test assembly	Fraction Test	Flux ratio
7.817E+13	0.455536	6.87804E+14	0.467714	8.80
6.561E+13	0.382343	5.95877E+14	0.405202	9.08
2.782E+13	0.162121	1.86885E+14	0.127084	6.72
1.716E+14	1.0	1.47057E+15	1.0	8.57

Table 4.13 Flux fractions and ratios for a VHTR test assembly near the core surrounded by Er_2O_3 and light water flux shaping assemblies.

INL report	Fraction INL	Test assembly	Fraction Test	Flux ratio
7.817E+13	0.455536	4.43056E+14	0.445056	5.67
6.561E+13	0.382343	4.08181E+14	0.410023	6.22
2.782E+13	0.162121	1.4427E+14	0.144921	5.19
1.716E+14	1.0	9.95507E+14	1.0	5.80

Note that the fast flux in the graphite configuration is higher than in the Er_2O_3 configuration but the fast flux fraction is higher in the Er_2O_3 configuration. Increasing the size of the Er_2O_3 pins did indeed increase the fast flux fraction, but it decreased the thermal flux fraction. If the thermal flux fraction was deemed less important to materials irradiation than the epithermal and fast flux fractions, it should be possible to increase the enrichment and Er_2O_3 pin size to maintain the proportion of epithermal and fast fluxes. This would decrease the thermal flux fraction, but the flux ratio for the epithermal group and the fast group would be the same. Similarly, increasing the size of the graphite pins increased the epithermal flux fraction but did not significantly impact the fast flux fraction. The size of the pins dictates the relative proportions of the epithermal and thermal groups, while the enrichment dictates the size of the fast group. Similarly, proximity to the core also affects the fast flux. Inserting flux shaping assemblies filled with graphite may result in a flux spectrum more closely resembling a PWR when the test assembly is placed near the core.

Shaping the neutron spectra for the VHTR test assembly far from the core follows the same philosophy as in the PWR test assembly far from the core. Light water will be used to create a high thermal flux, while the presence of absorber will reduce the thermal and epithermal components of the flux. The thermal flux fraction for the VHTR is greater than that for the PWR, so less absorber is used to depress the flux. Two different absorbers are used in this simulation. Depleted uranium proved ineffective to shape the PWR flux, but it proved very effective here. Er_2O_3 was also used as with the PWR test assembly. The locations for the VHTR test assembly and absorbing assemblies are the same as those used for the PWR test assembly. Therefore, the VHTR test assemblies far from the core will not be shown. The size of the pins used for the two absorbers as well as the enrichments were optimized along different lines. The depleted uranium configuration was optimized such that the flux ratios of the thermal and epithermal fluxes were kept as similar as possible without regards to the fast flux. The Er_2O_3 configuration was optimized such that the fast flux fraction was made to be greater than the VHTR fast fraction. 0.8% enriched fuel was used in the depleted uranium configuration, while 6.0% enriched fuel was used in the Er_2O_3 configuration. The depleted uranium configuration has a power density of 29.7 W/cm^3 while the Er_2O_3 configuration had a power density of 32.5 W/cm^3. The depleted uranium pins were 0.42 cm in diameter while the Er_2O_3 pins were 0.3 cm in diameter. Both had a cladding thickness of 0.0305 cm. Table 4.14 and Table 4.15 shows the 3 group data for the depleted uranium configuration and Er_2O_3 configuration, respectively.

Table 4.14 Fluxes and flux ratios for a VHTR test assembly far from the driver surrounded by light water and depleted uranium filled flux shaping assemblies

INL report	Fraction INL	Test assembly	Fraction Test	Flux ratio
7.817E+13	0.455536	2.30679E+14	0.457137	2.95
6.561E+13	0.382343	2.04018E+14	0.404303	3.11
2.782E+13	0.162121	6.99198E+13	0.13856	2.51
1.716E+14	1.0	5.04617E+14	1.0	2.94

Table 4.15 Fluxes and flux ratios for a VHTR test assembly far from the driver surrounded by Er_2O_3 and light water filled flux shaping assemblies.

INL report	Fraction INL	Test assembly	Fraction Test	Flux ratio
7.817E+13	0.455536	3.53179E+13	0.176036	0.45
6.561E+13	0.382343	1.31044E+14	0.653167	2.00
2.782E+13	0.162121	3.42668E+13	0.170797	1.23
1.716E+14	1.0	2.00629E+14	1.0	1.17

The depleted uranium case, although optimized for the epithermal and thermal flux ratios only, provided a reasonably high fast flux fraction. This promising sign should be weighed against the potential costs associated with depleted uranium, as outlined previously. While the Er_2O_3 configuration does exhibit the appropriate fast flux fraction, this is only made possible by skewing the spectrum to epithermal energies. Depending on the specific requirements of the irradiation test, this may be unfavorable. This spectrum more closely resembles the PWR spectra outlined previously, suggesting that more Er_2O_3 would bring the spectra closer to a prototypic PWR spectra.

The results outlined here do not exactly match the neutron spectra associated with a PWR and the VHTR. However the results presented here show that, with further revisions, it should be possible to more closely mimic neutron spectra in this reactor. Light water and graphite are both useful moderators, but the full range of absorbers has not be examined yet. Similarly, the full range of configurations for flux shaping assemblies has yet to be explored. The next sections, which will explore the static irradiation capsules and the general behavior of the moderating region, will present more suggestions for flux spectrum shaping.

4.5 Passive irradiation capsules

The scheme for analyzing the static irradiation capsules was simpler than the scheme for analyzing the test assemblies. No fissile material was used so it was unnecessary to increase the fast flux by depressing the thermal and epithermal fluxes by means of absorbers. Only moderators, graphite and light water, were used to shape the flux profile. For this reason, the irradiation positions had to be as close to the driver as possible. Forming an irradiation assembly out of an entire moderating assembly would maximize the volume for irradiation. Rather, it was decided to make the irradiation capsule smaller than the moderating assembly so that flux shaping material can be placed within the assembly. This would keep available as many irradiation positions as possible; otherwise, flux shaping would have to be provided by assemblies around the irradiation assembly, taking up positions. The capsule was restricted to a cylindrical object 2 cm in diameter. This was surrounded by a 0.5 cm thick layer of sodium coolant. A steel wall 0.1 cm thick separated the sodium from the moderator. Both the position of the test capsule within the assembly and the moderator were varied. This was performed with respect to the PWR; the high epithermal flux in the region could not be sufficiently moderated with light water to match a VHTR spectra. This effect will be shown first.

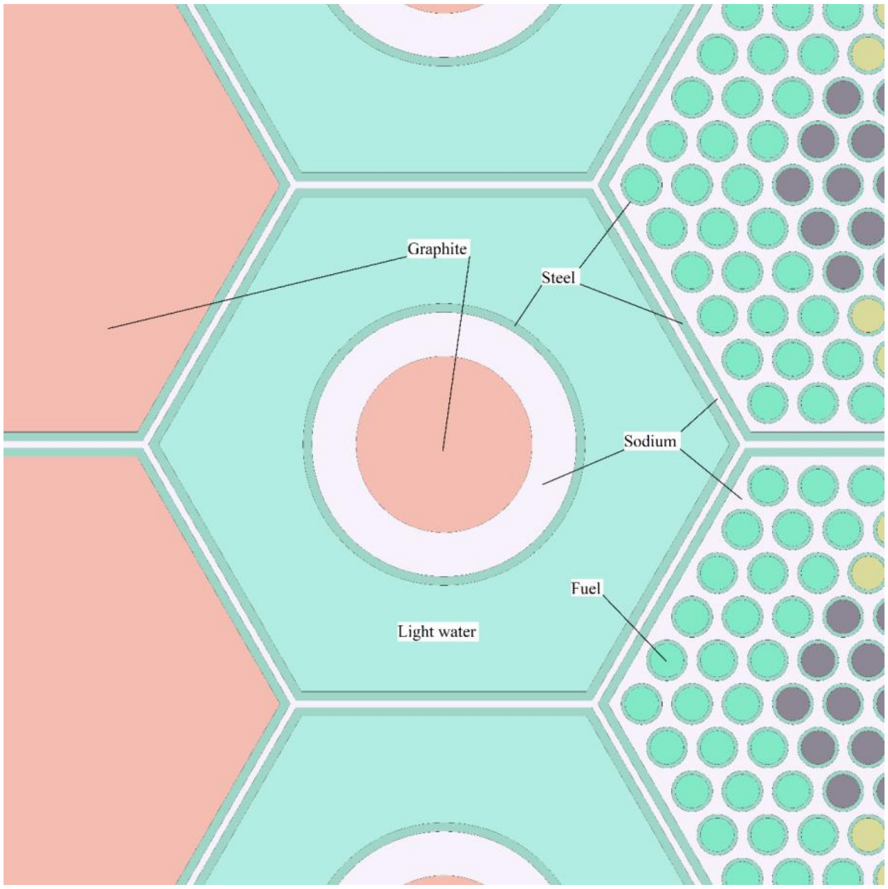

Figure 4.34 Graphite capsule in light water filled irradiation assembly

Mimicking the VHTR spectra was done by filling the entire region with light water. It was also decided that the VHTR irradiation material should be graphite; the PWR irradiation material was steel. This configuration was placed in the center of the assembly. Fig. 4.34 shows the VHTR irradiation configuration. Table 4.16 shows the flux data for the capsule. The first row tallies data for E < 2.023 eV, the second row from 2.023 eV to 0.18 MeV, and the third row tallies data for E > 0.18 MeV. The last row is total flux data. Flux is heavily skewed towards the fast flux, which has the greatest flux ratio. The epithermal flux was the greatest component of flux, resulting from incomplete thermalization of fast neutrons from the driver. Still, as will be shown in later analysis, this configuration represents the highest thermal flux fraction available. Fast neutron damage is accelerated by a factor of 29, far in excess of what a test assembly can provide. As fission power density is not a concern, materials can be degraded very quickly in this configuration. Flux is shown in Fig 4.35. The 120 group flux profile and the 4 group fluxes were tallied over different volumes. The 120 group flux profile was tallied over the irradiated graphite from -30 cm < z < 30 cm while the 4 group fluxes were tallied from -10 cm < z < 10 cm. The shorter flux bins for the 4 group flux represent the peak flux over that region. The longer flux bins represent the average flux over that region. In addition, the 120 group tallies would take longer to reach acceptable statistical errors, so they were tallied over more volume. The bottom and top 20 cm are affected by the MgO reflector above and below the core so they were not tallied.

Table 4.16 Fluxes, fractions, and ratios for a graphite capsule in the center of a light water filled assembly.

INL report	Fraction INL	Passive cap.	Fraction Pass.	Flux ratio
7.817E+13	0.455536	1.017E+15	0.307110	13.01
6.561E+13	0.382343	1.492E+15	0.450445	22.74
2.782E+13	0.162121	8.030E+14	0.242445	28.87
1.716E+14	1.0	3.312E+15	1.0	19.30

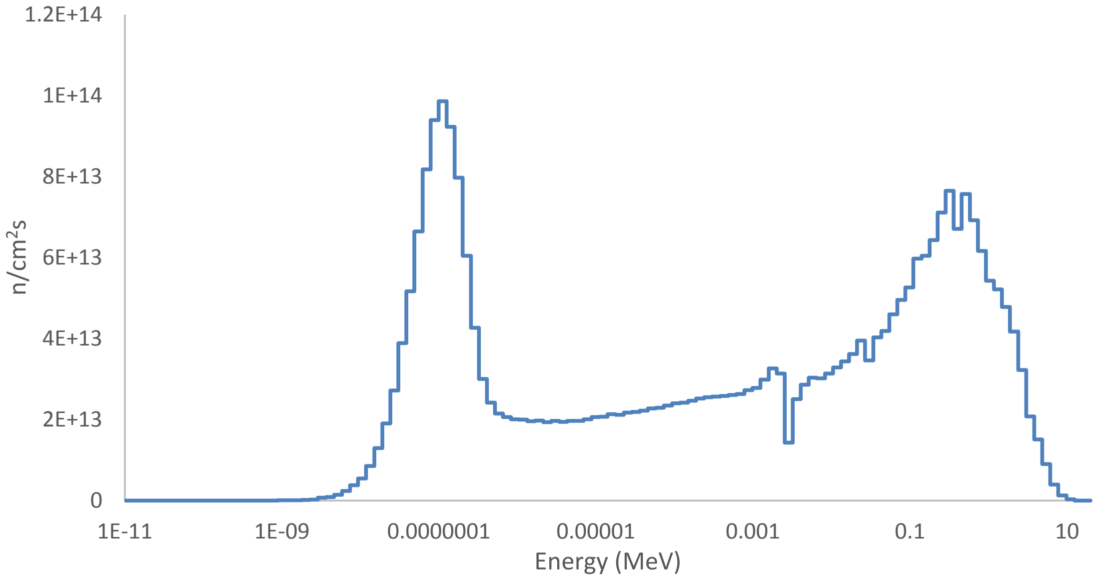

Figure 4.35 Flux in graphite capsule in light water filled irradiation assembly

Analysis of the PWR passive capsule is focused on how flux responds to different geometries and material compositions. Two analyses are performed. The first varies the location within the assembly of the irradiation capsule while the second varies the amount of light water and graphite within an assembly. In the first analysis, the assembly is filled with light water and the capsule is moved towards the driver. Flux was tallied at five locations; with the capsule centered at -1.2 cm, 0.6 cm, 0.0 cm, 0.6 cm, and 1.2 cm. -1.2 cm is to the furthest left; the capsule is close to the graphite assemblies that constitute the moderating region. 1.2 cm is to the furthest right; the capsule is close to the driver region. Fig 4.36 shows the assembly with the capsule at -1.2 cm and Fig 4.37 shows the assembly with the capsule at 1.2 cm. The material being irradiated is steel but it was modeled as a separate material in case it was desired to modify the material. It appears as a different color on the plot as the rest of the steel. Nine such capsules were inserted into the reactor and their results were averaged together. This reduces computational time but means that the flux data does not represent the peak flux for the capsule at the core center line.

Fig. 4.38 shows the 4 group fluxes and the total flux for all the irradiation positions. Each point represents the absolute value of flux for that energy group with the capsule centered at that position. The data is plotted on a line graph so that trends can be more easily identified. The fluxes varies as is to be expected. Thermal flux and epithermal flux are greatest towards the graphite moderator, while the fast fluxes are greatest towards the driver. One of the more unexpected features is the general flatness of all the curves. Fast flux from 0.1 MeV to 1.0 MeV dropped by 68% while fast flux greater than 1 MeV dropped by 78% moving from right to left. The total displacement was 2.4 cm, about an inch. Thermal flux and epithermal flux dropped 73% and 86%, respectively, going from left to right.

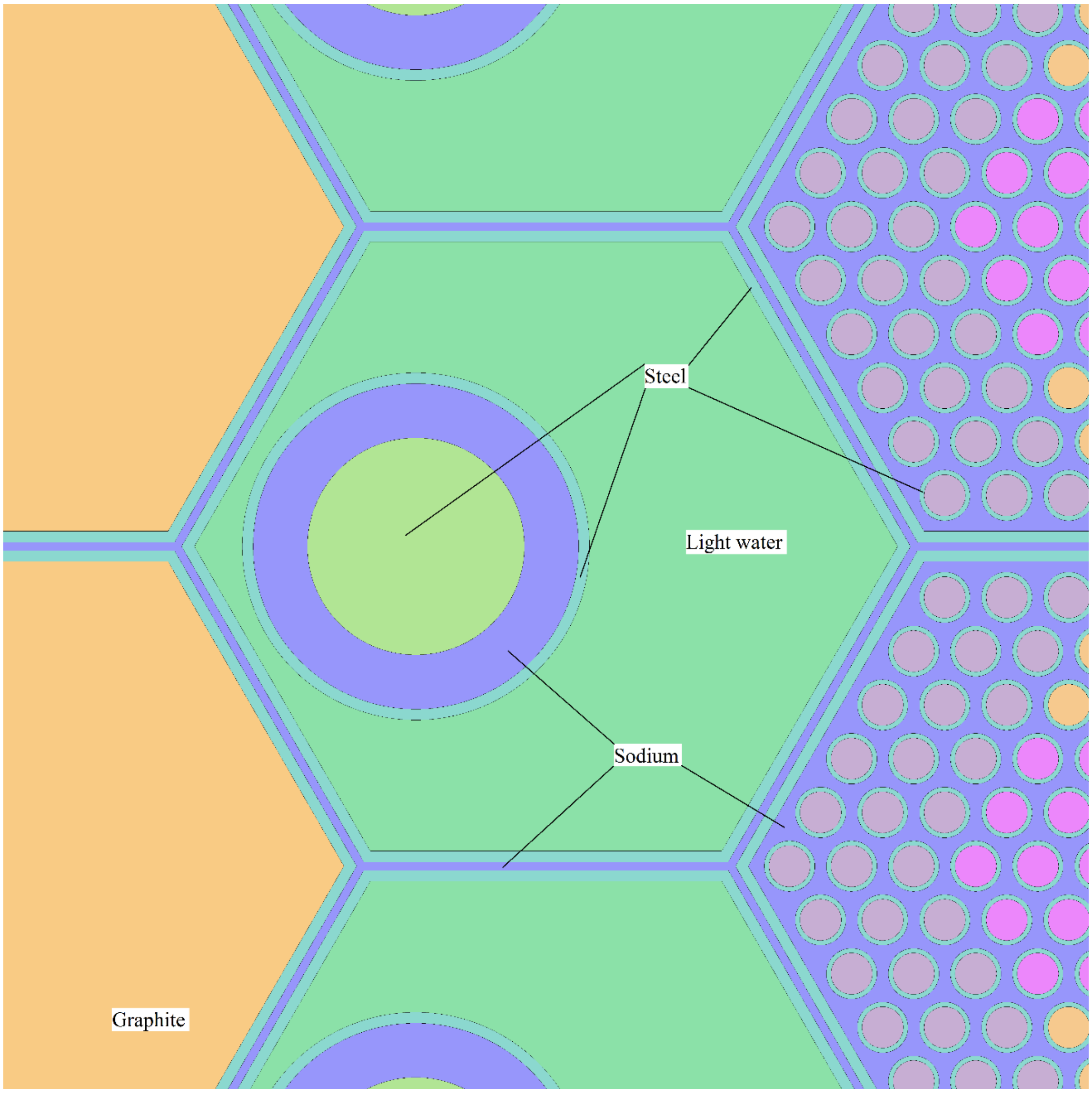

Figure 4.36 Steel capsule in light water filled irradiation position. The steel is shifted 1.2 cm to the left, or away from the driver. As the local origin of the assemblies is the center of each assembly, the steel is centered at (-1.2 cm, 0.0 cm, 0.0 cm).

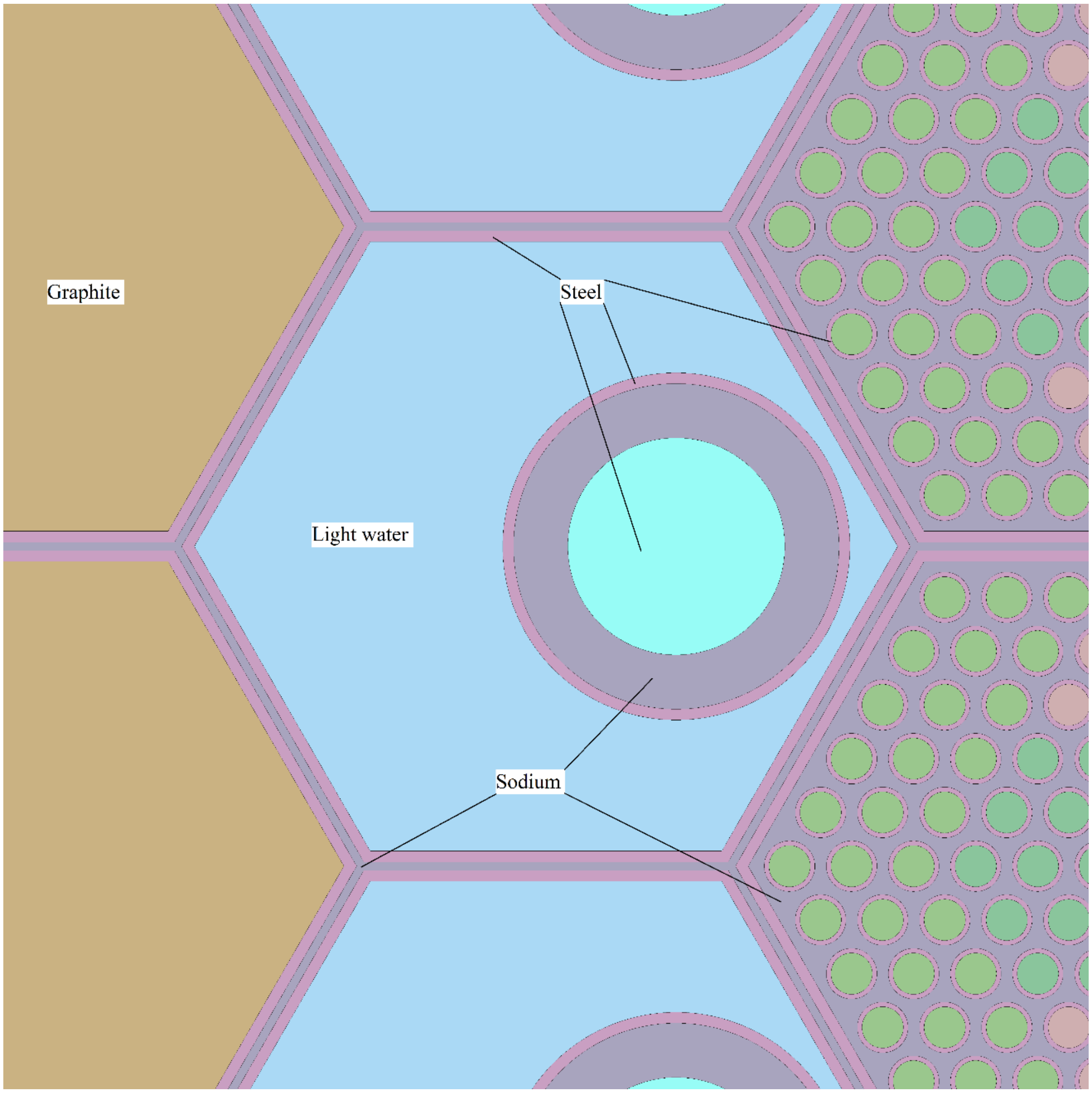

Figure 4.37 Steel capsule centered at 1.2 cm in a light water filled irradiation assembly.

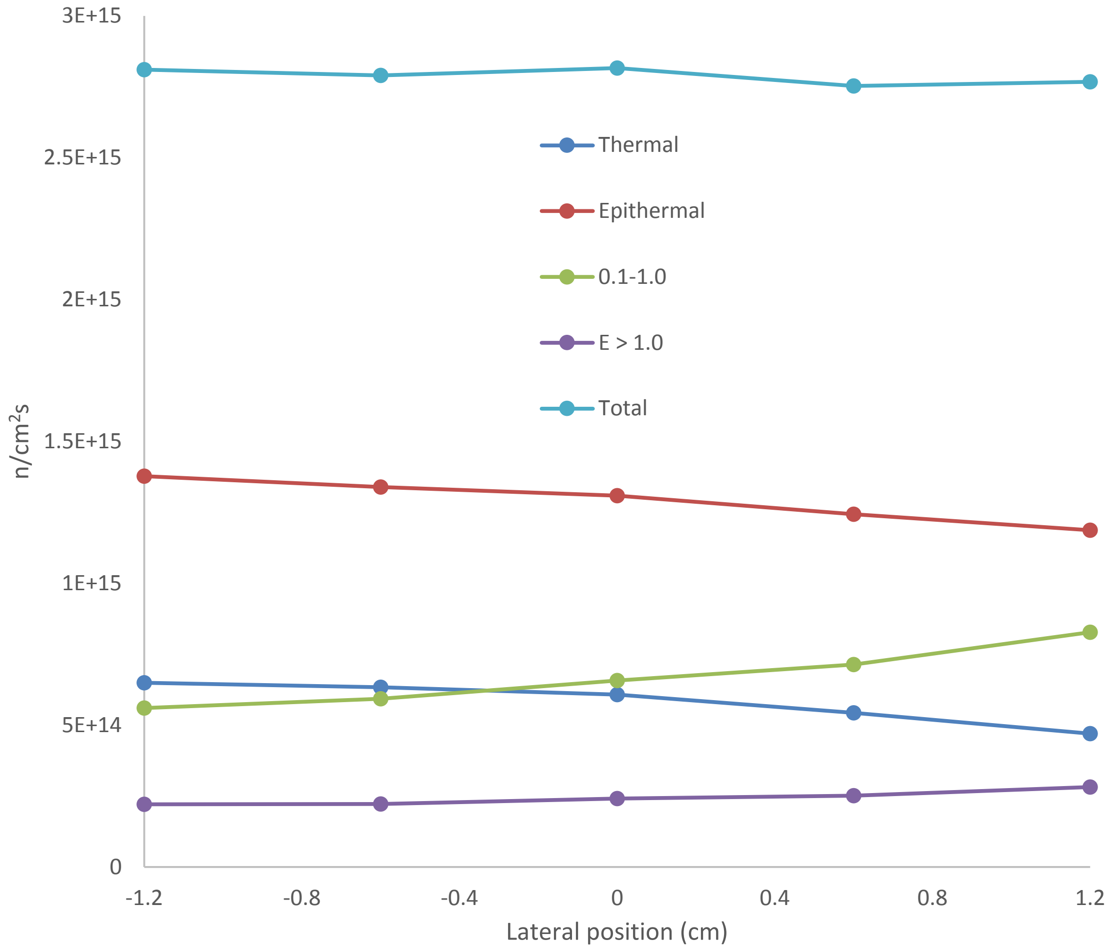

Figure 4.38 Flux in each group for the steel capsule at different positions in a light water filled irradiation assembly.

Fast flux in the assembly was moderated by the light water while also being absorbed. This helped offset the loss of thermal and epithermal neutrons absorbed in the capsule. Placing the capsule near the core introduces -0.9$ of reactivity whereas placing the capsule towards the moderator introduces -0.7$ of reactivity. This was calculated with 9 capsules; the effect of one capsule will be less. Table 4.17 gives flux data for the capsule centered at 1.2 cm. This represents the region of greatest fast flux. Five rows are present. In descending order they present data for the 4 group bin structure, while the last is total flux. It should be noted that the thermal flux fraction was in excess of that for a prototypic PWR in all the capsule locations. The position nearest the driver minimized the thermal flux and maximized the fast fluxes. Absorbers can be used to change the thermal flux fraction, but graphite can also be used to control the thermal and epithermal flux fractions as done in previous sections. In the next portion of this section, graphite is used to increase the fast flux and reduce the thermal flux while also reducing the negative reactivity of the capsule assembly. Fig 4.39 shows the relative flux spectra of the single pin and the capsule at 1.2 cm with only light water moderation.

Table 4.17 Steel capsule in light water filled assembly at position 1.2 cm.

Single pin	Fraction Single	Passive cap.	Fraction Pass.	Flux ratio
3.2727E+13	0.108916	4.70917E+14	0.17015565	14.39
1.2353E+14	0.411102	1.18686E+15	0.42884614	9.61
7.7363E+13	0.257469	8.27468E+14	0.29898763	10.70
6.6860E+13	0.222513	2.82321E+14	0.10201058	4.22
3.0048E+14	1.0	2.76757E+15	1	9.21

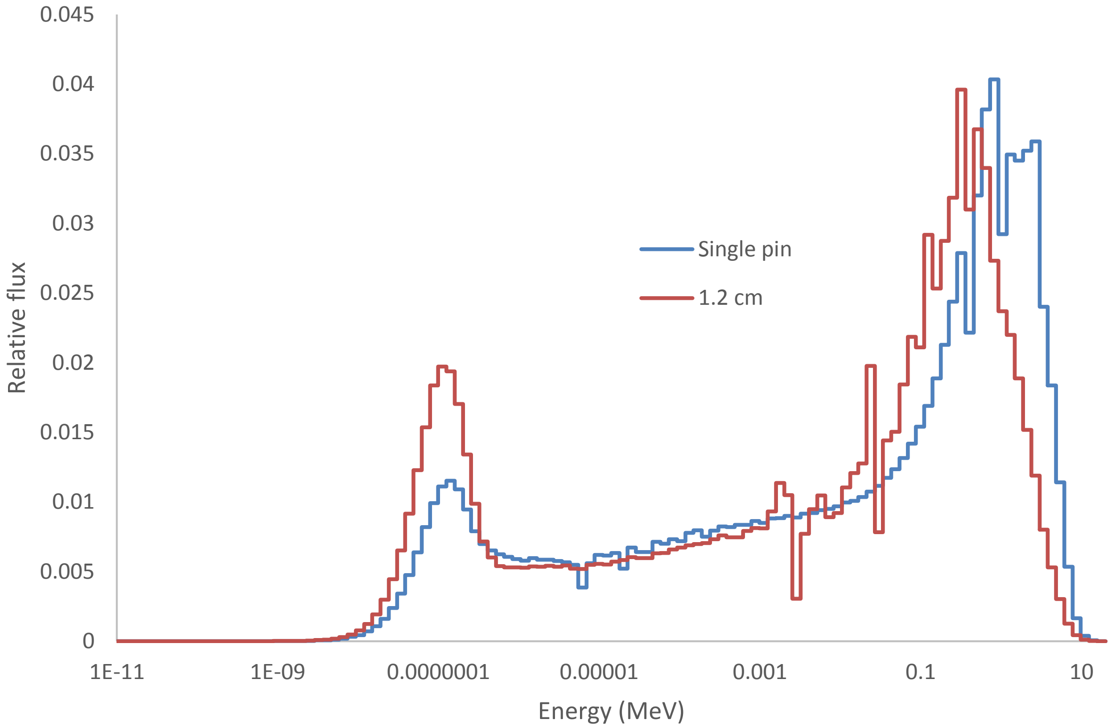

Figure 4.39 Relative flux for a steel capsule centered at 1.2 cm and a prototypic PWR.

Thermal flux in the capsules is clearly too large, while the epithermal flux is the right proportion. Fast flux of E > 0.1 MeV is too small, while the fast flux from 0.1 MeV to 1 MeV is too large. This fact is common to all the static capsules, where the only fast neutrons stream for the core. In the driver, ~80% of the fast flux is between the energies 0.1 MeV and 1 MeV, while in the PWR, ~50% of the fast flux is between the energies 0.1 MeV and 1 MeV. The reason for this is quite simple. In an elastic scatter with hydrogen, a neutron will lose half of its energy on average. This is enough to remove a neutron from the fast groups to the slow groups. However, in a fast reactor, low Z materials are not present. It takes more scatters to reduce the neutron's energy to epithermal energies in the fast reactor than in the PWR. Therefore, neutrons lose energy far slower in a fast reactor. Consider that 70% of neutrons are born with an energy above 1 MeV. These neutrons are at a higher energy and have a correspondingly higher velocity which translates to a higher flux, so that actual fission flux above 1.0 MeV is closer to 84% of the total fission spectrum flux. The fast portion of the driver fuel is skewed towards lower energies due to scattering, as mentioned previously. This skewing towards lower energies also happens in a PWR, but because the loss in energy per scatter is higher, neutrons leave the fast group quicker. This fact means that the fast flux in the static capsule will always be skewed towards lower energies when compared to the PWR. This effect can be reduced but not eliminated with more moderator, which reduces the absolute magnitudes of both fast fluxes but brings the flux fractions nearer to the PWR spectrum. An absorber with a large resonance around 0.5 MeV would also reduce flux in that bin, but this absorber could not have any significant absorption cross section at any other energies. Such an absorber would be difficult to find.

It was noted previously that to some degree the fast flux fractions can be controlled by moderator fractions and that the thermal flux inside the capsule was too high. The light water filled capsules also induced a little less than one dollar of negative reactivity. Graphite has a higher moderating ratio than water, but a smaller moderating power. Moderating power is the average logarithmic energy decrement times the elastic scattering cross section, and represents the total path length of a neutron to thermalize in a material. Moderating ratio is the moderating power divided by the absorption cross section, and considers both how far a neutron must travel to thermalize and the likelihood of it being absorbed (Rinard Neutron). The difference in moderating power between graphite and light water suggests that an assembly filled with some mixture of these materials would have thermal and epithermal flux fractions appropriate to a PWR and that the reactivity penalty associated with the assembly would be lessened. Placing the capsule near to the driver provided the highest fast flux, so in this analysis the capsule will be fixed at 1.2 cm. The first simulation performed was with only graphite in the assembly.

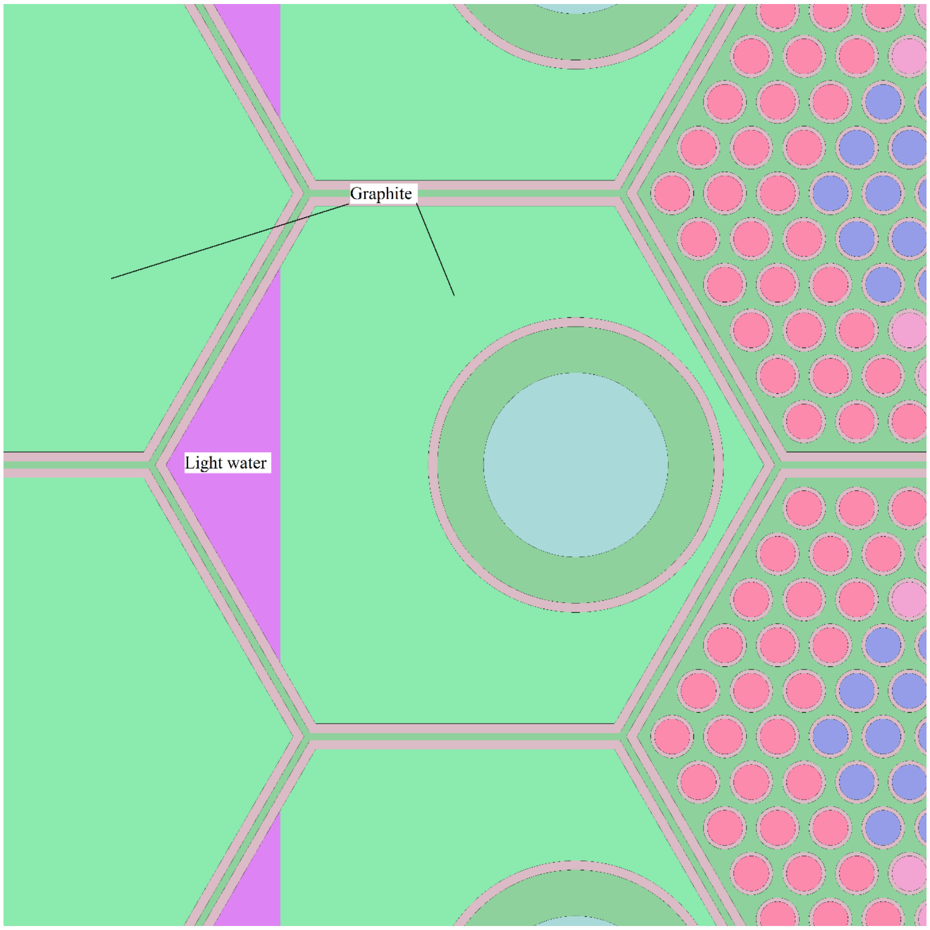

Figure 4.40 A steel capsule centered at 1.2 cm with a dividing line between light water and graphite at -2.0 cm

The second simulation was with graphite filling the assembly towards the core and light water filling the assembly towards the moderating region. The dividing line between the two moderators is at x=-3.0 cm. The next simulations places this line at -2.0, -1.0, 0.0, 1.0, 2.0, and 3.0 cm. Fig 4.40 and Fig 4.41 show the test assembly with the dividing line at -2.0 cm and 2.0 cm, respectively.

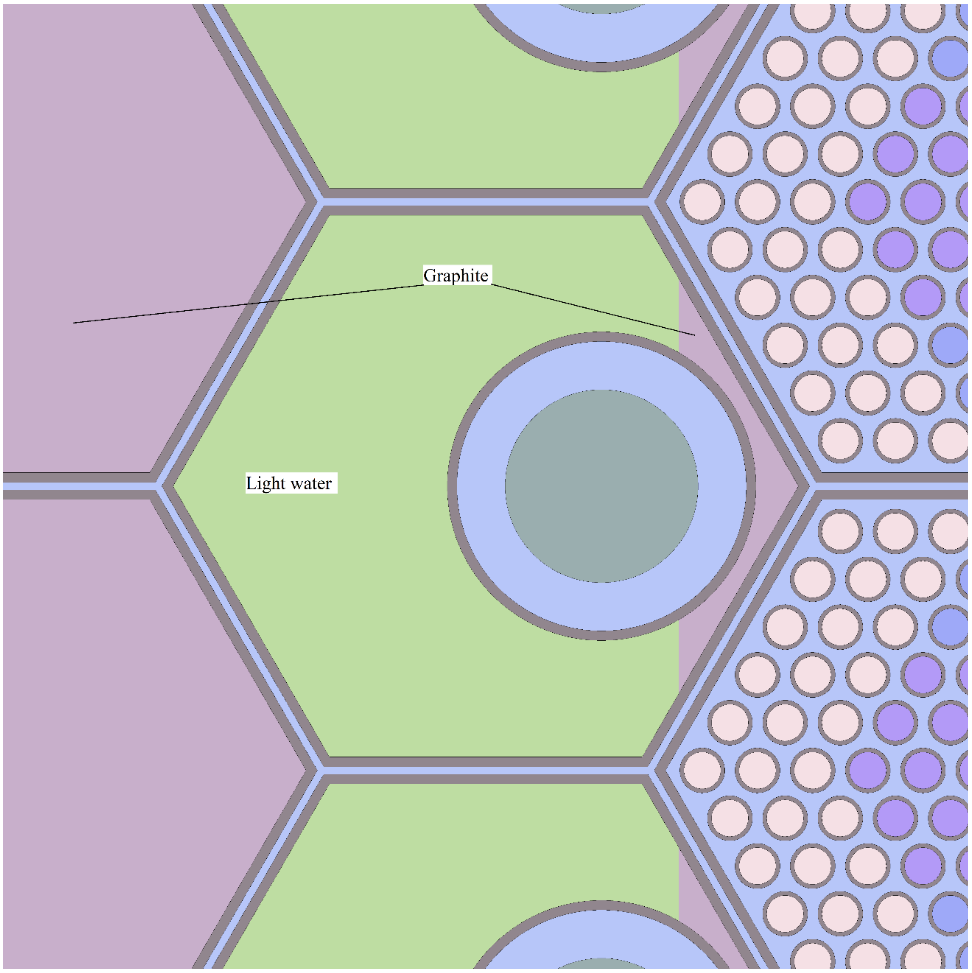

Figure 4.41 A steel capsule centered at 2.0 cm with the dividing line between light water and graphite at 2.0 cm.

Flux is presented in Fig 4.42. The locations listed on the horizontal axis do not represent the location of the capsule, but the location of the dividing line between the light water and the graphite. Light water is to the left of the line, graphite to the right. This information is presented as a line graph so that trends can be more easily identified.

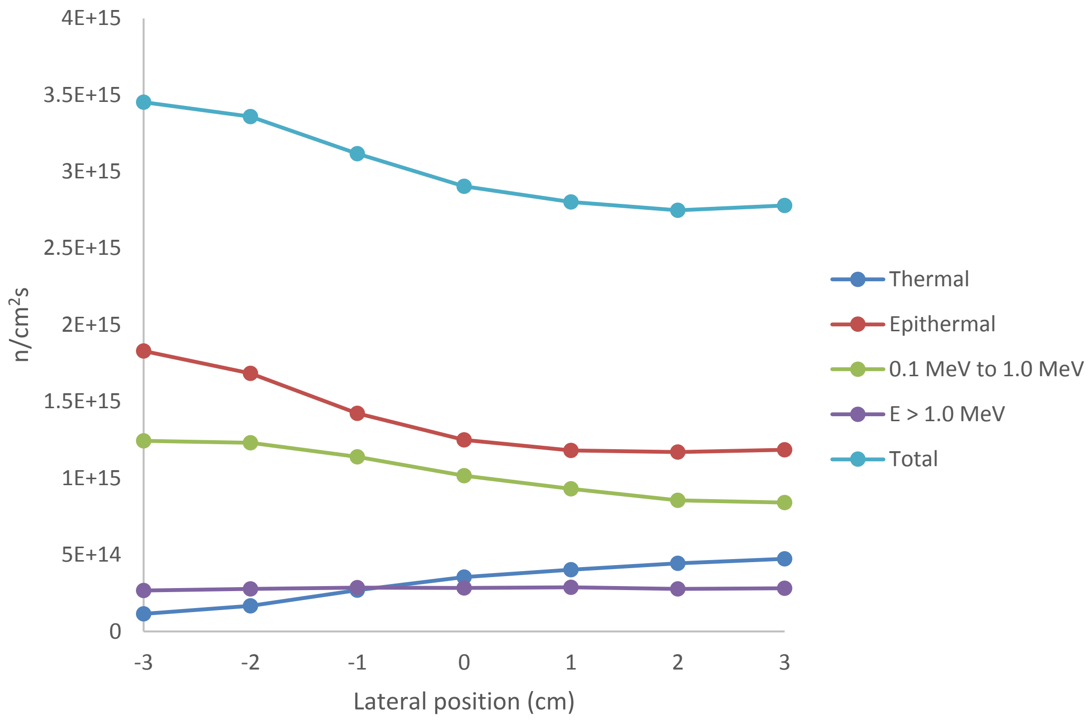

Figure 4.42 4 group fluxes and total fluxes for a steel capsule centered at 1.2 cm with different locations at the dividing line between light water and graphite

All the fluxes changed with different moderator configurations except for the fast flux above 1.0 MeV. Light water is an effective moderator, so the addition of light water reduces the epithermal flux in the capsule and increases the thermal flux. However, most interestingly, the fast flux between 0.1 MeV and 1 MeV decreased with more light water. Additionally, the flux changed with light water behind capsule, between the capsule and the moderating region. There are two possible explanations for this effect. The first is that fast neutrons from the driver travel into the moderating region. Some are reflected back towards the driver. The majority of these neutrons are in the epithermal region, but some have not lost as much energy and are still above 0.1 MeV. Light water would moderate these neutrons and make them epithermal. This effect may not be prevalent, as the epithermal flux in the region still increases despite these fast neutrons scattering into this energy range. Secondly, fast neutrons coming from the reactor may be backscattering off the graphite surrounding the capsule. As light water replaces graphite, backscatter becomes less likely due to hydrogen being as massive as a neutron and because scattering with hydrogen would probably cause a fast neutron to lose too much energy and fall into the epithermal range. Regardless of why this phenomenon occurs, fast flux from 0.1 MeV to 1.0 MeV is maximized when light water is minimized. When the plane dividing the light water and graphite was set at 0.0 cm, the thermal and epithermal flux fractions were the same proportion as in the prototypic PWR spectrum. This manifests as nearly identical flux ratios for the two groups. Table 4.18 shows 4 group data without any light water and Table 4.19 shows 4 group data with the plane separating the moderators at 0.0 cm. The flux spectrum for the test assembly with the dividing line between the graphite and light water at -3.0 cm and without any light water were virtually identical.

Table 4.18 Steel capsule in graphite filled assembly position centered 1.2 cm towards the driver.

Single pin	Fraction Single	Passive cap.	Fraction Pass.	Flux ratio
3.2727E+13	0.108916	1.08033E+14	0.031408	3.30
1.2353E+14	0.411102	1.83012E+15	0.532065	14.82
7.7363E+13	0.257469	1.23333E+15	0.358562	15.94
6.6860E+13	0.222513	2.68170E+14	0.077964	4.01
3.0048E+14	1.0	3.43965E+15	1.0	11.45

Table 4.19 Steel capsule centered 1.2 cm towards the driver with dividing line between light water and graphite at 0.0 cm.

Single pin	Fraction Single	Passive cap.	Fraction Pass.	Flux ratio
3.2727E+13	0.108916	3.54984E+14	0.122233	10.85
1.2353E+14	0.411102	1.24977E+15	0.430338	10.12
7.7363E+13	0.257469	1.01594E+15	0.349822	13.13
6.6860E+13	0.222513	2.83465E+14	0.097607	4.24
3.0048E+14	1.0	2.90416E+15	1.0	9.67

The thermal and epithermal flux fractions are a little bit higher than the prototypic PWR due to the reduced fast flux. The relative neutron spectrum for the simulation without any light water and the relative spectrum for the single pin are shown in Fig. 4.43. The relative neutrons spectra with the dividing line at 0.0 cm and that for the single pin are shown in Fig. 4.44. Fig 4.44 is the closest of all the plots given so far to the prototypic PWR spectrum, but it still differs from the benchmark with respect to the fast flux. The fast flux is skewed to lower energies, which also manipulates the epithermal flux. The low energy section of the epithermal flux is depressed, while the high energy portion of the epithermal flux is enhanced, a side effect of the skewing of fast flux.

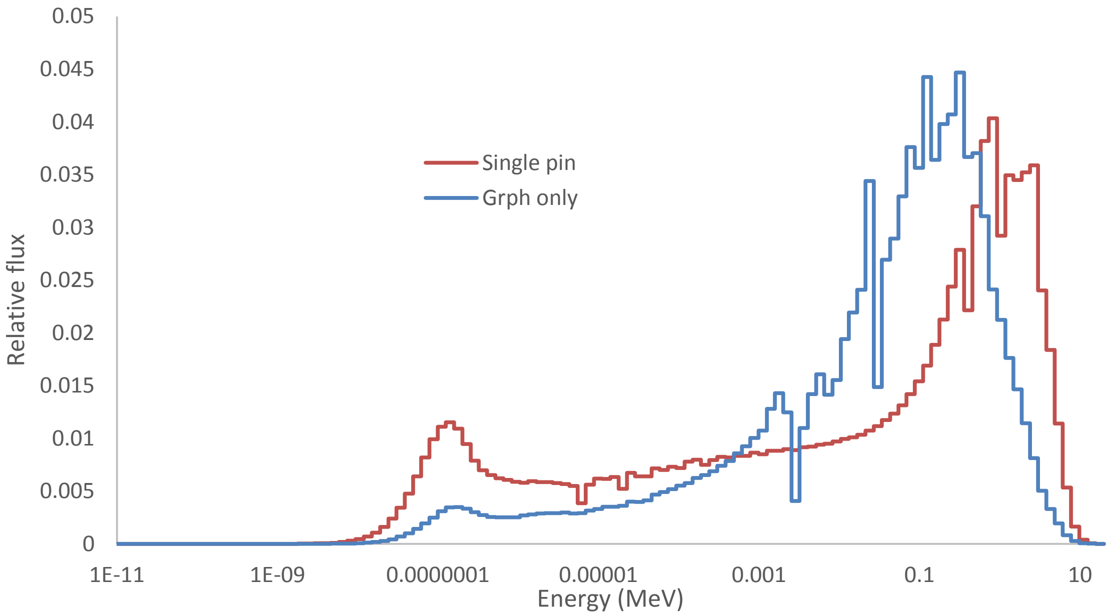

Figure 4.43 Relative flux of steel capsule centered at 1.2 cm surrounded by graphite in an irradiation assembly next to the driver and a prototypic PWR pin.

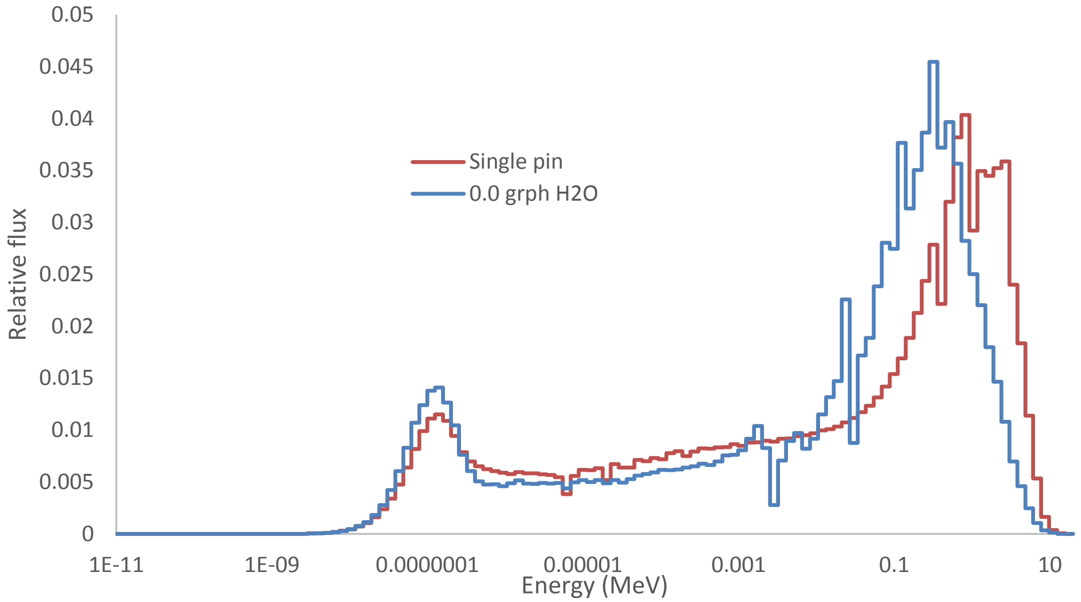

Figure 4.44 Relative flux of steel capsule centered at 1.2 cm surrounded by graphite in an irradiation assembly next to the driver with the dividing line between light water and graphite at 0.0 cm and a prototypic PWR pin.

5. CONTROL SYSTEMS

There were three main considerations when designing the control systems. Firstly, the operation of the control systems must affect flux within irradiation locations as little as possible. Secondly, the addition of the control systems to the base geometry must not reduce the fissile mass nor k_{eff} of the system when the control system is in its least reactive configuration. Lastly, the k_{eff} of the system with the control systems at maximum negative reactivity insertion must be less than 0.95. The last consideration is at odds with the first two considerations, but three different systems proposed in this section satisfy all three considerations to varying degrees of success. It will be shown that the best option of control systems for the core with a uniform enrichment of 19.9% is two sets of control rod banks, one inside the core and the other in the reflector. The set inside the core is halfway between the central irradiation position and the outer moderator, while the other set is on the interior of the outer reflector. The set inside the core is the shim rods, and are the primary way reactivity will be controlled thought-out the core lifetime. The set in the reflector are the shutdown banks, and provide enough negative reactivity to bring the core to a k_{eff} of 0.95. Control systems within the core have a deleterious effect on the fissile mass, initial k_{eff}, and core lifetime, so the number of control rods inside the core is minimized and the additional negative reactivity needed for shutdown is provided by the set outside the core. The reflector itself also contains irradiation assemblies, so the number of control rods in the reflector is balanced against the number of control rods inside the core.

Control rods banks used here were implemented by removing some of the fuel pins and replacing them with controls rods. The control rods are not followed by fuel, so the addition of the control rod banks decreases the fissile mass of the core, reducing k_{eff} and increasing flux. Withdrawal of the control rods decreases the flux magnitude within the central irradiation position and perturbs the axial flux profile. The second choice of control system uses rotating control drums to insert negative reactivity, does not decrease the fissile mass, and does not perturb the axial flux profile. Control drums take a great deal of space within the outer reflector, and change flux within the reflector. Unfortunately, the control drum systems cannot insert enough negative reactivity with a uniform fuel loading of 19.9% enriched, so some combination of control drums and control rods would have to be used. However, systems with lower enriched fuel that have lower initial k_{eff}'s and shorter core lifetimes would need fewer control rods if they used control drums as well. For systems with initial reactivity's less than approximately 4.00$ and where materials irradiation within the reflector is less important than within the core, control drums are recommended. Shutdown control rod banks would also be used. Control rods are recommended if the flux perturbations within the central irradiation position caused by the shim rods are not deemed significant. If these perturbations are deemed significant, then drums are recommended and the initial k_{eff} of the system (controlled by zoning the core) should be reduced.

5.1 Control rods

Calculations for the control rods were done with the inner four rings of fuel assemblies at 19.9% enriched and the rest of the core at 16% enriched, not with a uniform enrichment of 19.9%. Fuel volume was increased by 10%, so fuel rod diameter was 0.3996 cm. The total worth of the control rods will vary with the core loading, number of control rods, and location of the rods within the core.

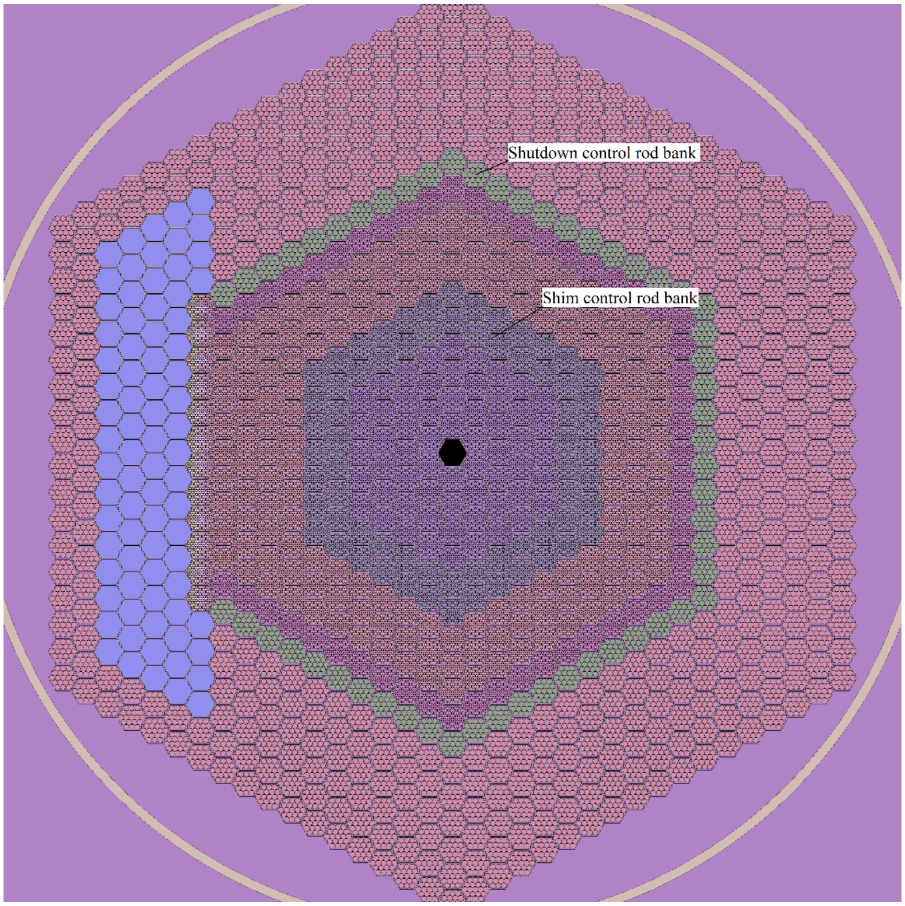

Figure 5.1 Locations of the control rod banks within the core and reflector

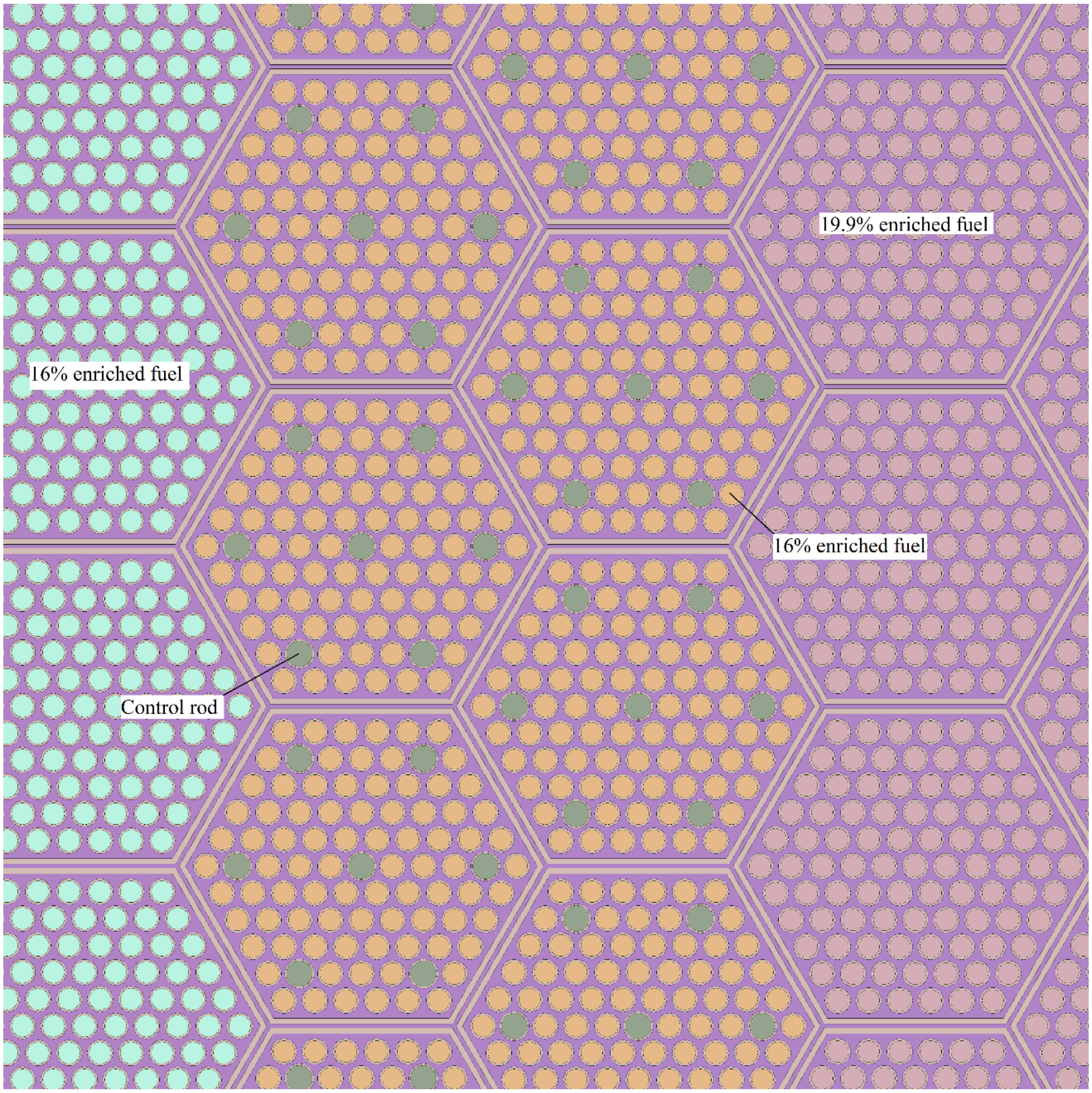

Figure 5.2 Control rods within the core

However, the differential rod worth should only depend on the design of the control rods, core dimensions, and the neutron spectra that it experiences. Different absorbers and absorber following materials were used, but B_4C followed by MgO was ultimately chosen. Natural boron was used. The control rods were 0.541 cm in diameter with 0.0305 thick steel cladding. There was no gas gap to accommodate the production of helium within the rods. The rods were 360 cm tall, the bottom 180 cm with MgO and the top 180 cm with B_4C. Fig 5.1 shows the locations of both control rod banks and Fig 5.2 shows the locations and relative sizes of the control rods within the core.

The fuel colors of Fig 5.1 and Fig 5.2 do not match. This is because the figures were taken at different elevations, and the core was zoned in the same manner outlined in previous sections. Only seven pins are present in each assembly and they are widely spaced. Such few pins per assembly means that the worth of each assembly is below 1.00$ of reactivity, meaning that a rod ejection accident involving a few assemblies would not insert more than 1.00$ of reactivity. Additionally, concentrating all the control rods together would depress flux within the fuel rods near the control rods more than spreading the control rods throughout the assemblies. Thus, spreading the control rods around decreases power peaking within the assemblies and assures a more even burnup behavior. The shutdown rods in then outer reflector are larger, and are intended to replace the standard MgO reflecting pins. These are not modeled with explicit height because it was not desired to know the differential rod worth's for these rods. These are shutdown rods; they will be inserted together for maximum effect. This was modeled by simply replacing the MgO with B_4C in those assemblies.

In the rod worth curves, the vertical axis gives the location of the bottom of the B_4C in the rods. The rods are initially inserted with the B_4C at -90.0 cm and moved vertically upwards. The last position is with the B_4C at 90.0 cm. Fig 5.3 shows the differential rod worth in dollars of reactivity per cm. Reactivity was measured relative to the previous measurement point and divided by the vertical distance that the rod traveled between the two measurement points. Integral rod worth is shown in Fig 5.4.

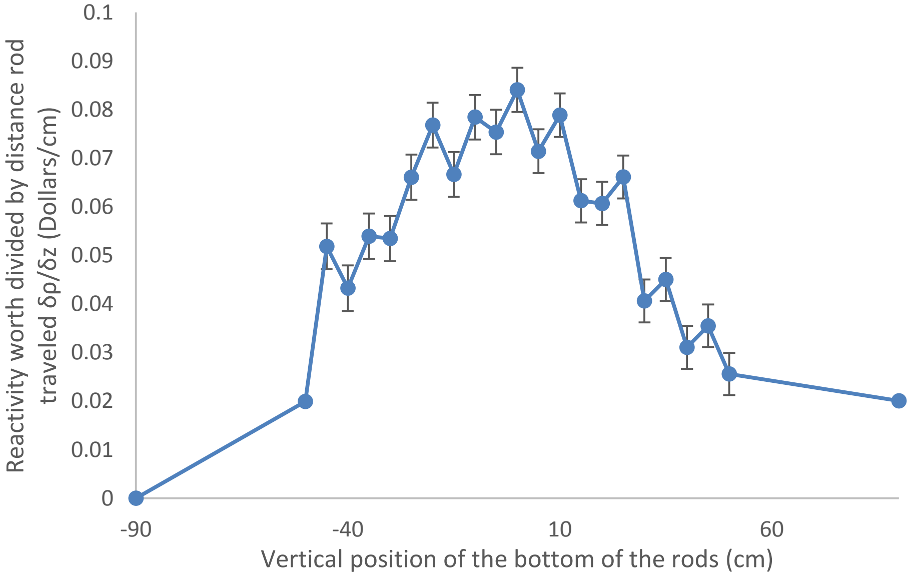

Figure 5.3 Differential rod worth

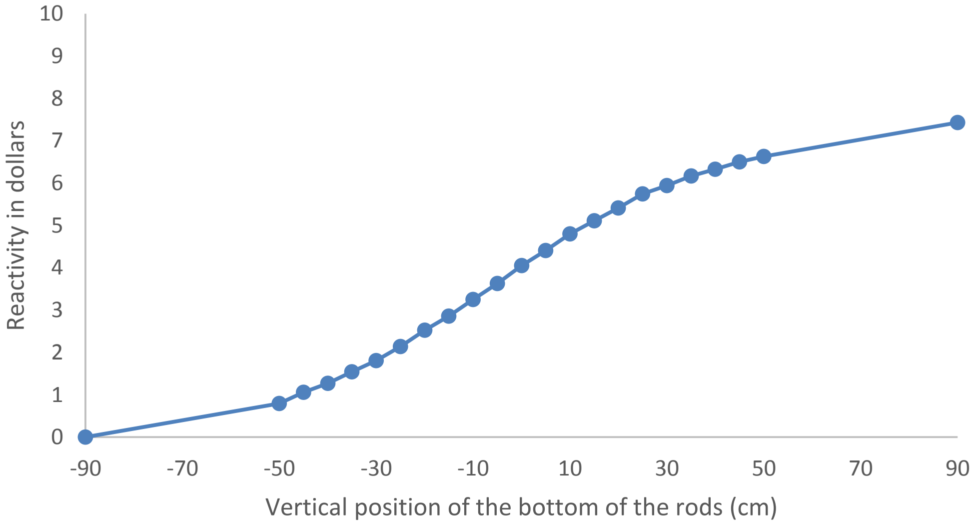

Figure 5.4 Integral rod worth

Several facts outlined in previous sections are relevant when explaining the rod worth curves. The first is that the geometry is highly reflected, which flattens the flux profile. The second is that the reflector reduces the energy of the neutrons when they are reflected, which means that an absorber with far larger thermal and epithermal cross section will have a greater effective absorption cross section nearer to the reflector even though the total flux is far lower in magnitude. The two effects counter each other somewhat, although the greater total flux at the center of the core coupled with the higher fast flux fraction means that rod worth peaks in the center of the core. Fig 5.5 shows the axial fast flux profile, Fig 5.6 shows the axial epithermal flux profile, Fig 5.7 shows the radial fast flux profile, and Fig 5.8 shows the radial epithermal flux profile. The first curve in each plot shows values with the rods at 90.0 cm and the second curve shows values with the rods at -90.0 cm. The axial flux profiles are plotted with flux on the x-axis and position on the y-axis, while radial flux profiles have flux on the y-axis and position on the x-axis. The very center of each profile is the same volume.

The axial flux profiles were tallied through the core center. Insertion of the control rods skews the axial flux profile towards the core center because of the enhanced absorption of epithermal neutrons far from the core center. Epithermal neutrons result from down scattering from the fission spectrum. Inside the core, a strong epithermal flux develops from the fissions within the region. The nearest control rod is 23 cm away from the core center, far enough away that epithermal flux within the central irradiation position is not significantly suppressed. In the upper and lower reflectors, epithermal neutrons are down scattered from neutrons leaving the core and reflected back towards the core. No fission source is directly driving epithermal flux within the reflector, so the absorber will suppress flux to a greater degree than in the core.

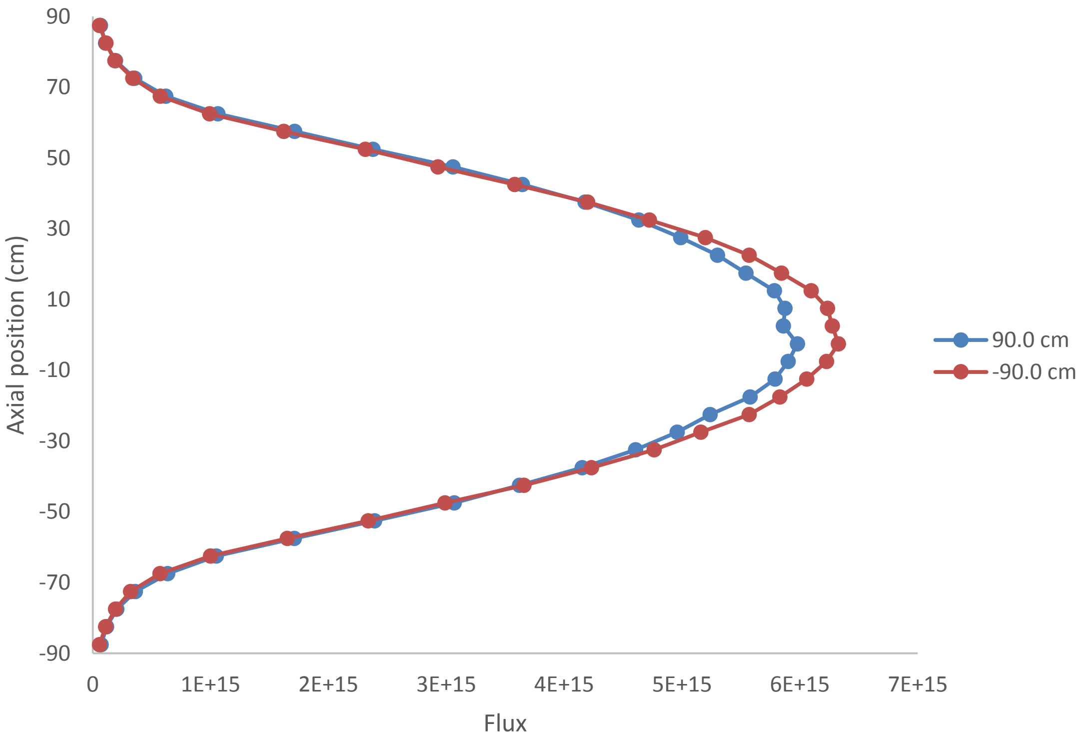

Figure 5.5 Axial fast flux

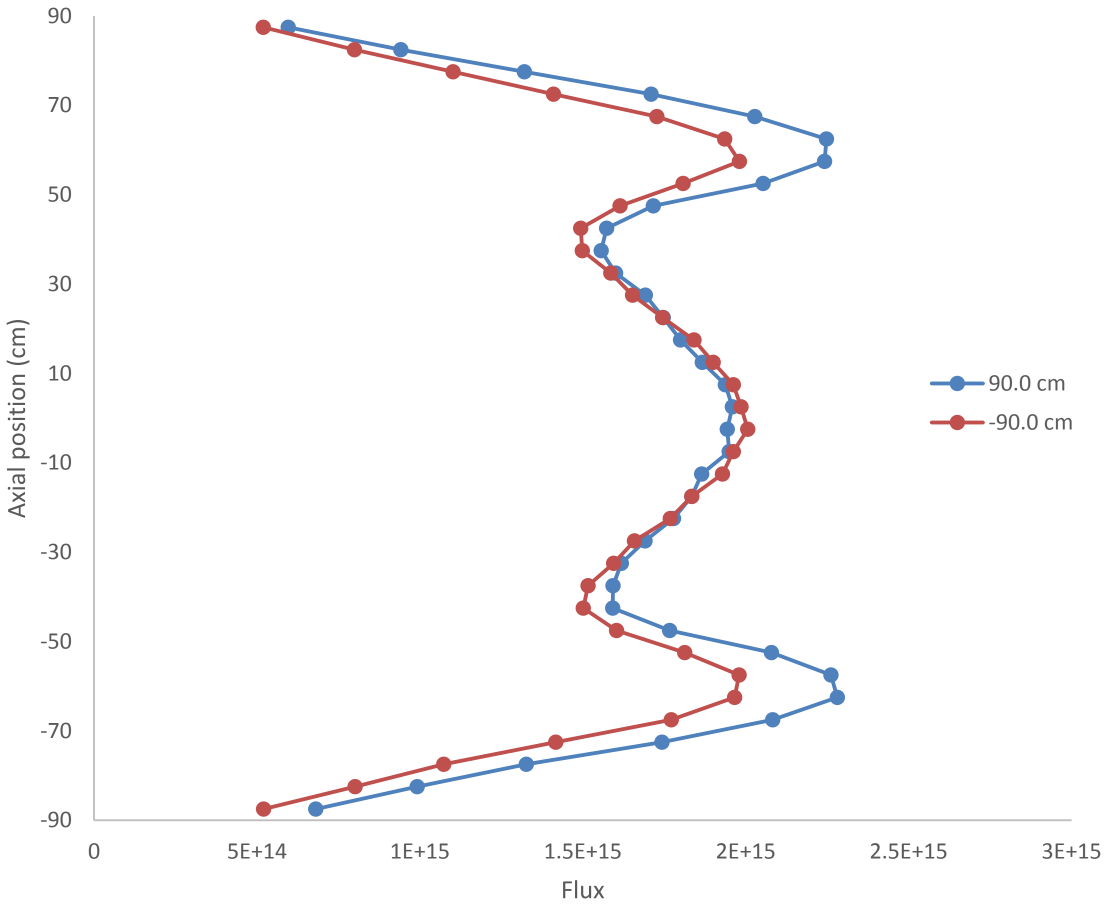

Figure 5.6 Axial epithermal flux

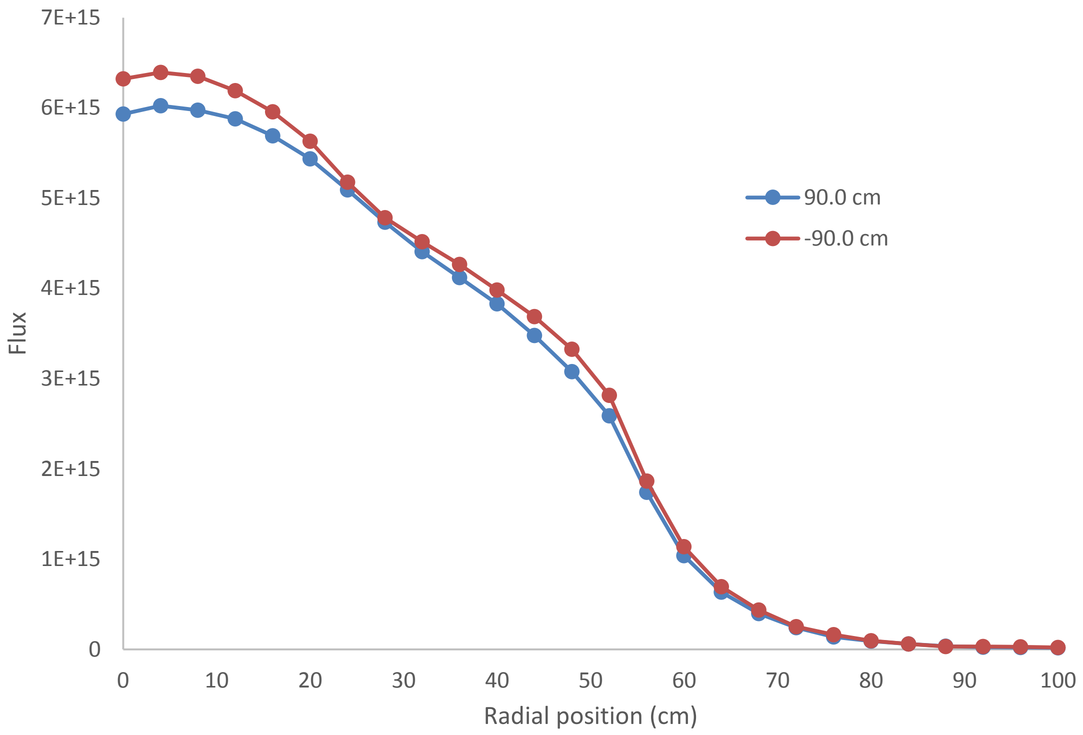

Figure 5.7 Radial fast flux

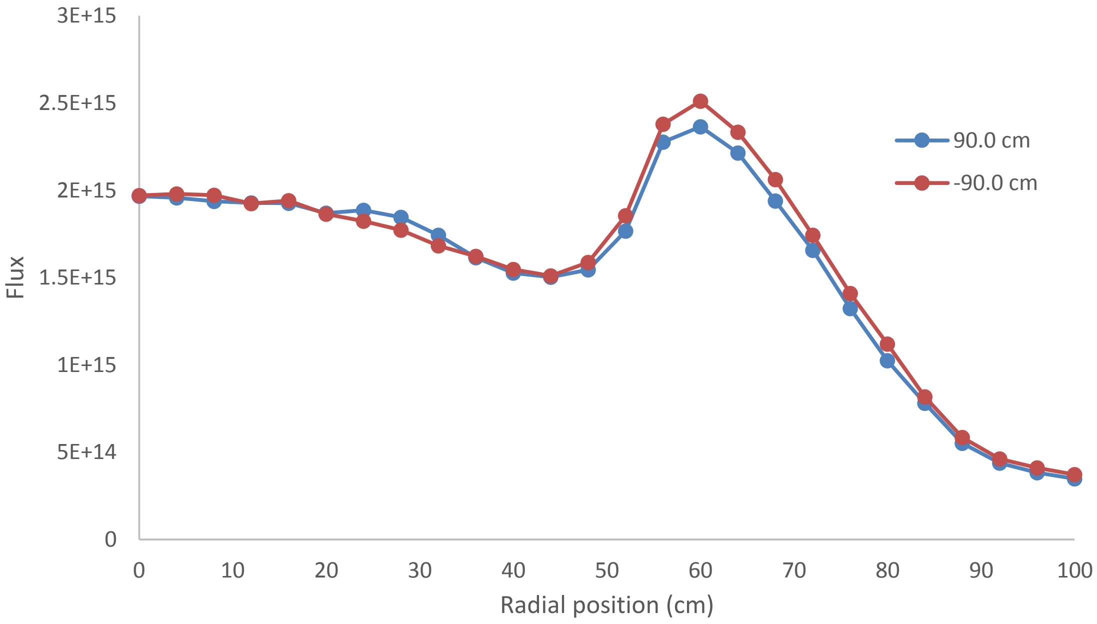

Figure 5.8 Radial epithermal flux

Fewer epithermal neutrons within the reflector translate to fewer neutrons reflected back into the core. This decreases the reactivity of the whole core and decreases the power density near the reflector, shifting the power density and therefore flux to the center of the core. Although not shown here, the fast flux fraction was higher throughout the axial region because of the control rods. Epithermal flux in the unperturbed core peaks in the reflector; epithermal flux peaks in the center with the control rods inserted in the core. The peak epithermal flux within the reflector decreased from 2.26E15 n/cm^{2}s to 1.97E15 n/cm^{2}s.

Peak fast flux measured increased from 5.92E15 n/cm^{2}s to 6.30E15 n/cm^{2}s; this is visible in the axial and radial plots of fast flux as they share the same volume at the very center of the core. The radial plot shows an increase in epithermal flux within the reflector. The control rods suppress epithermal flux around themselves. As no absorber is present in the radial reflector, epithermal flux will not be suppressed as in the axial flux profiles. The control rods also absorb fast neutrons, but the cross section is far higher for epithermal neutrons. Epithermal flux contributes to the fission density; near the rods power density is suppressed and fewer fast neutrons are born. The control rods are located from 23 cm to 34 cm in the radial plot, and fast flux and epithermal flux clearly decrease in those regions. As the overall core power is the same in both simulations, power density must distribute towards those region far from the control rods. As the control rods are in the center of the core, flux redistributes towards the core center and outer reflector. Combined with the suppression of epithermal flux in the axial reflector, fast flux is accentuated within the center of the core.

Withdrawal of the shim rods will perturb the axial flux profile. It was desired to estimate this effect, which was done by examining the fluxes in the top and bottom of the core with the rods at 0.0 cm, or half withdrawn. Flux split is defined as the flux in the bottom of the core divided by the flux in the top of the core. The top of the core is from 50.0 cm to 0.0 cm, and the bottom of the core is from 0.0 cm to -50.0 cm. The fast flux split is 1.16 and the epithermal flux split is 1.18. Put another way, the average fast flux in from 0.0 to -50.0 cm is 16% higher than the fast flux from 50.0 to 0.0 cm. The flux split at the center of the core is much lower than that near the periphery. The fast flux from 0.0 to -5.0 cm is 2% higher than the fast flux from 5.0 cm to 0.0 cm. If these values are undesirable, then control elements can be moved away from the core. However, more elements would have to be added as the worth of a control rod decreases further from the center. Moving the rods would also adversely affect the irradiation location in the reflector. Further research would be needed to balance the two effects.

Adding control rods to the core in the configuration shown above inserted -0.692$ of reactivity. Insertion of the control rods within the core reduced k_{eff} to 1.0012. The shim rods are intended to reduce reactivity to just subcritical; some slight change is necessary in order to attain this behavior. Perhaps one assembly could have more control rods; this assembly could be used as the regulating cluster. Perhaps the diameter of the rods or the density of the rods could be increased. Regardless, only a slight change would be needed to make the configuration slightly subcritical. The shutdown bank reduces k_{eff} from 1.0012 to 0.9232, providing more than enough negative reactivity for safe shutdown. These rods would not be used to control power during regular operation;

they would only be used to achieve safe shutdown. The worth of these rods could probably be increased so that they would able to shut down the reactor without the shim rods.

The work so far has be done in accordance with the core having a non-uniform enrichment throughout the core and an increased fuel volume. Behavior of the control rods within the base geometry will now be demonstrated. Control rods were placed in the core in the same location as previously shown. However, more rods had to be inserted to counteract the greater initial reactivity of the system. Inserting more control rods decreases the reactivity of the system when compared to the original core having no control systems. The starting k_{eff} for the system is now 1.0752, a 1.423$ decrease in reactivity compared to the original core. To make the core just subcritical using the shim rods, twelve rods had to be inserted compared to seven rods used previously. This is shown in Fig 5.9. k_{eff} with the shim rods fully inserted is 0.9926 for a total shim bank worth of -11.91$.

This core was burned to see how the decrease in fissile mass would affect the long time behavior. The estimated core lifetime is 315 days, compared to 378 for the original core. The core wide average burnup 45.7 MWd/kgU compared to 53.5 MWd/kgU for the original core. The average peak fast flux over the core was 5.74E15 n/cm^{2}s compared to 5.65E15 n/cm^{2}s. Fluence measured over the core lifetime is 18% greater for the original core. These values suggest moving some of the rods to the reflector. Again, this would have to be balanced against the flux perturbations that would affect the irradiation locations in the reflector. Cores with lower enrichments would need fewer rods in the core and will exhibit burnup behavior closer to the results from simulations performed without control systems.

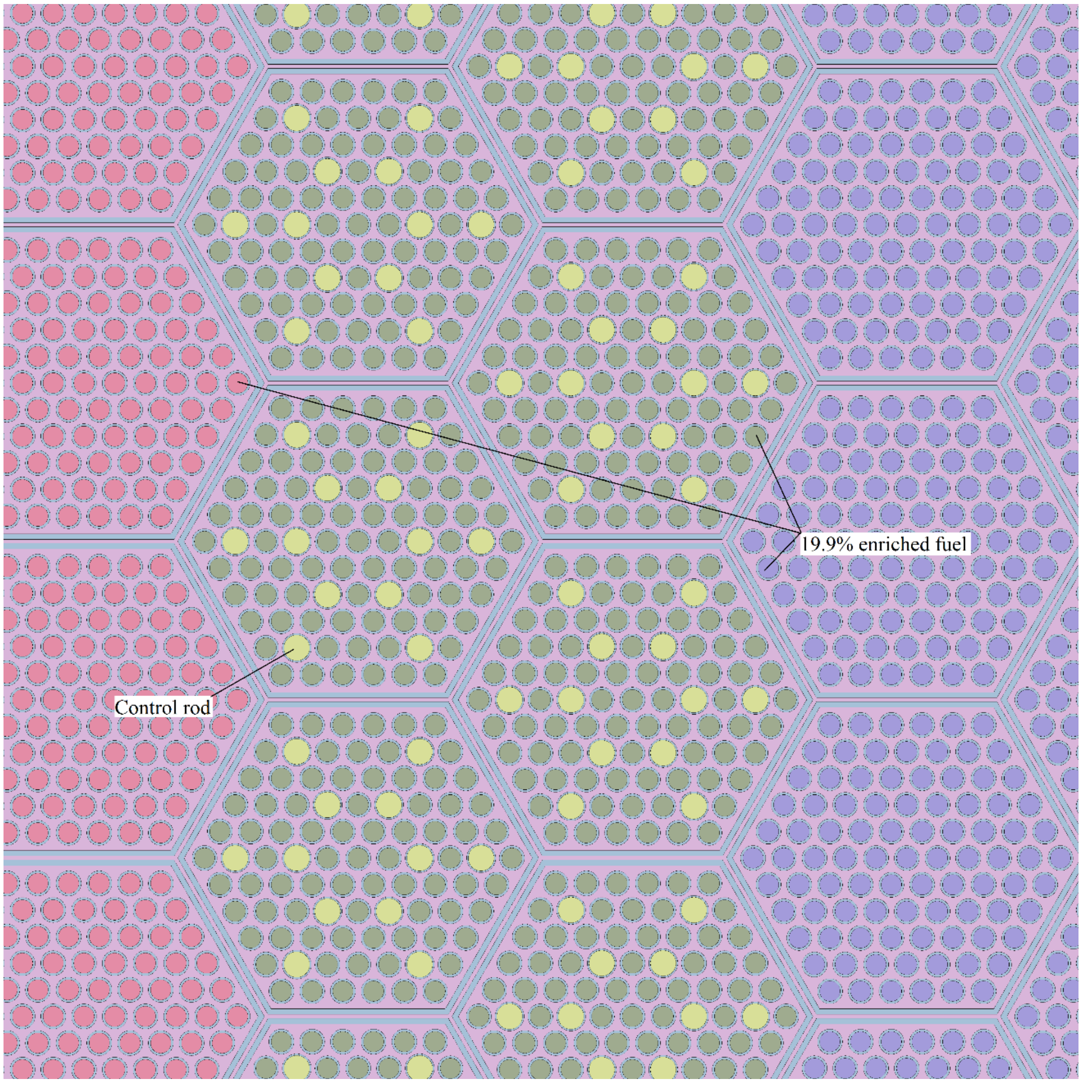

Figure 5.9 Locations of control rods in base geometry

The effect of different absorber materials was studied with the uniformly enriched core. The rods were inserted at -90.0 cm and k_{eff} was calculated for each material. Pins filled with Eu_2O_3 at a density of 7.4 g/cm^3 had a k_{eff} of 0.9993, slightly greater than with B_4C. Pins filled with Er_2O_3 at a density of 8.64 g/cm^3 had a k_{eff} of 1.0482, much greater than with B_4C. The effect of different following materials are studied with the non-uniformly enriched core. The rods were inserted at 90.0cm and k_{eff} was calculated for each material. Table 5.1 gives the material, the material's density, and the resulting k_{eff}. The relative error of all the simulations was 0.00011. The material with the highest k_{eff} is the most favored material. Materials are arranged in descending order of k_{eff}. MgO and graphite are nearly identical, and MgO was chosen because graphite tends to increase the power peaking factor in fuel around it. The other three options all had k_{eff}'s different from the k_{eff} of MgO to conclude that they are poorer options. Curiously, void produced a lower k_{eff} than otherwise. The void was extended over the whole length of the rod; thus, there was void within the upper and lower reflector. This may have reduced the effectiveness of the reflector and contributed to the lower k_{eff}. All the other materials will absorb and downscatter neutrons to varying degrees. Void has no effect on the neutrons within the core. It may be beneficial to change the geometry of the rods to benefit from void. MgO would fill the rods in the places where it is normally reflected, and void would fill the middle portion in the core. Given the very slight changes in k_{eff}, it probably isn't worth the effort to redesign the control rods.

Table 5.1 k_{eff} associated with different materials that follow the control rods. Calculated with a lower enriched core and rod height at 90.0 cm.

Material	Density in g/cm^3	k_{eff}
MgO	3.58	1.05211
Graphite	2.2	1.05208
Sodium	0.8	1.05180
Void	0.0	1.05126
Steel	7.8	1.05040

5.2 Control drums

As mentioned previously, the control rods perturb the axial flux profile and decrease the fissile mass of the core. Control drums, which operate by changing the effectiveness of the reflector, will not have either effect, but will change the magnitude of flux within the core and in the reflector. The drum itself is a large cylinder slightly thicker than the outer reflector with some portion containing an absorber. As the cylinder turns, the absorber is moved towards the core, where it will absorber neutrons before they can be reflected back into the core. The drums were made as large as possible so that the absorber away from the core has minimal effect of reactivity. Fig 5.10 shows the six drums within the core and Fig 5.11 shows the drums in greater detail. In both figures, the drums are turned away from the core. This is referred to as 0°. The drums take up a great deal of the reflector and moderating region.

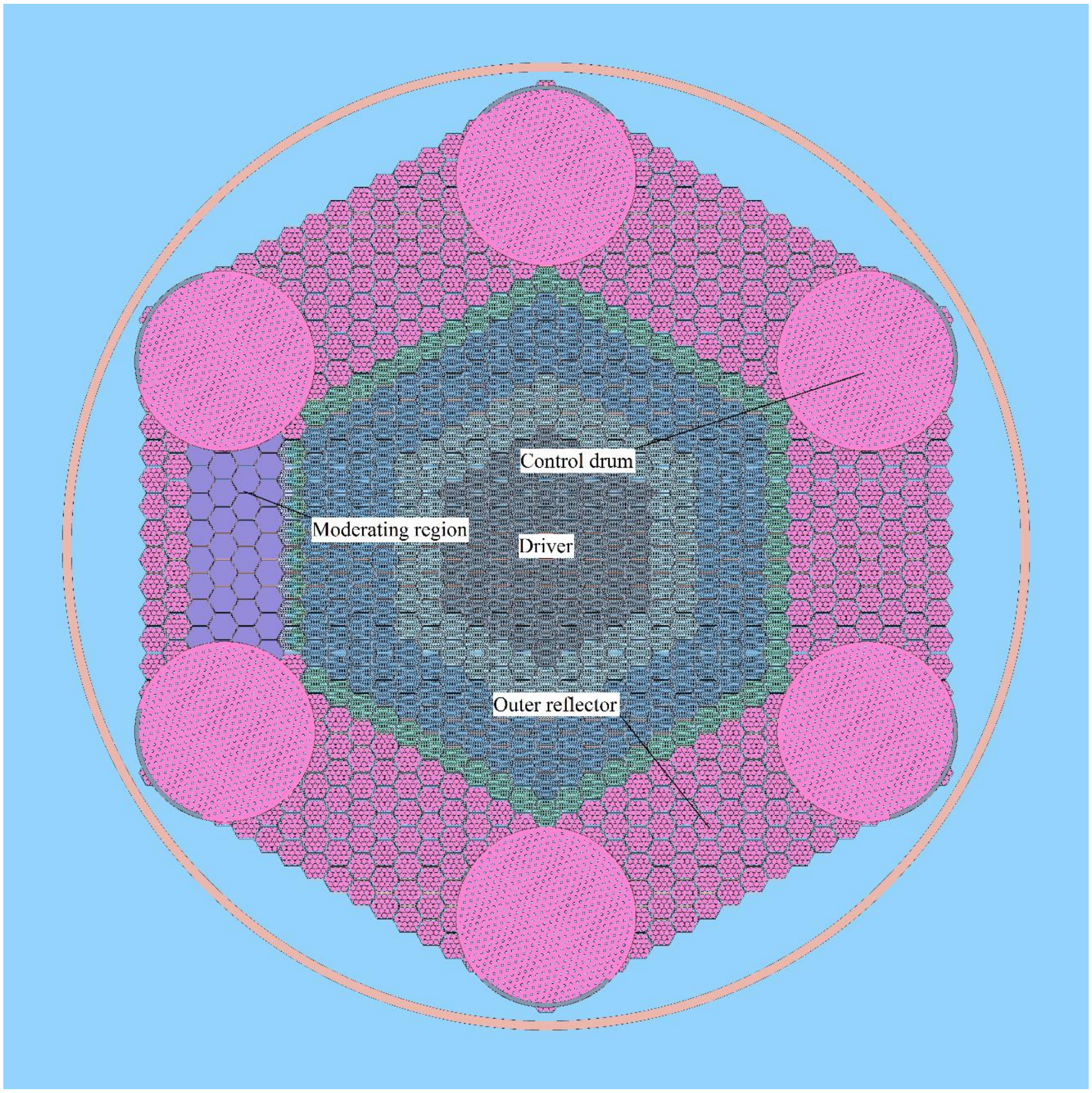

Figure 5.10 Control drums in the reflector fully away from the driver

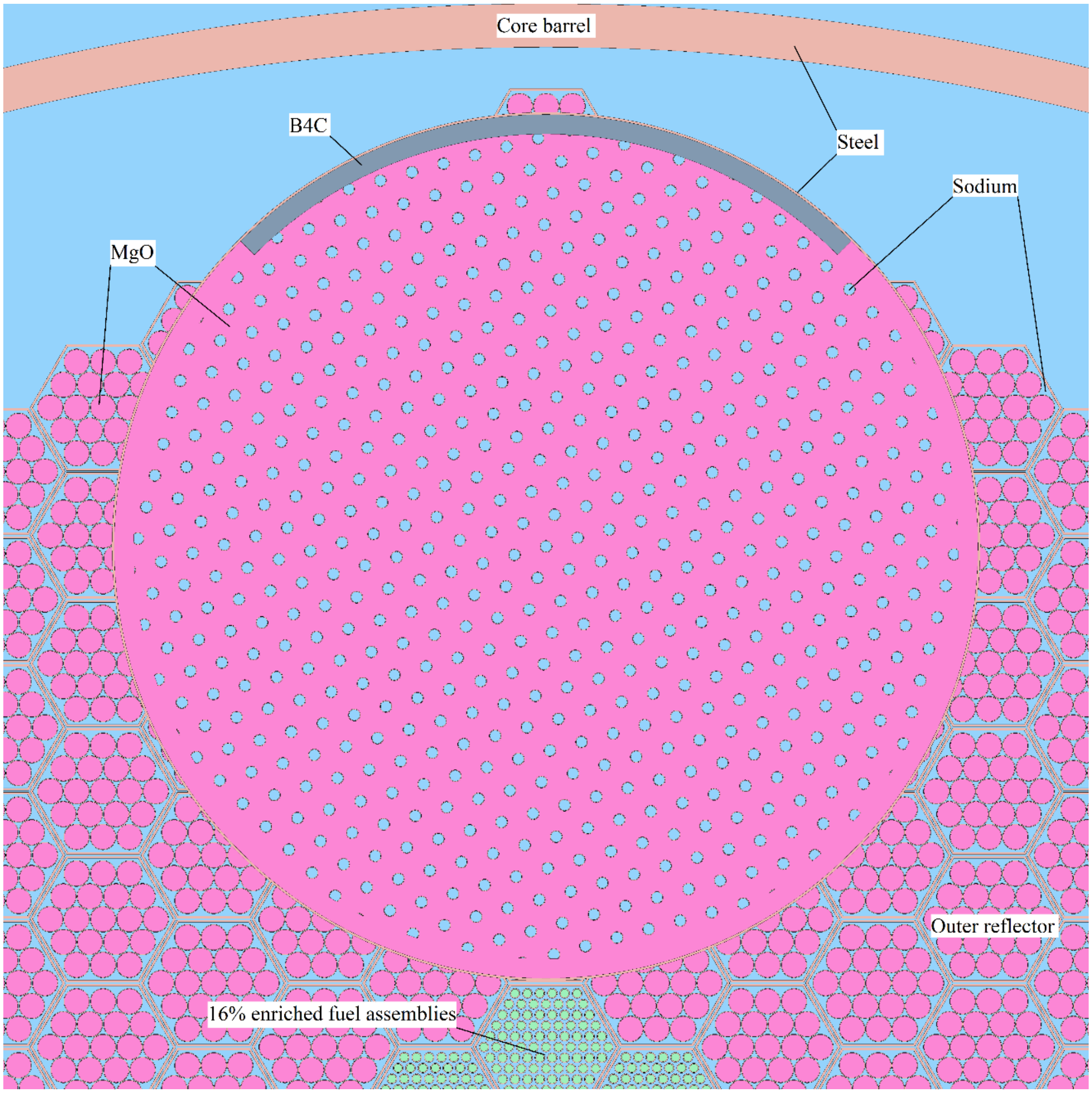

Figure 5.11 Close up of Figure 5.10

Reflector assemblies that border the drum are not realistically modeled; that is, they are cut apart to incorporate the drums. An actual core would not be designed in this way; those reflector assemblies that border the drums would be enclosed in some manner that would minimize the amount to steel and sodium in those assemblies. Such a degree of modeling fidelity is unnecessary in this investigation. The drum itself is 40 cm in diameter and has a 0.1 cm thick steel wall surrounding it. The interior of the drum is composed of an infinite hexagonal lattice of sodium cooling channel, steel walls, and MgO. The interior sodium channel is 0.5 cm in diameter, with a 0.0305 steel cladding. The pitch of the sodium cooling channels is 1.5057 cm, which corresponds to a sodium volume fraction of 10%. The MgO volume fraction is higher in the drums than in the reflector. This increases the worth of the drums by making the drums more likely to reflect neutrons into the core. The 0.9 cm thick portion between the interior hexagonal lattice and the steel wall is split into four quadrants. Three of these quadrants are filled with MgO, while the fourth is filled with unenriched B_4C. Fig 5.12 shows the core with control drums at 180°, or towards the core at the point of maximum reactivity insertion. Drum worth curves were not calculated; instead the reactivity's of the drums at 0°, 120°, and 180° were be presented. The reactivity of the drums at 0° is given relative to the original geometry. The higher volume fraction of MgO within the drums reflect more neutrons, and increase core reactivity even if some B_4C is located towards the core periphery. The initial excess reactivity of the geometry with the drums at 0° is 12.65$. Rotating the drums so that they all face inwards doesn't insert enough reactivity to make the reactor subcritical. Adding more drums would increase the reactivity worth, but eliminate nearly all of the irradiation positions in the reflector and moderating region. Based on the size of the drums, six more could be added. Assuming that these drums would have the same reactivity effect as the simulated six, then the maximum negative reactivity inserted would not be enough to make the core subcritical. This fact, combined with the near elimination of any irradiation position in the reflector, isn't a feasible option. Perhaps the most realistic option is to use control drums in conjunction with some rods, as suggested earlier. Control drums would appear to be the best control mechanism for core that are severely zoned, with lower enriched fuel towards the outside of the driver.

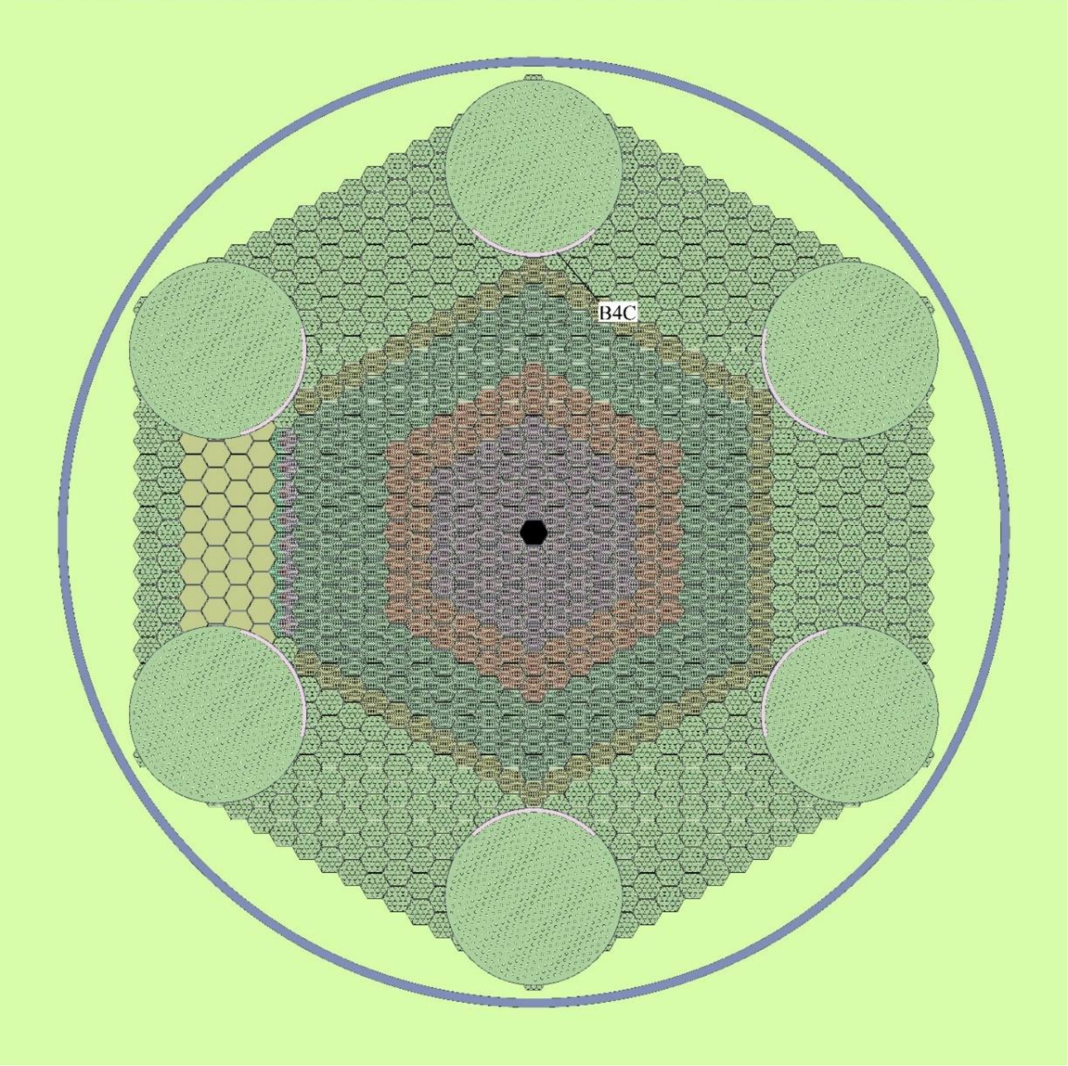

Figure 5.12 Drums at 180°

Table 5.2 Reactivity worth associated with drum position

Drum position in degrees	Reactivity in dollars
0	0.455
120	-1.877
180	-4.093

The simulation at 120° was performed with all the drums rotated 120° clockwise. Thus, a given section of reflector between two drums will have one part of it near B_4C and the other part will be away from B4C. Fig 5.13 shows this scenario. Lines denote areas over which flux was tallied to study the effect of the drums movement on flux within the reflector. There are three regions, a top, middle, and bottom. The top is near B_4C. Four group fluxes was tallied over each region for the drums at 0°, 120°, and 180°. Flux in each group for each region was compared to the relevant flux at 0°. Thermal flux decreased by 64% in the top, compared to 32% and 18% for the middle and bottom, respectively. Epithermal flux followed the same trend, dropping by 21%, 7%, and 4% from top to bottom. Fast flux also followed the same trend, but the reductions in flux were much lower than for epithermal flux. Fast flux dropped by 6%, 3%, and 2% from top to bottom. Flux values throughout the reflector changed more consistently with the drums at 180°. Flux in each group peaked in the middle and decreased towards the drums. Flux was lower for all groups in all regions. Thermal flux drops by 40% and 34% near the drums and in the middle, respectively. Epithermal flux drops by 13% and 8%, respectively. Fast flux drops by 6% and 3%, respectively. Fast flux also shifts downwards in energy, with the higher energy fast flux (E > 1 MeV) being more reduced than the lower energy fast flux. Higher energy fast flux drops by 10% and 4% near the drums and in the middle.

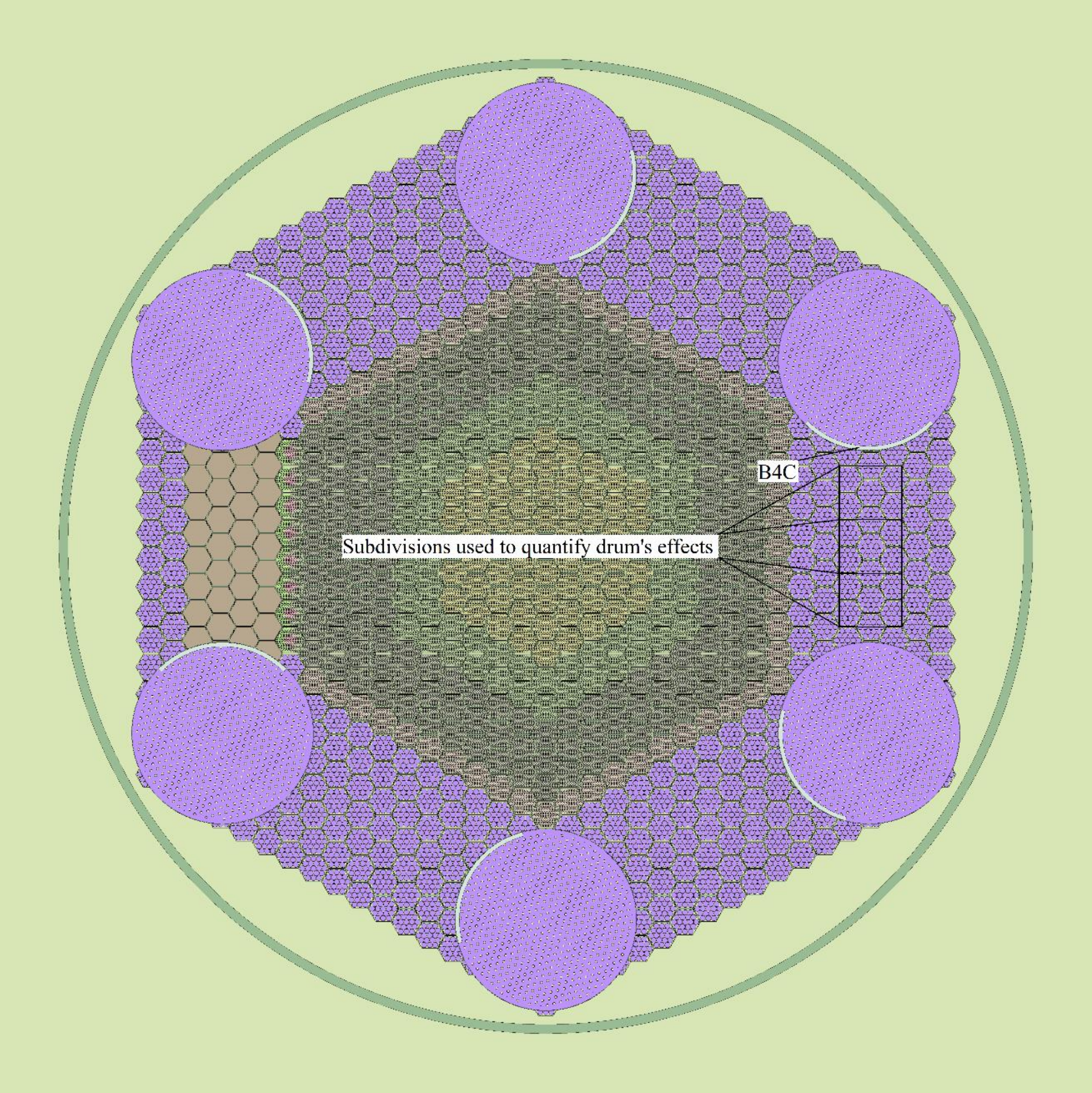

Figure 5.13 Drums at 120° with subdivisions of the reflector highlighted

The power density of the driver near the B_4C is reduced because fewer epithermal neutrons are reflected back into the core, which would reduce the total flux. B_4C preferentially absorbs thermal and epithermal neutrons over fast neutrons. The movement of the drums does not significantly affect the fast flux within the moderator. This fact may not be directly useful, as fast flux materials irradiation will take place within the core itself, not the reflector. Although thermal flux is present within the reflector, it is orders of magnitudes lower than within the moderating region. Thermal flux materials irradiation will take place there instead. The epithermal flux in the reflector is comparable to the epithermal flux within the moderating region, and materials irradiation under a high epithermal flux is feasible in the reflector. Epithermal flux near the drums drops by 21% with the drums at 120° and 13% with the drums at 180°, but epithermal flux between the drums drops by 7% and 8%, respectively. It is recommended that epithermal flux irradiation be performed in the middle assemblies between the drums. Flux will not drop more than 10% over the core lifetime in those locations. Materials irradiation could be performed anywhere within the reflector if the drop in flux and related shifts in neutron spectra are irrelevant.

6. CONCLUSION

Nuclear power in the US is based around LWR's, many of which are approaching the end of their original 40 year operating licenses. The majority of these plants have applied for and been granted 20 year license extensions. However, materials behavior after 60 years of continual operation requires more research, which is being performed in conjunction with the LWRS program. Neutron damage is mainly caused by fast neutrons. There is interest in the US and throughout the world in the development of advanced reactors. Although the terms advanced reactors comprise a bevy of potential options, fast reactors optimized for the breeding of fissile material or the destruction of actinides are a focus of research. Materials testing associated with a fast reactor would require a high fast flux, higher than in the ATR and HFIR. Therefore, from the standpoint of materials testing, there is a need for a high fast flux.

However, the choice(s) for the next US advanced reactor has not been made. For this reason, the NEAC report empathized the need to provide variable neutron spectra with different coolant types. The LWRS program will require irradiation conditions similar to prototypic LWR conditions. In particular, the NEAC report highlighted the need to perform transient testing and provide large irradiation positions. Bearing this in mind, a reactor configuration was chosen that would have a fast flux in the center which would be moderated in the core periphery. The composition of the fast section of the core, where the majority of heat generation would take place, is not specified in the NEAC report. Selecting the driver composition was aided by another requirement from the NEAC report. Before building full scale commercial advanced reactors, it is desirable to study their behavior on a smaller scale through demonstrator reactors. These aptly named demonstrator reactors will exhibit many of the same behaviors and utilize the same equipment as the commercial plant, albeit on a smaller scale. Ideally, the new reactor would serve as a demonstrator fast reactor and materials testing reactor. Sodium cooled fast reactors are the most extensively studies advanced reactor type to date, with numerous examples throughout the world, including at least five here in the US. Metallic fueled sodium cooled fast reactor, exemplified by the EBR-II, exhibit favorable swelling characteristics and severe accident behaviors. As such, the proposed reactor is a materials testing reactor with variable neutrons spectra where the driver is based on the metallic fuel technology.

Reactor capabilities stem from the NEAC report, but specific requirements stem from capabilities of other research reactors, both operating and planned. Firstly, the fast flux of the proposed reactor is greater than that of any planned or operating reactor. A fast flux measured as $E > 0.1$ MeV between 5E15 n/cm^{2}s and 7.5E15 n/cm^{2}s can be maintained in the central irradiation position. Fast flux $E > 1$ MeV over the same range is between 8.5E14 n/cm^{2}s 1.3E15 n/cm^{2}s. These number assume that flux of $E > 1$ MeV divided by flux $E > 0.1$ MeV is ~0.17. Such values are approximately 50% to 120% higher than the peak fast flux in an irradiation assembly as MBIR. Comparing flux values to the MYRRHA and JHR less precise, as they use different metrics for fast flux, $E > 0.75$ MeV and $E > 0.9$ MeV. MYRRHA generates a fast flux in the central channel during subcritical operations comparable to the fast flux in this reactor, but far 2.5 times lower when in critical mode. Additionally, fluxes throughout the proposed reactor are still higher than in off central channels of MYRRHA. In Section 2 of this thesis, fast fluxes in irradiation assemblies throughout the driver are given. Assuming that large irradiation positions in the outer driver are used, the fast flux E > 1.0 MeV is still expected to be 6.6E14 n/cm^{2}s, higher than corresponding values for MYRRHA when critical and subcritical. Peak fast flux in the proposed reactor is 50% to 140% higher than the peak fast flux in the JHR. Peak fast flux in the proposed reactor is 4 to 6 times greater than in the ATR.

While it is useful to compare peak fast fluxes, the volume of irradiation space must also be considered. Flux within the core changes with axial position, information that was not attained for other research reactors. Therefore, peak fast flux in a position will be multiplied by the area of that position and summed over the whole reactor. The units of this metric are n/s. More accurately, the metric is in units of n*cm/cm*s, neutron path length per unit axial distance. However, it is quoted as n/s for reasons of economy within this thesis. Configuration 6 will be used because it offered a core lifetime of over one year and has two large irradiation positions. The design of irradiation assembly varies between reactors, so the whole assembly area will be used in this comparison. The proposed reactor peak source in the irradiation positions of 2800E15 n/s E > 0.1 MeV and 480E15 E > 1 MeV. Assuming that all assembly positions are 7.22 cm flat to flat, the MBIR has an effective source of 2200E15 n/s E > 0.1 MeV. MYRRHA boasts an effective source of 330E15 n/s E > 0.75 MeV in subcritical mode and 190E15 n/s E > 0.75 MeV in critical mode. JHR has an effective source of 120E15 n/s E > 0.9 MeV, ignoring the smaller positions between assemblies. ATR has an effective source of 44E15 n/s E > 1 MeV. The proposed reactor offers both higher fluxes and higher total neutron path lengths in the driver than other research reactor, but at the cost of a much higher power. As mentioned previously, the limitations on enrichment and plutonium content will limit the effectiveness with which fuel is burned. With a higher fissile content per pin, core size and core power could be reduced while maintaining a critical geometry. However, the core geometry will maintain criticality for over one year at these high fluxes and higher total neutron path lengths.

Many burnup simulations were performed in conjunction with this investigation. In general, fissile content utilization improves with higher enrichments, although breeding improves with lower enrichments. If a reprocessing plant it used in conjunction with this reactor, then it may be worthwhile to reduce enrichments. Lower enrichments have higher fluxes and shorter core lifetimes. Given the limitations on core internal geometry and overall size, it is impossible to configure the core for homogeneous breeding, although heterogeneous breeding could be possible. Even to core wide burnups of 50 MWd/kgU, which corresponds to over one year of operation of the base geometry, the fuel isotopics are weapons grade plutonium. This represents a possible proliferation risk. A reasonable estimate of core shutdown time or capacity factor was not developed in this investigation, so it is impossible to optimize the core loading based on fluence in the irradiation positions. The exact options for fuel loading are outlined in Section 2. The base geometry is outlined at the end of this section, along with Configuration 6, which is the recommended core configuration.

While the driver is composed of metallic fuel in a configuration similar to EBR-II, the radial and axial reflectors are composed of MgO in the same configuration as the breeding blankets in the EBR-II. MgO was selected as the best reflector over BeO, spinel, graphite, steel, PbO, and natural uranium. This reflector could contain additional irradiation positions, although the fast flux will be low compared to the driver. Two items of interest are located in the outer reflector. This first are some of the control systems, which were outlined in Section 6 and will be briefly described in this section. The second item of interest are the transient testing locations. The driver operates at thermal conditions representative of an operating sodium cooled metallic fueled fast reactor. Thermal fatigue, or the gradual weakening of a material brought about my changing temperatures, is a potential problem for the driver. Similarly many of the materials being irradiated are going to be irradiated as constant temperatures. It was desired to perform transient testing in the outer reflector at constant core power, so as not to affect temperatures of any other part of the system. The manipulation of power in the test assembly is done by inserting control rods; the insertion of the rods must insert reactivity's on time scales that are manageable by the core control systems. Similarly, thermal hydraulic experiments such as subjecting a PWR test assembly to a LOCA accident change the reactivity of the core. These experiments must also insert reactivity on a time scale manageable by the core control systems. Three common types of reactor were chosen; the PWR, VHTR, and SFR representing the most common operating reactor and two advanced reactor types.

Test assemblies associated with these reactor types were developed. The PWR was based on the AP1000, the VHTR on the HTTR, and the SFR on a prototypic oxide fueled fast reactor. References for these reactor types are found in Section 3. Each test assembly was placed in the transient test trap, so called because it was designed to minimize the effect of neutrons in the trap on the rest of the core. Each test assembly was studied with the local control rods fully withdrawn and inserted, thus measuring the reactivity change associated with a given reduction in power. Although not directly modeled, it is intend that the control rods be individually movable so that any power can be attained. Individually movable rods can be manipulated so that the relative assembly axial power profile does not change, only the magnitude of the assembly power. Depending on the exact neutronics of the test assembly in the trap, reductions in power greater than 98% can be attained with insertions of reactivity of less than -0.10$ for each test assembly. In a LOCA, extensive voiding occurs in the core. This was modeled as a uniform quality of 0.20 in the PWR test assembly. This inserted less than 0.05$ of reactivity. The anticipated reactivity insertions should be manageable by the core control systems. Decoupling the core from the trap was accomplished through light water and cadmium. The transient test trap is located as far away as possible from the driver. The MgO assemblies immediately surrounding the trap are doped with cadmium, a thermal absorber. The control assemblies that surround the trap are filled with light water, a very effective absorber. Fast or epithermal neutrons entering the trap will be moderated by the light water. If they attempt to escape, they will be absorbed by the cadmium. However, cadmium has very low epithermal and fast cross sections. Neutrons at higher energies can enter, but it is intended that all neutrons that enter are moderated. From there, they cannot escape and affect the driver. Now, some neutrons escape by leaking from the sides or are ineffectively moderated, but this effect is minimal. Placing the trap in the outer reflector does not entail much loss in reactivity either.

A section of the reflector, 78 assemblies, was replaced with graphite. In this region fast neutrons streaming from the driver are moderated and large epithermal and thermal fluxes are developed. Graphite is a less effective reflector than MgO, so the number of assemblies was minimized. While the standard configuration for the reflector is a bundle of rods, the graphite blocks within the moderating region were solid. Each block had the same assembly wall thickness and gap between assemblies as every other section of the core. This makes the moderating region highly modular. Most of the moderating region was mapped out for the 10 cm around the core centerline. This region represents the locations of peak fluxes. Flux varies a great deal throughout the moderating region. Peak thermal flux with graphite is 4.51E14 n/cm2s but the peak thermal flux with light water is 1.17E15 n/cm2s but insert -1.92$. This reactivity is prohibitively expensive, so graphite was used to study the effects of cadmium and beryllium in the barrier assemblies. Cadmium is a thermal absorber, doping the steel within the barrier assemblies would reduce the thermal flux from entering the barrier assemblies and fissioning. This would reduce power peaking within the assemblies, enabling higher enrichments. All told, k_{eff} slightly increased while power peaking factor slightly increased. Beryllium, which has a (n,2n) cross section for neutrons above 2 MeV, was placed in the barrier assemblies near the graphite. Beryllium increased thermal flux and decreased fast flux, as anticipated for a small reduction in k_{eff}. If the steel and sodium are removed from the moderating region, making the entire region one contiguous section of material, thermal fluxes increase throughout the region. Thermal flux increase to 1.02E15 n/cm2s with graphite, and 2.02E15 n/cm2s with light water. These values are significantly higher than with steel and sodium, but reduce the modulatory of the region. 0.92$ of reactivity are inserted by removing cans with the graphite, and 0.45$ of reactivity are inserted by removing cans with light water. The light water without cans still reduces reactivity compared to graphite with cans. Peak thermal flux in graphite without cans compares well to peak thermal fluxes in JHR and ATR. Light water and the removal of cans brings thermal flux values much higher than in those reactors.

It was also desired to match spectral conditions and power generated in the pins of different reactor types. Static capsules and irradiation test assemblies were placed in the moderating region, both near and far from the driver, with and without flux shaping assemblies around them, such that the neutron spectrum within the tested materials resembled neutron spectra associated with a PWR or a VHTR. By controlling the amount of graphite and light water around the testing location, and the relative distance from the core, it should be possible to adequately mimic PWR and VHTR neutron spectra. A caveat is related to the difference in fast flux between PWR's and SFR's. The ratios of flux E > 0.1 MeV and flux E > 1 MeV are different due to the different scattering materials within the cores. Matching these ratios will be difficult in the passive conditions, and were not successfully matched in this investigation. Gamma heating was not quantified in this investigation. Back scattering from light water versus graphite will play a role in shaping fluxes. Active test assemblies like the ones used in transient testing were used as well. In these, both spectrum and fission heating are relevant. Absorbers were used in conjunction with moderators to match flux and power. Most absorbers used in this study depressed thermal flux more than epithermal flux and had little effect on fast flux. As few fast neutrons are present in the region, absorbers were used to depress thermal flux and raise fast flux with increasing enrichment. Overall, matching conditions with active assemblies is more complicated than with passive assemblies, but can be performed in this reactor.

Two separate methods of controlling the reactor were examined; rods and drums. Natural boron was used in B_4C; other absorbers were less effective. The rods replaced fuel rods within the assemblies. In order to minimize the worth of individual assemblies, rods were spaced over large sections of the core. With enough rods, it is possible to control reactivity to any degree necessary. However, rods are going to shift flux profiles within the core. This effect is quantified in Section 5. So as to minimize the number of fuel rods withdrawn, the excess reactivity of the in core rods was minimized. Control rods will also have to be located within the outer reflector. It is anticipated that the in core assemblies are used to control reactivity over the core lifetime, while the rods in the reflector are used to bring the core to the necessary degree of subcriticality for safe shutdown. The second method uses control drums. These are rotating cylinders in the outer reflector, 40 cm in diameter, filled with MgO, sodium and steel. The sodium and steel provide cooling. One quarter of the outer section contains a 0.9 cm thick section of

B_4C. Rotating this section towards and from the driver changes reactivity. The large size of the drums in necessary so that the B_4C section travels as great a distance as possible. The presence of B4C will be minimal when rotated furthest from the core. The drums take up a considerable volume of the reflector and will lower fluxes in the reflector when rotated. This effect is minimized for epithermal and fast fluxes between the assemblies. Drums maintain a constant relative axial flux profile throughout operation in the driver. However, the drums could not deliver enough excess reactivity to the base geometry. Cores with lower enrichments and lower initial k_{eff}'s could use drums.

6.1 Description of the base geometry

Throughout this work, the base geometry was referenced. Although all features of this geometry were described within, the base geometry is concisely summarized below. The shape of the core is a regular hexagon composed of smaller regular hexagons. It is standard in fast reactor design to position assemblies so that they appear to be more cylindrical; this was not done in the present investigation. Non-leakage probabilities for cylinders are higher than for hexagons of equivalent volume. For such a small, highly reflected system, this benefit would be minimal. Placing the assemblies in concentric hexagonal rings makes counting assemblies easier, aiding the design process.

Table 6.1 Base geometry

Driver pin outer diameter	0.442 cm
Driver pin cladding thickness	0.0305 cm
Driver fuel smeared density	75% of 17.7 g/cm^3
Driver fuel composition	90% U, 10% natural Zr
Driver cladding composition	87% Fe, 12% Mo, 1% Cr
Driver pin pitch	0.57192 cm
Driver pin restraint type	Steel wrapper
Blanket pin outer diameter	1.2 cm
Blanket pin cladding thickness	0.0305 cm
Blanket pin pitch	1.215 cm
MgO density	3.58 g/cm^3
Assembly pitch	5.893 cm
Assembly wall thickness	0.1016 cm
Assembly flat to flat width	5.817 cm
Active core height	100 cm
Height of sodium gap within assemblies	5 cm
Fission gas plenum	None
Height of axial blanket	35 cm
Total number of assemblies	919
Number of radial blanket assemblies	498

Table 6.1 continued

Number of moderating assemblies	78
Number of barrier assemblies	12
Number of 19.9% enriched driver assemblies	279
Number of 16.0% enriched driver assemblies	51
Number of irradiation assemblies	1
Inner material of irradiation assembly	Vacuum
Enrichment of barrier assemblies	6%, 12%, 15%
Number of pins in barrier assemblies at different enrichments	33, 19, 39, respectively
Inner material of moderating assemblies	Graphite at a density of 2.2 g/cm^3
Sodium density	0.8 g/cm^3
Steel density	7.8 g/cm^3
Temperatures and cross section libraries for various materials	Fuel-900 K, all other materials-600 K Graphite used ENDF/B-VII thermal scattering data at 600 K
Estimated core lifetime (k_{eff}=1.0000 at end of core life), no shuffling	373 days

The recommended long lifetime core is Configuration 6. 7 irradiation test assemblies in the inner driver and 2 large irradiation volumes in the outer driver. Fuel pins are 10% larger but have the same enrichment scheme. Then outer radial reflector is composed of MgO blocks like the moderating region. Different enrichment schemes are presented in Section 2 for shorter core lifetimes. Up to four transient test traps could be located in the radial reflector.

REFERENCES

Abderrahim, H. A. et al. “MYRRHA – A multi-purpose fast spectrum research reactor.” Energy Conversion and Management 63, 2012.

Bignan, G. “The Jules Horowitz Reactor: a new High performances European Material Testing Reactor (MTR) as an International Center of Excellence-Update status and focus on the modern Safety approach.” *International Conference on Research Reactors: Safe Management and Effective Utilization 14-18 November 2011, Rabat, Morocco.* International Atomic Energy Agency, 2011. Presentation.

Bignan, G. et al. “The Jules Horowitz Reactor: A New European Material Test Reactor (MTR) Open to International Collaboration — Update Description and Focus on Modern Safety Approach.” *International Conference on Research Reactors: Safe Management and Effective Utilization, 14-18 November 2011, Rabat, Morocco.* International Atomic Energy Agency, 2011. Paper.

Bignan, G. and Estrade, J. “The Jules Horowitz Reactor : A new high Performances European MTR (Material Testing Reactor) with modern experimental capacities : Toward an International User Facility.” *Joint IGORR 2013 and IAEA Technology Meeting; Daejeon (Korea, Republic of); 13-18 Oct 2013.* Vienna, IAEA, 2013. Paper.

Boyard, M. et al. “The Jules Horowitz Reactor core and cooling system design.” *JOINT MEETING of the National Organization of Test, Research, and Training Reactors and the International Group on Research Reactors September 12-16,* *2005 at the Holiday Inn, Gaithersburg, MD*. National Institute of Standards and Technology, 2005.

Bragg-Sitton, S. “Status of SiC Research for Accident Tolerant Fuels.” Idaho National Laboratory, US Department of Energy, 2013.

Camprini, P. C. et al. “Thermal Hydraulic and Neutronic Core Model for Jules Horowitz Reactor (JHR) Kinetics Analysis.” *Dipartimento di Ingegneria Energetica, Nucleare e del Controllo Ambiental.*. Bologna:Universita’ Di Bologna, 2011.

Chang, J. *Table of Nuclides*. Korea Atomic Energy Research Institute. Web. August 26, 2015.

Chang, Yoon Il. “Technical Rational for Metal Fuel In Fast Reactors.” *Nuclear Engineering and Technology*. Volume 39 No. 3 (2007): 161-170.

Dragunov, Y, G. et al. “MBIR Multipurpose Fast Reactor-Innovative Tool for the Development of Nuclear Power Technologies.” *Atomic Energy*, Volume 113, No. 1, November, 2012 (Russian Original Volume 113, No. 1, July, 2012).

Farrant, D. “The Jules Horowitz Reactor and its Role in UK R&D.” National Nuclear Laboratory, 2014.

Fast Reactor Database 2006 Update. Vienna: International Atomic Energy Agency, 2006. IAEA-TECDOC-1531.

“FY 2009 Advanced Test Reactor National Scientific User Facility Users’ Guide.” Idaho Falls: Idaho National Laboratory. INL/EXT-08-14709. 2009.

Gaillot, S. “The Jules Horowitz Reactor MOLY System.” *Joint Meeting – National organization of Test research & training reactors (TRTR) International Group on Research Reactors (IGORR) September 19-24, 2010, Knoxville, USA*. 2010.

Gerstner, D. and Davis, C. “Thermal-Hydraulic Analysis Results of a Seismically-Induced Loss of Coolant Accident Involving Experiment Out-of-Pile Loop Piping at the Idaho National Laboratory Advanced Test Reactor.” *EFCOG 2012 Safety Analysis Workshop May 2012 Santa Fe, NM.* Idaho National Laboratory, 2012. Presentation.

“Gold Spot Price & Charts.” *JM Bullion.* JM Bullion. Web. August 26, 2015.

Hackett, M. J. and Povirk, G. “HT9 Development for the Traveling Wave Reactor.” *Transactions of the American Nuclear Society* Volume 106 (2012): 1133-1135.

Hilton, B. A. et al. “U.S. Plans for the Next Fast Reactor Transmutation Fuels Irradiation Test.” *Proceedings of GLOBAL 2007 conference on advanced nuclear fuel cycles and systems*, La Grange Park: American Nuclear Society, 2007.

Leppänen, J. “Serpent – a Continuous-energy Monte Carlo Reactor Physics Burnup Calculation Code User’s Manual.” VTT Technical Research Centre of Finland. March 6, 2013.

“Light Water Reactor Sustainability Program Integrated Program Plan.” U.S. Department of Energy Office of Nuclear Energy, Revision 2, 2014.

Macdonald, R. R. and Driscoll, M.J. “Magnesium Oxide: An Improved Reflector for Blanket-Free Fast Reactors.” *Transactions of the American Nuclear Society* Volume 102 (2010): 488-489.

“MYRRHA Multi-purpose hYbrid Research Reactor for High-tech Applications.” Brussels: SCK•CEN, 2011.

Next Generation Nuclear Plant Pre-Conceptual Design Report. Idaho Falls: Idaho National Laboratory, 2007. INL/EXT-07-12967 Revision 1.

“Report of the Nuclear Reactor Technology Subcommittee.” Nuclear Energy Advisory Committee, US Department of Energy, 2014.

Rinard, P. “Neutron Interactions with Matter.” Los Alamos: Los Alamos National Laboratory.

Soppera, N. and Bossant, M and Dupont E., "JANIS 4: An Improved Version of the NEA Java-based Nuclear Data Information System", Nuclear Data Sheets, Volume 120, June 2014.

Sterbentz, J. W. Calculated Neutron and Gamma-Ray Spectra Across the Prismatic Very High Temperature Reactor Core. Idaho Falls: Idaho National Laboratory, 2008. INL/CON-08-13845 Preprint.

Thermophysical properties database of materials for light water reactors and heavy water reactors. Vienna: International Atomic Energy Agency, 2006. IAEA-TECDOC-1496.

Tomberlin, T. A. *Beryllium – A Unique Material In Nuclear Applications.* Idaho Falls: Idaho National Engineering and Environmental Laboratory, INEEL/CON-04-01869, 2004.

Tretiyakov, I.T. et al. “MBIR, a Reactor Facility for Validation of Innovative Designs.” Moscow: NIKIET, 2014.

Tsvetkov, P. V. et al. “VHTR-based systems for autonomous co-generation applications.” *Nuclear Engineering and Design*, Volume 240, No. 10, April 15, 2010.

Tuzov, A. “MBIR, a Reactor Facility for Validation of Innovative Designs.” *Joint IGORR 2014/ IAEA Technical Meeting 17-21 November 2014, Bariloche, Argentina.* Moscow, ROSATOM, 2014.

Van Tichelen, K. “MYRRHA Multipurpose hYbrid Research Reactor for High-tech Applications.” Kraftwerkstechnisches Kolloquium 2014: Kernenergestisches Symposium Dresden, Germany, 14-15 October, 2014.

Westinghouse AP1000 Design Control Document Rev. 19. United States Nuclear Regulatory Commission, 2011.

Xoubi, N. and Primm, R. T. III. “Modeling of the High Flux Isotope Reactor Cycle 400.” Oak Ridge: Oak Ridge National Laboratory. ORNL/TM-2004/251. 2005.

Zayko, I. V. “Neutron-Physical Characteristics of the MBIR core.” *Atomic Energy*, Volume 114, No. 4, August, 2013 (Russian Original Volume 114, No. 4, April, 2013).